RHEINISCH
WESTFÄLISCHE
TECHNISCHE
HOCHSCHULE
AACHEN

PITHA 95/37

Dezember 1995

The Detection of Faint Light in Deep Underwater Neutrino Telescopes

Christopher Henrik V. Wiebusch

III. Physikalisches Institut, Technische Hochschule Aachen

PHYSIKALISCHE INSTITUTE
RWTH AACHEN
52056 AACHEN, GERMANY

The Detection of Faint Light in Deep Underwater Neutrino Telescopes

Von der Mathematisch-Naturwissenschaftlichen Fakultät

— Fachbereich I —

der Rheinisch-Westfälischen Technischen Hochschule Aachen

zur Erlangung des akademischen Grades eines Doktors

der Naturwissenschaften genehmigte Dissertation

Vorgelegt von

Diplom-Physiker

Christopher Henrik V. Wiebusch

aus Bonn

Referent: Universitätsprofessor Prof. G. Flügge
Korreferent: Universitätsprofessor Prof. C. Berger

Tag der mündlichen Prüfung: 7. Dezember 1995

Abstract

The Detection of Faint Light in Deep Underwater Neutrino Telescopes

The new field of high energy neutrino astronomy gives the opportunity to open a new observational window to the universe. This provides a large variety of prospects to investigate new phenomena in astronomy and particle physics. This work concentrates on the two experiments, BAIKAL and DUMAND. Their goal is the permanent operation of large detectors in the deep natural water of lake Baikal and the Pacific Ocean near Hawaii. These detectors consist of a matrix of highly sensitive optical sensors built for the detection of Čerenkov-light of charged secondary particles, especially muons, originating from neutrino interactions. Because the sensors are sensitive to all sources of faint light such as bioluminescence or radioactivity, these experiments provide interdisciplinary aspects of research in Biology, Environmental and Ocean science. The design of the "European Optical Module" for DUMAND II is presented. This self-contained detector module consists of a new, large area photomultiplier (Philips XP-2600), fast read-out electronics, power-supplies and monitoring transducers packaged in a glass pressure-housing. Measured characteristics and the calibration of these modules show, that the so called "smart PMT" has excellent amplitude and time resolution properties, which will improve reconstruction accuracy and triggering. A second aspect of this work is the development of a general purpose Monte-Carlo program (DADA) for Underwater Neutrino telescopes on basis of the GEANT detector simulation library embedded in a data analysis package (SiEGMuND). In order to avoid long CPU time consuming calculations, specific parameterisations for Čerenkov-light from electro-magnetic, hadronic cascades and secondary energy loss processes during muon propagation are derived and their influence on measured detector signals, especially in the BAIKAL NT-200 detector, investigated. A comparison of simulation results for atmospheric muons with experimental data of the BAIKAL NT-36 detector shows good agreement and yields $(6.75 \pm 0.54) \cdot 10^{-7} cm^{-2} s^{-1} sr^{-1}$ for the vertical atmospheric muon intensity. The light, which originates from radioactive ^{40}K decays in the ocean, has to be considered as a background signal in muon measurements. On the other hand it provides a constant isotropic photon flux. A measurement of these signal rates allows a continuous measurement of the water transparency, which can be used for detector monitoring and applied research.

This work is supported by the *Claussen Stiftung im Stifterverband für die Deutsche Wissenschaft* (Projekt-Nr.:TS 082/48/92).

Contents

1 Introduction

Но он не страшен. Всё пройдёт. Страдания, муки, кровь, голод и мор. Меч исчезнет, а вот звёзды останутся, когда и тени наших тел и дел не останутся на земле. Нет ни одного человека, который бы этого не знал. Так почему же мы не хотим обратить свой взгляд на них? Почему?

Aber man braucht sich nicht zu fürchten. Alles wird vorübergehen: Leiden, Qualen, Hunger, Blut und Massensterben. Das Schwert wird verschwinden, aber die Sterne werden auch dann noch dasein, wenn von unseren Leibern und Taten auf Erden kein Schatten mehr übrig ist. Es gibt keinen Menschen, der dies nicht wüßte. Warum also wollen wir unseren Blick nicht zu den Sternen erheben? Warum?

Michail Bulgakov, Белая Гвардия *(Die weiße Garde), 1924*

In 1930 Wolfgang Pauli quipped "having done a terrible thing". He postulated the existence of an undetectable particle, the *neutrino*. Fortunately the un-detectability was disproved by Clyde Cowan and Fred Reines with the direct experimental detection in 1956. Since then the neutrino played a double role in the process of understanding the fundamentals of nature. On the one hand the neutrino is a "miraculous" particle, which hardly reveals its properties. It is still uncertain, whether it has a mass at all. On the other hand, the neutrino has been one of the most important sources of innovation in modern physics. Very dramatic examples have been the fall of the parity conservation law (1957) and the detection of weak neutral currents (1973). Deep inelastic scattering experiments with neutrinos and electrons onto nucleons established the parton model of the nucleon and thus the inner structure of matter. [135, 130]

A conclusion may be drawn after almost 40 years "neutrino–physics": The major challenge for a neutrino–experiment is to cope with an enormous relative background as a result of the tiny probability of a neutrino to interact with matter. Whenever experimentalist succeeded with this, they could be almost certain, that the neutrino probe would provide a very clean view into the subatomic world and often exciting new results.

Historically the achievement of the *"Standard model"* is comparable to the invention of the periodical table of elements by Mendeleev last century. It allows not only to order all known elementary particles, but also to understand the systematics of their interactions.
Within this model, matter is build up by a few fundamental point-like, spin 1/2 particles, *quarks* and *leptons*. Both families consist of 6 members, ordered in three "generations", each with two members. The charges within one generation are $+2/3$ and $-1/3$ for quarks and -1 and 0 for leptons. Each quark and lepton has a corresponding anti–particle which is identical except for an opposite value for the charge and the flavour quantum number (for quarks) and the lepton quantum number (for leptons).
Three fundamental forces, *strong*, *electro-weak* and *gravitation*[1] are responsible for all interactions between these particles. They are mediated by another class of fundamental particles, the *gauge-bosons*. The six quarks (*up-, down-, strange-, charm-, bottom- and top-*) carry "colour", which is the "charge" of strongly interactions. They interact *strong* via eight (also coloured) bosons, called *gluons*. In addition they experience *electro-weak* interactions via four gauge bosons, the photon (γ), responsible for electro-magnetic interactions, the Z^0 responsible for weak neutral currents and the $W^\pm$ responsible for weak charged currents. The six leptons, perform only electro-weak interactions. Three are charged: electron, muon and tau (e^-, μ^-, τ^-). Each of them has an uncharged partner, a neutrino: (ν_e, ν_μ ,ν_τ)[2]. Because neutrinos are uncharged, they can only interact weakly. [130, 124]
The neutrinos differ from the anti-neutrinos ($\bar{\nu}_e$, $\bar{\nu}_\mu$,$\bar{\nu}_\tau$) by their helicity, which is the projection of the spin onto the momentum vector. Neutrinos are found to be left–handed — anti–neutrinos are right–handed. One remaining fundamental question still is, whether neutrinos are identical with their anti–partners (Majorana type) or not (Dirac type). With the prerequisite of a finite mass it would

[1] Gravitation is far to weak to play a role in particle physics. Also every attempt to put gravitation into the framework of quantum physics has failed so far. Thus gravitation will be neglected in the following discussions.

[2] Though there is strong experimental evidence for its existence, no direct experimental detection of ν_τ-neutrinos has been successful yet.

be possible for the first case to change neutrinos into anti-neutrinos just by a transformation of the reference system. Thus the detection of a finite neutrino mass could be a hint for new physics beyond the standard model. [74]

Not only on the smallest known scales, in particle-physics, but also for the largest known scales, in astro-physics, neutrinos play an essential role in the understanding of nature.

A fundamental question of cosmology is the fate of the universe. Whether it will expand for ever (open universe) or whether it will finally collapse gravitationally (closed universe) depends crucially on its total mass. Theorists favour exactly the case between these two scenarios: a universe which asymptotically stops expanding in infinite time. In observations we see only so called "bright matter"; matter which is emitting electro-magnetic radiation. This matter adds up to less than 1% of the mass necessary to close the universe. There are strong experimental indications for large amounts of invisible, so called "dark matter" , but astro–physicists are not sure about its total amount and its nature. Because of the incredibly large number of neutrinos in the universe even a small neutrino mass could provide a large amount of the "missing mass".[36, 74]

A recently developed branch in cosmic ray physics, *neutrino-astrophysics*, aims at the detection of neutrinos from extraterrestrial sources.
Besides the photon, neutrinos are the only known <u>stable</u> and <u>uncharged</u> elementary particles. Not affected by interstellar magnetic fields, they do not change their direction and do not loose the information about their origin. The universe has been investigated throughout the total spectral range of electro-magnetic radiation. Investigations in a new spectral range were always accompanied by new fundamental results. Neutrinos are not absorbed in dense matter and provide complementary information to photons, especially from the inside of objects[3]. This gives rise to the hope to open a new, complementary observation window to the universe. The detection of cosmic neutrinos may provide information on another fundamental, still unanswered, question in astrophysics: the *origin* and the *acceleration* of high energy cosmic rays. Last but not least some postulated dark matter particles may decay or annihilate into detectable neutrinos.

These hopes are stirred by two[4] major breakthroughs in neutrino astrophysics.
The detection of solar neutrinos since more than 20 years in presently four experiments[5] gave birth to this discipline and also raised the until now unsolved "Solar Neutrino Problem". These experiments detect a smaller number of neutrinos than expected from the "Standard Solar Model". There is still dispute on the significance of these results due to uncertainties in experimental statistics and theoretical predictions. A possible solution to this problem could be a flavour change of the initial ν_e into ν_μ (or ν_τ), called "neutrino oscillation". This would imply a finite neutrino mass and is the presently most promising hint for new physics beyond the standard model. [121, 31, 15] Two new projects may help to clarify the "solar neutrino puzzle". The Sudbury Neutrino Observatory (SNO) will be capable of measuring all neutrino flavours and the differential energy spectrum, which is necessary to confirm the neutrino oscillation hypothesis. The Super Kamiokande detector is designed about 30 times larger than Kamiokande to detect the solar neutrino flux with high statistics.

The second breakthrough occurred on 23rd February 1987 with the detection of a total of 19 neutrinos in coincidence with the explosion of the supernova SN1987A in two proton decay detectors: IMB and Kamiokande, and a supporting measurement of 5 events in the Baksan neutrino-telescope [21]. The detected number of events matches the number expected from our knowledge on the violent death of a giant star. SN1987A released an energy of about $2.5 \cdot 10^{46} J$, mostly (99%) in form of neutrinos ($\approx 10^{57}$) producing an estimated neutrino-flux of $5 \cdot 10^{10} cm^{-2}$ on earth within a few seconds [121]. With

[3] The detection of solar neutrinos is the first direct experimental proof for the nuclear fusion processes in the Sun's core.

[4] A third important topic, the "atmospheric neutrino anomaly" will be discussed in section 2.2.

[5] Homestake, Kamiokande II & III, Sage, Gallex.

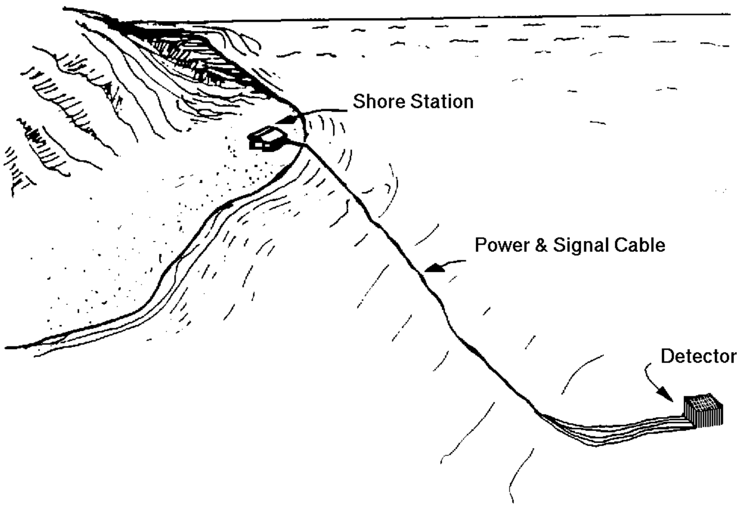

Figure 1.1: Principle of a DUMAND–type detector.

only 19 events many limits on properties of the neutrino like mass, life–time and magnetic moment were measured comparably precise or superior to terrestrial experiments [121]. Kamiokande III is sensitive to supernova explosions up to a distance of about $50 - 80kpc$. An explosion within our galaxy would produce several 100 events. No further supernova signal has been observed since 1987. Future experiments will be even more sensitive [28, 121]. Both experiments, IMB and Kamiokande, used the "Water–Čerenkov–technique" to detect neutrinos and showed that this is an appropriate detection method for neutrino telescopes.

Crucially for the construction of a neutrino–telescope are both the background due to other cosmic rays and the extremely rare occurrence of neutrino interactions. The first problem can be solved by locating the experiment several km underground with a large amount of matter on top as a shielding to absorb almost all other cosmic rays. A solution to the second problem is found by enlarging the detection volume as much as possible.
Within the DUMAND[6] approach natural water is used as detection medium to study high energy neutrino interactions and to search for high energy astrophysical neutrino sources. A schematic sketch is shown in figure 1.1. A detector is located deeper than $1km$ under water and connected to a shore station via cables for signal transmission and power supply. High energy neutrino interactions produce secondary (charged) particles which emit Čerenkov-light along their track. This light is detected with highly sensitive optical sensors. The clarity of natural water in this depth and the available space allows the realisation of large detection matrices.

The current step is to increase the sensitive volume from about $\sim 10^3$ to $10^4 m^3$ realized in underground experiments[7] to about $\sim 10^6 m^3$. This attempt has suffered from several drawbacks, particularly due to the remote location under "free nature conditions". It took several years for approval and development of appropriate technologies. After two decades of preparation with several test-detectors, the experiments: BAIKAL – NT-200, in the deep Siberian lake Baikal (Озеро Байкал), and DUMAND II , in the Pacific Ocean close to Hawaii, are in the stage of turning to permanent operation[8]. A first small detector, BAIKAL – NT-36, is in operation since spring 1993 [94].

The unique location in a natural environment implies a strong interdisciplinary cooperation between

[6] DUMAND = **D**eep **U**nderwater **M**uon **A**nd **N**eutrino **D**etection

[7] MACRO:$\sim 8 \cdot 10^3 m^3$, Kamiokande-II: $\sim 3 \cdot 10^3 m^3$, IMB:$\sim 7 \cdot 10^3 m^3$.

[8] Also the AMANDA experiment, using a similar approach in the deep clear ice of the antarctic glacier, is starting with permanent operation.

various scientific disciplines. When these detectors are completed, they will act as underwater laboratories and measure continuously environmental parameters such as temperature, salinity and currents in the deep water. Several subjects of research in biology, geology or environmental sciences are obvious: investigation of bioluminescence, sedimentation, seasonal and other long term variations of environmental parameters. Within an optimistic scenario a tomography of the inner earth seems possible if bright and time–stable sources of astrophysical neutrinos are found.
Apart from scientific subjects, technological aspects play an important role. The remote location deep underwater with rough conditions like extreme temperatures, pressure and strong corrosion in oceans require new technologies and strong checks on quality assurance. Within these experiments several major technological innovations have been born.

A further scientific step will be to increase the sensitive volumes further by several orders of magnitude to a detector of km^3 size. Several proposals have been made. Experience with present detectors and technologies under operational conditions are significant for the further development of this ambitious project. [42, 119, 100]

Within this treatise astronomical models for possible sources of high energy neutrinos and their detectability are reviewed in chapter 2. The Čerenkov effect used for the detection of charged particles deep underwater as well as other sources of faint light in deep water are described in chapter 3. Current experiments are discussed in section 4. Chapter 5 gives a close view on the development and properties of the highly sensitive optical sensors used in these experiments. The simulation and analysis software is described in chapter 6 and results are shown in chapter 7. Experimental results from the NT36–detector are compared with simulations in chapter 8. From these results, conclusions on the detection of faint light in next generation neutrino-telescopes are drawn.

2 High Energy Neutrino Astrophysics

2.1 Neutrino production

The atmosphere of the earth is steadily bombarded by an isotropic flux of various elementary particles, mostly protons and heavier nuclei, called *"primary cosmic rays"*[1]. Energies higher than $10^{20} eV$ have been observed. The energy spectrum follows a power-law

$$dN(E) \sim E^{-\alpha} dE \qquad \text{with} \begin{cases} \alpha \approx 2.7 & \text{for } E < 100TeV \\ \alpha \approx 3.0 & \text{for } E > 100TeV \end{cases} . \tag{2.1}$$

Instead of the *power-law index* α, frequently the *spectral index* $\gamma \equiv \alpha - 1$ is used. The spectrum steepens above $\sim 100TeV$ ($\alpha \sim 3.0$). Above $\sim 10^6 TeV$ the spectrum seems to flatten again to $\alpha \sim 2.7$.[22, 123, 129]
The mechanism generally thought to be responsible for the acceleration to highest energies is called "*first order Fermi acceleration*". It describes the acceleration of charged particles due to relativistic shock fronts moving through turbulent plasma. Calculations yield a power-law spectrum with $\alpha = 2+\delta$ where δ is a small number. A power-law spectrum with the value $\alpha = 2.0$ corresponds to acceleration with a constant amount of power per decade energy. A second mechanism "*second order Fermi acceleration*" also yields a power law-spectrum. It describes the stochastic acceleration of particles diffusing through turbulent moving plasma and is less efficient. It is generally assumed, that cosmic rays are mostly confined by magnetic fields within our galaxy. To compare the theoretical spectrum with observations it has to be taken into account, that the probability for a particle to escape from the galaxy depends on its energy. From the relative absence and abundance of certain elements in the composition of primary cosmic rays one finds a characteristic escape time $\tau(E) \propto E^{-\kappa}$ with $\kappa \approx 0.6$ below $100TeV$. A comparison with the primary spectrum yields

$$dN(E) \sim E^{-(2+\delta+\kappa)} dE \ , \tag{2.2}$$

and thus $\delta \approx 0.1$. This is consistent with the assumption, that the accelerator has a hard spectrum ($\alpha \approx 2.1$) as expected for shock acceleration. [129, 123, 22]

Though the origin of high energy cosmic rays is uncertain, many models predict point sources which also emit large fluxes of high energy gamma-rays and neutrinos. Excluding low energy neutrinos synthesised in the centre of the sun or during supernova explosions, only energies above $100MeV$ are considered during the following discussions.
These neutrinos are assumed to be produced in inelastic interactions of accelerated protons with a target. This mechanism is called "*astrophysical beam dump*". As sketched in figure 2.2 high energy protons hit onto matter and secondary pions and kaons are produced. Charged pions decay into muons and neutrinos and neutral pions into gamma-rays. Different production mechanisms suggest a further distinction by their energy range

- **Very High Energy** (VHE), $E_\nu > 100GeV = 10^{11} eV$

  Neutrinos of this energy are produced in collisions of accelerated nucleons with protons in a target gas around an astrophysical accelerator.

$$\begin{array}{lll} p+p & \longrightarrow & \pi^{\pm} + X \\ & & \hookrightarrow \ \mu^+ + \nu_\mu \quad (\mu^- + \bar{\nu}_\mu) \\ & & \qquad \hookrightarrow \ e^+ + \nu_e + \bar{\nu}_\mu \quad (e^- + \bar{\nu}_e + \nu_\mu) \\ & \longrightarrow & \pi^0 + X \\ & & \hookrightarrow \ 2\gamma \end{array} \tag{2.3}$$

[1] In contrast to *secondary cosmic rays* which are measured at the surface of the earth.

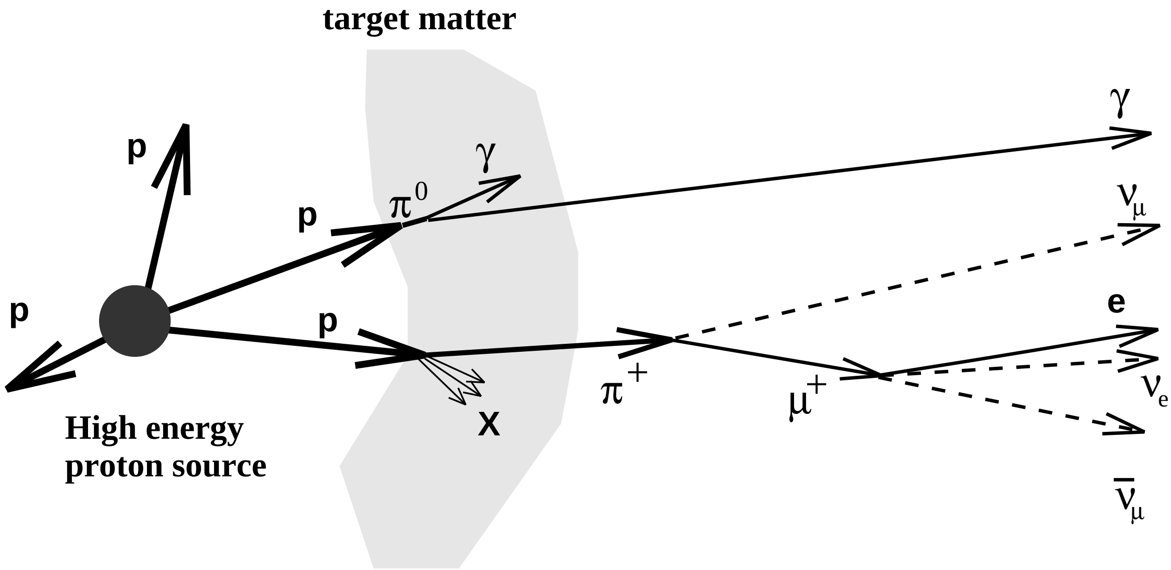

Figure 2.2: Principle of an "astrophysical beam dump"

If the material density in the target is too high ($> 10^{-6}gcm^{-3}$), charged pions do not decay but are reabsorbed; muons loose energy before they decay and the energy spectrum of neutrinos steepens.

- **Ultra High Energy** (UHE), $E_\nu > 1PeV = 10^{15}eV$
  Unlike the case of VHE–neutrinos a dense photon gas acts as a target, a situation realised in active galactic nuclei (**AGN**).

$$
\begin{aligned}
p + \gamma \quad &\longrightarrow \quad \Delta^+ \\
&\hookrightarrow \quad p + \pi^0 \\
&\hookrightarrow \quad n + \pi^+
\end{aligned}
\tag{2.4}
$$

The pions decay according to eq.(2.3). Other reaction channels are e.g. $p\gamma \rightarrow \Delta^{++} + \pi^-$. The pion production threshold depends on the temperature of the photon gas. For optical photons it is typically of the order of PeV in the laboratory rest frame.

The energy spectrum of these "point–source" neutrinos is expected to follow closely the hard power law spectrum of the accelerator itself ($\alpha \approx 2.1$). The matter density necessary for the generation of sufficiently large neutrino fluxes is not very high. Column densities of typical accretions disks ($25 - 50gcm^{-2}$) are high enough, but also thin coronae of these disks may produce up to 10% of the maximum possible neutrino yield. [13, 85, 123, 134]
In general the neutrino flux resulting from decaying mesons can be parameterized via

$$
\frac{dN_\nu}{dE_\nu} = \frac{N_0(E_\nu)}{1 - Z_{N,N}} \left(1.0 \cdot \frac{A_{\pi,\nu}}{1 + B_{\pi,\nu} \cos\theta E_\nu / E_\pi^C} + 0.635 \cdot \frac{A_{K,\nu}}{1 + B_{K,\nu} \cos\theta E_\nu / E_K^C} + (\ldots) \right) , \tag{2.5}
$$

where A, B, Z are constants which depend on the power-law index, hadronic interaction and decay parameters, θ is the incident angle of the proton. The first term represents the contributions from pions, the second from kaons and $(\ldots)$ further contributions due to other mesons. Each term is multiplied with a branching ratio factor (e.g. 0.635 for $K^\pm \rightarrow \mu\nu_\mu$). The competition of the two processes: decay and absorption, is represented by the critical energy factor E_i^C. For $E_\nu << E_i^C$ all parent mesons decay. [123, 37]

An important aspect for terrestrial observations is the comparison of the gamma and neutrino yield. It is characterised by the ratio

$$\mathcal{R}_{\nu/\gamma} \equiv \frac{N_\nu}{N_\gamma} \; . \tag{2.6}$$

In a simple balance of the production mechanisms (eq.(2.3) and (2.4)) one gets $\mathcal{R}_{\nu/\gamma} \approx 1$. In more detailed calculations, the absorption of pions, energy loss of muons, electro-magnetic cascading and absorption has to be taken into account. Though for high matter densities $\mathcal{R}_{\nu/\gamma}$ may become smaller 1. More realistic models predict a ratio from 1 to 30, due to absorption of gammas. Depending on the type and distance to the source, additional absorption mechanism occur and may dramatically reduce N_γ and thus increase $\mathcal{R}_{\nu/\gamma}$. These are

1. Absorption of gamma-rays in matter.

   Many sources are encapsulated by thick dust and gas clouds. These clouds are either directly correlated with the source, e.g. a thick accretion disk around a massive black hole, or the source lives in a region of dense interstellar gas. These sources are called "hidden sources".

2. Gamma gamma interaction within the source.

   At UHE energies gammas interact with thermal photons via $\gamma\gamma \rightarrow e^+e^-$. The threshold energy E_γ for this process is given by $\sqrt{E_\gamma \cdot E_{phot}} \geq m_e c^2$ and the absorption length is $\propto T_{phot}^{-3}$, with the temperature T_{phot} and the energy E_{phot} of the photons. PeV-gammas are suppressed by microwave photons and TeV-gammas by optical and UV photons. Especially accretion disk coronae of AGN show high UV-photon densities, that may reduce the gamma flux down to 10^{-5}.[85, 123, 134]

   A second process is pair production of gammas in strong transverse magnetic fields with the threshold condition $E[eV] \cdot B[G] \geq 4 \cdot 10^{18}$. A transverse magnetic field larger $4 \cdot 10^6 G$ suppresses TeV- and $4 \cdot 10^3 G$ suppresses PeV-gammas.[81]

3. Gamma gamma interaction with the micro-wave background radiation.

   At high energies gammas may interact with the $3K$ background radiation. The probability to become absorbed depends on the gamma energy and rises linearly with the distance to the source. The absorption is maximal for $E_\gamma \approx 2 \cdot 10^{15} eV$ and accounts typically for a factor of 5 for sources within our galaxy and several orders of magnitude for extra-galactic objects. Therefore the experimental observation of high energy gammas from distant sources is unlikely. [85, 123]

As a conclusion, neutrino fluxes might be of comparable magnitude but can not be directly derived from the flux of gammas. On the contrary predictions require a detailed knowledge of the specific astronomical object itself. A simultaneous measurement of both, neutrinos and gammas, is desirable, to reveal the characteristics of the source and thus determine information about the initial proton beam. [85]

2.2 Neutrinos from heaven

Predictions of neutrino and gamma fluxes from "cosmic accelerators" depend on specific models. However "guaranteed" sources of high energy cosmic neutrinos do exist and fluxes can be predicted with higher accuracy.

2.2.1 Atmospheric neutrinos

High energy neutrinos are produced in the earth atmosphere due to interactions of primary cosmic rays according to eq.(2.5). Typical values for the critical energies are: $E^C_{\pi^\pm} \approx 115 GeV$, $E^C_{K^\pm} \approx 850 GeV$ and

$E^C_{D^\pm} \approx 4 \cdot 10^7 GeV$. Muons with energies larger than $\approx 2GeV$ reach the surface of the earth and stop before decaying. Detailed calculations of the neutrino flux and its energy spectrum consider additional effects such as: details of the primary cosmic ray spectrum and composition, influences of the earth magnetic field (in dependence on the latitude and solar cycle) and energy loss of muons.
The result of these calculations is a uniform but not isotropic angular distribution (see figure 2.7 A). The energy spectrum follows the primary spectrum with a power-law index $\alpha \approx 2.7$ up to $\sim 100GeV$ and becomes steeper ($\alpha \approx 3.7$) above. The spectrum of electron neutrinos, which are produced by muon decay, is one power steeper. The spectrum has a broad maximum at $30 - 40MeV$ due to decays of stopped muons and pions. For the ratios of electron– to muon–neutrinos at sub GeV energies, one expects

$$\frac{\nu_e}{\nu_\mu} \approx 0.5 \ , \quad \frac{\bar{\nu}_\mu}{\nu_\mu} \approx 1 \ , \quad \frac{\bar{\nu}_e}{\nu_e} \approx \frac{\mu^-}{\mu^+} < 1 \ . \tag{2.7}$$

For high energies $\sim 100TeV$ the production of charmed mesons (e.g.$D^\pm$) becomes important. Due to the high value of $E^C_{D^\pm}$ charmed mesons always decay. Therefore the expected *"prompt neutrino"* spectrum is isotropic and follows the primary spectrum up to highest energies. Prompt neutrinos may dominate the atmospheric neutrino flux above $100TeV$. Predictions of the *"prompt neutrino"* flux are difficult, because cross sections depend on the small-x behaviour of the gluon structure function[2]. [37, 123]

Atmospheric neutrinos provide a standard source for the calibration of neutrino telescopes but also provide interesting aspects of investigations. So far physicists and other humans believe to have observed a few thousand atmospheric neutrino events mostly in the experiments Baksan, IMB and Kamiokande. In contratiction to expectations eq.(2.7), the measurements in IMB and Kamiokande show almost the same number of electron– and muon–neutrinos. These results are supported by the Soudan 2 experiment but are in contradicted by the Frejus and Nusex experiments; the latter three have a lower statistics. In addition to the "solar neutrino problem" (see chapter 1) these measurements may be an indication for neutrinos oscillations. Larger detectors will provide higher statistics and thus allow the investigation of the ratio in dependence of the zenith angle. This corresponds to a variation of the "oscillation length" in the range from $10km$ to 10^4km. More accurate predictions of the absolute fluxes for each neutrino flavour are necessary to judge whether a deficit of muon–neutrinos or an excess of electron neutrinos occurs. [37, 123]

2.2.2 The sun and the galactic plane

Similar to processes in the atmosphere, cosmic rays interact with interstellar gas in our galaxy. Produced mesons are not absorbed and the neutrino spectrum follows the primary spectrum with $\alpha \approx 2.7$. The flux depends on the density of the interstellar gas and the intensity of cosmic rays. Its origin is mainly the galactic plane and is eventually concentrating in point–like sources from gas clouds in spiral arms. Expected event rates in detectors are significantly smaller compared to atmospheric neutrinos and only marginally detectable. Even with the assumption of a locally higher cosmic ray intensity the total expected event rate for a large 10^5m^2 detector is of the order of ~ 10 and e.g.≤ 1 from the direction of Orion ($0.5kpc$ away). [37]

The solar atmosphere is much more tenuous than that of the earth, hence producing a harder ν-spectrum at high energies. Calculations predict more events from the direction of the sun compared to the atmospheric background from the same direction. Unfortunately event rates are small, and the detection becomes likely only for a large (km^3) detector. [37]

[2]Future results, especially from HERA, may help to improve calculations, e.g. [55].

2.3 Neutrinos from hell

In a standard model for the origin of cosmic rays one assumes that the acceleration takes place when shock waves from exploding supernovae move through the interstellar medium. However, due to the finite life time of the shock front, acceleration to energies higher than $100TeV$ is difficult to explain within this model. A popular solution are additional cosmic rays due to acceleration within the extreme conditions of some compact galactic objects and for the highest observed energies in extra-galactic objects. Two processes, accretion and strong magnetic fields, allow acceleration to highest energies in short time-scales. Several astrophysical objects show a tremendous amount of energy output and may well serve as "candidate hells" to produce sufficiently large neutrino fluxes. If these objects are indeed responsible for a highly efficient acceleration to highest energies, they have to be considered as the "hottest" regions known in the universe. [123]
Mainly three different categories of possible accelerators could gain sufficient power and neutrino luminosity:

1. Young type II supernovae remnants.
2. A neutron star or a black hole in a X-ray binary system.
3. Accretion of matter onto a super-massive black hole in galactic nuclei.

It must be pointed out, that other models, extending the basic supernova blast model, do not predict point sources of neutrinos or gammas. [37, 123]
A standard neutrino source may be defined as an accelerator of protons with the luminosity $L_p \approx 10^{41}$ submerged in a cloud of gas with low density located at a distance of $R_0 \sim 10kpc$. The neutrino luminosity Q^S_ν can be related to the proton luminosity of the source via

$$Q^S_\nu(E)dE = \Upsilon_{\nu_i} \cdot \frac{(\alpha-2)\cdot(\alpha-1)}{1-\kappa^{\alpha-1}} \cdot L^S_p \cdot E^{-\alpha} \cdot dE \ , \tag{2.8}$$

where $\kappa \approx 0.5$ is the fraction of energy retained by the proton in a nuclear collision. Υ_{ν_i} is the neutrino yield for the flavour ν_i and depends on the power-law index α. Calculations for $\alpha = 2.1$ predict typically $\Upsilon_{\nu_\mu+\bar{\nu}_\mu} \approx 12.8\%$, $\Upsilon_{\nu_e+\bar{\nu}_e} \approx 5.9\%$ and $\Upsilon_\gamma \approx 11.6\%$.[13]

2.3.1 Pulsars

Pulsars are young, fast rotating neutron stars. These objects have masses of $1-3$ solar masses compressed to an object of $\sim 10km$ diameter. Due to fast rotation and very strong magnetic fields at the surface, they are excellent accelerators for particles up to energies of more than $10^{20}eV$. Within a so-called "*light cylinder*"[3] around the rotation axis magnetic field lines are closed and co-rotate the star. Outside the field has a spiral character. (see figure 2.3)
The total amount of stored rotational energy is of the order of $\sim 10^{50}erg$. The energy loss may be up to $10^{39}erg/s$ and is not expected to be emitted as magnetic dipole radiation, but rather to drive a relativistic wind of electrons and positrons. Especially near the light cylinder also ions may be accelerated to relativistic energies. The total energy for the *Crab* pulsar is assumed to $2.5 \cdot 10^{49}erg$ and the energy loss $6.4 \cdot 10^{38}ergs^{-1}$. [132, 89]
Particles may stream along the unclosed polar magnetic field lines. Material flows onto the polar regions, where the magnetic fields reaches typically[4] $10^{12}-10^{13}G$. A rough estimate of the maximum

[3] The radius is given by $R_c \equiv c/(2\pi\nu)$, with the speed of light c and the rotation frequency ν.
[4] This high values can be explained by the reduction of the radius of a progenitor star. A typical main sequence star has a surface magnetic field of $100G$.

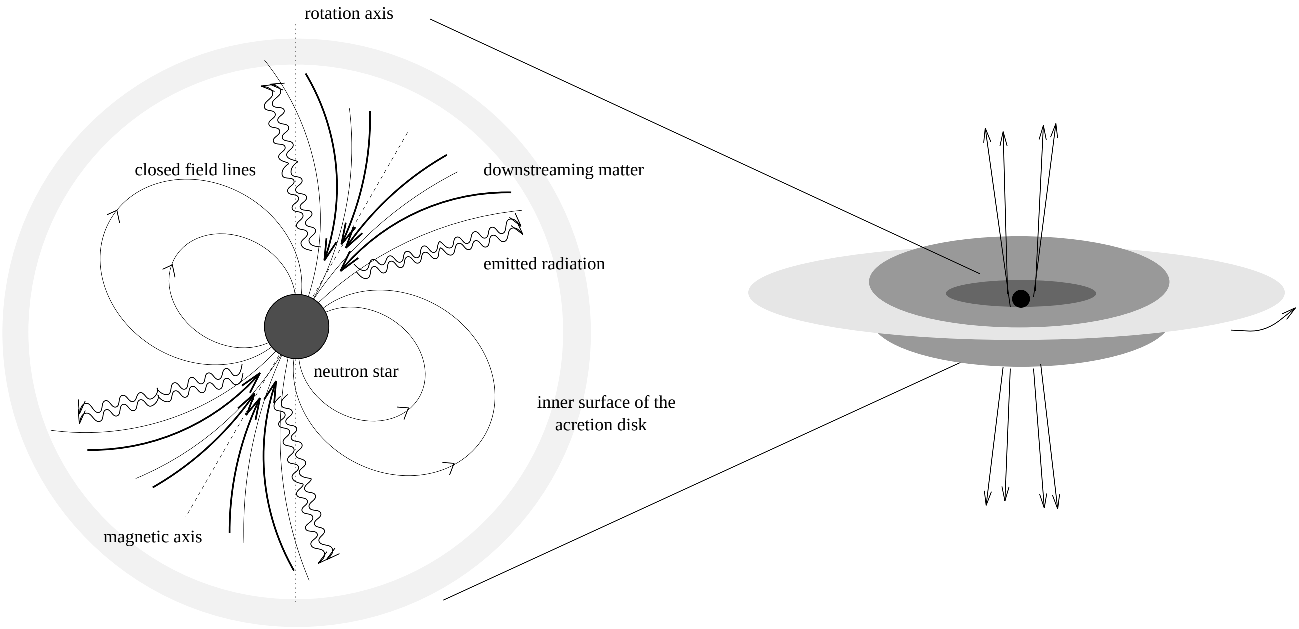

Figure 2.3: Accretion onto a neutron star.

proton luminosity is given by the Eddington luminosity

$$L_{Edd} \approx 1.4 \cdot 10^{38} \cdot \frac{M_{neutronstar}}{M_{\odot}}[\frac{erg}{s}] \ , \tag{2.9}$$

which corresponds to the maximum X-ray luminosity that does not stop accretion. For the effective proton luminosity one has to consider a duty cycle in the order of 10% due to the interception of new accretion material. Different scenarios consider: shock fronts and turbulent magnetic fields in the accretion plasma flow, differences in the rotation of the accretion disk and the neutron star, interactions with atmospheres of possible companion stars. Which scenario is preferred depends on the magnetic field of the neutron star. The accretion onto a neutron star is sketched in figure 2.3. [132, 37, 123]

Isolated pulsars are weaker candidates for "bright" neutrino point sources due to the absence of surrounding matter, necessary to generate an "astrophysical beam dump". However a few objects should not be ruled out as candidates for detectable neutrino sources:

Crab is the remnant of a supernova explosion observed in the year 1054 by Chinese astronomers. This system consists of a pulsar (PSR 0531+21) surrounded by a nebula and is approximately $2kpc$ away from the earth. It is the brightest and most energetic source for high energy gammas detected with energies up to $20TeV$ and high statistical significance ($> 45\sigma$). Opposite to lower energies, *Crab* shows no pulsed but steady emission at high energies. Its luminosity above $1TeV$ was measured $\approx 2 \cdot 10^{34} erg/s$ producing a photon flux of $2.5 \cdot 10^{11} cm^{-2}s^{-1}$ with a power-law index $\alpha = 2.4$. [110, 58, 122]

Vela is a similar but older pulsar ($\approx 11000yr$). It is a bright γ-ray source at moderate energies with a distance of only $0.4kpc$. [110, 127]

Geminga is the brightest gamma ray source in the constellation Gemini. It's nature has been recently established as a pulsar giving testimony to a supernova explosion several 10^5 years ago. Though probably an isolated neutron star, its appealing attribute is its extreme close distance to earth which is about $100pc$, probably less than $50pc$. High energy γ observations confirmed pulsed emission with a total luminosity of $6 \cdot 10^{30} erg/s$ above $1TeV$. The power law index between $100MeV$ and $1TeV$ was measured to 2.2. [46, 58]

2.3.2 Supernova remnants

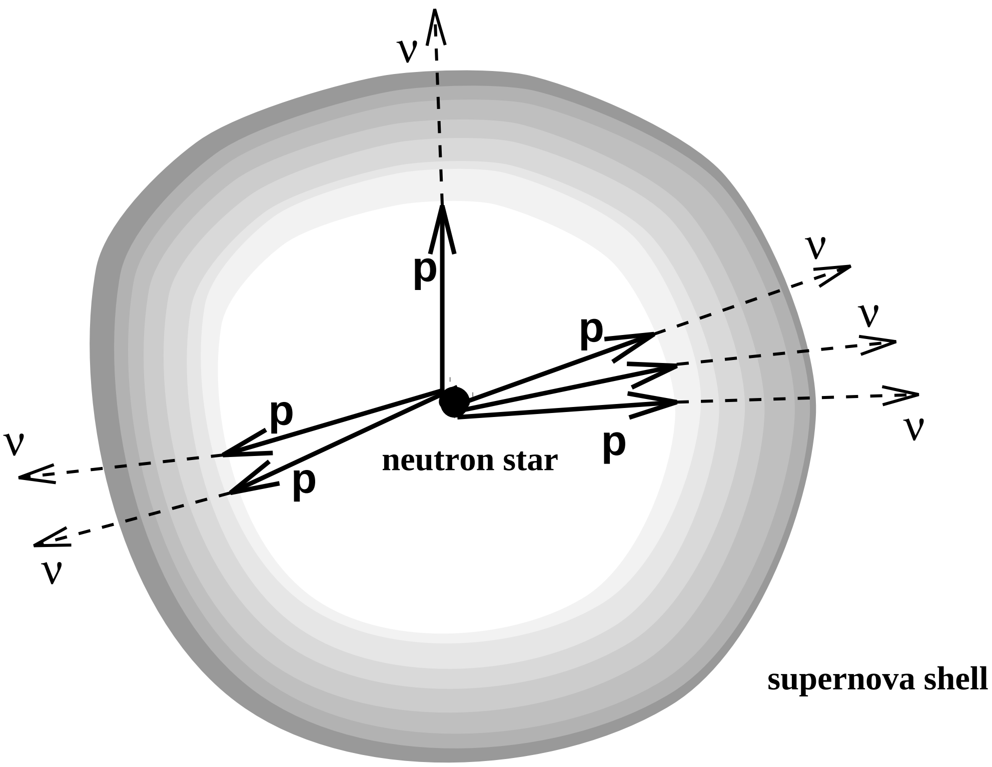

Figure 2.4: Neutron star in a young supernova remnant. Accelerated protons hit onto the expanding supernova shell.

Within young supernova remnants protons may be accelerated either in the strong magnetic field of a fast rotating neutron star or via accretion onto a black hole or neutron star. As sketched in figure 2.4 these protons interact with the expanding shell. High proton luminosities may be gained ($\sim 10^{40} ergs^{-1}$) as well as maximum energies up to $100PeV$. Within two typical times $t_1 \sim 1 - 10$ days and $t_2 \sim 1 - 10$ years these objects correspond to a standard neutrino source eq.(2.8). Before t_1 the shell is too thick, after t_2 only a fraction of the accelerated protons interact and the neutrino luminosity decays quadratically with time. [13, 37, 85]

In addition neutrinos may be generated in the supernova's blast wave itself, due to shock fronts refracted from stellar winds of the progenitor star. This mechanism is very sensitive on the mass loss of the pre supernova and may yield a neutrino signal comparable to the above mechanism for the first 100 days. [13, 37]

SN1987A is the only recently observed close supernova. SN1987A shows no pulsar activity above $10^{37} erg/s$ and is more distant ($50kpc$) than typical galactic supernovae ($10kpc$). Constraints on the proton luminosity derived from the absence of VHE neutrinos $L_p < 10^{42} - 10^{43} ergs^{-1}$ and gamma observations $L_p < 10^{39} ergs^{-1}$ are less stringent than expectations. Neutrino detectors, capable of supernova detection, found no evidence for galactic supernova collapses during the recent years. [13, 37, 67]

2.3.3 X-ray binary systems

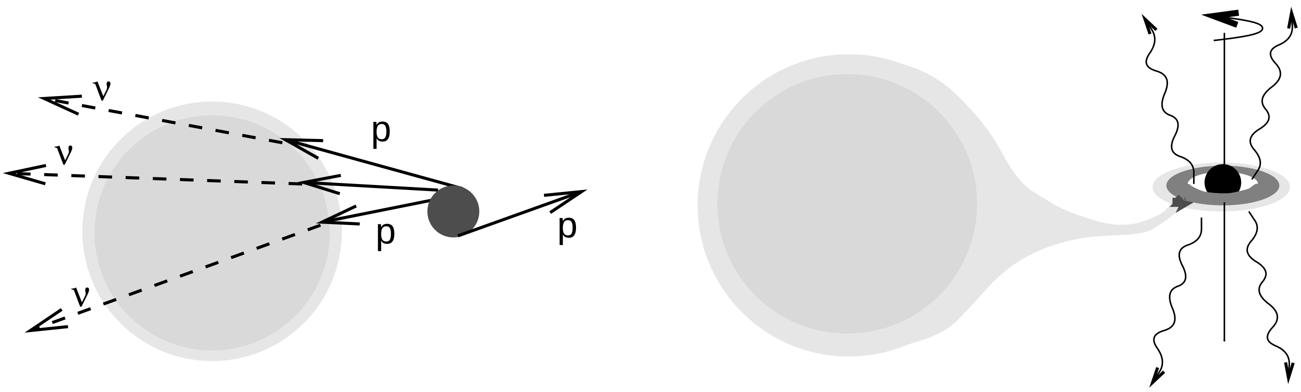

Figure 2.5: X-ray binary systems as high energy neutrino sources. The system is composed of a neutron star or a black hole together with a massive companion star. Protons gain energy either by accretion or magnetic acceleration. Both, the accretion disk itself or the close companion star may serve as target for a "cosmic beam dump"

X-ray binary systems consist of a compact component (black hole or neutron star) together with an ordinary companion star, eclipsing at a short distance. Mass from the star is transferred and accreted onto the compact object. Strong X-ray radiation is released during thermalising of the accreting matter. Emissions show a typical phase modulated character which allows to determine dynamical kinematic parameters of the system. This configuration is sketched in figure 2.5. [44]
These objects are the most luminous objects in our galaxy and may produce proton luminosities up to typically $10^{37} - 10^{38} erg/s$. In early 80' detections of UHE gamma rays with luminosities up to $10^{39} erg/s$ have been reported from the two most prominent objects, *Cyg X-3* and *Her X-1*. These observations have not been confirmed by much more sensitive experiments, scaling down the upper limit for steady gamma flux at UHE energies by an order of magnitude. [132, 123]

Cyg X-3 is obscured by dust of the galactic disk but has to be considered as one of the most luminous objects in our galaxy. One assumes that a neutron star orbits extremely close to a massive Wolf–Rayet-type star. The neutron star may move through the stars envelope inducing strong shock fronts. It's distance is about $10kpc$ and the proton luminosity is estimated to be up to $6 \cdot 10^{38} erg/s$. [81, 76, 123]

Her X-1 Her X-1 is an optically visible binary system consisting of a main sequence star and a neutron star approximately $4kpc$ away from earth. The pulsar has a moderate period but a strong surface magnetic field ($\sim 5 \cdot 10^{12} G$). It's proton luminosity is estimated up to $10^{37} erg/s$. [132, 76, 123, 127]

Cyg X-1 This systems consists of the blue giant star $HDE226868$ ($m \approx 20 - 30 m_\odot$) with an invisible companion of $9 - 15 m_\odot$, which is one of the strongest candidates for a black hole, only $2.5kpc$ distant from earth. This object shows indication for the existence of a pulsar, but a high random-like variability, showing strong radiation bursts of millisecond duration. Its total luminosity is of the order of $10^{37} - 10^{38} erg/s$. [132, 127]

Besides these systems there are further binary objects with X-ray luminosities in the range $10^{33} - 10^{38}$ at distances between 0.5 and $10kpc$. Other objects have been found in the Magellanic clouds. Their emission shows both periodic and random variability with time scales down to milliseconds. Many contain an identified pulsar as compact component. Some have also been reported as very high energy gamma sources. [132, 110, 58]

2.3.4 Other galactic objects

In addition to the frequently occuring X-ray binary systems two other objects within our galaxy[5] have to be considered as detectable neutrino sources.

SS433 is strange object, probably a neutron star or a black hole in a binary system, at $4-5\ kpc$ distance. This object strongly accrets matter. A jet structure with outstreaming gas allows to estimate the total luminosity up to $10^{40} erg/s$. The central engine is strongly obscured by dust preventing this source to be a brilliant gamma source. Observations suggest a situation similar to active galactic nuclei (see section 2.3.5). If a rescaling of the AGN model down to stellar dimensions is appropriate, a possibly high neutrino luminosity and its close distance mark this object as a strong candidate for a detectable neutrino source. [81, 33, 127]

SGR A* (galactic centre) is a strong radio source[6] located at the dynamical centre of our galaxy ($8.5 kpc$ distance), a region which is optically invisible. The emission comes from a central region of a few astronomical units. High rotation speeds of clouds lead to the assumption of a massive ($\sim 10^6 M_\odot$) black hole. Observations show, that the current accretion rate is low[7] and the total proton luminosity does not exceed $10^{39} erg/s$. However the confirmation or exclusion of SGR-A as a power–full neutrino source will yield information about the inner nature of our galaxy. [34, 110, 127]

2.3.5 Active galactic nuclei and quasars

Since the inclusion of the p-γ mechanism (see section 2.1) into earlier models, active galactic nuclei (AGN) have attracted a lot of attention — very high neutrino fluxes with hard spectra are predicted.[86] Observations of AGN show strong variability of typically $100s$ implying a very small emission region. This leads, together with the high luminosity in all spectral regions, to a generic model of AGN and quasars assuming a very massive central black hole ($10^4 - 10^{10} M_\odot$), which is accreting matter at the Eddington limit (eq.(2.9)). Quasi spherical infalling matter builds a shock-front at a radius $R = 10 - 100 \cdot R_s$ with R_s the Schwarzschild radius. Accelerated protons at the shock-front cannot escape due to the instreaming matter, but are dragged into the black hole. $p\gamma$ interactions produce high energy neutrinos, neutral pions initiate electromagnetic cascades. Photons from these cascades are coupled back as target for inflowing protons. Due to the high radiation density (but simultaneously low matter density) high energy gammas interact via $\gamma\gamma \to e^+e^-$. Thus only UV-, X-ray- and soft gamma-ray- radiation escape from the source. The photon gas can be modelled by a combination of the power-law spectrum from the AGN engine and a black body thermal component leading to an UV–bump. Models for neutrino emission from AGN are normalised to the electromagnetic spectral shape and the absolute luminosity of UV and X-ray observations. The total luminosity of AGN ranges from $10^{42} erg/s$ up to $> 10^{48} erg/s$, depending on the mass of the black hole. This corresponds to a typical accretion mass of $1 M_\odot$ per year. The proton luminosity depends on the ratio of the Schwarzschild– and the shock radius and is typically $1\% - 10\%$ of the total luminosity. The maximum achievable proton energy is limited due to energy loss processes. It is approximately proportional to the total luminosity (for $L > 10^{44} erg$). Maximum energies of $10^{19} eV$ can be achieved only by the most luminous quasars. [13, 88, 134, 37]

[5]Other galaxies in our local group may also give lodge to detectable neutrino sources (e.g. LMC-X4) or may be measured as a point-like source themselves, e.g. the Andromeda galaxy (M31).

[6]Recently also detected in the X-ray and gamma light.

[7]There are indications for are stronger activity in the past.

One limitation of this generic model is, that strong constraints on properties of the accretion disk are required in order to satisfy limits on the emission of high energy gammas (diffuse cosmic gamma background). Alternate models do not assume the spherical accretion, but e.g. a proton acceleration in inner disk–accretion regions or at the bases of the jets. Despite of quite different production assumptions, the resulting neutrino flux is comparable (due to X-ray luminosity constrains). [134, 37, 60, 116]

Several AGN (> 25) have been detected recently in GeV gamma rays by the EGRET-experiment on the Gamma Ray Observatory . All these sources are so called "Blazars" (BL-Lac objects), which seem to be AGN with their perpendicular jets pointing into our direction. Acceleration within jets serves as an additional feature of the AGN and provides a large fraction of AGN luminosity and may also produce neutrinos. This is not only supported by several models, but also by the detection of one EGRET source, Mkn421, in TeV gamma rays by the Whipple observatory (see below). A confirmation of even higher energies would clarify if protons are accelerated in AGN. Unfortunately this is unlikely, even for this relatively close AGN due to gamma absorption by IR–background radiation. Though much more powerful, more distant sources are expected to be undetectable in high energy gammas due to the strong attenuation. [134, 37, 116, 115]

The gross of active galaxies is too distant to produce significant individual neutrino fluxes — only a few are relatively close to earth and have a chance of being detected with large neutrino telescopes.

Markarian 421 is the closest (EGRET–)blazar to earth (distance $125Mpc$, red-shift $z = 0.03$). This is the first active galaxy identified with high statistical significance ($> 6\sigma$) in VHE gamma rays ($> 1TeV$) with a flux of $7.5 \cdot 10^{-12} cm^{-2} s^{-1}$ above $0.5TeV$. Its high energy gamma luminosity is calculated to exceed $10^{43} erg/s$. A combined fit to EGRET-Whipple results yields a power-law index of $\alpha = 2.06$. Recently the Whipple observatory reported the detection of a second Blazar **Markarian 501**, $z = 0.034$, with a flux of $8 \cdot 10^{-12} cm^{-2} s^{-1}$ above $0.3TeV$ and a statistical significance of about 10σ. [47, 116]

3C273 is one of the closest quasars ($z = 0.158, \sim 600Mpc$). The X–ray luminosity is of the order of $10^{47} erg/s$. Though detected by EGRET in the GeV range, the detection of high energy gamma-rays is unlikely. Another often quoted "close-by" quasar is the bright "EGRET–source" **3C279** ($z = 0.54$). [134, 127]

Cen A (*NGC 5128*), a large elliptical galaxy, has a very luminous nucleus with an X-ray luminosity of $10^{42} erg/s$. Bursts of typically 50 days are reported in X-rays, but also at UHE energy gamma rays reach luminosities of $10^{43} erg/s$. With $\sim 5Mpc$ *Cen A* is the closest known active galaxy to earth. Two other close active galaxies have to be mentioned. **M87** at a distance of ($\sim 15Mpc$) shows strong jets. **NGC 4151** ($\sim 20Mpc$) is the closest Seyfart galaxy with an X-ray luminosity exceeding several $10^{43} erg/s$. [116, 134, 127]

2.3.6 Diffuse neutrino flux

Though AGN are individually only marginally detectable, the summation of neutrino emission from all AGN and quasars yields a large isotropic (diffuse) neutrino flux. The calculation proceeds similar to calculations of the diffuse X-ray background via an integration of the AGN-luminosity as a function of the red-shift. The total flux is expected to exceed the total atmospheric neutrino flux above $10 - 100TeV$, becoming the dominant source of high energy neutrinos on earth. Already detectors under construction may confirm predictions or set new significant constraints on theoretical models. These prospects are discussed in more details in section 2.4. [134, 37, 60]

2.4 Neutrino detection on Earth

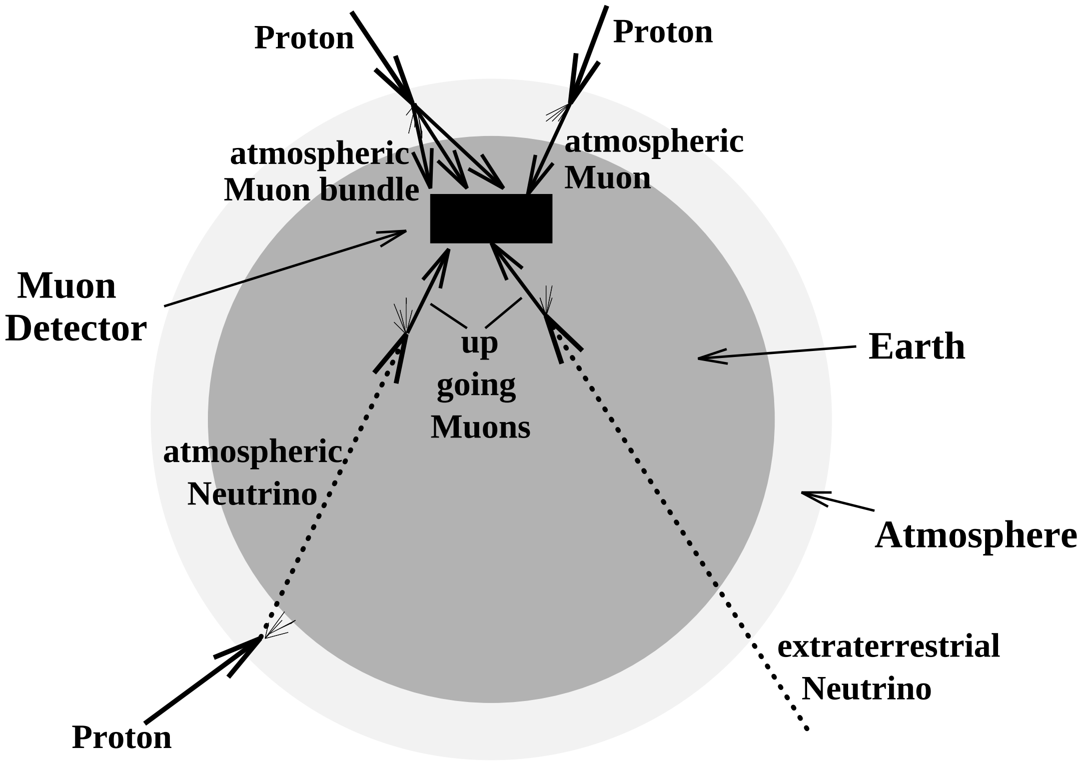

Figure 2.6: Principle of a muon and neutrino telescope.

When neutrinos reach earth, most of them pass entirely unaffected through it — sometimes interactions via the weak force occur — sometimes close to a detector. In case of (anti) muon neutrinos ν_μ a charge current interaction with a nucleon produces a charged muon $\mu^\pm$ and a hadronic cascade X

$$\nu_\mu(\bar{\nu}_\mu) + N \longrightarrow \mu^-(\mu^+) + X \ . \tag{2.10}$$

The muon points almost into the initial direction of the neutrino and may travel a long distance (several km) through matter, possibly passing a detector. The cross section $\sigma_{\nu N}$ for this interaction rises linear with the energy up to $\sim 3TeV$ and changes into a logarithmic growth above. Averaged over ν and $\bar{\nu}$ below $3TeV$

$$\sigma_{\nu N} \approx 0.5 \cdot 10^{-38} cm^2 \cdot E_\nu[GeV] \ , \tag{2.11}$$

and reaches $\sigma \sim 10^{-33} cm^2$ for energies $\sim 10^7 GeV$. The average scattering angle ϑ between the initial neutrino and the muon below $3TeV$ can be approximated by

$$\sqrt{<\vartheta^2>} \approx \sqrt{\frac{m_p}{E_\nu}}[rad] \approx \begin{cases} 5.7^\circ & \text{for } E_\nu = 100GeV \\ 1.8^\circ & \text{for } E_\nu = 1TeV \end{cases} \ . \tag{2.12}$$

[123, 130, 136]

The detection of a muon in a detector and the reconstruction of its direction allows to operate this detector as a *muon telescope*. Figure 2.6 sketches the principle of an underground muon and neutrino telescope. Muons from interactions close to the detector pass through the detection medium. Not all arriving muons in an underground detector are induced by neutrinos. As seen from figure 2.6 muon events are classified as follows:

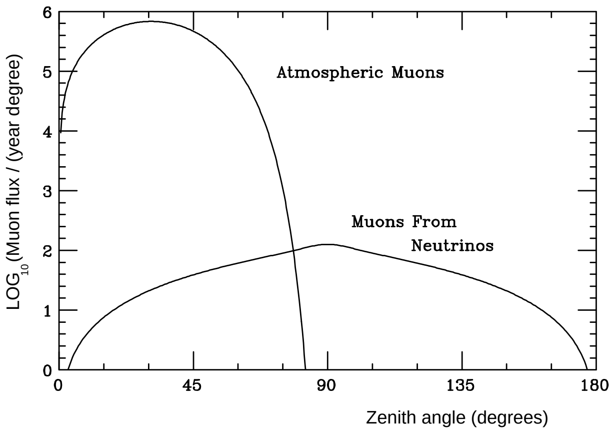

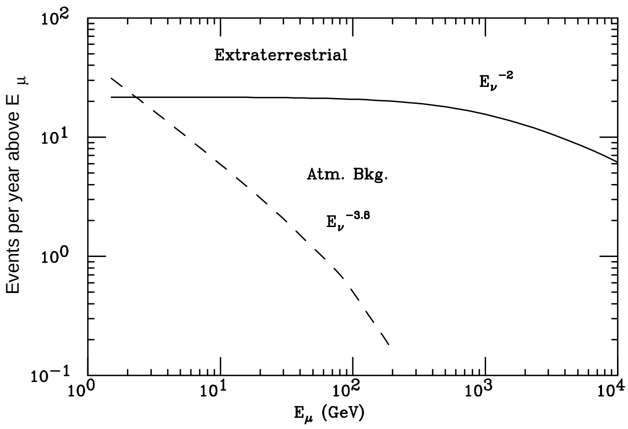

Figure 2.7: Signal and background muon fluxes for neutrino telescopes. (A) shows the angular distribution of atmospheric muons and muons induced from atmospheric neutrinos in DUMAND II . (B) shows the number of upward going muons within 1° above a threshold energy for in the DUMAND II detector from atmospheric neutrinos and an imaginary point–source producing 20 events per year with a power-law index $\alpha = 2.0$ (from [113])

1.Muons induced by cascades from initial protons in the atmosphere reach the detector from above. These muons provide a large flux, but can not travel through the earth and therefore do not arrive from below. Atmospheric muons may arrive in "bundles", which is a group of parallel traveling muons originating from the same initial cascade. (figure 2.7 (A))
2.Muons induced by atmospheric neutrinos arrive from all direction but have a characteristic angular distribution. Their flux falls steeply with the energy. (figure 2.7 (A),(B))
3.Muons induced by extraterrestrial neutrinos, are expected to arrive from all directions and have a hard energy spectrum. (figure 2.7 (B))
An *upward–going–muon*, provides a clear signature for a neutrino induced muon. A selection of these muons enables the operation of a muon telescope as a *neutrino telescope.* [61, 108]
Besides muon neutrinos all neutrino flavours may be detected via charged current or neutral current reactions. Usually the final state particles induce an electro-magnetic or hadronic shower (e.g. $\nu_e N \rightarrow X + e^-$). In contrast to upward going muons, these interactions are harder to detect. This is especially the case for conventional underground experiments, because the effective volume for showers is limited to the geometrical volume of a detector. DUMAND−type experiments are capable of detecting Čerenkov light from these cascades outside of their geometrical volume. This is mainly limited by the attenuation of the Čerenkov light. Especially at ultra high energies extremely large effective volumes are established. At these energies an additional important reaction occurs:

$$\bar{\nu}_e + e^- \rightarrow W^- \rightarrow \left\{ \begin{array}{lll} l^-\nu_l & : & 32.2\% \quad (\mathrm{l: lepton}) \\ \mathrm{hadrons} & : & 67.8\% \end{array} \right. . \tag{2.13}$$

This reaction, called *Glashow resonance*, becomes dominant at an energy of $E_0 = m_W^2/(2m_e) \approx 6.4PeV$. The resonance has a width of $\Gamma = \Gamma_W \cdot m_W/m_e \approx 0.44PeV$. The number of resonant events N_R can be calculated analytically for a power-law neutrino spectrum

$$N_R = \Omega \cdot N_e \cdot \sigma_{eff} \cdot (\alpha - 1) \cdot F_{\bar{\nu}_e}(> E_0) \ , \tag{2.14}$$

with N_e the number of electrons in the detector, Ω the angular acceptance of the detector, G_F the Fermi coupling constant and $F_{\bar{\nu}_e}$ the isotropic neutrino flux above the resonance energy. [13, 136]

For the search of astrophysical neutrinos, the muons from atmospheric cascades and muons induced by atmospheric neutrinos have to be considered as background signals in neutrino telescopes. Figure 2.7 (A) shows the angular distribution as calculated for the DUMAND II detector (see section 4.2.1). Though not traveling upwards, atmospheric muons may be falsely reconstructed and appear as upward going muons, so called *"fake muons"*. The rate of down-going muons R_{down} strongly decreases with depth. Therefore it is possible to reduce this background by locating the detector deeper underground. For the detection of diffuse neutrinos like atmospheric neutrinos or neutrinos from AGN, the rate of fake muons R_{fake} should not exceed the expected signal rate R_{up}. Therefore the rejection factor $\epsilon_R \equiv R_{fake}/R_{down}$ must be

$$\epsilon_R \leq \frac{R_{up}}{R_{down}} \ . \tag{2.15}$$

Typical required values are $\epsilon_R \approx 10^{-6}$ for BAIKAL and $\epsilon_R = 10^{-4}$ for DUMAND.
Searching for astrophysical point sources is easier than for the diffuse flux from atmospheric muons due to two reasons

1. The rate of background signals R_{back} due to atmospheric neutrinos and fake muons is $R_{back} \propto \pi\delta^2$, with the mean reconstruction error δ. In a straight forward estimate[8] the required rejection factor ϵ_R becomes

   $$\epsilon_R \leq N_{pix} \cdot \frac{R_{up}}{R_{down}} \ . \tag{2.16}$$

   N_{pix} is the number of angular "pixels" given by the solid angle of observable lower hemisphere ($2\pi\ sr$) divided by the size of one pixel $9.56 \cdot 10^{-4} \cdot \delta^2\ [deg^2]$

   $$N_{pix} \approx \frac{6566}{\delta^2[deg^2]} \ . \tag{2.17}$$

   Therefore a good angular resolution strongly improves the background rejection of both atmospheric muons and neutrinos.

2. Both, the cross section and the muon range, rise with the energy. Therefore the resulting muon flux induced by neutrinos of a hard spectrum is almost flat in the range of $1GeV - 1TeV$. While a higher detection threshold reduces a possible astrophysical neutrino signal only marginally, the flux of atmospheric neutrinos decreases rapidly with the energy. The higher detection threshold $(10 - 50GeV)$ of deep underwater muon detectors reduces the background rate compared to currently operating underground detectors ($\sim 1GeV$).

Figure 2.7 (B) shows the example of a hypothetic point source, that produces ~ 20 events in the DUMAND II experiment with the expected hard spectrum of a cosmic accelerator ($\alpha = 2$). The picture shows, that the rate of background muons due to atmospheric neutrinos falls off much stronger with energy. It must be pointed out, that background rates in experiments like BAIKAL NT-200 and DUMAND II can be reduced below 1 per pixel and year. These experiments are not "background–limited", but "signal–limited" and the capability of detecting a point source depends mostly on the flux of neutrinos. [101, 110]
The sensitivity to detect a possible neutrino (muon) signal depends on the "size" of the detector. As sketched in figure 2.8 a neutrino interaction occurs outside the detector and a muon passes through the detector. The perpendicular area around the detector within which muons are detected and reconstructed defines the *effective area* A_{eff} of the detector. The effective volume V_{eff} is given by

$$V_{eff} \equiv R_\mu \cdot A_{eff} \ , \tag{2.18}$$

[8] Because of the annual and daily rotation of the earth a source has no fixed position in local detector coordinates. A full calculation considers the explicit angular distribution of fake muons and atmospheric neutrinos convoluted with the reconstruction accuracy and the observation time of the source in a certain direction.

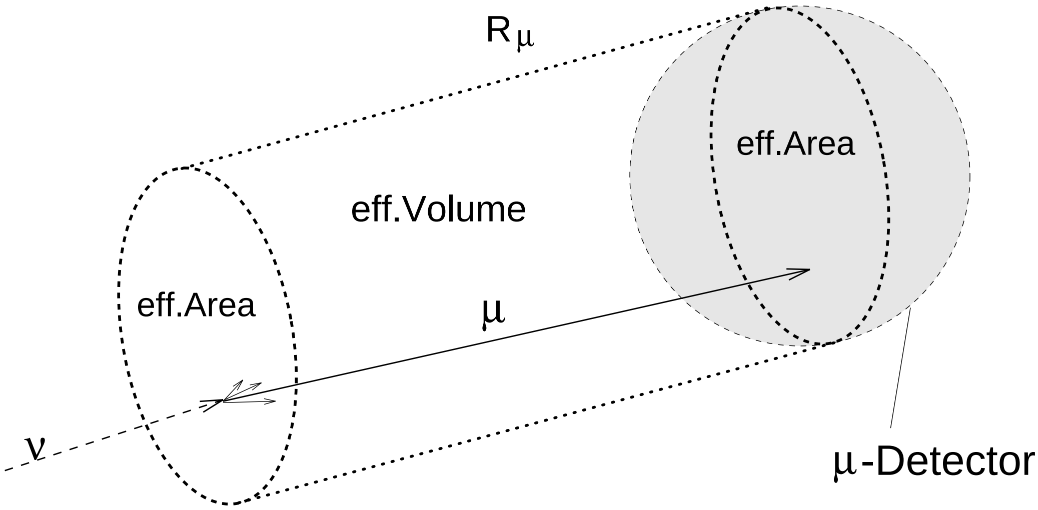

Figure 2.8: Effective area and volume for underground muon telescopes.

with the mean muon range $R_\mu(E)$. Opposite to conventional underground detectors, DUMAND−type detectors have no boundaries and are not limited by their geometrical volume, but rather by their capability of detecting and reconstructing tracks passing outside. On one hand this strongly enlarges the effective volume, on the other it complicates the determination of the quantitative value for the effective area. Both the muon range R_μ and the energy loss rise with larger muon energy giving also a larger A_{eff} and V_{eff}. The effective area is calculated via Monte–Carlo simulations or by comparison of a measured event rate with a known flux, e.g. from atmospheric muons or neutrinos. The effective area depends the efficiency function of a detector for triggering ϵ_{trig}, reconstruction ϵ_{rec} and quality cuts during analysis ϵ_{cut}, which themselves depend on the muon energy E_μ and the direction of the muon $\vec{\Omega}_\mu$.

The actual calculation is performed by simulating a large number N_I of random muons vertices on an initial plane F_I and counting the number of events N_F, that survive all analysis steps

$$F_{eff}(E_\mu, \vec{\Omega}_\mu) = F_I \cdot \frac{N_F(E_\mu, \vec{\Omega}_\mu)}{N_I} \ . \qquad (2.19)$$

Published values for the effective area are usually given for a specific energy and direction or for an event class, averaged over energies and directions.

To quantify the sensitivity of the neutrino telescope one uses the term *"minimum detectable flux"* (**MDF**). This is defined as the minimum neutrino flux producing a 4.5σ excess of a muon signal N_S above a background N_B

$$\frac{N_S - N_B}{\sqrt{N_B}} = 4.5 \ . \qquad (2.20)$$

To calculate the muon flux above a detection threshold $F_\mu(> E_\mu)$, passing through the effective area of a detector one has to convolute the differential neutrino spectrum $f_\nu(E)$ with the neutrino–nucleon cross section and the mean muon range. In the next step $F_\mu(> E_\mu)$ has to be convoluted with the effective area and the observation time of the candidate source, which is the time fraction the source is below the horizon ϵ and the operation time of the detector. Typical values for the MDF are: $F_\nu \sim 1 \cdot 10^{-9} cm^{-2} s^{-1}$ (BAIKAL NT-200) and $F_\nu \sim 1.2 \cdot 10^{-10} cm^{-2} s^{-1}$ (DUMAND II) for a threshold energy $E_\mu > 1TeV$. Comparing VHE gamma fluxes of Crab and Mkn-421 one needs a factor $\mathcal{R}_{\nu/\gamma} \approx 20$ (see eq.2.6) for these sources to be detectable in DUMAND II . [48, 101, 110, 38]

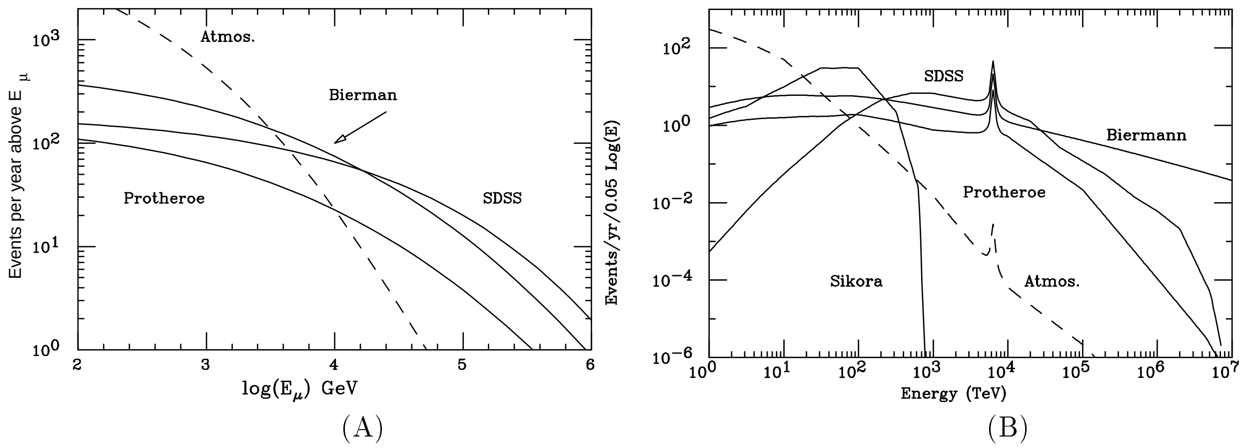

Figure 2.9: Total event rates from AGN according to several models in comparison with atmospheric neutrino events. (A) shows the expected number of upward going muons in DUMAND II versus the muon energy. (B) shows the number of $\bar{\nu}_e$ cascade events in DUMAND II versus the energy. (from [113])

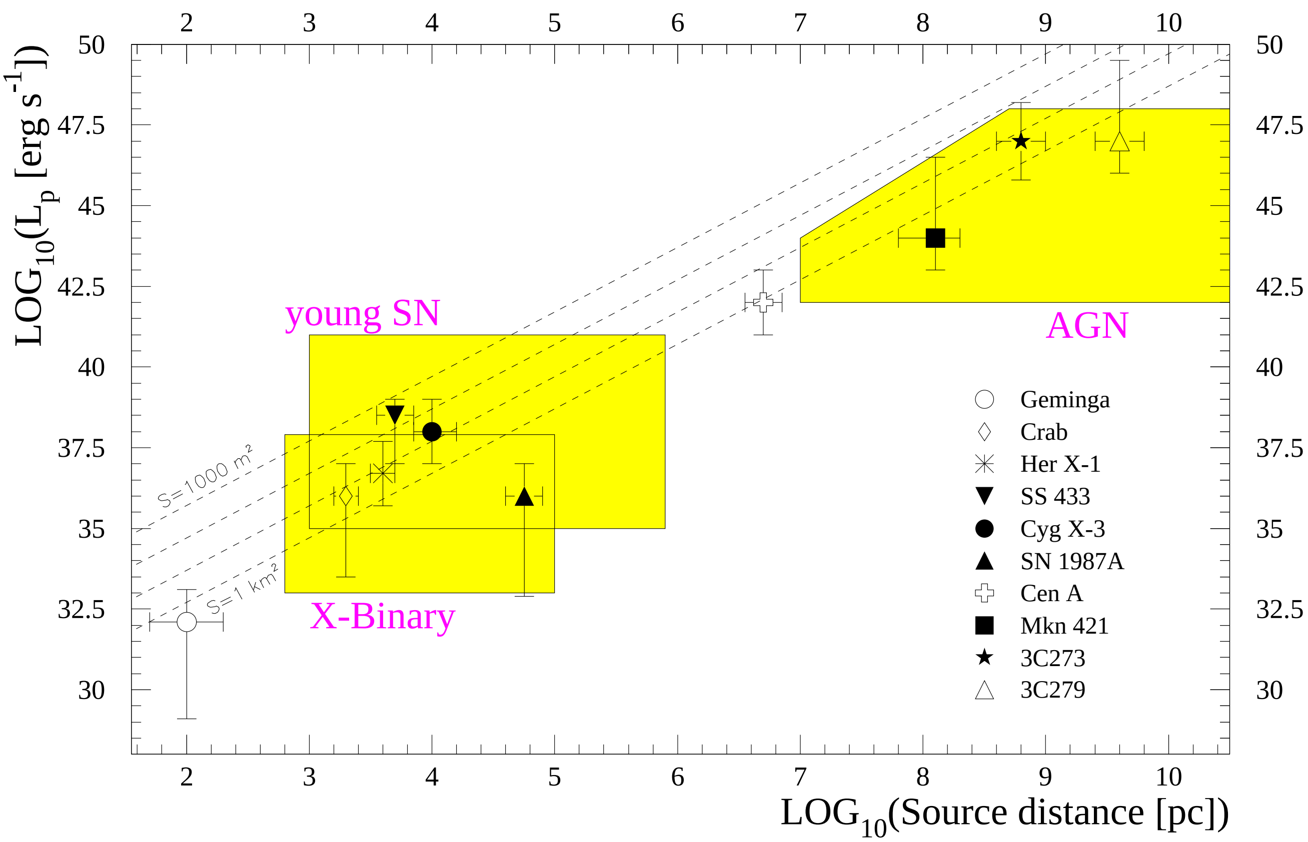

Figure 2.10: Proton luminosity and detectability of individual cosmic neutrino source candidates versus distance. The plot assumes a standard neutrino source eq.(2.8),[13] and the production of about 10 muon events per year above $0.1 TeV$. Dashed lines show typical sensitivity limits of detectors ranging from $1000 m^2$ to $1 km^2$ for 1 year operation. The shaded regions show the areas where typical populations: young supernova remnants, X-ray binaries and AGN reside. The error bars indicate errors of the resulting neutrino flux and the detectability of this source. Especially in case of Mkn 421 the model of a standard neutrino source yields a smaller ν flux than expected from the VHE γ observation. If protons are accelerated in a jet pointing into our direction a larger fraction of the proton luminosity contributes to the ν flux on earth.

The situation is different for diffuse extra-galactic neutrino flux, which is not limited by gamma observations, but rather by the observed X-ray luminosities and measured power-law indices from AGN. Figure 2.9 shows the number of events due to diffuse AGN neutrinos expected in the DUMAND II experiment. Figure 2.9 (A) shows, that the total number of high energy muons exceeds the atmospheric background above $\sim 10TeV$ with a still detectable rate. The importance of the "Glashow resonance" (eq.2.13) at UHE energies becomes clear with a discussion of figure 2.9 (B). The figure shows the expected number of detectable cascade events in DUMAND II versus the energy. The resonant peak is visible at $E_0 \approx 6.5PeV$, producing a clear signal above the background due to atmospheric neutrinos.

It is important to mention, that the earth becomes opaque to neutrinos at UHE energies and the expected angular distribution of events becomes enriched around the horizon. One important application is to use the strong attenuation of the isotropic AGN-neutrino flux to map the inner earth's density profile. If the flux rates are large enough, AGN neutrinos provide a probe to measure the inner earth's composition. [13, 30]

Figure 2.10 shows a summary of estimated luminosities of some discussed candidate sources versus their distance. A small detector is generally bounded to "close-by" sources within our galaxy. Short-time supernova remnants are detectable within our local group. The visibility of X-ray binaries is limited to sources within our galaxy. Individual AGN are only detectable for large detectors. The large gap in detectable sources between the scales of our galaxy to cosmological distances is remarkable. The error bars give only rough estimates on possible errors. Any confirmation or disconfirmation of expected neutrino fluxes will improve the understanding of these objects. [13, 37, 110]

2.5 Neutrinos from dark matter

In addition to the previous discussions, cosmic neutrinos are also powerful probes for the investigation of new and exotic phenomena. Especially in case of super-symmetric dark matter particles, neutrinos may help to identify the nature of dark matter and also to obtain parameters for super-symmetric theories.

Research on the nature of dark matter gave birth to a large variety of candidates, from axions ($10^{-5}eV$) to massive black holes ($10^4 M_\odot$) — a mass range of 75 orders of magnitude. A large class of suggested particles are thermal relics of the early universe. These stable particles mostly annihilated with their anti-particles in the early universe, until their density became small and their annihilation probability negligible. Under the assumption, that they are massive enough to close the universe, the cross–section for these thermally created particles turns out to be on the weak scale, and their masses in the $GeV - TeV$ range. Therefore they are named **WIMPS**[9]. [41]

Several theories, motivated by extensions of the "standard model", predict further particles on the electro–weak scale, which are also in reach for future accelerator experiments. A currently popular theory, the *minimal super-symmetric model* (MSSM), will be considered representatively for other theories. Within the MSSM three possible candidates for the lightest super-symmetric particle (LSP) exist: the neutralino, the gravitino and the sneutrino. The sneutrino is ruled out by direct searches. If the gravitino is strictly stable, cross sections are to small to predict any observable effect, . However the most attractive candidate for the LSP is the neutralino χ, a Majorana particle, which is a linear combination of four neutral spin 1/2 fields

$$\chi = Z_1\tilde{W}_3 + Z_2\tilde{B} + Z_3\tilde{H}_1 + Z_4\tilde{H}_2 \; . \tag{2.21}$$

$\tilde{W}_3, \tilde{B}, \tilde{H}_1, \tilde{H}_2$ are the so called "wino", "bino" and the two "higgsinos". The constants Z_i depend on the parameters of the MSSM. A postulated discrete symmetry, *R-parity*, is conserved. To normal particles $R = +1$ is attributed, their super-symmetric partners have $R = -1$. [13, 14, 32]

[9] **W**eakly **I**nteracting **M**assive **P**article**s**

2.5.1 Neutralino annihilation in the Earth and in the Sun

Though their average density is small, thermal neutralinos are expected to accumulate in the sun and the earth, due to gravitational capture after neutral current scattering with nucleons. Neutralinos annihilate via

$$\chi\bar{\chi} \longrightarrow \begin{cases} l\bar{l} \quad (l\ : \text{lepton}) \\ gg \quad (g : \text{gluon}) \\ q\bar{q}\ (+g) \quad (q : \text{quark}) \\ W^+W^-, Z^0Z^0, W^+H^-, Z^0H_i^0 \ldots \end{cases} \qquad (2.22)$$

The actual branching ratios depends on the choice of the MSSM parameters. Depending on the mass m_χ not all channels (e.g. W^+W^- or t^+t^-) are allowed. Decays into fermions are dominated by heavy quarks, because the cross section is proportional to m_f^2. Further hadronisation and decays yield neutrinos. In thermal equilibrium the number of captured neutralinos equals the annihilation rate. [32, 14]
A resulting upward going muon signal either from the direction of the sun or from the core of the earth is expected to exceed the atmospheric neutrino flux. Future neutrino telescopes are sensitive to a large range of MSSM parameters and neutralino masses beyond present accelerator limits. A 10^5m^2 detector may yield typically 20 events per year for a $500GeV$ neutralino. Smaller telescopes than 10^4m^2 may be sensitive for $m_\chi \approx 1TeV$. [37, 32, 14]

2.5.2 Neutrinos from R-parity violation

If R-parity is not a fundamental symmetry, it is likely to be violated and neutralinos may decay[10]. In order to contribute to dark matter, the life time τ_χ must be larger than the age of the universe t_0. An appealing signature for neutrino telescopes are mono-energetic neutrinos with $E_\nu \approx m_\chi/2$ resulting from two body decays. If the violation mechanism of R-parity is due to spontaneous R-parity breaking with a remaining Majoron J (a massless Goldstone boson), the decay $\chi \rightarrow \nu + J$ is the dominant decay channel. The neutrino flux is given by

$$I_\nu \approx 2.5 \cdot 10^3 \frac{t_0}{\tau_\chi} \cdot \frac{10GeV}{m_\chi} cm^{-2}s^{-1}sr^{-1} \ . \qquad (2.23)$$

The rate of neutrino events inside a detector ($\propto I_\nu \sigma_{\nu N}$) is independent of m_χ

$$N_\nu \approx 2 \cdot 10^7 \cdot \frac{t_0}{\tau_\chi} \cdot h_0^2 kt^{-1}a^{-1} \ , \qquad (2.24)$$

with h_0 the normalised Hubble constant ($\sim 0.5 - 0.8$). Future 10^4kt–detectors are sensitive down to $t_0/\tau_\chi \sim 10^{-11}$! Such a weak R-parity violation is far beyond the bounds of accelerator experiments. [13, 14]

2.6 Cosmological neutrinos

During propagation of highest energy cosmic rays with $E > 3 \cdot 10^{19}eV$ through the cosmic microwave background, photo-pion production occurs.

$$p\gamma \rightarrow \Delta^+ \rightarrow n\pi^+ \quad (p\pi^0)$$

The cross section reaches its maximum at $\sim 5 \cdot 10^{20}eV$. The universe becomes opaque with a mean interaction length of about $2Mpc$. The neutrino flux is calculated by assuming the maximum proton

[10] In this case also the decay of gravitinos may produce observable results.

energy similar to the maximum observed energies of cosmic rays. The contribution due to close-by sources ($d \approx 10 Mpc$) is marginal. The flux may be drastically increased by sources with large red-shifts, due to cosmological reasons: The energy density of the microwave background scales with the red-shift $\propto (1+z)^4$. In some cosmological models sources are much more luminous in the younger universe, e.g. during the bright phase of galaxies. The resulting cosmic ray spectra after propagation has to be normalised on the observations of highest energy cosmic rays. The resulting neutrino flux may exceed the expected flux due to AGNs above $10^{18} eV$. [37, 13]

Several exotic cosmological models involving super–conducting cosmic strings prophesy large neutrino fluxes at highest energies. E.g. strings loose energy into massive fermions ($M_F \sim 10^{15} GeV$), which further decay. The neutrino spectrum extents up to the Planck mass and is enriched at $E > 10^{19} eV$ due to strings at large red-shift. [37, 134]

3 Faint light Deep Underwater

A neutrino telescope deep underwater is composed of a matrix of highly sensitive optical sensors. These sensors register optical light which is emitted from charged relativistic tracks via the Čerenkov effect. In order to operate a Čerenkov neutrino telescope it is essential to examine in details; the propagation of secondaries originating from a neutrino interaction, the optical properties of the deep water, and all ambient sources of light.

3.1 The Deep Underwater Environment

The ocean is a desert with its life underground
— and a perfect disguise above.

America - Horse with no name (1971)

Deep water provides extreme but time-stable environmental conditions. Many properties are comparable between the BAIKAL experiment, located $3.6km$ offshore at a depth of $1370m$ in the fresh-water lake Baikal in Siberia, and the DUMAND experiment, located about $30km$ offshore the "Big Island" of Hawaii at a depth of $4700m$ in the Pacific ocean. To cope with high pressure (> 100 atmospheres) and corrosion all components have to be pressure tested and materials have to fulfill long-term duration requirements. The optical sensors are deployed in high pressure housings made from transparent boron-silicate glass. Connectors and other components are preferably made from titanium.
Water currents are generally low ($\sim 3cm/s$) with slight daily and seasonal variations. Low temperatures, $4°C$ (BAIKAL) and $1.3°C$ (DUMAND), improve the noise characteristics and time stability of deployed electronics, especially of the optical sensors.
Another important aspect for long-term deployment is the sedimentation rate. Though it is small, highly sensitive surfaces of optical sensors are interfered. The accumulated matter is mostly of organic origin — dead bio mass from the surface water layers. An accidently lost optical apparatus from an early DUMAND–test-experiment (TTR IV) showed no signs of organic grows on its surface after its recovery 1 1/2 years later. However slightly warmer surfaces of an apparatus under operation, may provide a comfortable climate for dwellings of organic populations. These concerns are not so serious for the BAIKAL experiment with 1 year operation cycles and low power consumption close to optical apparatus. This was proved by the BAIKAL experiment in the years 1993 and 1994. Down-looking optical surfaces of the NT-36 detector, showed no significant reduction of the sensitivity. Upward looking surfaces are stronger affected than those looking down and show a 50% reduction of the sensitivity after 1 year of operation. [101, 113, 110]
Surface layers of natural water are dominated by solar radiation. Going deeper the light intensity fades off exponentially until one reaches the abyssal zone at $\sim 1km$ in the ocean and $600m$ in Lake Baikal. Here the solar radiation is below a threshold of $1\ photon\ cm^{-2}s^{-1} \approx 10^{-19} W cm^{-2}$. The depth for this flux threshold depends strongly on the surface properties and the (spectral) attenuation length of the water.
Though long assumed as a cold dead dessert, the abyssal zone is inhabited by about 98% of known marine species, mostly bacteria. Little is known about these complex *eco*-systems, except that direct sun-light has only a small influence on them. Many of these species produce light themselves, bioluminescence. Other sources of faint light also become important, cosmic rays and natural radioactivity. [126, 26]

3.2 The Čerenkov effect

While passing through matter charged particles loose energy. One major contribution is due to inelastic collisions with atomic electrons — a quasi continuous ionisation of atoms along the particles path. This process is described by the well known *Bethe–Bloch formula.* Included is a tiny contribution,

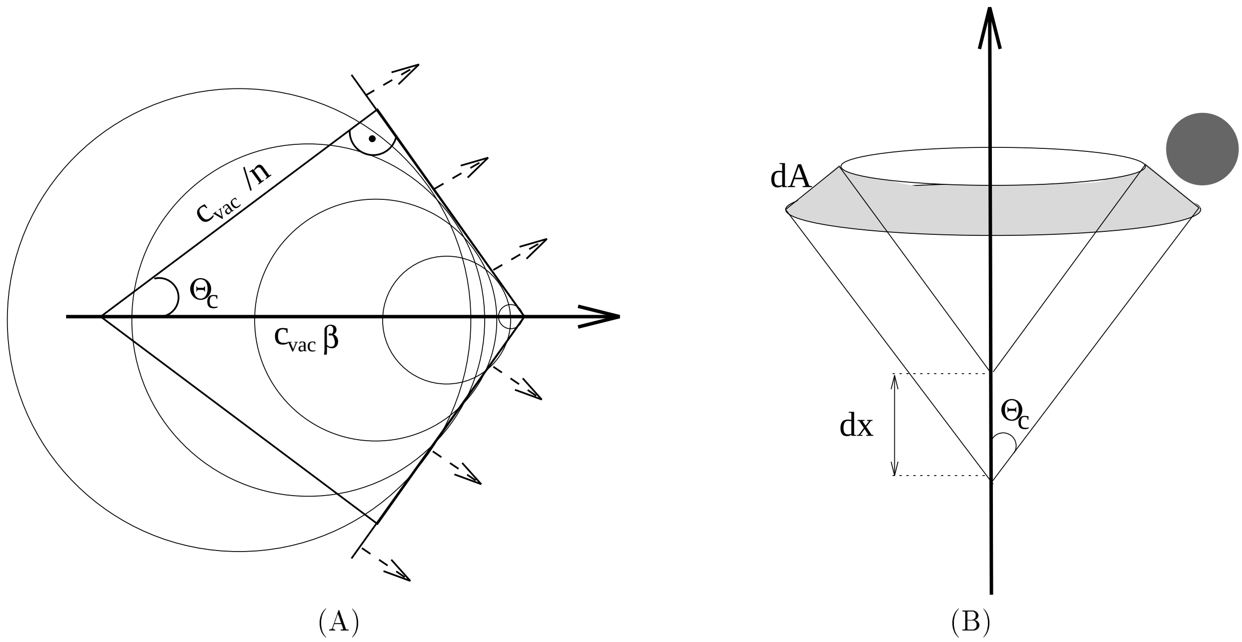

Figure 3.11: Geometry of the Čerenkov cone. (A) Huygens construction. (B) A Čerenkov cone hitting an optical sensor (OM).

that occurs if particles travel faster than the speed of light in the medium with index of refraction n: $v \equiv \beta c_{vac} \geq c_{med} \equiv c_{vac}/n$. This defines the *Čerenkov threshold*

$$\beta \geq \frac{1}{n} \ . \tag{3.25}$$

Above this threshold some energy is released in form of a coherent electromagnetic wavefront. In general the index of refraction depends on the frequency of the emitted photons. The total amount of released energy is calculated via an integration over all frequencies ν for which $n(\nu)$ fulfills relation eq.(3.25)

$$-\left(\frac{dE}{dx}\right)_{\text{Čerenkov}} = \frac{2\cdot\pi\cdot\alpha}{c_{vac}} \cdot \int_{\beta\cdot n(\nu)\geq 1} \left(1 - \frac{1}{\beta^2\cdot n^2(\nu)}\right) d\nu \ , \tag{3.26}$$

with the fine-structure constant α. However in a small frequency (wavelength) window, defined by the optical transparency of the medium and the acceptance of a sensor, the index of refraction does not change with the frequency. A calculation for water $n \approx 1.33$ yields about $400 eV cm^{-1}$ for optical photons ($400nm \leq \lambda \leq 700nm$), corresponding to ~ 200 emitted photons per cm. The spectral distribution of the emitted photons is given by

$$\frac{d^2N}{dx d\lambda} = \frac{2\pi}{137\cdot\lambda^2} \cdot \left(1 - \frac{1}{n^2\cdot\beta^2}\right) \ . \tag{3.27}$$

[128, 130, 136]

The total Čerenkov energy loss, typically $10^{-3} MeV cm^{-1}$, is marginal compared to the total ionisation loss $\approx 2 MeV cm^{-1}$ for minimal ionising particles. The relative importance of Čerenkov light comes from the fact, that all photons are emitted with a fixed angle Θ_c, in a cone around the trajectory; in close analogy to the emission of acoustical waves released from a plane moving at supersonic speed. In case of relativistic particles ($\beta \approx 1$) the *Čerenkov angle* is independent on the particle's energy. Figure 3.11 shows a Huygens construction of the wavefront. The Čerenkov angle is given by

$$\cos\Theta_c = \frac{c_{vac}/n}{\beta c_{vac}} = \frac{1}{\beta\cdot n} \ . \tag{3.28}$$

For water ($n \approx 1.33$) it is $\Theta_c = 41.2°$. [128, 130]
The Čerenkov threshold energy can be calculated via

$$E_c > \frac{m}{\sqrt{1 - \frac{1}{n^2}}} \; . \tag{3.29}$$

This corresponds (with $T_c = E_c - m_0 \cdot c^2$) to a kinetic threshold energy of $T_{c,H_2O} = 0.264 MeV$ for electrons and $T_{c,H_2O} = 54.6 MeV$ for muons in water.

3.3 Cosmic rays deep underwater

The underground flux of cosmic rays is dominated by down-going atmospheric muons. This flux is decreasing down to a depth of $\sim 10km$, where the intensity falls below the flux of isotropic neutrino–induced muons. Atmospheric muons are created by an initial shower in the top of the atmosphere, e.g.due to a high energy cosmic nucleus. Depending on the primary cosmic ray composition, energy and incident angle single muons or bundles of parallel muons may reach an underground detector. Accessible to experimental observations are the vertical muon intensity, the energy and angular distribution, the multiplicity and the separation of muons in a bundle. [123]
The total flux J_2 from above is given by

$$J_2 = \int_{\theta \le \pi/2} j(\theta, \phi)\ \sin\theta\ d\theta\ d\phi \;=\; 2\pi I_v \int_{\theta \le \pi/2} f(\theta)\ \sin\theta\ d\theta \; , \tag{3.30}$$

with the directional intensity $j(\theta, \phi)$, the vertical intensity I_v and the angular distribution $f(\theta)$ ($f(\theta) \equiv 1$) [136]. The vertical muon intensity I_v is measured in chapter 8.1.4 and compared with results of other experiments in figure 8.82. The multiplicity κ_{mult} may be defined as the ratio

$$\kappa_{mult} = \frac{N_{\ge 2}}{N_1} \; , \tag{3.31}$$

with N_i the relative abundance of i muons in a bundle. Another characteristic value is the mean multiplicity $\bar{N} = \sum_i N_i \cdot i$. The characteristics of these muons depends mainly on the depth of the detector.
Several calculations have been performed to calculate these parameters either using empirical formulae and simulate the propagation of muons down to depths of a detector or by using complex Monte Carlo simulations of the initial shower itself [123, 27, 65, 72, 43, 125].
This work concentrates on the approach of Boziev et.al.[25], as it is implemented in the BAIKAL Monte Carlo Program [139, 49] (see appendix C.2). For the BAIKAL detector (depth$\approx 1170m$) one gets of $\kappa_{mult} \approx 16\%$, $\bar{N} \approx 1.22$ and for DUMAND–(depth$\approx 4700m$) $\kappa_{mult} \approx 4.1\%$, $\bar{N} \approx 1.04$. These values depend on the energy threshold and the maximum allowed separation necessary for the detection of the muons.

In order to search for the "needle in the haystack", rare neutrino interactions, one can summarise following signatures:

Electron Neutrinos ($\nu_e, \bar{\nu}_e$) perform weak charged and neutral current interactions with atomic nuclei. A hadronic cascade and an electromagnetic cascade[1] occurs at the point of interaction. All charged secondaries in the cascade produce Čerenkov light. If the shower dimension is small compared to the dimensions of the detector volume, the interaction produces a bright point-like source of light.

[1] Only for charged current interactions.

At UHE energies an additional channel opens for $\bar{\nu}_e$, the resonant interaction with atomic electrons at the *Glashow resonance.* (see eq.(2.13), fig.2.9) According to branching rations of the W^- decay, bright electromagnetic or hadronic cascades occur in $\approx 80\%$ of the decays. The remaining 20% are shared by μ^- and τ^-.

Muon neutrinos $\nu_\mu, \bar{\nu}_\mu$ perform charged current interactions with nuclei. A hadronic cascade and a muon are generated. The muon travels large distances and emits Čerenkov light along it's trajectory. This is the standard detection reaction and has been discussed in chapter 2.4. Neutral current interactions produce a hadronic cascade similar to ν_e interactions.

Tau neutrinos $\nu_\tau, \bar{\nu}_\tau$ are not predicted to be emitted from astrophysical accelerators with a photon gas beam dump. If they occur, they perform the same interactions as ν_μ. The resulting τ decays immediately $\sim 3 \cdot 10^{-13} s$. It's decay gives birth to a electromagnetic, a hadronic cascade or a mixture of both. In about 18.% of the decays a muon is generated.

It has been recently proposed that UHE ν_τ interactions may provide a clear signature, when they generate an ultra relativistic τ traveling several $10m$ before it decays. The large hadronic cascade from the $\nu_\tau N$–interaction and the cascade from the τ decay may possibly be identified individually if they occur inside a neutrino detector — generating a so called "double-bang" event. These ν_τ may occur in case of neutrino oscillation from an initial ν_μ or ν_e during the journey from the cosmic source to earth. [113]

The physics of the three phenomenological classes of underground events: muons, electromagnetic cascades and hadronic cascades will be exploited further in the following paragraphs.

3.3.1 Muon propagation

While passing through matter, muons loose energy via *Ionisation*, *Pair production*, *Bremsstrahlung* and *Nuclear interactions.* The total energy loss is determined by a summation of the individual contributions[2].

$$-\frac{dE}{dx} = \left(\frac{dE}{dx}\right)_I + \left(\frac{dE}{dx}\right)_B + \left(\frac{dE}{dx}\right)_P + \left(\frac{dE}{dx}\right)_N \quad . \tag{3.32}$$

Because the ionisation loss is almost constant above $\sim 1GeV$ and losses due to the other mechanisms rise approximately linearly with the energy, the mean total energy loss is often parameterized via

$$\begin{aligned} -\frac{dE}{dx} &= a_I(E) + b(E) \cdot E \\ \text{with} \quad b(E) &= b_B(E) + b_P(E) + b_N(E) \ . \end{aligned} \tag{3.33}$$

A simple approximation can be achieved assuming the parameters a_I and b_B, b_P, b_N to be constant

$$-\frac{dE}{dx} \approx a + b \cdot E \ . \tag{3.34}$$

Typical values for H_2O, derived from several calculations, are $a_I = 2\frac{MeV}{cm}$, $b = (1.7{+}1.3{+}0.4) \cdot 10^{-6} cm^{-1}$ for H_2O. [57, 123, 72, 64, 104, 106]
The solution of the differential equation (3.34) gives the energy E as function of the initial energy E_0 and the travelled distance r

$$E(r, E_0) = \left(E_0 + \frac{a}{b}\right) \cdot \exp\left(-b \cdot r\right) - \frac{a}{b} \ . \tag{3.35}$$

[2] In compound materials (like natural water) the individual energy loss for each element has to be summed according to their relative atomic weight.

The mean range R of a muon is

$$R = \frac{1}{b} \cdot \ln\left(\frac{bE_0}{a} + 1\right) \quad . \tag{3.36}$$

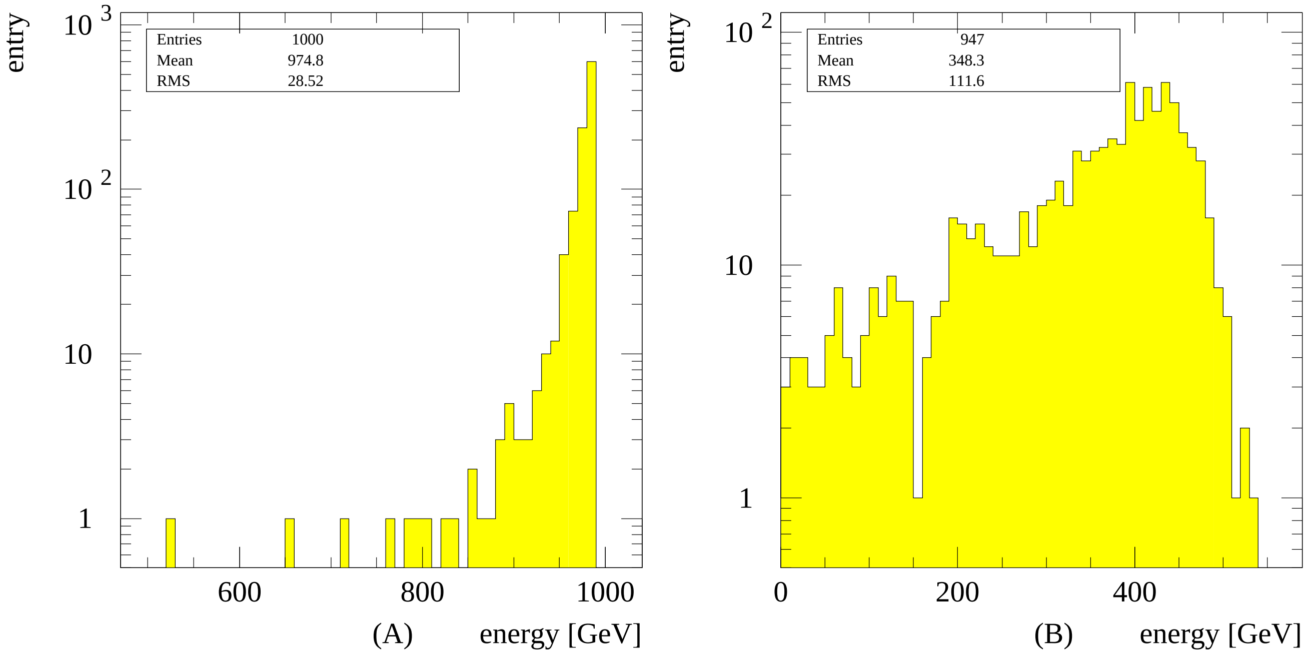

Figure 3.12: Stochastic character of muon energy loss The picture shows distributions of the final energy of 1000 simulated muons (initial energy $1TeV$) after passing (A) $50m$ and (B) $1500m$ of fresh water, simulated with GEANT (section 6.2)

A detailed description of the muon propagation through matter has to take account of the extremely stochastic character of the individual energy loss processes as demonstrated in figure 3.12. Even after a short distance of $50m$ (fig.3.12 (A)) some muons have experienced dramatic energy losses. Though after $1500m$ distance the average energy is still $\approx 350GeV$ already 5% of the muons have been stopped. One has to distinguish between the quasi continuous losses (e.g. ionisation) and so called *"catastrophic"* losses, mostly due to hard interactions like bremsstrahlung and nuclear interactions[3]. The catastrophic losses occur rarely but give birth to large local energy depositions generating electromagnetic and hadronic cascades. Calculated cross sections for all processes are plotted in figure 6.43.

The phenomenology of these effects is demonstrated in figure 3.13. The pictures show muon tracks including all secondary tracks above the Čerenkov threshold, simulated with GEANT (see section 6.2). Especially for higher energies large densities of secondary tracks may locally accompany the muon. The total amount of Čerenkov light emitted along the muon track is proportional to the total amount of track-length of charged particles above the Čerenkov threshold. Therefore a high energy muon occurs brighter, but the clear angular characteristic of Čerenkov light with a sharp angle Θ_c is distorted. A detailed investigations of the effective Čerenkov light characteristic is performed in chapter 7.2.

[3]The most catastrophic energy loss process, decay of the muon, has been neglected in this discussion, but is included in the simulation (chapter 6.2)

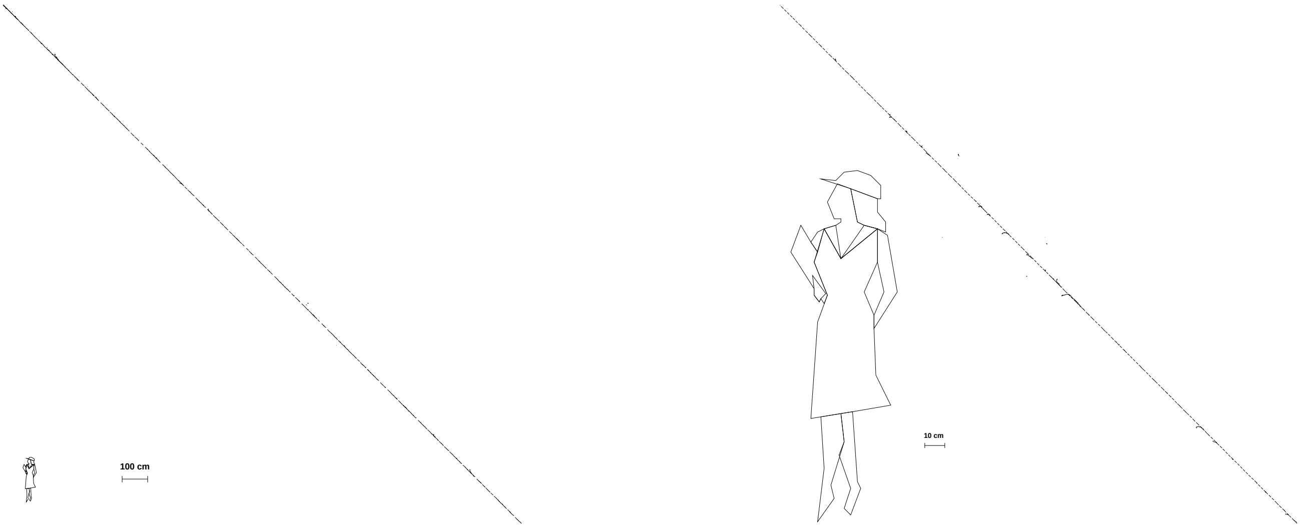

$(100GeV)$

$(1TeV)$

$(10TeV)$

Figure 3.13: Typical muon tracks and charged secondaries above the Čerenkov threshold for different energies in two zoom levels.

3.3.2 Electromagnetic cascades

The energy loss of electrons is composed of two parts, electromagnetic radiation (bremsstrahlung), and ionisation loss. The radiative energy loss rises proportionally with the energy, the ionisation losses only logarithmically. Above the critical energy E_c radiation processes dominate the energy loss. The critical energy may be approximated

$$E_c \approx \frac{610MeV}{Z+1.24} \approx 92MeV \quad \text{for } H_2O \ , \tag{3.37}$$

with the atomic number Z. Secondaries from a radiative process experience strong radiative interactions themselves and generate new secondaries. As a result of this cascading process electrons, unlike muons, do not travel long distances through water, but immediately produce an electromagnetic shower. Figure 3.14 shows typical electromagnetic cascades for three different initial energies simulated with GEANT (see section 6.2). [128, 136]
A second characteristic quantity, the radiation length L_{rad} yields the distance after which the energy of an electron is reduced by a factor of $1/e$. It may be approximated via

$$L_{rad} = \frac{1}{\rho} \cdot \frac{716.4[gcm^{-2}] \cdot A}{Z(Z+1)\ln(287/\sqrt{Z})} \approx \begin{cases} 36.1cm & \text{for } H_2O \\ 35.8cm & \text{for fresh water} \\ 34.9cm & \text{for sea–water} \end{cases} , \tag{3.38}$$

with the density ρ and the atomic weight A. For mixtures of materials (e.g. water) the radiation length is given by

$$\frac{1}{L_{rad}} = \sum_i w_i \cdot \left(\frac{1}{L_{rad}}\right)_i \tag{3.39}$$

with w_i the relative weight fraction of material i. [128, 136]
The longitudinal energy deposition of the shower can be parameterized with a gamma distribution

$$\frac{dE}{dt} = E_0 \cdot b \cdot \frac{(bt)^{a-1}\exp(-bt)}{\Gamma(a)} \ , \tag{3.40}$$

with $t = x/L_{rad}$ the number of radiation lengths. The total integrated track-length of charged particles is proportional to the initial energy E_0. The maximum of the energy deposition t_{max} scales logarithmically with the initial energy

$$t_{max} = \frac{a-1}{b} = 1.0 \cdot (\ln Y + C_i) \tag{3.41}$$

with $Y = E_0/E_c$. The parameter C_i is -0.5 in case of an electron induced shower and $+0.5$ for a photon induced shower. The "‘shower length"’ is defined as

$$X_s = \frac{L_{rad}}{b} \tag{3.42}$$

[136, 130]
Numerical values for a, b in fresh water and the effective Čerenkov light is evaluated in chapter 7.1.

3.3.3 Hadronic cascades

Hadronic cascades are induced whenever nuclear interactions (e.g. with muons or neutrinos) occur, or the decay of heavy particles gives birth to new hadrons. Analogous to electromagnetic cascades

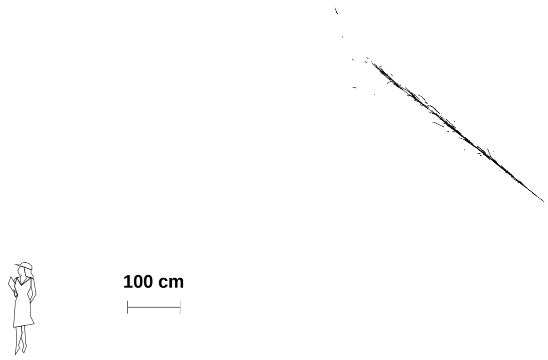

$10GeV$

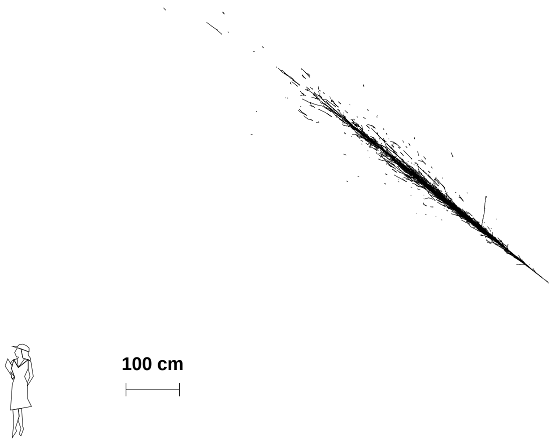

$100GeV$

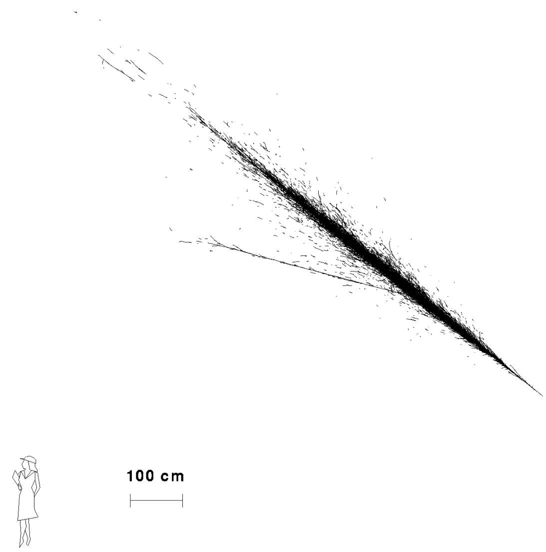

$1TeV$

Figure 3.14: Typical electromagnetic cascades in fresh water for three different initial energies. Plotted are only charged tracks above the Čerenkov threshold. Though the longitudinal size of the shower does not change largely, the number of particles increases strongly with the energy. The pictures are postscript graphics, which sizes increase as follows: $85kB$, $466kB$, $4000kB$!

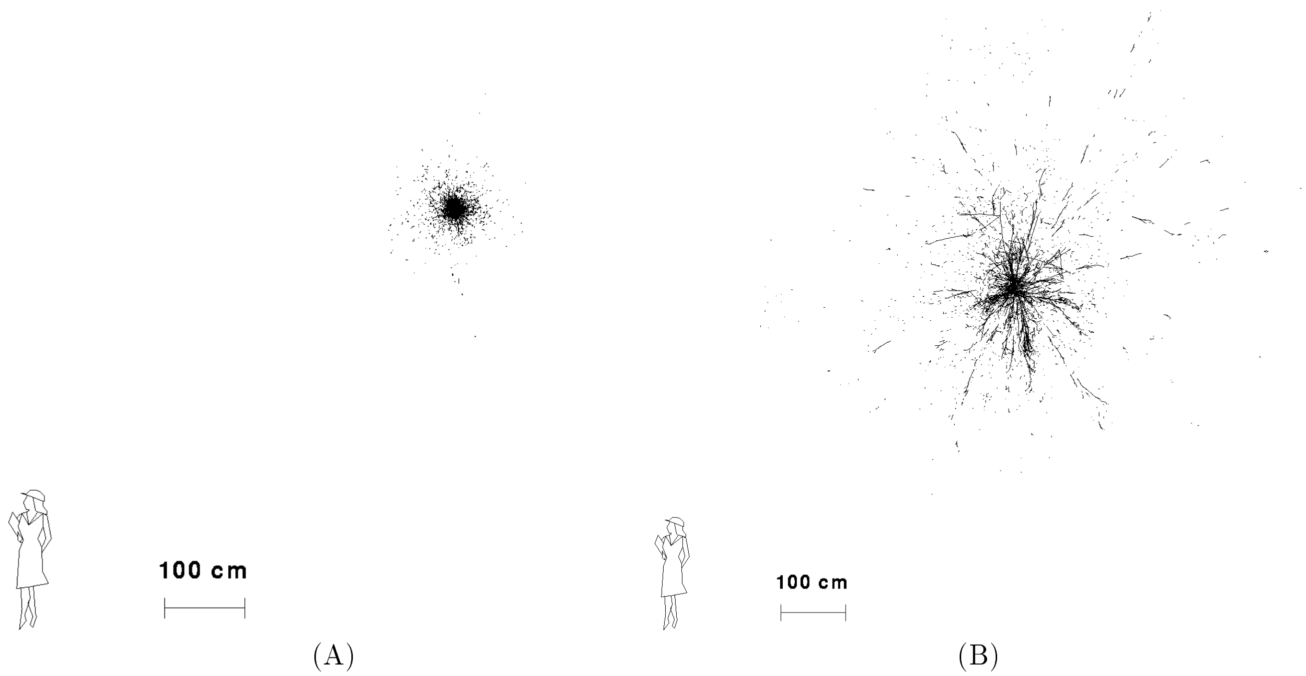

Figure 3.15: Transversal spread of electromagnetic and hadronic cascades. The observer views into the initial direction of the cascade. (A) shows a $100GeV$ electron, (B) a $100GeV$ pion cascade. The picture shows charged tracks with kinetic energies above $500keV$.

secondary hadrons re-interact with nucleons producing a hadronic cascade. The typical longitudinal length scale is determined by the nuclear interaction length given roughly by

$$\lambda_I \approx 35gcm^{-2}A^{1/3} \approx 75cm \quad \text{for } H_2O \tag{3.43}$$

Hadronic cascades are generally broader than electromagnetic cascades. The average position of the shower maximum is

$$t_0 = \frac{z}{\lambda_I} \approx 0.2 \ln\left(E_0[GeV]\right) + 0.7 \tag{3.44}$$

Hadronic cascades are accompanied by an electro-magnetic component. Individual cascades show large fluctuations in length and corresponding energy deposition. This is mainly due to 2 effects

- Generated neutral pions (π^0) immediately decay $\pi^0 \rightarrow 2\gamma$. The produced gamma-rays induce electromagnetic cascades. These particles do not contribute further to the hadronic evolution of the shower.

- Charged pions or other hadrons can decay into muons. These muons do not further contribute to the shower, but may travel farther than the other shower particles.

If these processes happen during an early stage of the shower evolution, they strongly determine the later development of the cascade. [136]
The effective Čerenkov light from hadronic cascades and differences to electromagnetic cascades are studied in section 7.1. Differences between electro-magnetic and hadronic cascades are also demonstrated in figure 3.15 which shows the transversal spread of charged tracks. The electromagnetic cascade is very homogeneous, mostly pointing into the forward direction, the hadronic cascade has a larger transversal spread and shows bigger inhomogeneities. The total production of Čerenkov light is slightly bigger for electromagnetic cascades.

3.4 Optical properties deep underwater

Unlike conventional detectors in high energy physics water Čerenkov detectors do not directly measure the trajectories of particles, but rather detect secondary light and reconstruct these trajectories off-line. The propagation of light strongly influences the detectability and the reconstruction accuracy. Mainly two microscopic processes affect the propagation: *absorption* and *scattering*.
Experimentally observable is the diffuse *attenuation* of a beam of light after traveling a path-length x through water. One gets an exponential decrease of the irradiance[4] $\mathcal{I}$, defining the diffuse attenuation coefficient κ

$$\mathcal{I}(x, \lambda) = \mathcal{I}(0, \lambda) \cdot \exp\left(-\kappa(\lambda) \cdot x\right) \quad . \tag{3.45}$$

κ, the inverse *attenuation length*, is a function of the wavelength. [126]

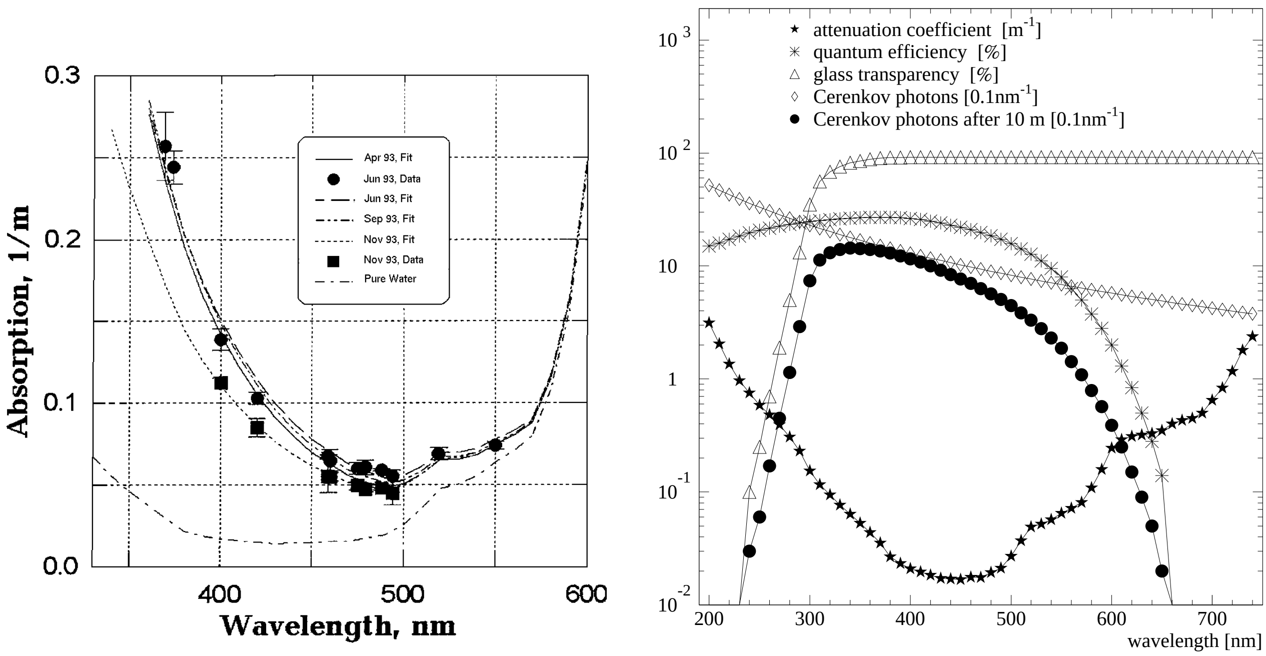

(A) (B)

Figure 3.16: Light attenuation for lake Baikal and clearest natural water versus the wavelength. (A) Measured diffuse attenuation coefficient κ in lake Baikal (from [94, 10]) (B) Effective Čerenkov photon spectrum for clearest natural water. The initial distribution of Čerenkov photons is attenuated in water ($10m$ path) and the glass of the pressure housings. A typical quantum efficiency curve for a bialkali photocathode is plotted (To calculate the effective Čerenkov photon distribution only the relative quantum efficiency distribution was used). (data from [50])

The diffuse attenuation coefficient κ is an *apparent* property and is not directly accessible through a microscopic theory, which yields only *inherent* properties. It can be calculated from the total (microscopic) attenuation coefficient c and the *scattering function* $\beta(\theta)$. The scattering function gives the differential light intensity scattered into the direction θ from a volume element dV illuminated from an incident beam of light. c is generally written as

$$c = a + b \tag{3.46}$$

where a is the absorption and b the scattering coefficient. In order to calculate c for natural water one calculates c for pure water and adds the scattering and absorption coefficients derived from calculations

[4] The value irradiance is defined as the radiant flux through an infinitesimal area (unit Wm^{-2})

for additional dissolved and suspended materials. Absorption and scattering properties are derived from the electromagnetic and molecular properties. The scattering coefficient b can be calculated from the scattering function β via

$$b = 2\pi \int_0^\pi \beta(\theta) \sin\theta d\theta \ . \tag{3.47}$$

The forward b_f and backward b_b scattering coefficients are defined as the corresponding integrals (eq.(3.47)) of β over the forward and backward hemisphere respectively. Approximately κ is given by

$$\kappa \approx c - b_f = a + b_b \ . \tag{3.48}$$

[126, 80]
Figure 3.16 (A) shows several measurements of the attenuation κ in lake Baikal 1993. Small seasonal variations are observable. The total maximum attenuation length is $\approx 20m$, the scattering length (b^{-1}) was individually measured to $\approx 15m$. In comparison an additional curve shows the values for pure water.
The attenuation curve has a minimum in the wavelength range from $400nm$ to $500nm$ coinciding well with the maximum sensitivity of a bialkali photocathode. This allows the use of large area photomultipliers as optical sensors. The effective photon spectrum detectable by a bialkali photocathode is shown in figure 3.16 (B). The data for clearest natural water is used to calculate the photon distribution $10m$ away from the Čerenkov radiating track including the transmission of pressure housings and the relative response of the photocathode. Geometrical effects are not included. The effective photon spectrum is bounded by the glass transmission to the UV and by the photocathode efficiency to the red. [10, 80, 50]

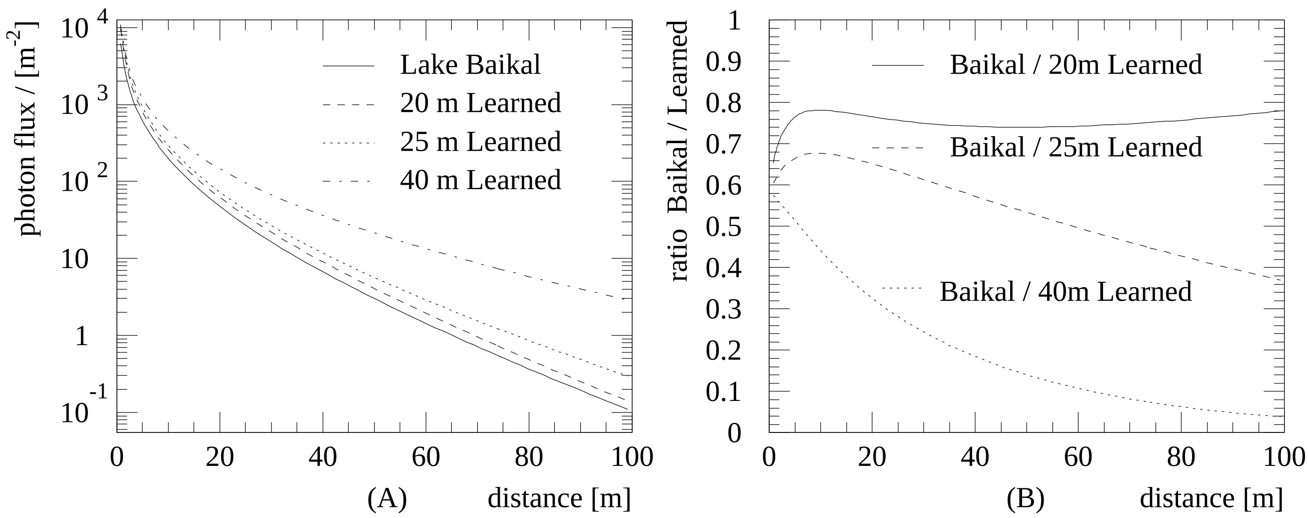

Figure 3.17: Parameterization of the effective photon flux versus distance. ([51, 139]) (A) The photon flux for different types of water. (B) Ratio of the Baikal function to the Learned parameterizations.

The density of photons $\rho_\gamma(d)$ hitting an optical sensor as calculated in appendix A.2 (eq.(A.127)) depends on the number of generated photons and their attenuation. The function $n_\gamma \cdot \epsilon(d)$ gives the effective number of photons per unit track that survived after traveling the distance d. This function is calculated by an integration over the distance including the wavelength and distance dependent effective photon spectrum of figure 3.16(B). This is parameterized by J.G.Learned via

$$\epsilon(d) \cdot n_\gamma = \frac{a_1}{(d + a_2)^{a_3}} \cdot \exp(-a_4 d) \tag{3.49}$$

for several types of water, characterised by different sets of attenuation data. Numerical results are plotted in figure 3.17 in comparison to the attenuation used in the BAIKAL simulation program. The comparison yields a constant ratio ≈ 0.8 between the BAIKAL parameterization and Learned for $20m$ attenuation[5] The consequences for the detection of these photons and the design of a detector are discussed in section 4.4. [50, 51, 139]

The usage of photomultipliers as optical sensors implies the usage of PE as a natural unit for the amplitude of individually registrated signals. The number of PE gives the number of coincident measured photo-electrons due to simultaniously converted photons at the photocathode. Both, the initial number of photons and the electrical signal of the photomultiplier, in case of ideal photomultiplier, are linearly related to the number of PE. Though naturally an integer number, the PE value represents a floating value due to the finite pulse-height resolution of the photomultiplier.

3.5 Natural radioactivity

Natural radioactivity is an inherent property of ocean water. Especially β–decaying isotopes contribute to the underwater photon flux, if the energy of the resulting electrons (or positrons) is above the Čerenkov threshold. Whereas the contamination and thus the resulting photon flux is negligible for fresh water, deep ocean experiments suffer and profit from additional light due to ^{40}K, which is the dominant isotope. Potassium is an abundant ingredient of salinity in the ocean. A small fraction of potassium isotopes, 0.0117%, is made up by the ^{40}K, which has a half-life period of $1.28 \cdot 10^9$ years. The activity can be calculated from the salinity[6] $\mathcal{S}$ via

$$\mathcal{A} = 3.33 \cdot \mathcal{S}[Bqm^{-3}] \tag{3.50}$$

Typical salinity values range between $33 \cdot 10^{-3}$ and $38 \cdot 10^{-3}$ in open oceans. It's value is generally constant at one location. The value $\mathcal{S} = 35 \cdot 10^{-3}$ gives a ^{40}K activity of $12 \cdot 10^3\ Bq\ m^{-3}$. [39, 90]

Two dominant ^{40}K decay modes occur via a β^--decay $^{40}K \rightarrow\ ^{40}Ca + \beta^- + \bar{\nu}_e$ with a branching ratio of 89.3% and via electron capture (EC) followed by a prompt γ-decay $^{40}K \rightarrow\ ^{40}Ar^*(+\nu_e)$, $^{40}Ar^* \rightarrow\ ^{40}Ar + \gamma$ with 10.5%. The electron from the β-decay has a maximum energy of $1.3116MeV$ and an average energy of $0.562MeV$. About 93% of β-decays produce an electron above the Čerenkov threshold. The γ from EC-decays has $1.461MeV$ energy, which is converted into Compton electrons capable of emitting Čerenkov light. [39, 90]

For electrons with the mean β-energy one gets about 20 detectable Čerenkov photons. However including the energy spectrum of electrons yields a mean value of typically 40 photons $(300 - 650nm)$ per decay with an electron above the Čerenkov threshold; a continuous distribution which extends up to ≈ 120 photons for the maximum β energy. A volume integration of the activity convoluted with the optical attenuation yields a typical isotropic photon flux of $\approx 120cm^{-2}s^{-1}$. [39, 90, 26]
It is important to note, that the angular distribution of emitted photons has a strong influence on the pulse-height distribution of individual registered Čerenkov signals. Due to multiple scattering of the electron the photons are not emitted into a sharp Čerenkov cone around the initial direction. The opposite assumption, an isotropic emission also leads to wrong results. Scattered electrons have a lower energy and therefore a smaller Čerenkov angle. Hence most photons are emitted into a solid angle $\Omega \approx \pi\ sr$ around the forward direction. Within this angle the distribution is approximately isotropically. In addition electrons scattered at large angles provide a small fraction of light into all

[5] The ratio needs not necessarily to equal 1, because Baikal water has a stronger attenuation to smaller wavelengths (see fig3.16(A)) than ocean water. The result is a smaller value for n_γ. The used BAIKAL parameterization includes the signal-amplitude of the specifically used optical sensor. The back calculation of the photon flux provides a systematic error of about 15%. Following values have been assumed: quantum efficiency: $\varepsilon = 0.15$, radius $R_0 = 38cm$.

[6] The salinity $\mathcal{S}$ expresses the weight percent contribution of dissolved materials. Usually it is calculated from the chlorine C content via $S = 1.80655 \cdot C$.

directions. The size of the angle Ω strongly influences the ratio of the rate of larger to smaller registered signals. [39, 90, 91]

It also has to be noted, that the detection of higher amplitudes than 1PE is generally unlikely — more than 98% of registered signals are 1PE. The capability to discriminate against these low energy signals improves the triggering and reconstruction of muons signals. [54, 91]

To evaluate[7] the rate of registered signals larger than a certain amplitude A_{PE} in the optical sensors (in units of photoelectrons PE) one may integrate the probability of each space point to produce a signal

$$R(> A_{\mathrm{PE}}) = \int d^3r \cdot \mathcal{A} \cdot P(> A_{\mathrm{PE}}, \bar{m}(\vec{r})) \ , \tag{3.51}$$

with the ^{40}K activity $\mathcal{A}$, the probability $P(> A_{\mathrm{PE}}, \bar{m})$ to produce a signal $> A_{\mathrm{PE}}$ from the space point $\vec{r}$ and $\bar{m}(\vec{r})$ the mean expected number of photoelectrons from the space point $\vec{r}$. The probability $P(> A_{\mathrm{PE}}, \bar{m})$ is given by a summation over the cumulative Poisson probability to produce a signal $> A_{\mathrm{PE}}$. This is given by the incomplete gamma function $\mathcal{G}(PE, \bar{m})$ (, see appendix A.4)

$$P(> A_{\mathrm{PE}}, \bar{m}(\vec{r})) = \mathcal{G}(A_{\mathrm{PE}}, \bar{m}(\vec{r})) \cdot \frac{\Omega}{4\pi} \ . \tag{3.52}$$

with the mean solid angle Ω for the emission angle of Čerenkov photons. The integration can be performed via a Monte-Carlo integration, which allows ot include additional effects such as the distribution of electron energies. The calculation is described in details in appendix C.5 and results are compared to experimental data in section 8.2.

The integration method can be also used to calculate the coincidence rate of several N optical sensors due to a single decays. Assuming the optical sensors are located at space points $\vec{R}_i$, the probability function $P(> A_{\mathrm{PE}}, \bar{m})$ in eq.(3.52) has to be replaced by

$$\tilde{P}(> A_{\mathrm{PE}}, \bar{m}(\vec{r})) = \left(\frac{\Omega}{4\pi}\right)^N \cdot \prod_{i=1}^{N} \mathcal{G}(A_{\mathrm{PE}}, \bar{m}(\vec{r}, \vec{R}_i)) \ . \tag{3.53}$$

The coincident rates due to single decays have to be compared to random coincidences due to independent ^{40}K-decays. This random rate can be calculated from the individual counting rates R_i and the coincidence window τ. Calculations show, that coincident signals due to one decay are rather unlikely for typical detector configurations, with distances between the optical sensors larger than a few meters. Only for close distances of optical sensors $\approx 1m$, the rate reaches the same order of magnitude as random coincidences. [91]

Figure 3.18 shows the characteristics of registered deep ocean light signals. (A) shows count rates of signals with about $A_{\mathrm{PE}} \geq 0.5$PE. An almost constant count rate [8] due to ^{40}K is superimposed by large photon fluxes due to bioluminescence (see chapter 3.6). The cumulative distribution of measured rates is shown in figure 3.18 (B). It shows that the rate of ^{40}K is a constant inherent source of signals with a rate $> 50kHz$ in case of the OM's used in DUMAND II (see also section 8.2).

3.6 Light of biological and chemical origin

If the reader considers, that a large fraction of our planet is covered with oceans and that the production of light is an inherent attribute of all kinds of marine species, she may come to the conclusion, that the

[7] It has to be noted this method is also appropiate for the calculation of other physic processes, such as expected hit rates in coincidence with a close supernova explosion.

[8] The large count rates in one optical module (OM 3) results from internal noise signals, which occur if the ultra sensitive cathodes have been exposed to bright sun light before usage. This noise decays away down to typically $\approx 5kHz$. Within the time of measurement $2.7h$ the rate of this OM decreased by 27%.

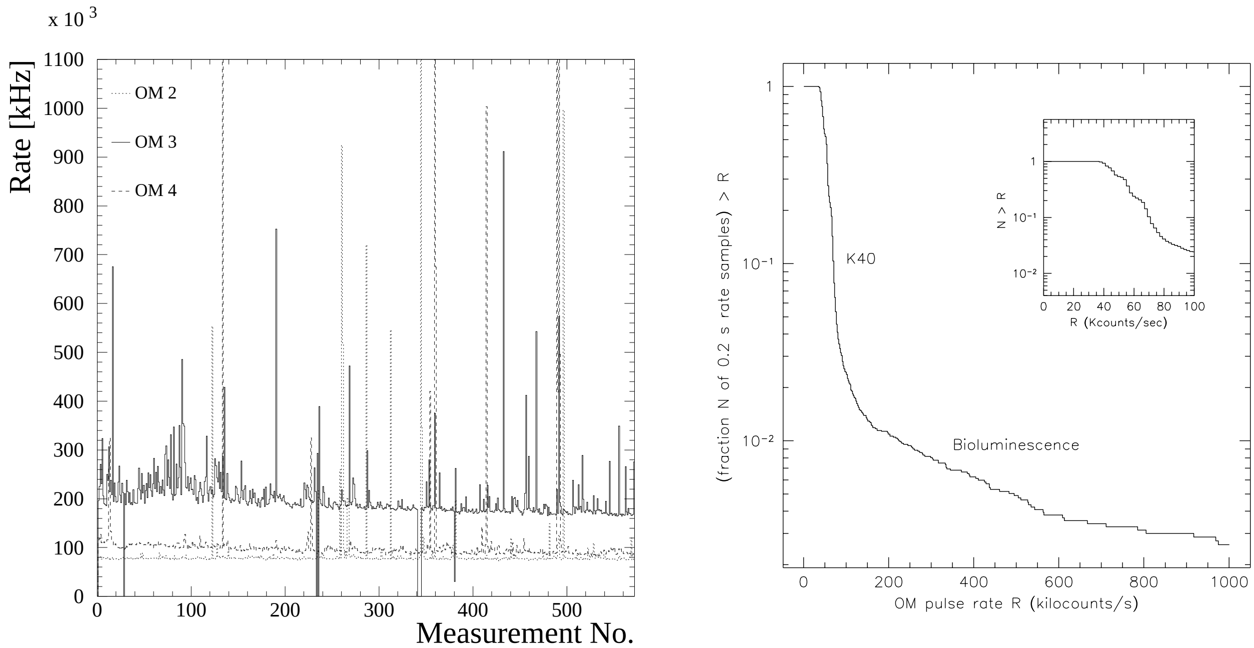

(A) (B)

Figure 3.18: Ocean noise measured during the first phase of the installation of the DUMAND II detector, Dec.1993. The data contains 571 subsequent "snapshots" of the count rate of 13 optical modules in a time window of $0.2s$ and a delay of $17s$ between each measurement. The measurement spans about 2.7 hours of real time corresponding to a live time of 1.9 minutes.
(A) Count rate of three neighbouring optical modules ($10m$ distance).
(B) Fraction of all rate samples that are above a rate threshold (from [113])

production of light is also an inherent property of life on earth. Luminescent organisms can be found in all kinds of marine species ranging from bacteria and fungi, to larger fish. Also underground and in freshwater luminescent animals have been found[9]. Reasons to produce light, some are still speculative, are mainly obtaining food (Illumination or luring of prey), defence (camouflage, alarm or blinding) and propagation of species (mating ritual and attraction). In order to do this many animals possess highly developed light emitting organs, others emit luminescent clouds or are engaged in symbiotic relations to luminescent bacteria. Bioluminescence is observable *in situ* and in the laboratory. An important feature is, that the emission of light can be stimulated mechanically or photically. Bioluminescence is generally produced in a continuous spectrum whose peak emission lies mostly in the region of maximum water transparency ($\lambda_{max} \sim 450 - 500nm$). Several types of chemical reactions are used by organisms to generate light. The simplest reaction occurs via the oxidation of the organic molecule luciferin L via the enzyme "luciferase"

$$LH_2 + O_2 \overset{\text{luciferase}}{\longrightarrow} \text{light} \ .$$

The intensity and time characteristics of the light emission depends strongly on the specific species. The emission duration ranges from short ms-pulses up to several minutes. The pulses often show a fast rise time and a long decaying tail, with more or less complex substructures (e.g.depending on the stimulus). Intensities can be small, exceeding the photons due to ^{40}K only at short distances ($\sim m$), up to the emission $> 10^{12}$ photons s^{-1}. [126, 90]

As seen in figure 3.18 pulses from bioluminescence occur occasionally above a constant background rate due to ^{40}K. Most rate excess peaks in this data set show no correlation between the neighbouring

[9]Biological light is also a major source of background light in lake Baikal.

sensors, suggesting a uniform distribution of individuals with low intensity. The duration times follow an exponential distribution with $\tau \approx 20s$. However a few extremely bright pulses have durations of several minutes. Also some coincidences are visible, e.g.OM-2 and OM-3 at measurement[10] 345 and 360. [84]
Already on basis of the distributions of duration times, count-rates and coincident rates estimates of the spatial distribution, density and species are possible for the small data-set above. Most important feature in the analysis is, that differences in spatial distribution and intensities are differently affected by attenuation. The result is a changed distribution of the excursion rate versus the frequency of occurrence. Without attenuation one expects for a volume density ρ_0 of roughly equally bright individuals (intensity I_0) a frequency distribution $N(q)$ of recorded flashes larger the size q

$$N(q) \propto \rho \cdot I_0^{3/2} \cdot q^{-3/2} \ . \tag{3.54}$$

Including attenuation into calculations allows to separate ρ and I_0 in the distributions. The data of a series of background measurements for the DUMAND I experiment was analysed and yields the mean intensities of the population. Strong mechanical stimulations are observed, when the detector is moving through water. The intensity-depth relation in the pacific ocean ($> 2km$) was found to decrease roughly exponentially with $1/e \sim 1km$. [26, 84]

Future permanent underwater laboratories allow investigations with high statistics on a long term basis. The optical sensors sample the time characteristics of individual pulses down to $\approx 100ns$. After the selection of pulses according to different time characteristics, an analysis according to eq.(3.54) can reveal the characteristics of individual species. The complex infrastructure allows to deploy additional measurement devices e.g. to perform stimulations and to do video recordings.

3.7 Exotic physics

Due to the large amount of monitored volume, underwater neutrino telescopes are extremely sensitive to a class of predicted super-heavy exotic particles, that may move through the water with non-relativistic speed. Most popular representatives are *magnetic monopoles* as predicted by theories beyond the standard model, further unifing the known fundamental forces. These monopoles have masses ranging from $10^8 - 10^{21} GeV/c^2$ with a velocity of typically $\beta \approx 10^{-4}$. The key signature to detect magnetic monopoles is the *Rubakov*–effect, which predicts a magnetic monopole M to catalyse the decay of protons along it's trajectory

$$M + p \longrightarrow \begin{cases} M + e^+ \ (+\pi) \ , \\ M + e^+ + \mu^+ + \mu^- \ , \\ M + \mu^+ + K^0 \ , \\ M + \mu^+ + K^+ + \pi^- \ . \end{cases}$$

This results in subsequent deposition of the energy of typically $1GeV$ thus with Čerenkov radiating particles along the track. The characteristic distance between two proton decays, depending on the velocity and the catalysis cross section, is typically of the order of less than a meter, characteristic times in the order of $1\mu s$. It is possible to identify the track directly or to search for an excess of the counting rate of two coincident optical sensors within a small time–window of a few μs above the background given by a poisson distribution. The second method was applied by the BAIKAL experiment in two series of measurements in the years $1984 - 1990$ and $1993, 1994$. These prototype experiments already gained the same sensitivity as comparable searches. Results yield upper flux limits in the parameter space of the cross section σ_{cat} and the velocity β comparable and better to the previous knowledge. [11, 18, 101]

[10] A count-rate of $0Hz$ in OM-3 corresponds to an excess of the maximum count-rate of typically $1MHz$. This happens 3 times during the measurement in figure 3.18.

4 Deep Underwater Experiments

A large variety of factors determine the detection capabilities and possible success of a neutrino telescope. A detailed comparison of the current projects is difficult due to many specific individual characteristics and the absence of experience under full operational conditions. Therefore a final judgement of the best design must be awaited until these projects are completed.

4.1 The BAIKAL Experiment

The BAIKAL experiment is the first project, which managed to deploy a 3 dimensional grid of optical modules and to run a muon telescope under permanent operation.[97]

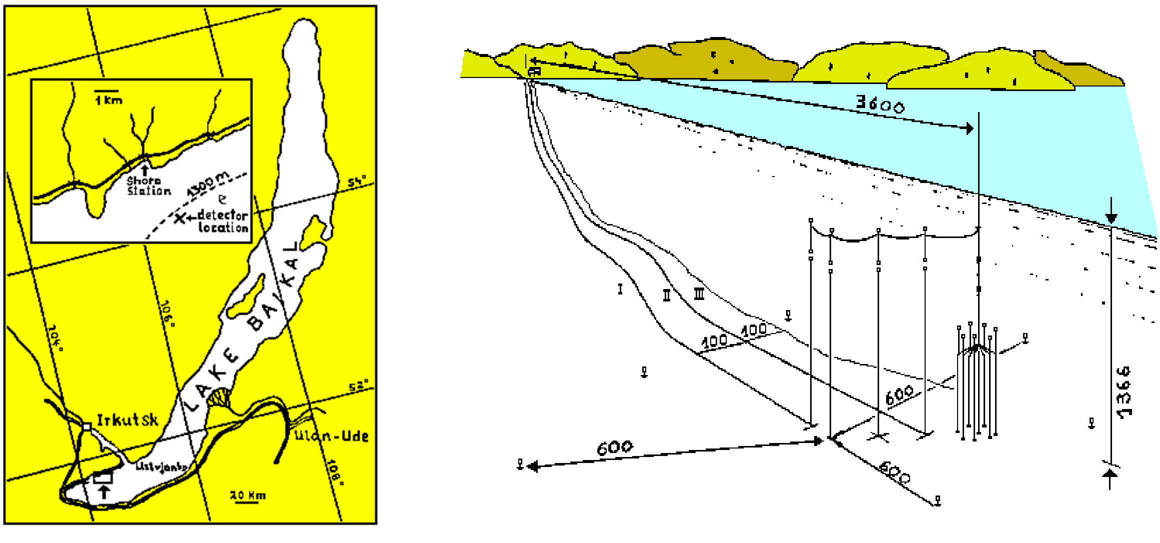

(A) (B)

Figure 4.19: Location of the BAIKAL experiment (A) Geographical location (B) Sketch of the site

The experiment is located in the southern part of Lake Baikal ($51°50'N, 104°20'E$) at about $4km$ distance from shore (figure 4.19). Lake Baikal is the deepest lake on earth and contains a significant part of our planets fresh water. The water transparency reaches almost the quality of deep ocean water (see figure 3.16(A)). The depth at the site is $1370m$. The dominant background light originates from bioluminescence — its intensity is comparable to natural radioactivity in the deep ocean.[101]
As sketched in figure 4.19 (B), the detector consists of several strings attached to the centre and the 7 arms of an umbrella-like glass fibre enforced epoxy frame, called HEPTAGON. The construction is balanced with buoys and its exact position is measured via a hydro-acoustic triangulation system allowing to monitor the positions of optical modules with an accuracy of $0.2m$. The detector is connected to shore via 2 multi-wire cables. A third optical cable is deployed but not yet in operation.[101, 11]
Lake Baikal is usually covered with a up to $1m$ thick layer of ice during the months March and April. This natural stable platform is one of the big advantages of this project. It is possible to move heavy instrumentation like winches trucks and Кунг's right on top of the detector. During the yearly winter expeditions the HEPTAGON is hauled up to a depth of a few meters below the ice surface. This allows yearly maintenance, repair and improvement of the detector. Strings with optical modules are installed or removed from the arms of the HEPTAGON through small holes in the ice. All modules are attached directly to string cables. The assembly of cables happens during installation of other devices (There is plenty of space on the ice). Several working-groups may work in parallel on different strings. During the total deployment the detector is connected to the shore station. The detector or individual

strings may be lowered to deep water at any time, allowing to perform detailed tests on subparts or the complete system in situ. [101]

4.1.1 From NT-8 to NT-200

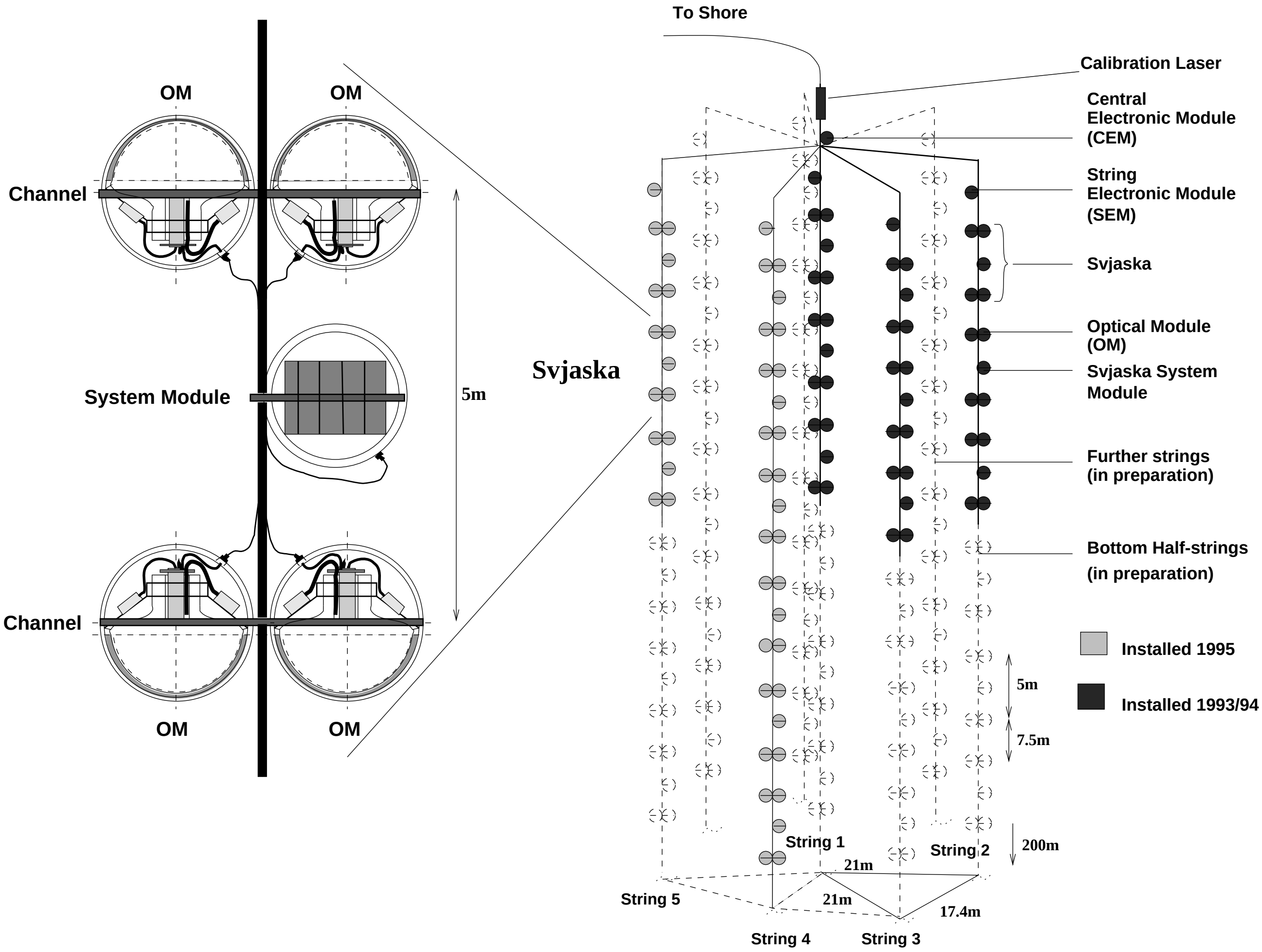

Figure 4.20: Sketch of the NT-200 detector and its predecessors NT-36 (1993/94) and NT-72 (1995). (Not to scale!)

The present goal of the BAIKAL experiment is the installation of the NT-200 detector. NT stands for "**N**eutrino **T**elescope", 200 for the number of optical modules: $192 \approx 200$. After the succesfull performance of smaller test experiments the installation of cables and infrastructure since 1981, the HEPTAGON-frame was installed in 1991 together with an 8-module test-string (NT-8), which was remotely operated from the shore station for two days. In 1992 the two string array: NT-14 was deployed and operated for six months. The full permanent operation as a muon telescope with the capability to reconstruct muon tracks in three dimensions began 1993 with the deployment of the 3-string array NT-36. In 1994 the radius of the HEPTAGON was enlarged from $15m$ to $21m$ and some electronic systems modified. The next step towards NT-200 took place 1995, with an upgrade to the 5 string detector NT-72. However the experiment is still limited by a relatively high failure rate of OM's, which reduces the effective area of the detector. It is aimed to solve these problems within the next recursion steps. [11, 101, 63]

Figure 4.20 shows a sketch of the NT-200 detector including the smaller NT-36 and NT-72 detectors. The full detector contains 8 long strings. The detector has a radius of $21m$ and a height of $\approx 70m$ with an enclosed mass of $\approx 94kt$. The distance to the bottom of the lake is $\approx 200m$. The detector aimes at an effective area of $2300m^2$ (for muons at $1TeV$) with a pointing accuracy of $2.4°$ and a minimal detectable flux of $2.5 \cdot 10^{-9}s^{-1}cm^{-2}$. The smaller NT-36 detector (1993) reaches the effective area of $270m^2$ with an angular resolution of $7.7°$ for moderate cuts. [101, 49]

Optical modules (OM's) are arranged in pairs with the same geometrical orientation, switched to a local time coincidence. Such a pair defines a so called *channel*. The electronics, such as coincidence logic, fast readout and power supply is provided in a separate module, the *System Module* (SM). Each SM serves 4 OM's (2 channels). These modules together build a hierarchical unit called *Svjaska* (Связка).[101]

The original layout assumes that half of the channels have an orientation with the photo-cathodes pointing downwards, the other half pointing upwards. The distances for two channels within one Svjaska are $5m$, looking into opposite directions, the distance between two modules of different Sjaskas is $7.5m$. However it has to emphasized, that this geometrical design is not fixed but rather under development. Especially for the two new strings of NT-72, this geometry was modified, aiming a larger spacing with the majority of the channels (14 out of 18) looking downwards.[101]

Each half-string is equipped with a so called *String Electronic module* (SEM). The total detector is controlled via the *Central Electronic Module* (CEM) located $\approx 40m$ above the detector. A fast laser for time calibration is located above the detector. It is directly connected to all channels via optical fibres of the same length. For additional calibrations each OM is equipped with an LED. Central element of the optical module is the hybrid PMT *Quasar-370* with a cathode diameter of $37cm$, which will be discussed in details in section 5.1.2. [101, 63]

4.1.2 Signal processing

Signals are processed in a strong hierarchical order, with the aim to reduce the data already within the detector.

On the lowest level the Svjaska-SMs form the local coincidences of the OM-pairs and a fast charge to time conversion of the OM amplitudes using a complicated logic scheme [101]. This logic is described in the following in a simplified way. If both OM's of one channel show a signal above ≈ 0.3PE within a time-window of typically $\approx 15ns$, the local trigger condition is accomplished and a pulse is transmitted from the SM to the string electronic module (SEM). The leading edge of this signal represents the "response-time" of the channel, given by the time of the earliest of the OMs. The summation and charge–integration of the two PMT-signals with an integration time of about $100ns$ determines the "channel amplitude" and the width of the resulting signal. The local coincidence reduces the signal rates of $50kHz$-$100kHz$ per individual OM's down to a rate $100Hz$-$300Hz$. The amplitude is measured from 1PE up to ≈ 1000PE with good linearity up to ≈ 100PE. An additional mode for adjustment of the thresholds and calibration allows to stretch the scale for the amplitude or to exclude one or both OM from the amplitude measurement. [101, 63]

Upon receiving a pulse from a channel, the SEM sends a trigger signal to the central electronic module (CEM) and starts the digitisation of the "response-time" and the "channel amplitude" with TDCs. If within the typical time of $\approx 500ns$, necessary for a muon to pass through the detector, the number of signals arriving at the CEM fulfills the detector trigger condition, a signal is transmitted back to the SEMs, which stops the time-TDCs. If within $5\mu s$ no detector trigger arrives at the SEM the digitisation is cancelled. The time-TDC's yield an accuracy of $\approx 1ns$ ($11bit$). The TDC's for the amplitude digitisation have a resolution of $10bit$ with typically $1bit$/PE. [101, 63]

The detector trigger is defined by two numbers A/B, with A the minimum number of hit channels and B the minimum number of hit strings. A typical trigger, 3/1, yields an event rate of a few Hz

in NT-36. In addition to this a second trigger may be applied at the shore station (typically 6/3). The digitised hits are read out from the SEM's via a special "First-in-first-out" buffer, multiplexed and transmitted to the shore station via serial modem. The data connection may transmit data up to $4kByte/s$. [101, 63]
An additional signal branch in the SEM's is designed to search for events due to slowly moving particles e.g. magnetic monopoles, which may catalyse several Baryon decays in the detector within a time window of $0.1ms - 8ms$. The number of hits in each channel are counted within this time window, yielding a strongly Poisson-like frequency–distribution. If the number of hits in a channel exceeds a threshold of typically ≥ 3 hits this value is transmitted to shore. [11, 101]
Heart of the DAQ-system at the shore is a transputer-farm, which is hosted by the *Main-PC* connected to a local area network of PC's. The transputer system extracts "events" from the data-stream and performs a preliminary error analysis. These events are written to a mass storage ($8mm$-"Exabyte" tapes). One major feature of the transputer system are complex online-monitoring capabilities. A *Monitor–PC* allows to interactively display various characteristic histograms such as pulse-height distributions during the run. The parameters of the electronic modules in the detector are controlled by an additional computer, which handles requests from the *Main–PC* to the detector and reads back detector information. [101]

4.1.3 Calibration

The calibration of the detector is done during specific calibration runs. The analysis of these runs allows the determination of characteristic constants, for the calculation of times $[ns]$ (*time calibration*) and amplitudes [PE] (*amplitude calibration*) from the raw digitised values. The "raw"–data files are transformed into calibrated data-files allowing further analysis. [87, 147]
To carry out the time calibration one needs to calculate the true time t from a digitised 11-bit word d_t using the time offsets t_j^0 and a scale factors β_j for the channel j.

$$t_j = d_j^t \cdot \beta_j - t_j^0 \; . \tag{4.55}$$

The factors β_j are measured using a special mode, where the digitising TDCs are started by an uncorrelated noise signal and stopped with a $1MHz$-signal. The result are uniform distributions of times within the TDC ranges. The width of these distribution gives $1/\beta_j$. [87, 20]
The measurement of the time offset t_j^0 is a more complicated process. The calibrated time t does not require a high accuracy in terms of absolute "world-time" but an accuracy of $\approx 1ns$ relative to the other channels. Thus one needs to measure the time-differences between OM response times and a reference-signal. A natural approach is to use the time-differences between two channels due light from downgoing atmospheric muons. Due to the broad angular and spatial distribution of these muons, this method allows an accuracy of a few ns, but depends on Monte-Carlo simulations [73]. The experiment uses a direct method instead: A calibration laser (see figure 4.20) is located above the detector and connected to each channel with optical fibres of equal length. Thus an equal arrival time of the light at each channel is guaranteed. The Laser-system consists of a Dye-laser $\approx 475nm$, driven by an N_2 laser, which yields a maximum amplitude of $\approx 10^6$PE at each channel and a time-accuracy of $0.5ns$. The light intensity can be controlled by certain fractions, determined by an attenuating disc, which is rotated by a stepper motor. The system automaticly runs sequences of typically 200 laser shots at different intensities. The events within one sequence, which have a fixed frequency $\approx 9.1Hz$, have to be filtered out of the data-stream including background hits due to atmospheric muons. An analysis of these events allows a measurement of the t_0^j with a statistical error better than $1ns$. [63, 87]
To perform the amplitude calibration one calculates an amplitude A ([PE]) from the digitised $10 - bit$ value d_j^a via

$$A_j = (d_j^a - d_j^{ped}) \cdot \alpha_j \; , \tag{4.56}$$

using the pedestal d_j^{ped} and the scale factor α_j. The pedestal can be directly derived from amplitude distributions of noise.

The constant α_j can be determined via 3 methods. For the first (standard) method one uses the amplitude of 1PE signals. The OMs are operateded in a mode which expands the amplitude–distribution with a fixed factor γ. Using the mean amplitude $\bar{d}_a$ of 1PE pulses this yields

$$\alpha_j = \frac{\gamma}{\bar{d}_a - d_j^{ped}} \ . \tag{4.57}$$

The two alternate methods use the amplitude distributions of multi-PE pulses. The distributions are generated by the calibration–laser or an LED, which is attached to each OM. The calibration constant α_j may be calculated from the mean $\bar{d}_j^a$ and the width σ_j^d of the distribution via

$$\alpha_j = \frac{\bar{d}_j^a - d_j^{ped}}{(\sigma_j^d)^2} \cdot \kappa_j \ . \tag{4.58}$$

The value κ_j depends on the energy resolution of the OM, which can be measured with the width of the distribution of single photoelectrons signals (see eq.(5.79). Different intensities allow to check the linearity of the Q-T integration. [87, 20]

The water parameters are measured independently with a "hydrological string" close to the detector ([101]). The response of the detector to distant sources of light was measured 1994 and 1995 using a laser-system, analogous to the calibration laser, shining directly into the water. Different optical setups were used for the geometrical light emission, e.g. an isotropic emitting ball or a straight laser-beam. [11, 66]

4.2 The DUMAND Experiment

The beginning of the DUMAND[1] experiment may be dated back to a first workshop in 1975. DUMAND is thus the oldest underwater neutrino project. The experiment intends to install a detector array in a subsidence basin about $30km$ offshore the big Hawaiian island "Hawaii" at a depth of $4.8km$. The array is connected to a shore station in the areal of the "Hawaii Natural Energy Laboratory" at "Keahole point" (see figure 4.21). The headquarter of the experiment is located at the University Hawaii in Honolulu on the Hawaiian island "Oahu". The Hawaiian islands provide an excellent infrastructure, especially concerning marine technology. [110, 98]

The experimental program started 1980 with a series of test experiments, mostly examining light background due to radioactivity and bioluminescence. This stage ended 1987 with a successful test experiment (DUMAND I), the deployment of a short prototype string (SPS) from a ship. This string contained all subsystems, necessary for the permanent operation of a larger detector. The experiment operated several hours at various depths. The vertical flux of atmospheric muons was measured. The detector gained an effective area of $\approx 400m^2$ for down-going atmospheric muons. [5, 29]

The next step is to construct the permanent underwater detector DUMAND II , in two stages:

The first step is the installation of an array consisting of 3 strings and total 72 OM's, the TRIAD. DUMAND II will be completed with the installation of further 6 strings to a total of 216 OM's, the OCTAGON . The TRIAD reaches an effective area of $\approx 3000m^2$ ($E_\mu > 10TeV$) with an angular resolution of $\approx 3°$. The OCTAGON aims at the effective area of $\approx 20000m^2$ (at $E_\mu > 10TeV$) with an angular resolution better 1°. The minimal detectable neutrino flux for DUMAND II is $1.2 \cdot 10^{-10} cm^{-2} s^{-1}$ above $1TeV$.[110, 113]

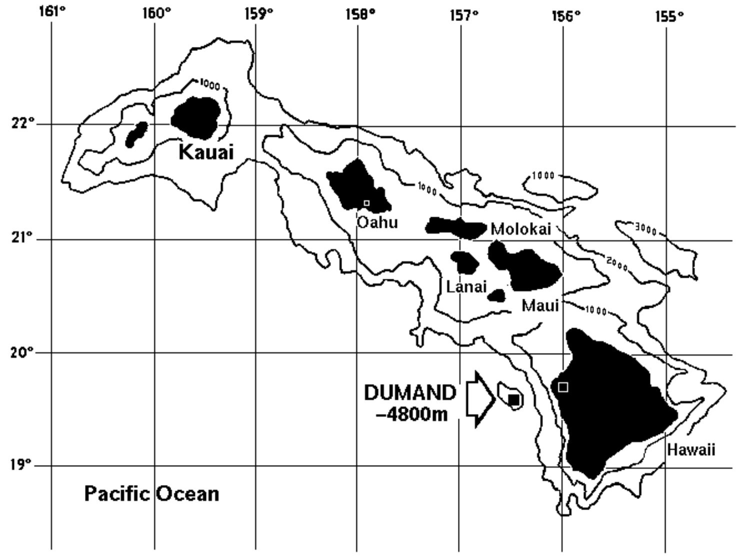

(A)

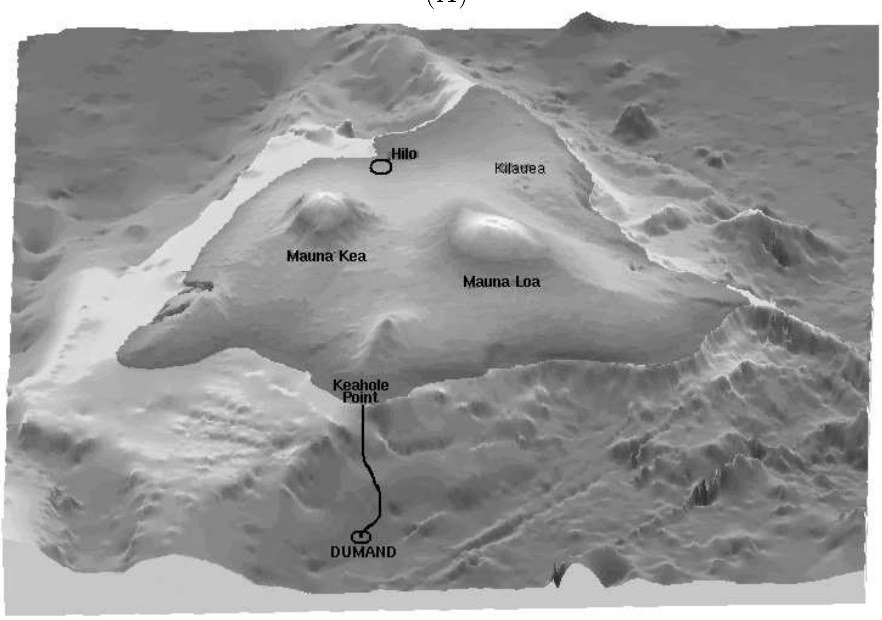

(B)

Figure 4.21: Location of the DUMAND experiment

4.2.1 The DUMAND II detector

Figure 4.22 shows a sketch of the proposed OCTAGON. Eight strings are arranged in an octagon around a centre string. The horizontal spacing is about $40m$. Each string contains 24 optical modules (OM) with a vertical spacing of $10m$. The total string length is $\approx 390m$, the instrumentation starts about $100m$ above ground. Floats at the top and within the strings provide the necessary string tension. Central element in each string is the so called "String Controller" (SC), which performs both: the fast digitisation of signals from the optical modules and the control of all modules in the entire string (see

[1]**D**eep **U**nderwater **M**uon **a**nd **N**eutrino **D**etection

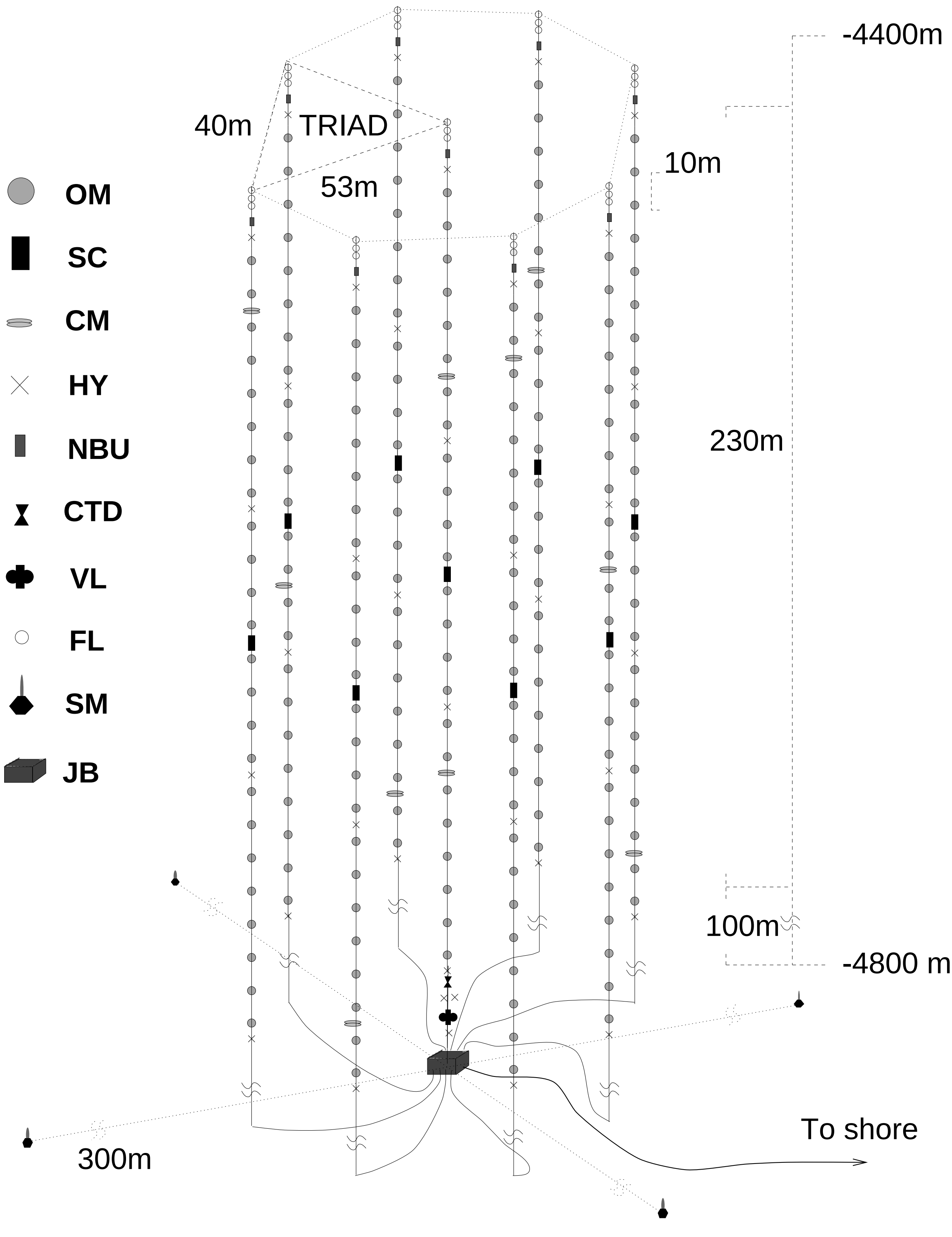

Figure 4.22: The DUMAND II detector (Not to scale!). OM: Optical Module, SC: String Controller, CM: Calibration Module, HY: Hydrophone, NBU: Neil Brown Unit, CTD: Conductivity-Temperature-Depth meter, VL Video & Light, FL: Floats, SM: Sonar Module, JB: Junction Box.

section 4.2.2). Two different types of OM's are used, the JOM[2], based on the conventional large area photomultiplier Hamamatsu *R 2018*, and the EOM[3], based on a new type hybrid photomultiplier Philips *XP 2600*, which uses a combination of an electro-optical pre-amplifier with a small conventional PMT. The diameters of the Hamamatsu and Philips photomultipliers are $38cm$ and $35.5cm$. (see section 5.1.1) [1, 113]

Calibration modules (CM), alternating one or two per string, are mechanically and electronically similar to OM's but contain a laser calibration system for the detector. A scintillator ball, $1m$ distant from the CM is illuminated by two lasers and produces isotropic bright UV-flashes, which are measured by the OMs in the detector. A small photomultiplier inside the CM monitors the reference time of the flash and sends it to the SC. This allows the calibration of the relative response-times and and pulse-heights of the OMs as well as the in-situ measurement of the light attenuation length. [113]

The power to the detector ($20kW$, $1kV$ DC) is provided via an electro-optical cable and a sea return, using a pair of platinum electrodes, one at the shore the other at the detector. The cable ends at a passive box at the bottom of the ocean, the junction box (JB). Each of the total 12 of optical fibres in the cable is lead to a single port. Each string is plugged into one port, either using a deep submergence vehicle or a remotely operated robot. This allows a direct link between each string controller and the shore station. [113]

Several systems to monitor environmental data are integrated within the detector. Attached to the JB is a small environmental string (JBEM), which is mechanically integrated into the centre string. It is also directly connected to the shore, using one of the spare optical fibres. It contains a conductivity-temperature-depth meter (CTD) and a video-camera system and acoustical devices. Each string contains a Neil-Brown-Unit (NBU), which integrates a current meter together with a CTD. Integrated in the SC-pressure housing is an additional environmental system including a compass and a tiltmeter. [110]

The experiment is equipped with a sophisticated acoustical system, containing 53 hydrophones (HY) (5 in each string, 3 at the JBEM, 5 elsewhere) for two reasons. First the accurate reconstruction of muon tracks requires a very precise monitoring of the positions of the OM's and CM's. Secondly it is intended to study the possibility of an acoustical detection of UHE neutrino interactions. This method, if successful, could provide an inexpensive experimental technique for the realisation of very large detection volumes. The acoustic properties of the deep ocean are measured continuously and provide long-term environmental data. The locating system gains an accuracy better than $10cm$ for the relative locations of modules and an absolute geographic position accuracy of a few meters (limited by the GPS accuracy) allowing to maintain celestial coordinates better than 1°. The data-stream from the HYs is digitised in the SCs. [1, 113]

The first attempt to begin the installation of the TRIAD detector in December 1993 was only partly successful. The first string was deployed together with the junction box and the shore cable. However after a few hours the central string controller failed due to a hair-leak in one of its connectors. The central string operated for a few hours, measuring mostly light due to radioactivity and bioluminescence (see figure 3.18 and section 8.2). This demonstrates the disadvantage of a strongly hierarchical design of a remotely operating experiment, since the failure of a central element may significantly harm the total detector. The string was recovered after triggering an acoustic release in January 1994. Since the junction box and the shore cable are still operating it is intended to finish the installation of the three strings of the TRIAD early 1996. It has to be noted, that the DUMAND project is strongly handicaped by an inadequate funding and the unreliability of avaliable ship-time to perform installations. [113]

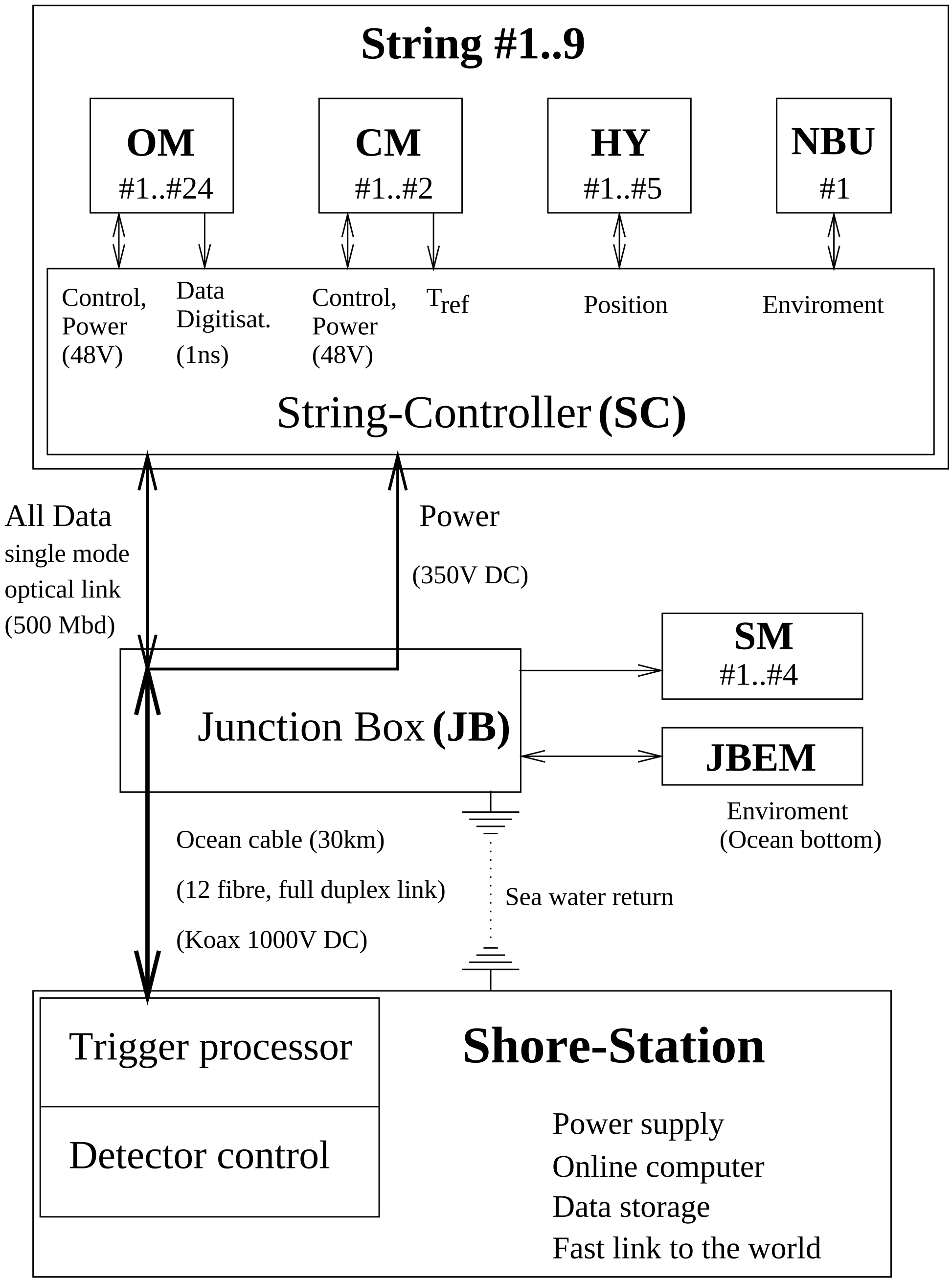

Figure 4.23: Schematic overview on the DUMAND II detector

4.2.2 Signal processing and triggering in DUMAND II

Figure 4.23 shows a schematic diagram of the DUMAND II detector. Each string controller is connected to the shore-station via a passive connection at the junction box. Each OM is connected to the SC via two cables, a coaxial cable for power-supply and slow modem-link and a multi-mode optical fibre for fast data transmission. A computer in each SC, equipped with a 68000 microprocessor running an $OS/9$ operating system, controls the power-supply of all modules in the string. The modem-communication, which is superimposed onto the DC-power-supply allows to connect to each OM,

[2]JOM: **J**apanese **O**ptical **M**odule
[3]EOM: **E**uropean **O**ptical **M**odule

which are also equipped with a computer running OS/9. This link allows to individually control and monitor each OM's internal parameters, e.g. high voltages (see section 5.1.1). Both types of optical modules, JOM and EOM, are interchangeable in terms of communication and system compatibility.

Besides the micro-computer the OM's are equipped with a fast-readout for the photomultiplier signals, which is designed to the specific photomultiplier. The EOM-readout performs a fast charge integration and produces a charge to time (QT) converted signal. The JOM measures the pulse-duration above an amplitude threshold (Time Over Threshold, TOT) and performs, in case of a higher amplitude, also a QT conversion (see section 5.1.1). These resulting pulses are immediately transmitted to the SC via the optical link. [53, 1, 110]

The arrival time and pulse-width of each OM signal is digitised in the SC and transmitted to shore via a full duplex optical link with $500MBd$. Heart of this system is a monolithic multi-hit time-to-digital converter chip. This chip was especially developed for DUMAND II and contains about 200 000 transistors implemented in a $GaAs$ gate array. It is driven by a frequency doubled clock with $750MHz$ to $1GHz$, providing a digitisation accuracy down to $1ns$. It achieves continuous digitisation of 27 channels without dead-time, a pipelined buffering of a total of $\geq$ 48 pulses and a continuous transmission rate of up to $100kHz$ per OM. [1, 53]

Because of the full transmission of the raw detector data to shore, complex trigger strategies for various physical purposes may be implemented at the shore station. The nine serial data streams from the strings are put onto parallel busses and fed into a four level trigger-processor, whose first three levels are resident in a single VME-crate. The first level, implemented in a custom built circuit board, parses the data stream and searches for local coincidences on a single string level. The next two levels, which search for higher level coincidences involving several strings, use commercially avaliable digital signal processors. Finally the data is transmitted via Ethernet to the fourth level, a cluster of workstations. This cluster performs control and monitor functions of the underwater systems, a preliminary data-analysis and the data storage. It is intended to enable access to data and the detector operation via worldwide network communication. [53, 1, 111]

The presence of high background noise rates and the absence of local triggers in the detector requires a fast, efficient, trigger scheme. The expected number of noise hits per $1\mu s$ is of the order of 13 (assuming a single noise rate of $60kHz$ per OM), which is in the same order as the expected signal from a muon event. Even a trigger with more than 25 hits per μs would yield a rate with random noise events of $\approx 1kHz$. [52]

Since the noise signals are almost entirely 1PE signals, but muons generally produce higher signals (at least in one PMT), a simple "energy trigger" on the number of photoelectrons larger than a specific value yields a better suppression of noise. This trigger condition is called $TE > x$PE. This approach can be improved employing optical modules with a good energy resolution in the multi-PE regime. This approach requires a linear read-out for the pulse-height of the OM signal (see section 5.1). [52, 54]

The majority of muon hits involve a hit coincidence in three neighbouring OM's in any string. The time difference Δt fulfills the relation

$$\Delta t \equiv |\ |t_1 - t_2| - |t_2 - t_3|\ | < 15ns\ . \tag{4.59}$$

yielding an efficient trigger called "T3". An alternative is the combination of a local energy trigger with a local coincidence, requiring a large amplitude in one of two OM hits in coincidence or generally a larger TE on basis of one string. [52]

A combination of these triggers can be implemented in the first stage trigger processor, reducing the rate of the noise by a factor of ≈ 1000 and efficiently trigger muon events on a single string basis. [52]

For analysis in later trigger-stages, more effective triggers mainly use the combination of above triggers for several strings. A useful notation is

$$(4.60)\quad T-a-b-c \quad \text{with} \quad \begin{cases} c & : \text{ Value of the coincidence, e.g. } 3 = T3, \\ b & : \text{ Number of c-coincidences in each string, e.g. 2 times T3,} \\ a & : \text{ Number of strings with } b \text{ coincidences of type } c \text{ each.} \end{cases}$$

As an example effective trigger combinations to reduce the noise rate below $1Hz$ without dramatic reduction of the effective area were found for the TRIAD detector to: $T-1-3-3$, $T-2-1-3$, $(T-1-1-3) \wedge (TE > 11\text{PE})$ in case of $60kHz$ OM noise rates and $(T-1-3-3) \wedge (T-1-2-2)$, $(T-1-2-3) \wedge (T-2-1-3)$, $(T-1-1-3) \wedge (TE > 14\text{PE})$ for $100kHz$ OM noise. It has to be noted that 5 hit neighbour OMs fulfil the $(T-1-3-3)$ condition. [68]

It has to be noted that the above trigger-conditions are not valid for non relativistic particles. These require additional hardware components in the trigger processor.

4.3 Other projects

Two other experiments, AMANDA and NESTOR , are also important in discussion of current high energy neutrino detectors and the design of a future km^3 detector. The community of the four current projects is sometimes named BAND[4] A further in-situ test experiment was carried out in the Atlantic ocean by the JULIA project early 1991.

4.3.1 AMANDA

Within the AMANDA experiment the extremely transparent deep ice of the antarctic glacier is used as detector medium instead of deep water. Despite of this it has a similar physical approach and made enormous progress over the last years. It is the only experiment at the southern hemisphere and is thus complementary to neutrino experiments at the northern hemisphere. The experiment is directly located at the south pole using the local infrastructure of the U.S. research station: "Amundsen-Scott". During the months of the antarctic summer holes are melted into the ice and strings with optical modules are installed in depths deeper than $1km$. The detector is not accessible during the rest of the year. On the one hand this installation technique provides the advantages of an easy installation with the possibility to walk and work right on top of the detector, on the other hand it is impossible to recover parts of the detector for repair. It thus requires a very robust design and choice of components. The detector can be expanded very flexible without limitations due to previous installations. Close to the experiment is the location of the SPASE air shower experiment, which allows to measure coincidences between down-going muons and air showers detected at the surface. [6, 99]

A further advantage marks out this experiment: The ice is a sterile medium with a constant temperature $\approx -55°C$. This provides stable operation of electronic components and low noise-rates of the photomultipliers. Furthermore the ice itself contains no radioactive isotopes like ^{40}K and biological matter. Therefore the total signal rate per OM is low ($\approx 2kHz$) allowing simple trigger schemes. [6]

During winter 93/94 four strings with total 80 OMs have been installed in a depth of $800m$ to $1000m$. Since the data acquisition electronics is located close to the detector it is possible to transmit the analogical PMT signals directly to the surface via coaxial cables. In consequence the optical module was designed in a very simple and reliable way containing only $20cm$ ($8''$) diameter photomultipliers[5] without further electronics. Each OM is directly connected to the laboratory without a hierarchical data acquisition scheme inside the detector. During winter 94/95 the data acquisition and calibration systems were upgraded together with an additional system to detect neutrinos from supernova bursts. [3]

[4] **B**aikal **A**manda **N**estor **D**umand.

[5] This PMT has about 30% of the sensitive area compared to BAIKAL and DUMAND II .

Unfortunately it turned out, that the scattering length is very small at this depth but slowly improving with the depth ($12-25cm$). Emitted Čerenkov photons are multiple scattered and perform a "random walk". Thus they loose their initial time information preventing a good reconstruction of the initial muon. However several muons have been detected in coincidence with the air shower array. The strong scatter properties of the ice originates mainly from small air bubbles enclosed in the ice. It is expected, that these bubbles disappear at depths below $1000m$ due to a phase transition. At these depths the scattering lengths may reach several $10m$, limited by dust enclosed in the ice (e.g. due to historic volcanic eruptions). Despite of this it turned out in absorption measurements that the ice is more transparent than expected[6] in the optical region ($500nm$) yielding $\approx 60m$, similar to attenuation in purified water. Furthermore, several independent methods show indirect evidence for an extremely large attenuation length at smaller wavelengths up to more than $200m$ below $400nm$. In consequence the number of detectable Čerenkov photons per unit track rises in comparison to water (see figure 3.16). [3]
The aim for winter 95/96 is to deploy 6 further strings, containing 80 OMs to a depth of $1500m$ to $2000m$. With regard to the expected improvement of optical properties, the spacing between OM's will be significantly enlarged. The deep location requires a modification of the optical modules, in order to be able to transmit the OM signals with the required accuracy. [3]

4.3.2 NESTOR

The Nestor is an European experiment located in the Mediterranean, approximately $15km$ south-east of the coast of the Peleponnisios (Greece), at a depth of $3.5km$. Though many technological aspects are closely related to DUMAND II the geometrical design is different in order to achieve a lower energy threshold for the detection of muons. [77]
The first phase consists of a tower, $200-300m$ tall, which is built of 12 hexagonal (horizontal) structures with a vertical spacing of $20-30m$ between each hexagon. A hexagon consists of 6 arms with a radius of of $16m$. Each hexagon consists of 14 large area OMs with two in the centre and two at the end of each arm. The OMs of each pair look into opposite directions, one down — one up, in order to achieve a $4\pi sr$ sensitivity for the detector. In further expansions of the detector it is intended to deploy 6 additional towers at distances of about $100m$-$150m$ around the first tower, yielding a detector with an effective area of $\approx 10^5 m^2$ and 1176 OMs. [77]
This design may lower the energy threshold for muon detection below $5GeV$ making this detector sensitive for long baseline neutrino oscillation experiments. This may be done by measuring the atmospheric neutrino flux versus the zenith angle, yielding oscillation length from $10km$ to $13000km$. As an alternative, a long baseline oscillation experiment with a neutrino beam from CERN to NESTOR would yield several 1000 events in one tower and thus a good coverage of small mixing angles. [77]
First experimental tests have been performed in situ, lowering one hexagon attached to a cable to depths below $4km$. The small detector was equipped with batteries, CAMAC-electronics in pressure housings to process the data and a computer to record the data to tape. Relative muon fluxes at several depths have been obtained. [77]

4.3.3 JULIA

The aim of the JULIA [7] project was to construct a neutrino telescope with a strong inherent aspect to use this detector as a permanent deep underwater laboratory for interdisciplinary research. [24]
During a small test experiment[8] in the Atlantic ocean, close to the Canary island "Gomera", a small

[6]Previous laboratory measurements showed only absorption lengths in the order of $25m$

[7]**J**oint **U**nderwater **L**aboratory and **I**nstitute for **A**stro-Particle-Physics

[8]This was done in a cooperation between the University of Technology RWTH Aachen (III.Physikalisches Institut, Institut für Lagerstättenlehre) and DESY IfH Zeuthen together with the companies Philips and AEG (Kabel Rheydt).

string containing three optical modules was lowered from a research vessel. The purpose of this cruise was to test advanced but robust technologies for future detectors. Main research aspects have been:

- Each OM was individually connected to a DAQ-system aboard the ship, to avoid a hierarchical structure and thus sophisticated signal processing underwater. This requires a signal transmission link capable of transmitting asynchronous signals from an OM via several km distance preserving a time-jitter better than $1ns$. Links with several km mono-mode optical fibres have been tested. Results show only a marginal degeneration of the time resolution after $4km$ fibre $< 100ps$. Under experimental conditions this system gave proof of reliable working, despite of a water leak in the signal cable. This opens the possibility of transmitting individual signals from OMs over several tens of kilometers, e.g.to a shore station, without significant dispersion and loss of timing accuracy. [24]
- Construction of prototype optical modules containing the new type hybrid photomultiplier, Philips XP2600, together with a fast, self triggering charge integrating readout. The European Optical Modules, described in section 5.2, are based on this development. [2, 63, 24]

The JULIA project did not receive further funding, but experiences have been useful for the BAIKAL and DUMAND II experiments. [63, 140]

4.3.4 Perspectives of underwater neutrino physics

Detector	year	V_{geo} $[10^3 m^3]$	A_{eff} $[10^3 m^2]$	reference
First stage				
NT-36	1993	3	0.27 ($1TeV$), 1 ($10TeV$)	[49]
NT-72	1995	20	0.6 (atm.ν)	[7]
NT-200	$>$ 1996	90	2.3 ($1TeV$), 4.1 ($10TeV$)	[49, 101]
DUMAND II (TRIAD)	$>$ 1996	250	0.3 ($1TeV$), 3.5 ($10TeV$)	[1]
DUMAND II (Oktagon)	$>$ 1998	2000	12 ($1TeV$),26 ($10TeV$)	[70, 69, 113]
AMANDA	$>$ 1996	3000	20	[3]
NESTOR (first tower)	$>$ 1997	250	9 ($1TeV$), 18 ($10TeV$)	[77]
Second stage				
BAIKAL II	—	—	$>$ 100	[42, 119]
AMANDA II	$>$ 1999	30000	$>$ 100	[3]
NESTOR (7 tower)	—	150000	$>$ 100	[77]
km^3 stage				
KM3 (Halzen)	—	990000	750	[119, 42]
KM3 (Learned)	—	785000	1000	[119, 42]

Table 4.1: Parameters of various underwater detectors

In 1994 several workshops were held with the aim to form international working groups to design a large (km^3) detector for high energy neutrino astrophysics. Several design proposals have been done. Table 4.1 gives a summary on various detectors, which are proposed or under construction. [119, 100]

4.4 Mean visual range and the design of a Deep Underwater Muon Detector

The history of the past years showed that considerations such as a robust experimental strategy, easy access to the experimental apparatus and low costs for deployment expeditions have a much larger impact than expected in the early years of the projects. Therefore the primary management consideration is not necessarily the costs of the optical sensor itself.
Despite of this, a fundamental question is the optimisation of a geometrical detector configuration under the prerequisite of a given (fixed) number of optical modules [83]. A second important item is the choice of the appropriate optical sensor itself and the design of the optical module [101, 109].

Assume a cubic grid with the side length L and N optical modules fixed to vertical strings, filling the volume of the detector. The optical modules are horizontally and vertically separated by the *spacing* b. The number of sensors N is

$$N = \left(1 + \frac{L}{b}\right)^3 \approx \frac{L^3}{b^3} \; .$$

Since the total volume is given by $V = L^3$ the detector volume per optical sensor v is

$$v = \frac{V}{N} \approx b^3 \; . \tag{4.61}$$

In order to maintain a big (inexpensive) detector volume, it is highly desirable to achieve a large spacing b of optical modules. The best spacing is derived from a full analysis of the detector perfomance, especially concidering effective area and good track reconstruction capabilities (see also chapter 2.4 and [101, 110]).

In order to determine the largest possible spacing a first order estimate may be achieved, investigating the *mean visual range* L_{vis} of an optical module. L_{vis} depends mainly on the light attenuation in the water, the sensitivity of the optical sensor and the minimal detection threshold per OM. Sensitivity and attenuation are closely connected. A more sensitive OM may detect smaller photon fluxes from a more distant muon. A stronger attenuation requires a more sensitive sensor to maintain the same visual range[9] (see also chapter 3.4 and appendix A.2). The minimal detection threshold depends on the specific detector. In order to understand this the reader may assume a muon passing through a detector with several layers of optical modules. For a small detector a clear identification requires a hit in every layer, which is not necessary for a detector with a larger number of layers. Therefore the required detection probability and thus the minimal detection threshold is smaller for larger detectors. Obviously a smaller detection threshold is equivalent to the use of a more sensitive optical module.
A calculation of L_{vis} requires a full integration over the probability P of a muon to generate a signal above the threshold A_{PE}

$$L_{vis} = \sqrt{2 \cdot \int_0^\infty r \cdot P(> A_{\mathrm{PE}}, \bar{m}(r)) \cdot dr}. \tag{4.62}$$

$\bar{m}(r)$ is the mean number of photo-electrons[10] for a muon passing at the perpendicular distance $d_\perp = r$. The probability P to produce a signal above the threshold A_{PE} is given by the incomplete gamma function analogous to section 3.5, which yields the cumulative Poisson probability function to produce a signal above A_{PE} [91, 158]

$$P(> A_{\mathrm{PE}}, \bar{m}(r)) = \mathcal{G}(A_{\mathrm{PE}}, \bar{m}) \; . \tag{4.63}$$

Figures 4.24 demonstrates the above discussions. The diagram shows the mean number of photo electrons $\bar{m}(r)$ [11] from a minimal ionising muon track for different light attenuation. Using the contour

[9] It has to be noted, that due to the geometry of the Čerenkov effect the distance d, the light travels is longer than the perpendicular distance $d_\perp$ to the track, which is equivalent to L_{vis}. It is $d = d_\perp / \sin\Theta_c \approx 1.5 \cdot d_\perp$.

[10] $\bar{m}(r)$ is given by eq.(A.130) using $d = r/\sin\Theta_c$.

[11] This is calculated from the photon density (figure 3.17) using eq.(A.130), appendix A.2, assuming a peak quantum efficiency $\varepsilon = 0.15$ and the diameter $2 \cdot R_0 = 38cm$ for a full illuminated optical sensor.

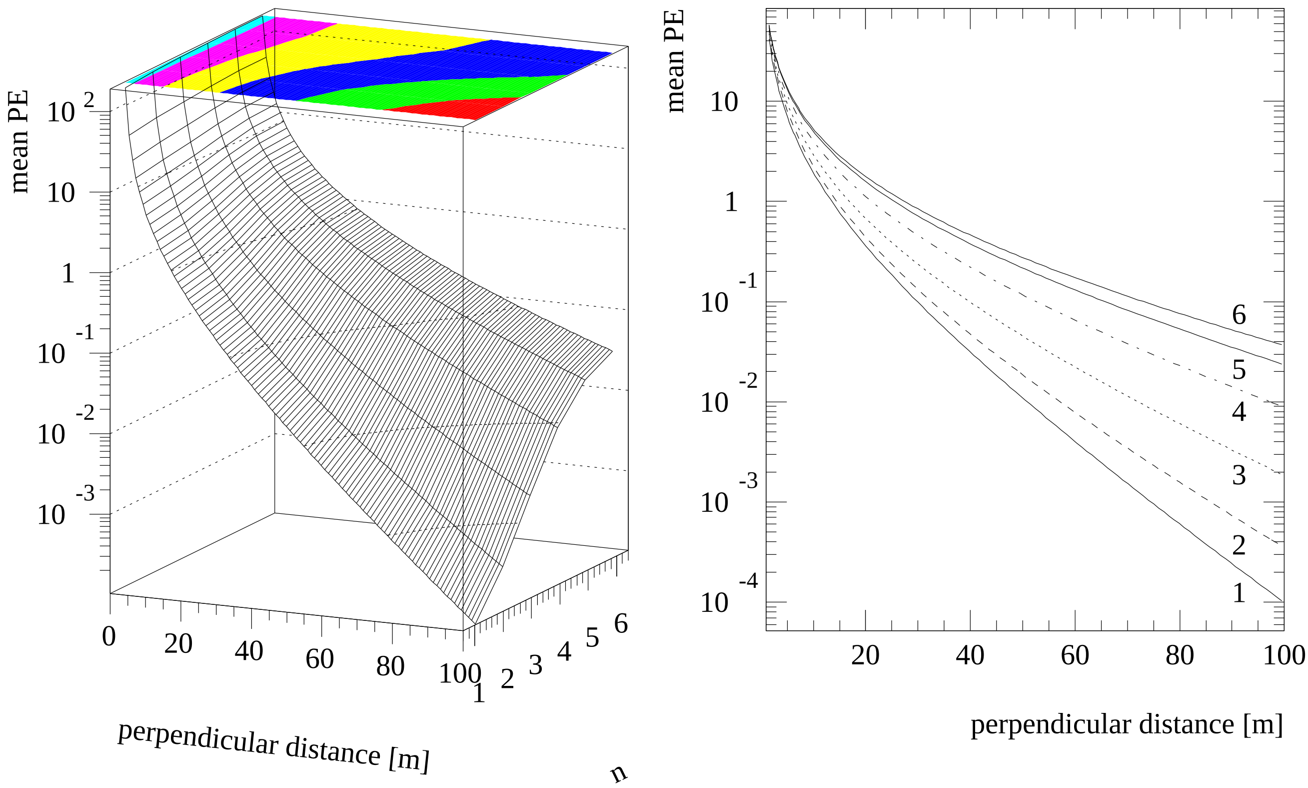

Figure 4.24: Number of photoelectrons from a minimal ionizing track versus distance for several types of water ([51]) $n = 1 \ldots 6$ corresponds to attenuation lengths: $20m$, $25m$, $30m$, $40m$, $50m$, $60m$. $20m$ corresponds to lake Baikal water, $40m$ to DUMAND−water, $50m$ to clearest observed ocean water and $60m$ to purified water of proton decay experiments.

lines in figure 4.24 (A) or drawing a horizontal line into figure 4.24 (B) at a given threshold yields the variations of the mean visual range for different attenuations. A less sensitive (smaller) sensor or an illumination from the side corresponds to a higher threshold in the figures. It can be seen, that for high thresholds (small OM's) the influence of the attenuation is much smaller than for low thresholds (large OM's).
Considering the detectability of a certain muon flux the visual area $A_{vis}\pi \cdot L_{vis}^2$ becomes important (see eq.(4.62). A_{vis} depends on the radius of the optical module R_0. Neglecting attenuation and using a sensitivity proportional to the OM area ($\propto R_0^2$) one gets

$$A_{vis} \propto R_0^4 \; . \tag{4.64}$$

However especially for low detection thresholds and a large radius R_0, this is not realistic. Using the parameters of present experiments one gets a much weaker dependency

$$A_{vis} \propto R_0^{1.2 \ldots 1.8} \; . \tag{4.65}$$

It has also to be noted, that it is not realistic to increase the sensitivity of optical modules in the deep ocean above the present values, because of a strong increasion of the count rates due to ^{40}K decays. [82, 42]

Another important aspect is the use two OMs switched to a local coincidence (BAIKAL) instead of individual OM's (e.g.DUMAND).

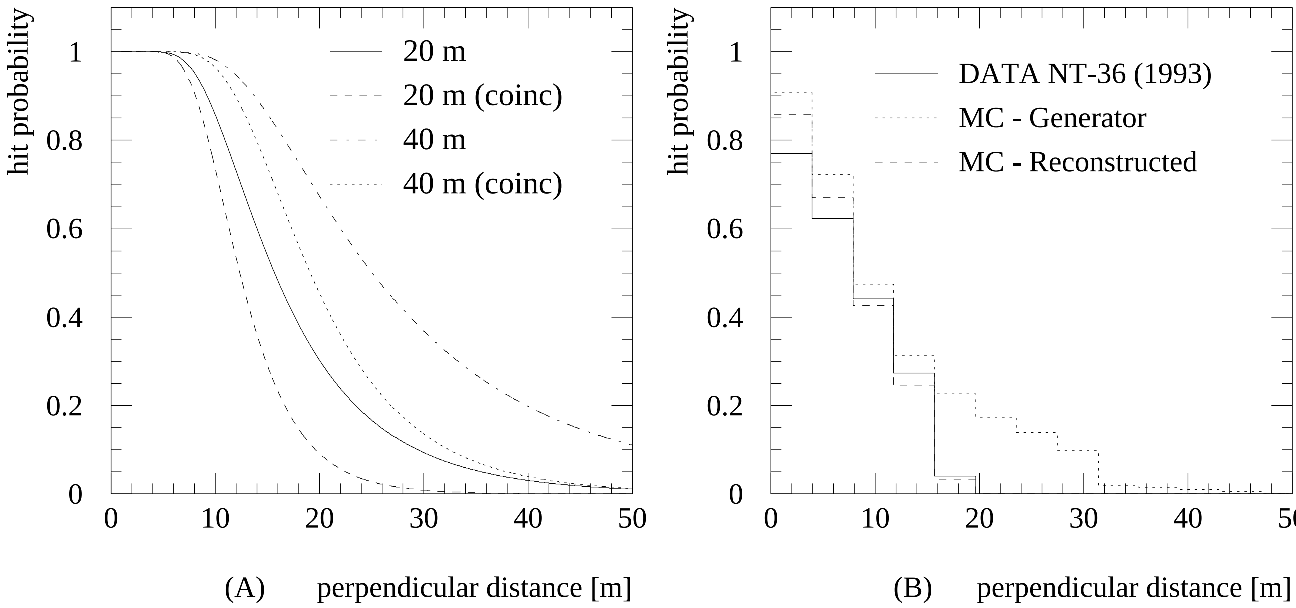

Figure 4.25: Hit efficiency versus distance to the OM. (A) shows the calculated hit probability for full illuminated single and coincident OM's, each for $20m$ and $40m$ water. (B) shows experimental and Monte Carlo data from the NT-36 detector. The MC-data includes a simulation of atmospheric muon bundles and a reconstruction ([49]). Plotted are the distributions for all generated tracks (MC-Generator) and for all reconstructed tracks, which pass all quality criterias (DATA,MC-Reconstructed).

This brings the disadvantage that the required number of optical modules is doubled and due to the coincidence condition the mean visual range on becomes smaller. L_{vis} may be calculated modifying P in eq.(4.63) via

$$P \equiv \mathcal{G}(A_{\mathrm{PE},1}, \bar{m}_1) \cdot \mathcal{G}(A_{\mathrm{PE},2}, \bar{m}_2) = \mathcal{G}(A_{\mathrm{PE}}, \bar{m})^2 \ . \tag{4.66}$$

The right part of the equation is valid for identical sensors and thresholds.

The advantages are a much easier signal processing (see sections 4.1.2, 4.2.2 and 7.2.4) and the possible use of simple and fast reconstruction algorithms without the need of sophisticated noise reduction algorithms[12]

Figure 4.25 (A) shows the calculated hit probability for $20m$ and $40m$ attenuation length of the water for single OM's and two coincident OM's. Assumed is an OM with fully illuminated photocathode and 100% trigger efficiency for 1PE signals ($A_{\mathrm{PE}} = 1.0$). For short distances the hit probability for coincident and single OM's does not differ largely.

Figure 4.25 (B) shows a comparison between Monte Carlo and experimental data for the NT-36 detector. The hit probability does not reach 1 for small distances, because sometimes modules show no hit for close tracks. This is an effect of different orientations of optical modules to atmospheric muons and the dead-time of the modules themselves. Because NT-36 is a small detector, tracks more distant than $20m$ from an OM's mostly pass outside of the detector. Therefore these tracks are likely to fail trigger conditions or quality criteria after reconstruction.

Eq.(4.66) can be generalised to n identical optical sensors with the same threshold located at the same

[12] To demonstrate the difference: Each event in DUMAND II contains about 50% hits which are due to noise. In the BAIKAL NT-36 detector only 0.1 % of all events contain one channel with a noise hit.

space-point. Requiring at least m hit OMs out of n yields

$$P = \sum_{k=m}^{n} \binom{n}{k} \cdot (\mathcal{G}(A_{\mathrm{PE}}, \bar{m}))^k \cdot (1 - \mathcal{G}(A_{\mathrm{PE}}, \bar{m}))^{n-k} \tag{4.67}$$

As an example the requirement of at least 2 hit out of 3 OM gives

$$P = \mathcal{G}^3 + 3 \cdot \mathcal{G}^2 \cdot (1 - \mathcal{G}) \ .$$

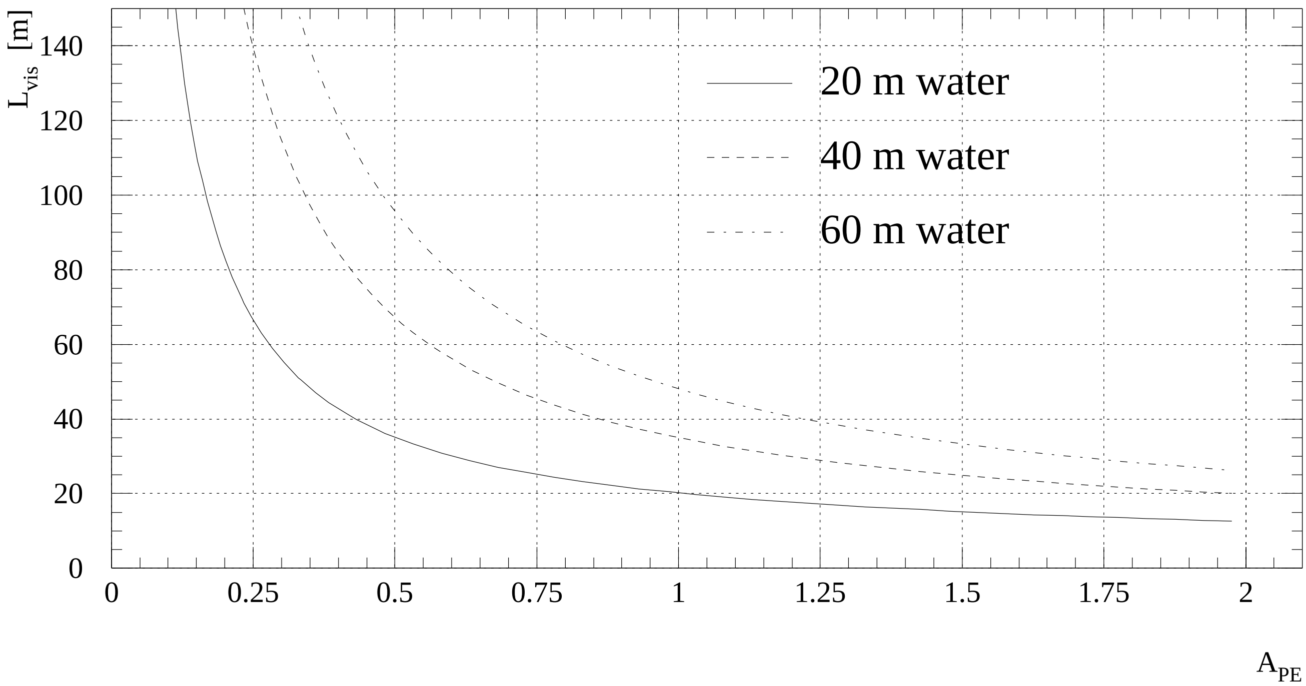

Figure 4.26: Mean visual range for a single OM versus amplitude threshold for $20m$ and $40m$ water

A calculation of the mean visual range requires setting A_{PE} to the appropriate value and performing the integration eq.(4.62). An ideal photomultiplier allows only natural values for $A_{\mathrm{PE}} = 1, 2, \ldots$. However using the argument for a big detector (page 51), that not necessarily each OM, which should have a hit, must indeed have a hit, a fractional value of e.g. $A_{\mathrm{PE}} = 0.5$ may be interpreted as an amplitude threshold of 1PE with a hit efficiency of only 0.5. Figure 4.26 shows the results for A_{PE} ranging from $0.1PE$ to $2PE$. For smaller amplitudes the differences between the different attenuation lengths become larger. Thus a large km^3 detector with a lower threshold allows a significantly larger spacing if the detector operates in clearer water.

5 The Optical Sensors

5.1 Optical Modules for DUMAND II and BAIKAL

Optical modules may be designed in a large variety. While the OMs for AMANDA consist only of a naked photomultiplier glued into a glass pressure housing, the OMs for DUMAND II also contain a complex control system and fast readout for the photomultiplier. As an example figure 5.27 shows a sketch of the European Optical Module (EOM) for DUMAND II .

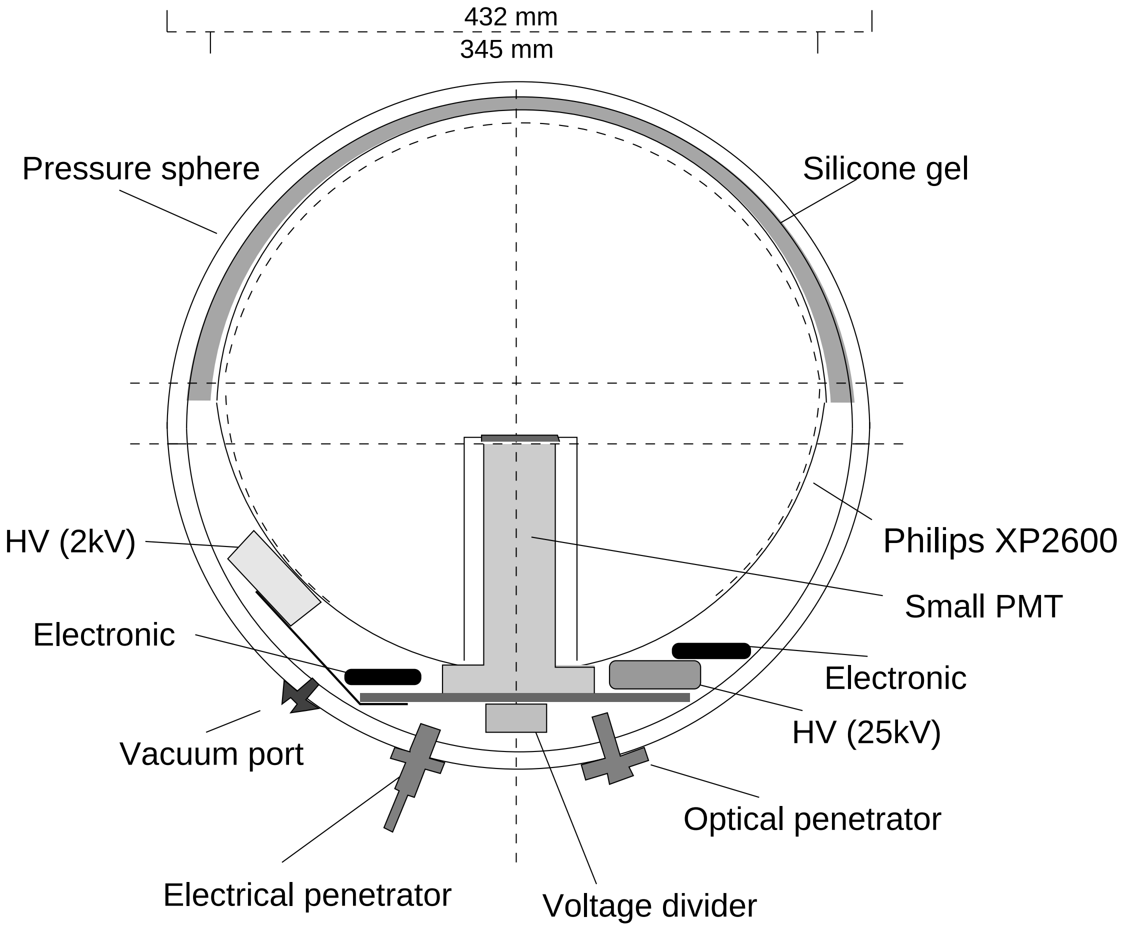

Figure 5.27: Sketch of the EOM.

Two types of optical modules, the EOM for DUMAND II and the Baikal OM (BOM), contain a new type of large area photomultiplier (PMT). The principle of a hybrid PMTs and its advanced properties will be discussed exemplarily for the EOM in the following.

5.1.1 Optical Modules for DUMAND II

DUMAND II contains 2 different OMs, which have been designed in a parallel development in Japan (JOM) and Germany (EOM). They are interchangeable in respect of the interfaces to the rest of the detector. [53]

The EOM was developed on basis of the JULIA OM, using the large area phototube, Philips XP2600, and the fast read-out, “DMQT”. The phototube is constructed according to a new principle, the combination of an optical pre-amplifier with a small $23mm$-diameter photomultiplier XP2982. This technique yields advanced characteristics with respect to time and amplitude resolution ("smart PMT" [108]). The fast read-out DMQT performs a fast charge integration and produces a rectangular signal, whose leading edge gives the response-time of the photomultiplier and whose width is proportional to the integrated charge (number of PE). For high amplitudes the width scales logarithmically with the number of PE. A detailed description of the design is given in section 5.2 and its properties in 5.3. [1, 2, 140]

The JOM is a significantly improved descendant of the OM used for the DUMAND I experiment. Similar to the EOM, the JOM is composed of a large photomultiplier with a fast read-out, power-supply and a remote control unit (RCU) based on a 68301-CPU. Heart of the JOM is the $38cm$ diameter photomultiplier Hamamatsu $R2018$. Major advantage of this PMT are short pulses, allowing to detect consecutive hits, which are separated by more than $20ns$. It is aimed to take advantage of this for the identification of muon bundles. The timing and pulse-height characteristics are injured by the general approach, to increase the cathode area to a large diameter with a spherical shape and do not reach excellent values of small photomultipliers. However the timing characteristics and pulse-height resolution have been significantly improved compared to its predecessor due to an optimisation of the cathode shape and the dynode structure. The PMT reaches a transit-time-accuracy (FWHM) of about $6ns$ for 1PE signals in full illumination. The transit-time differences with respect to different angles of illumination are of the order of $< 3ns$. A single photo-electron peak is visible in distributions of dark noise. In order to achieve a full sensitive cathode area, the PMT has to be shielded by a μ-metal grid against the earth magnetic field. [4, 1, 112]
The fast readout measures the pulse duration (time over threshold, TOT) and additionally measures the integrated charge (Q) for pulses larger 3PE. The OM produces a rectangular pulse, whose leading edge gives the response-time of the PMT and its width the TOT. If a Q measurement is present a second $200ns$ delayed pulse is produced, with a width proportional to the logarithm of the integrated charge. [1, 112]

5.1.2 The Optical Module for BAIKAL

The optical module for BAIKAL consists mainly of the photomultiplier "Quasar-370". This hybrid photomultiplier is an advanced copy of the Philips XP-2600. It has a mushroom shape, which is optimised in respect of transit-time differences from different cathode points. Values better than $1ns$ have been achieved. Other properties are similar to the XP-2600. [59, 19, 101]
The glass pressure housing was especially developed for the BAIKAL experiment. Because BAIKAL is located relatively shallow (1.1 km) the housing has thinner walls compared to deep ocean pressure housings. The optical contact between the cathode and the pressure-sphere is achieved by liquid glycerine, which is sealed by an equatorial ring of poly-urethane. The OM is not transparent from the back.
High voltage-supplies, a voltage divider and a LED are included inside the OM pressure-sphere. The control and read-out electronics is housed by the "Svjaska Electronic Module" (see sect.4.1). The pulse-charge is linearly integrated. A Q-T transformed pulse is transmitted whose width is linearly proportional to the number of PE. The dynamic range goes from 1PE to several hundred PE. A good linearity is guaranteed up to 100PE. [19, 101]

5.2 Design of the European Optical Module

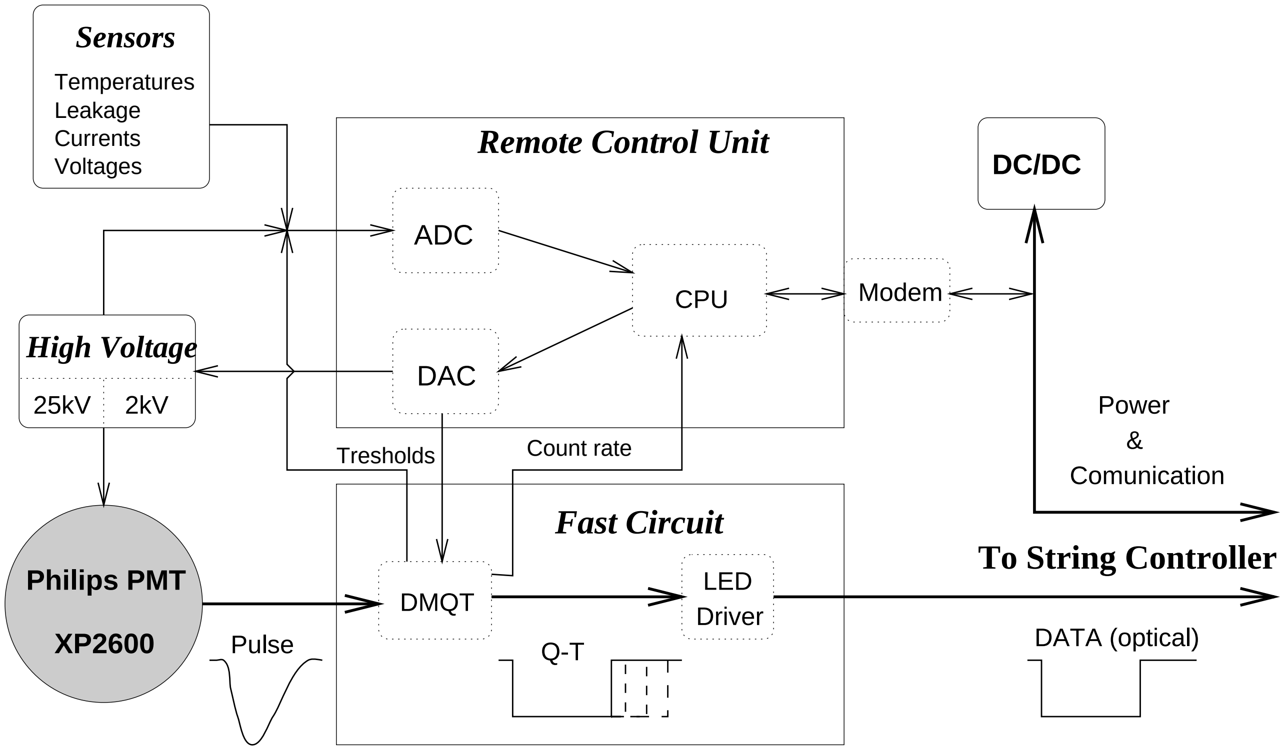

Figure 5.28: Schematic diagram of the EOM

The EOM is a self-contained detector for faint light. All functional parts are included in a glass pressure housing ($43cm$ outer diameter), which is available for standard deep ocean applications. The functional units are schematically drawn in figure 5.28, and a sketch is shown in figure 5.27. These are:

- The large photomultiplier (section 5.2.1).
- The "fast electronics" (section 5.2.3).

  PMT-signals are charge integrated in a fast circuit called DMQT. The Q-T signal is converted to an optical signal and directly transmitted to the outer world via a multi-mode optical fibre through an optical penetrator in the pressure sphere.
- A Remote Control Unit (RCU), called the "slow electronics"(section 5.2.4).

  A specially designed ROM-based micro computer handles monitoring and setting of various module parameters. It communicates to the outer world via a serial modem link, which is superimposed onto the power-supply to the OM.
- The OM receives $48V$ DC power via an electrical penetrator. DC-DC converters generate the supply voltages for the electronic circuits.
- The Philips PMT requires two high voltage supplies. One of these is fixed to $25kV$, but can be switched on and off by the RCU. The other is adjustable from 0 to $1.7kV$.

In order to discuss further details of the design it is necessary to introduce the concept of a hybrid PMT with the Philips PMT taken as example.

5.2.1 The "smart" photomultiplier XP-2600

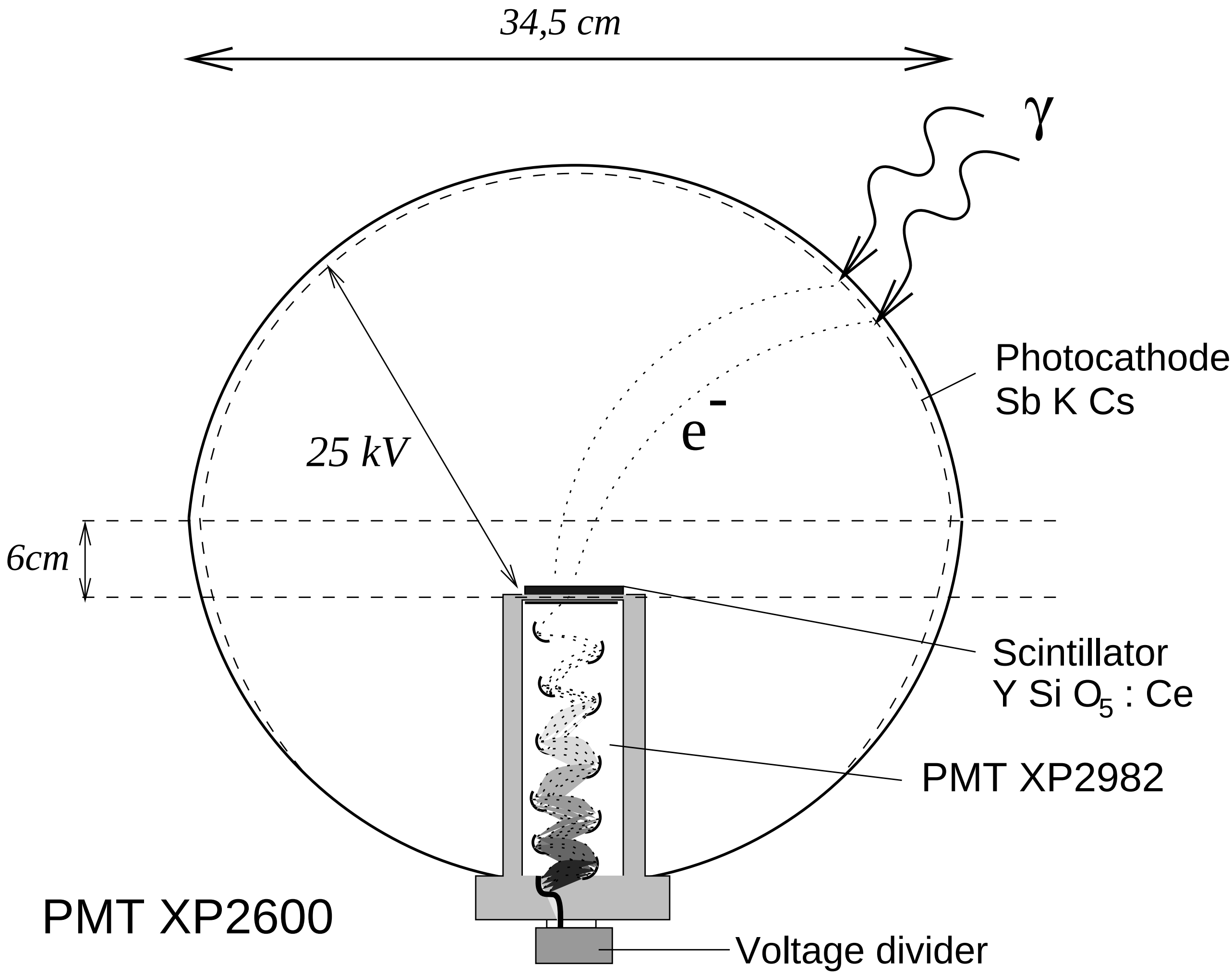

Figure 5.29: The "smart" photomultiplier Philips XP2600

The photomultiplier consists of the combination of an electro-optical pre-amplifier with a conventional small phototube.
Photoelectrons, emitted from a large area hemispherical photocathode, (35 cm diameter) are accelerated by a high voltage ($25kV$) to an aluminium coated scintillator placed near the centre of the glass–bulb. This scintillator is read out by a small, fast, 11–stage phototube (Philips XP2982), placed in a recess at the back of the photo tube.

$$\xrightarrow{\gamma} \underbrace{\boxed{\text{cathode } \emptyset 35cm} \xrightarrow[25kV]{e^-(1\text{PE})} \boxed{\text{scintillator}}}_{\text{optical pre-amplifier}} \xrightarrow{\approx 300\gamma} \boxed{\text{conventional fast PMT}} \xrightarrow{\approx 30\text{PE}}$$

This method yields several major advantages ([2, 91, 35]):

1. The photomultiplier achieves a very high gain, typically 30, in the first stage. Usually statistical fluctuations in the first stage dominate the energy-resolution and the time resolution of a PMT.

This high gain provides excellent time and energy resolution-properties for low PE energies. The time jitter is $\approx 5ns$ and the energy resolution $\approx 50\%(FWHM)$[1] for 1PE signals.

2. The scintillator converts the photo-electron energy isotropically into secondary light. This avoids typical problems of large area PMTs. The gain (secondary emission factor) is independent of the point on the cathode, from which a photo-electron originates and thus the PMT shows a uniform amplitude response. Also no pre-pulsing due to badly focussed electrons occurs.

3. The high voltage provides a high collection efficiency ($\approx 100\%$) and thus uniform sensitivity over almost the total cathode area. The PMT is only weakly influenced by magnetic fields and does not have to be shielded against the earth-magnetic field. A Mu-metal cylinder around the small PMT provides a good shielding for the later amplification stages.

A sketch of the PMT is drawn in figure 5.29. The glass bulb is covered up to $3\pi sr$ with a bialkali ($SbKCs$) photocathode, which has a high quantum efficiency combined with a low thermionic emission. Due to its spherical shape and it's backward transparency the PMT is capable of detecting light from all directions.

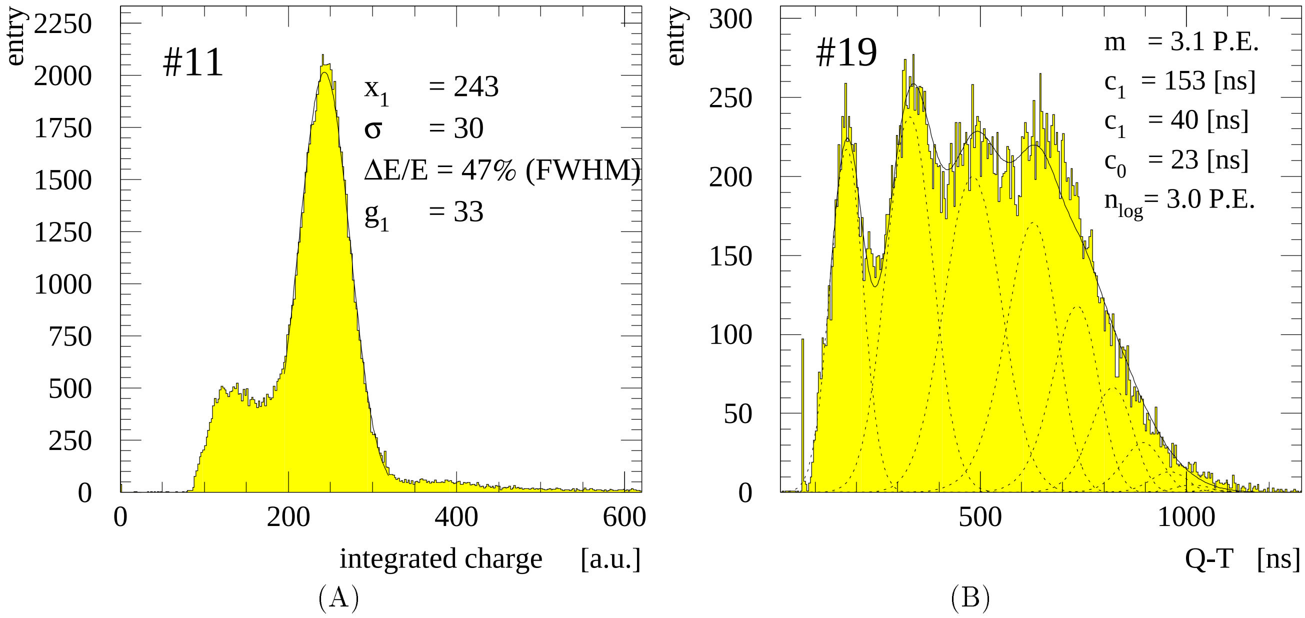

Figure 5.30: Typical charge distributions of the "smart" PMT.
(A) A distribution of the integrated charge of dark noise pulses (PMT # 11). A Gaussian with the width σ and the centre value x_1 is fitted to the distribution.
(B) Pulse-width (QT) distribution of EOM # 19 for illumination with a fast LED (mean intensity: $\bar{m} = 3.1$PE). Clearly visible are peaks due to 1, 2 and 3 converted photo-electrons. A fourth peak occurs due to a change of the energy scale from a linear to a logarithmic scaling at ≈ 3PE. The amplitude function, described in section 5.3.2, is fitted to the distribution. Contributions due to different photo-electrons are plotted with dotted lines below the distribution.

Figure 5.30 shows typical energy distributions. Dark noise pulses consist mainly of thermionic electrons emitted from the cathode and have thus mostly an amplitude of 1PE. The distribution of 1PE signals can be described well by a Gaussian (figure 5.30 (A)). Typical values for the energy resolution range between 45% and 70% (FWHM) for different PMTs. If one assumes a constant secondary emission factor $\bar{g}$ for the small PMT, the gain of the first stage g_1 can be calculated from the energy resolution

[1] **F**ull **W**idth **H**alf **M**aximum

via

$$g_1 = 5.52 \cdot \left(1 + \frac{1}{\bar{g} - 1}\right) \cdot \left(\frac{\Delta E}{E}\right)^{-2} . \tag{5.68}$$

[91, 137]
The distributions of individual photo-electrons are clearly visible and allows a good separation up to several PE (see figure 5.30 (B)).

A good energy resolution is important for following purposes:

- For triggering in the ocean it is highly desirable to discriminate against the background due to ^{40}K decays, which consists almost entirely of 1PE pulses. E.g. for 45% energy resolution and a trigger threshold at 1.4PE it is possible to reject 98.2% of 1PE signals with the loss of only 1.3% of multi PE signals. With the energy resolution of 65% it is still possible to reject 92.6% of 1PE while loosing 6.3% of multi PE signals. [54, 91]
- An OM with good energy resolution can be calibrated in situ without external light, using the clear signature of the 1PE dark noise peak (see figure 5.30 (A) and appendix B.3). Internal discriminator thresholds and the high voltage can be adjusted until dark noise below 1PE (due to the small PMT) is efficiently cut out.

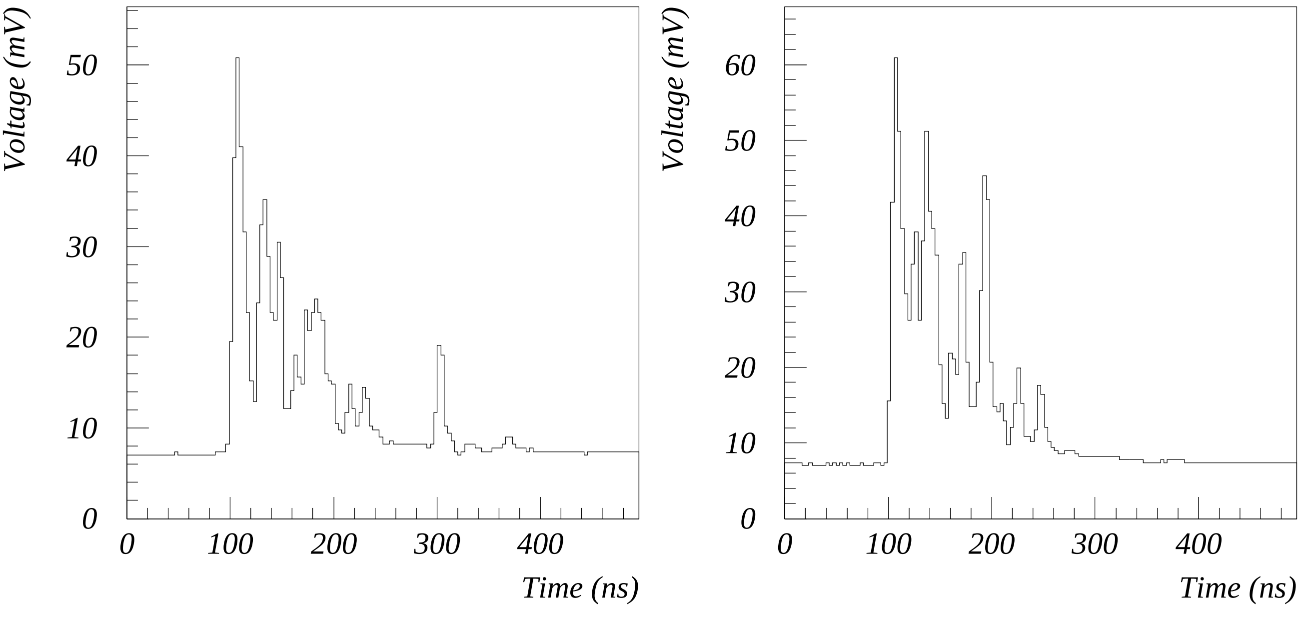

Figure 5.31: Pulse structure of the "smart" PMT. The figure shows two typical 1PE pulses sampled with a FADC ($300MHz$, $8bit$ amplitude resolution [142]).

The achievable time resolution is mainly limited by two reasons which are discussed in details in section 5.3.3. The first is due to geometrical transit time differences for the emission of photoelectrons from different points of the photocathode. Typical transit time differences are 4-5ns between zenith angles 0° and 90° in point-illumination. With the construction of the Russian "smart" PMT *Quasar-370* it was demonstrated, that it is possible to reduce transit time differences below $1ns$ using a mushroom shape of the PMT. It was calculated, that this is also possible for the Philips XP-2600. [59, 91] For full illumination and amplitudes higher than 1PE the time uncertainty due to geometrical transit-time differences is much smaller ($< 1ns$). [91, 92] The second contribution occurs mainly due to the internal time jitter of the PMT during the signal conversion. Figure 5.31 shows two typical PMT pulses. One sees the stochastic emission of photons from the scintillator, which are individually detected by the

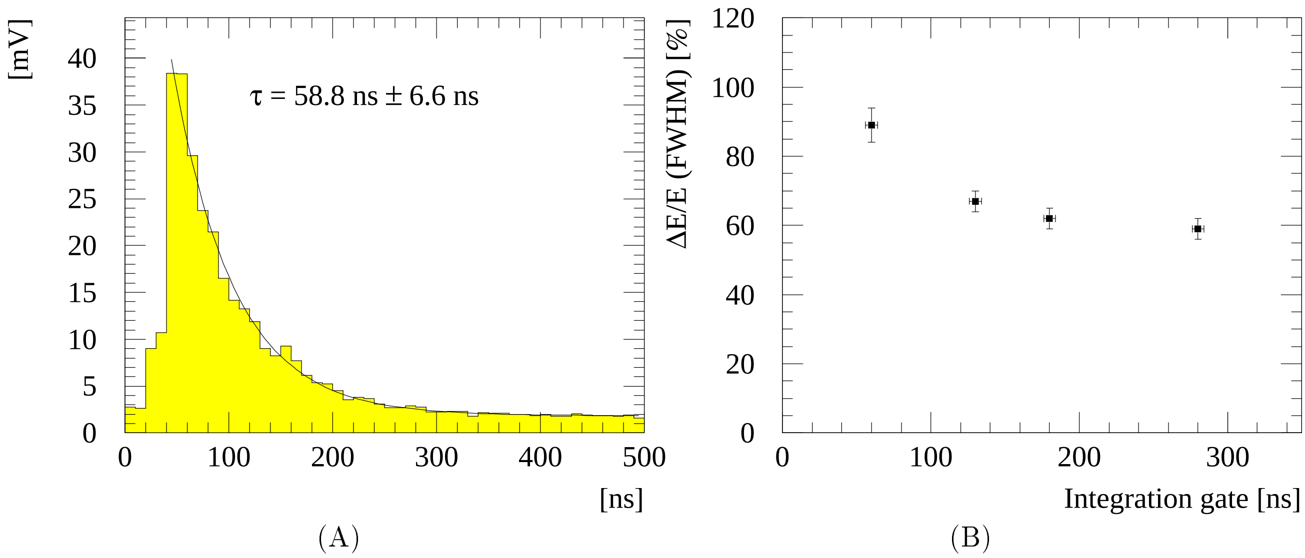

Figure 5.32: Scintillator decay and integration time for the "smart" PMT.
(A) shows the scintillator decay of (PMT #27). 100 1PE pulses, which were sampled with a FADC ($100MHz$, $6bit$ amplitude resolution [142]), are superimposed. An exponential decay is fitted to the data. (B) shows the energy resolution (FWHM) for the 1PE peak as a function of the time used for the charge integration.

fast small PMT (time resolution $\approx 0.5ns$). For the XP-2600 the time resolution is mostly limited by the long decay time τ ($\approx 60ns$) of the scintillator. Figure 5.32 (A) shows a measurement of the scintillator's decay time, which was done for each EOM [93]. Several pulses have been sampled and superimposed. An Exponential with the decay time τ is fitted to the distribution.
A characteristic quantity for time resolution is the value τ/g_1, where g_1 is the gain of the first stage. This value can be improved by both: first a faster and second a more efficient scintillator. In addition the light yield in the first stage can be increased with a better optical coupling of the small PMT to the scintillator. This was done during the assembly of EOMs (see section 5.2.5). An improvement of the light yield also improves the energy resolution. [91, 35]

5.2.2 Read-out considerations

A general consideration for the design of a fast read-out is the decision between charge integration (Q-T) or the measurement of the time-duration above a threshold (TOT). Advantage of the TOT method is, that it can be realized in a very fast circuit with almost no dead-time. On the other hand this method gives only a logarithmic dependence to the pulse-charge and small pulse fluctuations strongly influence the energy resolution. It is obvious from figure 5.31, that in case of the EOM a TOT method is ruled out, due to the bunched time structure of the PMT signals.
Another choice is a linear charge conversion to a Q-T signal (as done for the BOM) or a logarithmic conversion (as done for the JOM) with the aim to achieve a higher dynamic range. In case of the BOM the dynamic range is limited to a few 100PE, and in order to see the distribution of 1PE dark noise pulses the BOM has to be run in a special operational mode. In case of the JOM the integrated charge is measured only for signals above 3PE and the TOT method (which is equivalent to a logarithmic dependency) yields in general only a poor energy resolution.
The EOM performs a mixture of linear and logarithmic conversion of the charge. Though the read-out itself performs a strictly linear charge conversion, the measurement turns over to a logarithmic scaling above typically 3PE. An amplifier with a dynamic input range of $2V$ is switched before the fast read out. As result the signal's charge above this threshold is not integrated and the charge conversion

Amplitude	Pulses above this threshold [%]			$\frac{RMS}{Mean}$
$\mathrm{PE} = 1.0$	$> 1.5\mathrm{PE}$	$> 3.0\mathrm{PE}$	$> 6\mathrm{PE}$	
True	0.0	0.0	0.0	0.0
EOM-QT	4.3	0.0	0.0	0.29
JOM-QT	—	4.0	0.02	—
JOM-TOT	25.0	7.1	0.8	1.19
$\mathrm{PE} = 100.0$	$> 150\mathrm{PE}$	$> 300\mathrm{PE}$	$> 600\mathrm{PE}$	
True	0.0	0.0	0.0	0.0
EOM-QT	0.0	0.0	0.0	0.03
JOM-QT	3.9	0.1	0.0	0.26
JOM-TOT	19.	2.0	0.1	0.68
$\overline{\mathrm{PE}} \approx 1.0$	$> 1.5\mathrm{PE}$	$> 3.0\mathrm{PE}$	$> 6.0\mathrm{PE}$	
True	26.6	2.0	0.01	0.98
EOM-QT	24.9	5.9.	0.2	1.05
JOM-QT	—	7.6	0.4	—
JOM-TOT	23.1	9.0	1.9	1.61
$\overline{\mathrm{PE}} \approx 10.0$	$> 15\mathrm{PE}$	$> 30\mathrm{PE}$	$> 60\mathrm{PE}$	
True	5.0	0.0	0.0	0.32
EOM-QT	6.2	0.0	0.	0.33
JOM-QT	7.8	0.0	0.0	0.39
JOM-TOT	21.4	3.2	0.2	0.83
$\overline{\mathrm{PE}} \approx 100.0$	$> 150\mathrm{PE}$	$> 300\mathrm{PE}$	$> 600\mathrm{PE}$	
True	0.0	0.0	0.0	0.10
EOM-QT	0.3	0.0	0.0	0.17
JOM-QT	5.0	0.08	0.0	0.29
JOM-TOT	19.7	1.9	0.04	0.67
$\overline{\mathrm{PE}} \approx 1000.0$	$> 1500\mathrm{PE}$	$> 3000\mathrm{PE}$	$> 6000\mathrm{PE}$	
True	0.0	0.0	0.0	0.03
EOM-QT	1.6	0.0	0.0	0.20
JOM-QT	34	17.5	9.3	(175000)
JOM-TOT	19.5	1.7	0.04	0.65

Table 5.2: Comparison of the JOM-TOT, the linear EOM QT and the logarithmic JOM QT read-out. 10^5 pulses have been simulated using the description of the JOM [71] and the EOM (section 5.3.2). The table shows the percentage of pulses above a threshold after re calculation of the initial amplitude. It gives also the RMS-deviation divided by the mean of the input amplitude. Simulations have been done for fixed signal amplitudes ($\mathrm{PE} = 1, 100$) and Poisson distributed mean amplitudes ($\bar{\mathrm{PE}} = 1 \dots 1000$).

becomes similar to a time over threshold measurement[2]. This yields a larger dynamic range with an excellent resolution for a few PE.

In order to preserve the energy resolution capabilities and to separate between 1, 2, 3 and more photoelectrons a linear read-out is necessary. A logarithmic read-out produces asymmetric non-Gaussian distributions. If an additional jitter, e.g. due to the electronic and the signal transmission, is convoluted with the signal, a back transformation becomes rather unstable and has the tendency of imitating large pulse energies. This can be seen in table 5.2, which shows simulations of the pulse-amplitude for the EOM and JOM including electronic effects.

[2]For very high amplitudes ($> 100\mathrm{PE}$) internal saturation effects in the PMT and the voltage divider yield a further logarithmic flattening of the PMT gain.

From the investigation of the JOM-TOT conversion it can be concluded, that on the one hand the energy resolution is too poor to efficiently discriminate 1PE signals (ocean noise) against higher amplitudes. E.g. assuming a 1PE ocean noise rate of $80kHz$ the imitation rate of signals above 3PE is still $5.5kHz$. On the other hand the TOT method is stable with a constant energy resolution achieving a dynamic range up to $>$ 1000$\overline{\text{PE}}$. The TOT is the fastest read-out method, which enables a double pulse resolution of subsequent OM hits, if they are separated several tenth of ns.
Comparing the linear and logarithmic charge integration it can be seen, that for intermediate[3] amplitudes ($\overline{\text{PE}}$: 10-100PE) both methods yield comparable results and thus an equivalent quality concerning muon detection. Since the JOM Q-pulse-width is limited below a maximum value of $580ns$ the back conversion becomes rather unstable for high energies ($\overline{\text{PE}} \approx 1000$). The charge can not be efficiently measured, e.g. for 10^5 signals (Poisson distributed, $\overline{\text{PE}} = 1000$) the reconstructed energy reaches up to 10^8PE. Therefore JOM QT-widths equivalent to more than a few 100 PE can not be physically interpreted. The logarithmic charge conversion in the JOM does not yield a larger dynamic range as e.g. the linear read out of the BOM.

5.2.3 The "smart" read-out DMQT

The EOM read-out, DMQT, was initially designed by F.Beissel and V.Commichau according to the following requirements [141]:

- The circuit is directly fed from the PMT anode signal. Its rectangular ECL output drives an LED driver circuit. The leading edge of the output signal has a delay of about 10 ns to the start of the original PMT signal.
- The circuit is self triggering. In order to reject noise from the small PMT a high discriminator threshold is set to an amplitude corresponding to about 0.2PE.
- The circuit measures the response-time of the PMT. A second discriminator threshold is set to a small value ($\approx$ 0.05PE). This threshold obtains the leading edge of the PMT-signal without being affected by fluctuations of the rise time. A coincidence to the high threshold defines the trigger and starts the output pulse.
- Both thresholds are externally set and monitored by the RCU.
- The circuit linearly measures the integrated charge of the PMT signals. The duration has to be proportional to the measured charge. As seen in figure 5.32 (B) the minimal integration time should be about $150ns$ to obtain a good energy-resolution. Higher amplitudes require a longer integration. Commercially available charge integrating circuits using a fixed integration gate of about $300ns$ have conversion times of the order of micro-seconds. This is unacceptable under the consideration of the dead-time involved by $100kHz$ ocean noise. Therefore a different solution was found. After a short time ($\approx 40ns$) the conversion already starts during the charge collection. Furthermore the conversion is done with variable duration. This leads to small conversion times for frequently occuring 1PE PMT-pulses and requires only long integration times for rarely occuring large PMT signals. This gives a typical dead-times of $150ns$ for 1PE plus $100ns$ for each additional PE. These values were achieved with the DMQT prototypes for the JULIA experiment[4]. However due to timing problems on the produced circuits-boards for EOMs this dead time had to be increased to typically $200ns$ per PE. Also the energy resolution does not reach the excellent values of the DMQT prototypes (see table B.12). A sketch of the circuit is shown in figure 5.33

[3] No QT-signal is generated in the JOM for small amplitudes ($<$ 3PE).

[4] This conversion time is limited by the length of the PMT signals. It is possible to significantly decrease these values for PMT with shorter pulses

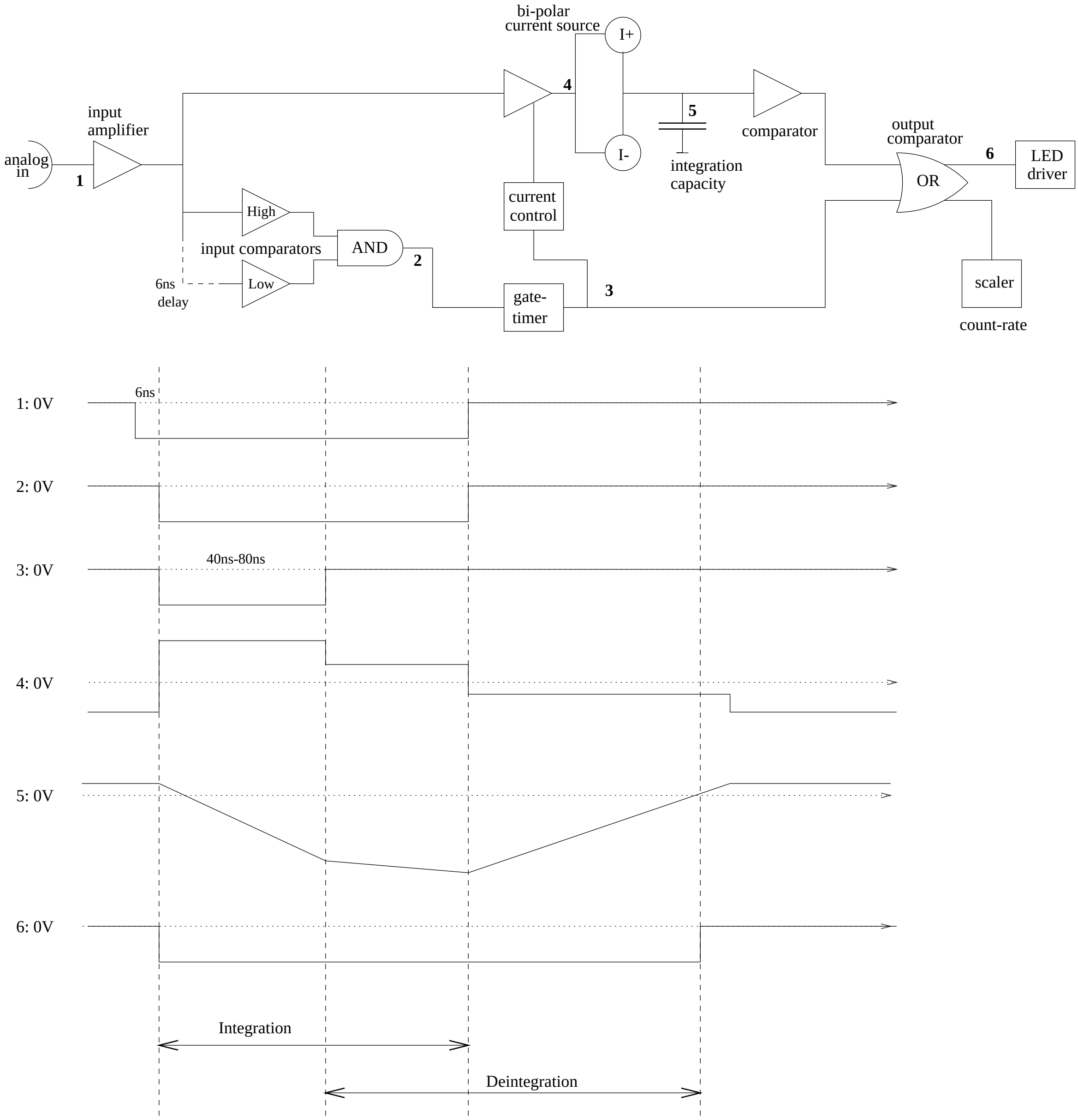

Figure 5.33: Block and timing diagram of the DMQT.

- The circuit has a soft transition from a linear to a logarithmic charge measurement for high input amplitudes of the PMT (typically above 3PE). This is achieved via a limited dynamic input range, which cuts off pulse-heights above about $2V$ (see section 5.2.2).

A block diagram of the fast read-out and the internal timing is shown in figure 5.33. A bipolar current source charges and discharges the integration capacity. The current is controlled by the input pulse amplitude and the current control, which starts the conversion after a fixed time. The circuit is built in ECL and has a power consumption of about $2.5W$. More detailed information can be obtained from [141, 140].

In order to test the linearity of the QT conversion a photomultiplier was illuminated with a LED fixed to a mean intensity of about 4PE. Each PMT signal is measured with a charge sensitive ADC (Lecroy 2249A) and the DMQT circuit. The correlation between these two measurements is plotted in figure

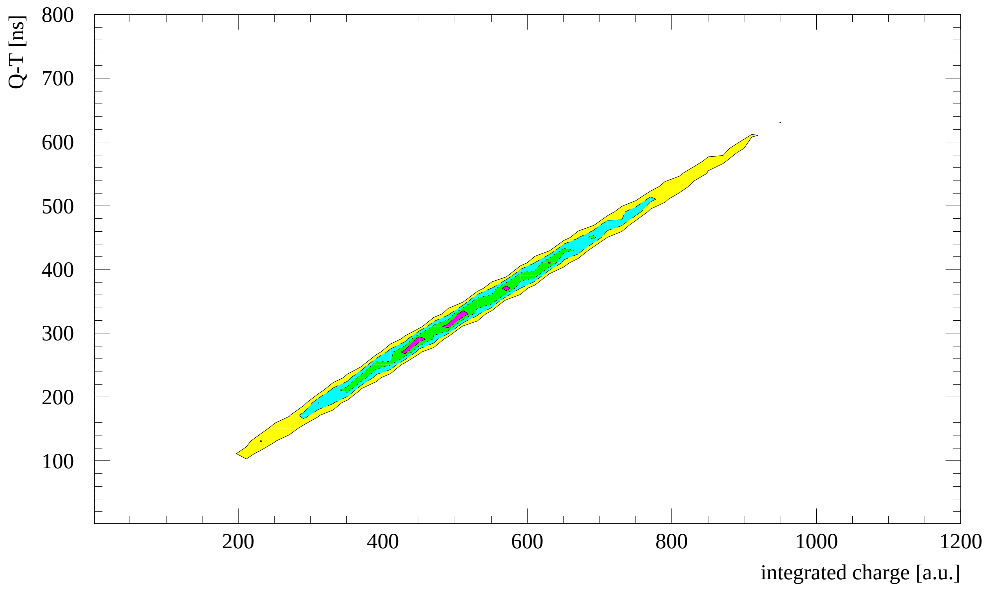

Figure 5.34: Measurement of the linearity of the DMQT. The plot shows the correlation between measurement of the integrated charge and the width of the QT signal for about $1 \cdot 10^5$ photomultiplier pulses. 95 scale units on the x-axis and 70ns on the y-axis correspond approximately to 1PE.

5.34, showing an excellent linearity.

5.2.4 The Remote Control Unit

Main purpose of the RCU is to set and monitor internal parameters of the EOM (see figure 5.28). Heart is a microprocessor TMP 68301 (Toshiba), which integrates three serial interfaces, a 16 bit parallel interface and a 68000 core. The computer has a 16 bit data bus accessing 256 kbyte random access memory and 256 kbyte read only memory (EPROM). The ROM holds an OS-9 operating system and the basic application software. Communication to the OM is possible via a serial modem link ($300Bd$), which superimposes signals onto the power supply line. The implemented software allows three different communication modes. In the standard mode[5] a *control*-program is executed, which sets all internal parameters to default values and enables a bidirectional communication to the string controller according to a special protocol. The *control* program also monitors and reports the internal parameters on demand, or in case of special emergency conditions (e.g. a water leak). A second mode allows to download software onto a ram-disk, via the *kermit* protocol (e.g. a new *control*-program). Finally it is possible to execute a terminal program and operate the computer on a command shell. [140, 16]

Four internal parameters are set via an 8*bit* DAC :

- The two DMQT thresholds in the range 0 to $200mV$.
- The high voltage of the small PMT from $0V$ to $1700V$.
- The $25kV$ supply for the large PMT can be switched on and off.

In addition it is possible to switch on the LED (of the fast circuit) for a certain amount of time. Following parameters are continuously measured via a 10*bit* ADC:

- The thresholds of the DMQT.

[5]This is the default mode after booting.

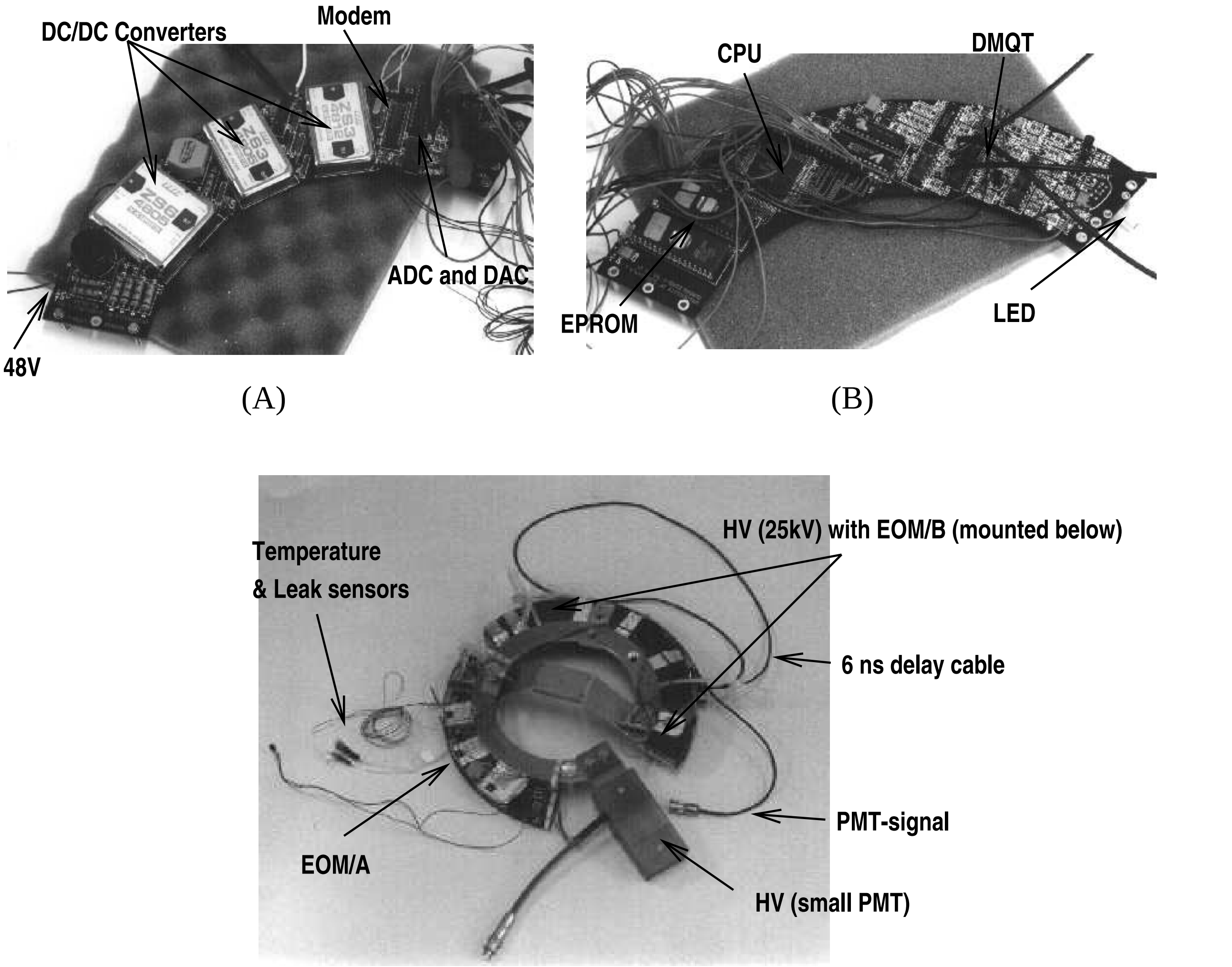

(C)

Figure 5.35: Electronic circuits boards of the EOM (A) EOM/A, the "power-board". (B) EOM/B, the "fast-board'. (C) All electronic devices assembled onto a retaining aluminium ring.

- The high voltage of the small PMT and the on/off state of the $25kV$ supply.
- Three temperatures at different locations.
- The three supply voltages, $\pm 5V$, $+12V$.
- The current for each of the three voltages.
- Detection of water inside the module via a leak sensor.

The counting-rate of the PMT is pre-scaled by a factor of 64 and is measured witht the timer input of the CPU. [140, 16]

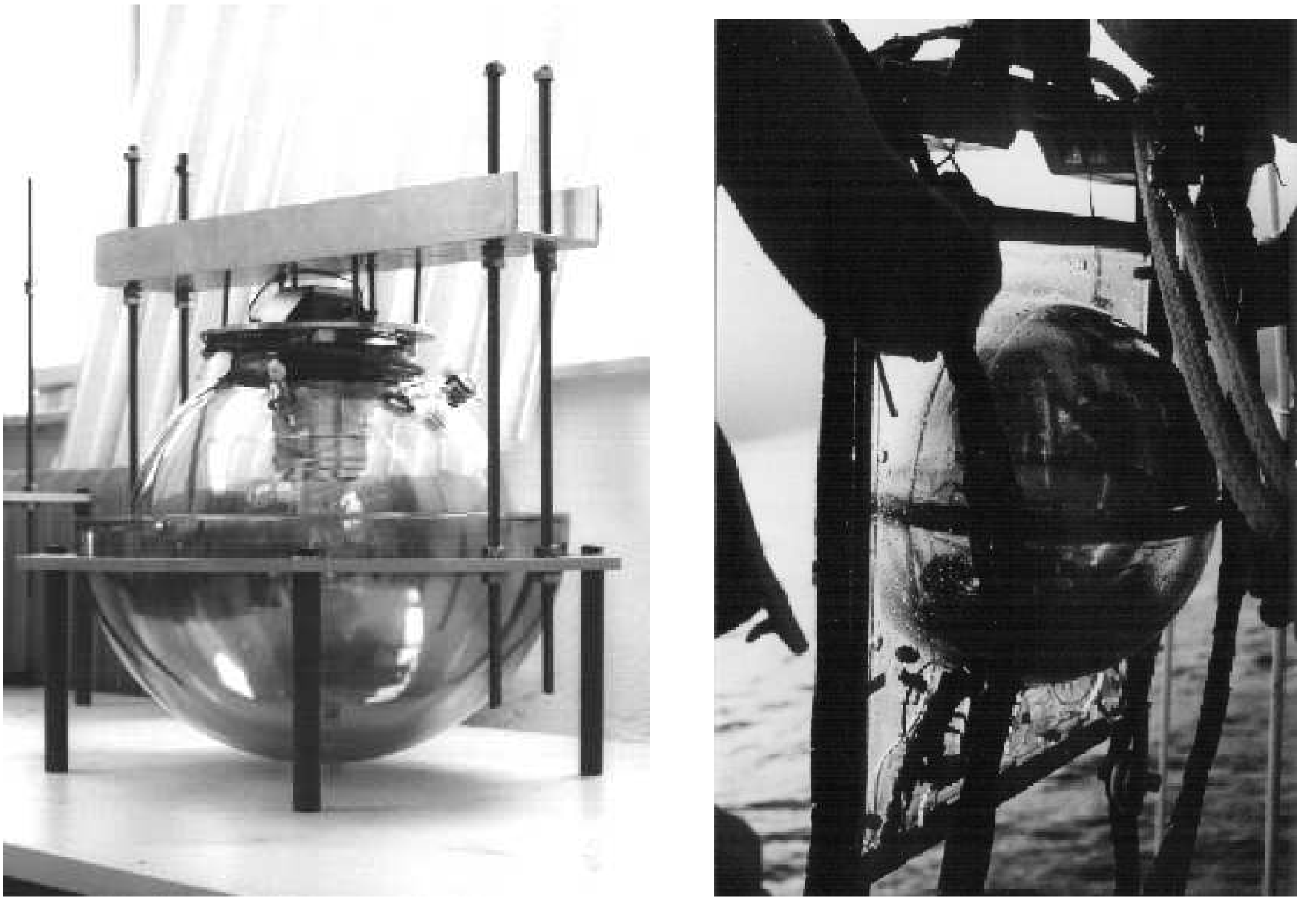

(A) (B)

Figure 5.36: The mechanical assembly of the EOM (A) Glueing of the PMT into the pressure housing. (B) An EOM in a DUMAND string during the test experiment of September 1993

5.2.5 Mechanical design

Due to the lack of available space inside the pressure housing, the electronic circuits are realized in two sickle-shaped 7 layer circuit boards, which are populated (with mostly SMD[6] circuits) from both sides. The first board *EOM/A*, the so called "power board" contains the DC/DC converters, the modem, DAC and ADC units. The second board, *EOM/B*, the '"computer–board", contains the fast circuit DMQT, the LED, and the RCU-computer. Connections between the boards are realised with wire-wrap cables. Figure 5.35 shows a photos of these circuit boards ((A),(B)). All electronic parts are attached to an aluminium ring which itself is fixed to the neck of the PMT (see figure 5.27 and 5.35 (C)).

The PMTs are glued into a pressure housing made by *Nautilus Marine Service* with optical transparent gel. The pressure housing consists of two hemispherical parts made from borsilicate glass with a good transmission ($> 90\%$). It is transparent down to $\approx 340nm$ (50%, $8mm$ glass). The refraction index is 1.472. The halves are combined at their equatorial cut and sealed with neoprene tape. The optical gel *Wacker Semicosil 912* is a solvent free addition–curing RTV–2 silicone rubber with good transmission properties down to $250nm$. It is a two component gel which vulcanises within several hours (room temperature) to a low viscosity (depending on the mixture ratio) gel with distinct tackiness. Figure 5.36 (A) shows the glueing of a PMT into a pressure housing. The PMT is fixed to an adjustable

[6]Surface Mounted Device

support fixture, which allows to position the PMT with an accuracy of $\approx 1mm$. [138, 17]
The complete OM is mounted into an acrylic hardhat, which is fixed to the string. Figure 5.36 (B) shows an EOM assembled in a DUMAND II string.
Two penetrators connect the OM to the outer world — the electrical "E0'–style produced by "Crouse Hinds" and an optical penetrator suitable for multi-mode optical fibre, which was designed by Bern University and manufactured by "Diamond SA". A titanium vacuum port allows to control the inside pressure. Three holes for these penetrators are drilled into the top half pressure sphere. The sphere is pressure tested with installed penetrators up to $600bar$. [113, 40]
The small PMT is glued into the the recess of the large PMT with optical gel in order to improve the optical contact to the scintillator . This operation significantly improves the energy resolution of the PMT. A measurement of PMT # 11 yielded an improvement of the energy resolution from 56% to 47%. (see figure 5.30 (A)). A complete filled recess with too stiff gel leads to strong tensions, which may damage the PMT. This is the reason for two lost EOMs. A third EOM was lost due to insufficient space inside the pressure housing. The spheres shrink several mm under high pressure in the deep ocean.

5.3 Properties and calibration of the EOM

The final calibration of DUMAND II OMs is done in a large water tank at the University Hawaii. This includes measurements of the angular sensitivity, amplitude and time response to a laser light-source and Čerenkov light from muons passing through the water [113]. Prior to the delivery, several sequences of test- and pre-calibration measurements have been performed with the EOMs at the University Kiel. Table B.10 gives a summary of all tested EOMs. The test procedure covers following points

- The relative angular dependency of the sensitivity of the photocathode is measured by point illumination of 49 locations. (see appendix B.1)
- The amplitude and time response is measured for selected cathode points, different light intensities, thresholds and high voltage (see sections 5.3.2 and 5.3.3)
- Measurement of the counting-rates and amplitude distributions of dark noise pulses as a function of the thresholds and the high voltage. (see appendix B.3)
- Measurement of the amplitude response for high light-intensities and high pulse rates. [91]
- Measurement of the after-pulse rate as a function of the delay time. [93]
- For each PMT 200 typical PMT pulses have been digitised with a $100MHz$ FADC for $10\mu s$. This measurement yields the decay constant of the scintillator and the characteristics of pulses and after-pulses. (see figure 5.32, [93])
- Estimation of standard settings for the high voltage and the thresholds as well as the calibration of all internal DACs and ADCs. (see appendix B.3,[140])

5.3.1 Sensitivity

Optical Modules, which are hit by Čerenkov light from a muon, are usually exposed to an almost plane-wave light front. Therefore the angular sensitivity of a fully illuminated OM is an important quantity, which has to be calibrated.
In addition to the standard calibration in the water tank, one EOM (# 42) was measured in full illumination from a green LED approximately $3m$ distant to the OM at DESY IfH Zeuthen. The

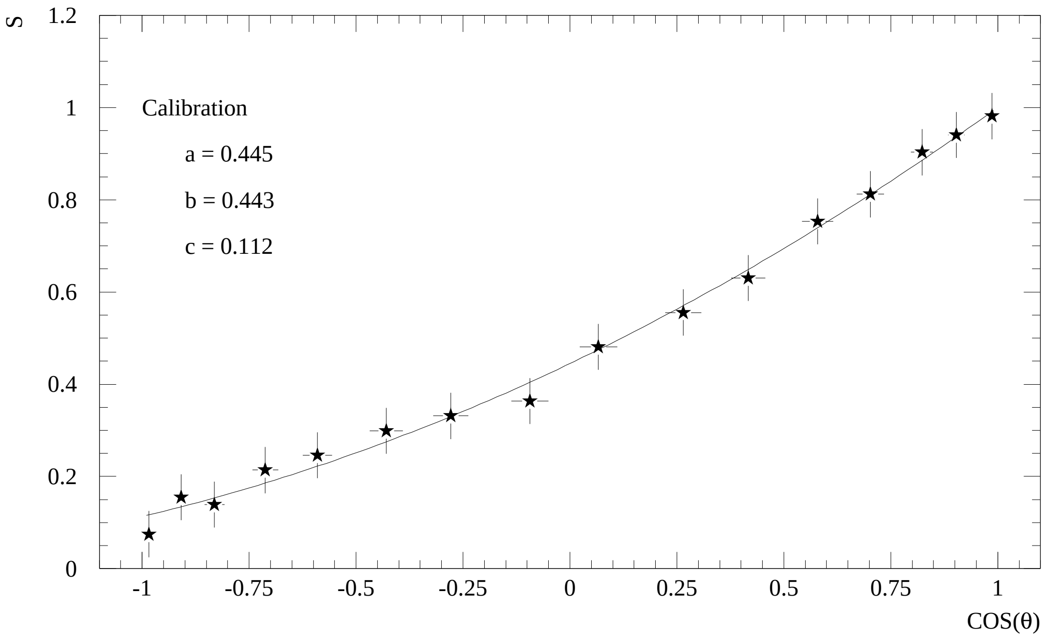

Figure 5.37: Relative angular sensitivity of the EOM. The measurement was done with full illumination of a green LED. E.q.(5.69) was fitted to the data.

measurement[7] was done with fixed intensity of the LED at 4 different azimuth angles as a function of the zenith angle ϑ.
The relative angular sensitivity $S(\vartheta)$ was parameterized with

$$S(\vartheta) = a + b \cdot \cos\vartheta + c \cdot \cos^2\vartheta \ . \tag{5.69}$$

The result of this measurement is shown in figure 5.37.

Because the full illumination is an integral measurement, local differences in the cathode quality are hard to detect with a fully illuminated OM. The cathodes of 12 OMs have been examined in point-illumination. A LED was directly attached to the surface of the PMT. Results of this measurement are shown in appendix B.1. Most PMTs show a very uniform photo-cathode, which is sensitive to zenith angles larger than 90°. For some PMTs the sensitivity increases at 90°, corresponding to an emission of photoelectrons from the photo-cathode from the opposite side of the PMT.

5.3.2 Signal amplitude

During the standard DUMAND calibration scheme the mean pulse-width response of OMs is measured versus the distance of muons passing through a water tank. Several applications, especially in Monte Carlo, require in addition a parameterisation of the actual shape of the amplitude distributions for a given incident light intensity.

It was shown in [54, 91], that the amplitude distribution of the “smart” PMT is well approximated by superimposed, equidistant Gaussian distributions G_i. Their relative weights are given by a Poisson distribution P_i for the mean number of photoelectrons $\bar{m}$

$$P_i = \frac{\bar{m}^i e^{-\bar{m}}}{i!} \ . \tag{5.70}$$

[7] More details on this measurement are given in [92].

The width of the i-th Gaussian σ_i scales as

$$\sigma_i = \sqrt{i} \cdot \sigma_1 \ , \tag{5.71}$$

with the width σ_1 of G_1. The distance between two Gaussians is given by the constant c_1 and the pedestal of the distribution by c_0. Thus the centre value of the i-th Gaussian x_i is

$$x_i = c_0 + i \cdot c_1 \ . \tag{5.72}$$

The energy resolution $\Delta E/E$ (FWHM) can be calculated via

$$\frac{\Delta E}{E} = \frac{\sigma \cdot 2 \cdot \sqrt{2 \cdot \ln 2}}{c_1} = 2.35 \cdot \frac{\sigma}{c_1} \ . \tag{5.73}$$

It is thus possible to describe the pulse-height distribution of the PMT for arbitrary light intensities with only three parameters c_0, c_1, σ_1. [56, 54, 91]
For a parameterisation of the amplitude characteristics of the complete EOM one has to consider also the Q-T conversion in the fast read-out. The pedestal is changed and the energy resolution may become worse, e.g. due to electronic defects. The PMT amplitude is cut off above an amplitude $\approx 2V$. This corresponds to the threshold value n_{log} (in units PE) above which the integration becomes logarithmic. The equivalent pulse width x_{log} is given by

$$x_{log} = c_0 + n_{log} \cdot c_1 \ . \tag{5.74}$$

A description of the EOM pulse shape in the logarithmic region can be achieved via the approximation, that the amplified input signal to the DMQT is described by an exponential decaying function with an infinite rise-time, which is cut off above a certain threshold. Further electronic distortions are neglected. This yields the relation for the position of the i-th peak ($i > n_{log}$)

$$x_i = x_{log} \cdot \left(1 + \ln \frac{i}{n_{log}}\right) \tag{5.75}$$

and a logarithmic transformation of the initial Gaussian distributions. The complete "amplitude function" describing the EOM in the linear and the logarithmic region is

$$\begin{aligned} G(x) \quad &= \quad \sum_{i=0}^{i \le n_{log}} P_i \frac{1}{\sqrt{2\pi} \cdot \sigma_i} \exp\left(-\frac{(x-x_i)^2}{2 \cdot \sigma_i^2}\right) \\ &+ \sum_{i > N_{log}}^{\infty} P_i \frac{n_{log} \cdot c_1}{\sqrt{2\pi} \cdot \sigma_i \cdot x_{log}} \exp\left(\frac{x - x_{log}}{x_{log}} - \frac{c_1^2 \cdot \left(n_{log} \cdot e^{\left(\frac{x - x_{log}}{x_{log}}\right)} - i\right)^2}{2 \cdot \sigma_i^2}\right) \end{aligned} \tag{5.76}$$

with x_i, σ_i from equations (5.72) and (5.71).
Appendix B.2 shows fits to measured EOM QT distributions. It can be seen that the above estimations do not yield a good description of the logarithmic region, but shows the right scaling behaviour at the cost of only one additional parameter n_{log}. The description can be improved by e.g. an additional parameters c_2 in eq.(5.75) which respects an incorrect logarithmic conversion performance

$$x_i = x_{log} \cdot (1 + c_2 \cdot \ln(i/n_{log})) \ . \tag{5.77}$$

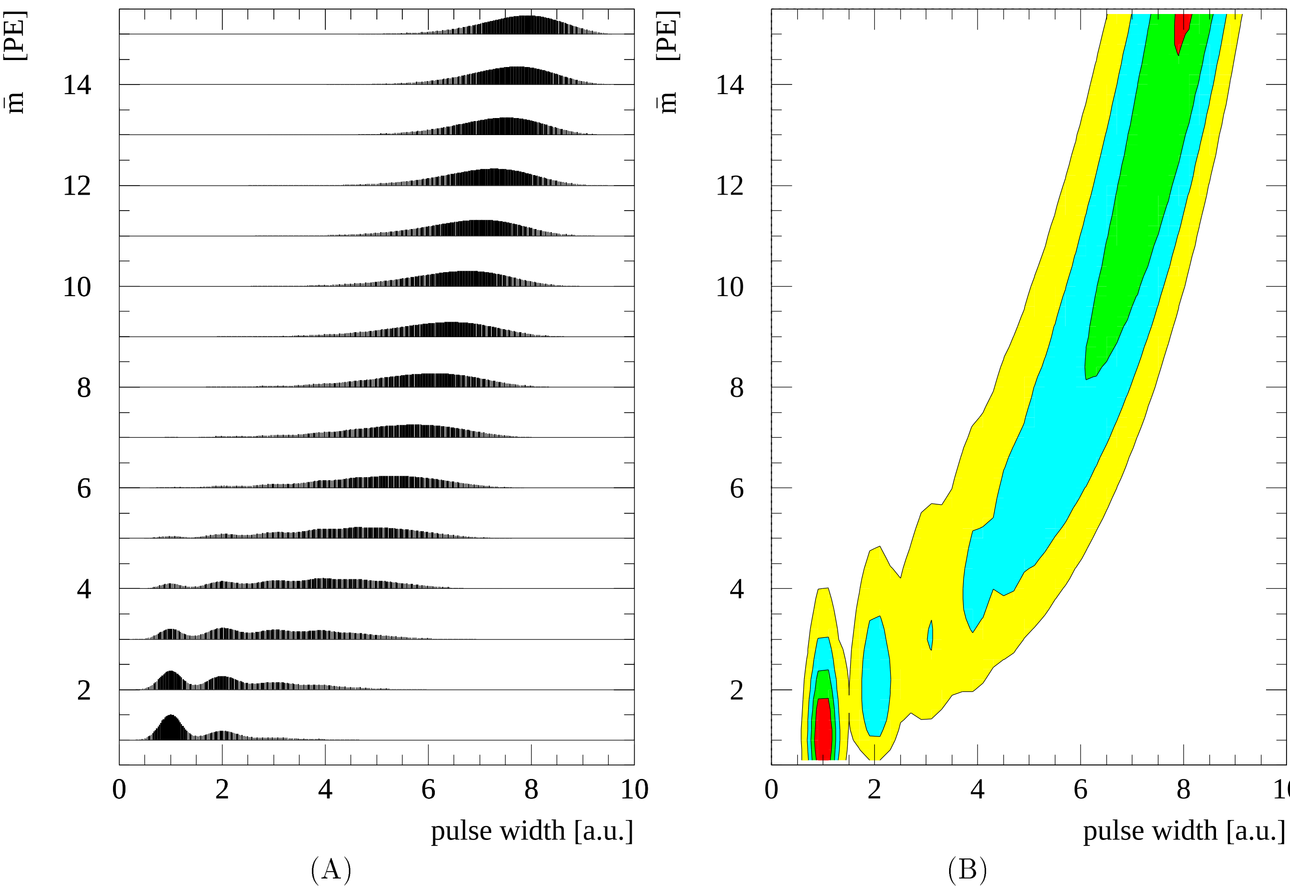

Figure 5.38: The "amplitude function". The parameters have been set to $c_1 = 1$ $c_0 = 0$, $\sigma_1 = 0.213$, $n_{log} = 3$. The pictures show two dimensional plots of the pulse width for different mean values of photoelectrons ($\bar{m}$). (A) shows the distributions for 15 different values $\bar{m}$. The sizes of the boxes represent the function value. (B) a contour plot of the amplitude function.

Figure 5.38 shows a plot of the amplitude function for different light intensities.
The energy resolution for various EOMs as calculated via eq.(5.73) are given in table B.12.
In case of a linear read-out and Gaussian amplitude distributions it is possible to calculate the mean number of photoelectrons for high amplitudes from the mean $\bar{x}$ and deviation σ of the energy distribution. Using the expectation values for Poisson and Gaussian distributions one evaluates for the combination of both

$$\bar{m} = \left(\frac{\bar{x}}{\sigma}\right)^2 \cdot \kappa \; , \tag{5.78}$$

where κ is closely related to the energy resolution of the OM.

$$\kappa = 1 + \left(\frac{\sigma_1}{c_1}\right)^2 \; . \tag{5.79}$$

If the pedestal constant $c_0 \neq 0$, the values $\bar{x}$ has to be corrected to the pedestal $\bar{x} \rightarrow \bar{x} - c_0$ before it is inserted into eq.(5.78). [87]

5.3.3 Time properties

The time accuracy of an OM is the most critical parameter to allow a successful reconstruction of a muon track. A PMT signal appears delayed by a certain signal *transit time* relative to the time of the incident photons. The time accuracy is given by the deviation relative to the intrinsic transit time of the OM.

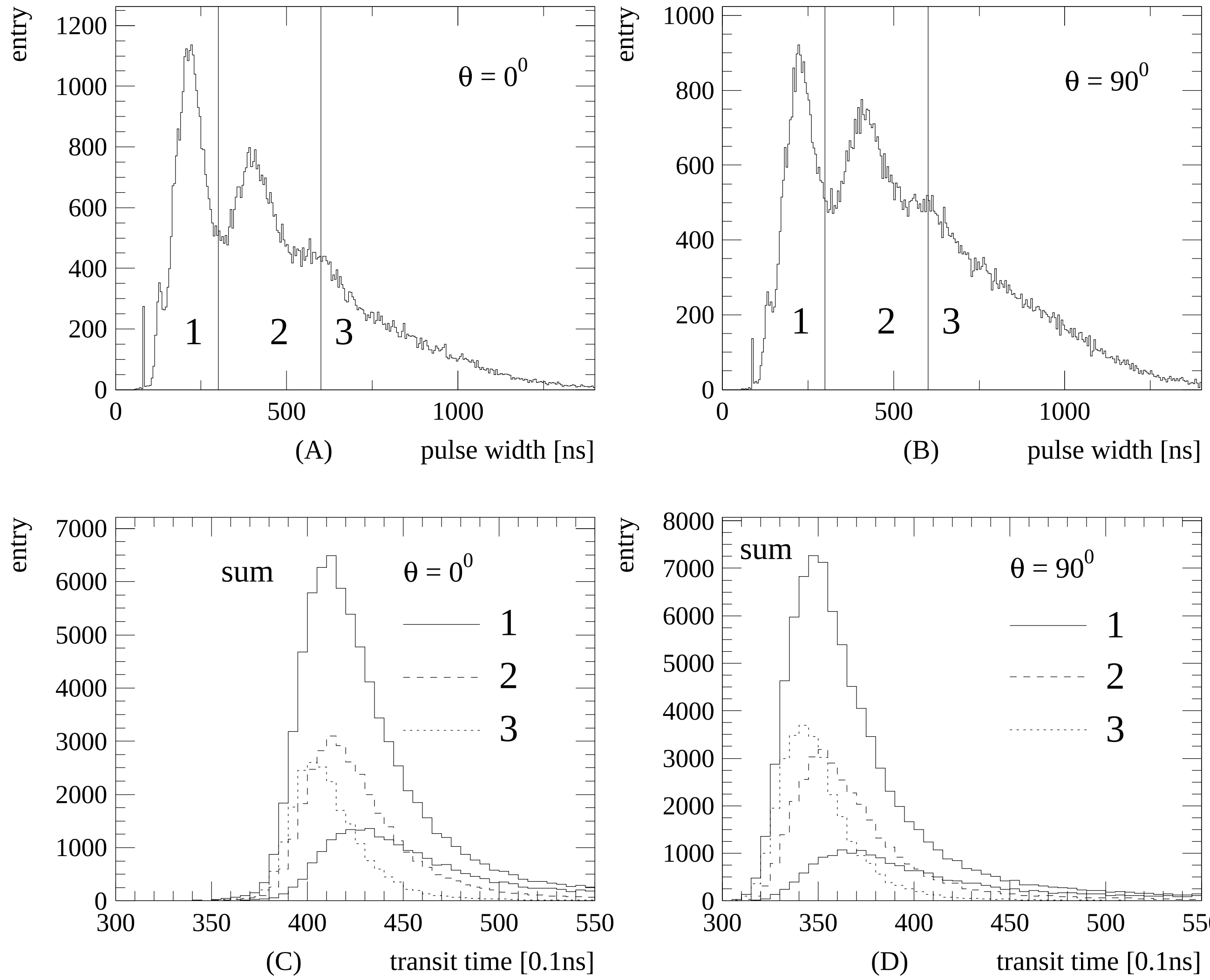

Figure 5.39: Energy and time distributions for two different zenith angles. EOM #33 was illuminated with a fast green LED (point illumination). (A) and (B) show the distributions of the pulse energy. The energy is divided into three regions (1,2,3). (C) and (D) show the transit time distributions for pulses of each energy region separated. The summed time distribution is plotted on top of these distributions.

Figure 5.39 shows energy and transit time distributions for two different zenith angles θ. The intensity of the LED is fixed, but due to a different relative angular sensitivity of the OM the relative weight of each peak (the contributions for each photoelectron level) changes. The positions of the peaks remain constant. The corresponding transit time distributions are plotted below (sum). They have a width of about $4.5ns$ (FWHM). To investigate the transit-time for different energies, 3 regions of energy have been defined (1,2,3). The transit-time distributions of the pulses which fall into one of these energy region are separated and plotted below the "sum" curve. In these pictures one can identify the three major effects, which determine the time-accuracy.

Geometrical transit time differences Photoelectrons emitted from different regions of the photocathode have to traverse different path-lengths. The distributions (C) and (D) show a shift of about $4ns$ in the transit-time. For full illumination the distributions for cathode areas of different zenith angles are superimposed, weighted with their relative sensitivity. Assuming a mean zenith angle 45° with uniform transit time deviations $\Delta t = 4ns$ one achieves a mean time uncertainty

$$\sigma_{t,geo,1\mathrm{PE}} \approx \frac{\Delta t}{\sqrt{12}} = 1.15ns \tag{5.80}$$

This value is to be taken as a worst case. Due to the spherical shape of the photocathode and inhomogeneous sensitivity usually one cathode region dominates the transit-time. This effect decreases for high amplitudes because the cathode region with the fastest transit time dominates stochastically.

Time jitter This quantity is related to the intrinsic time-spread of the photomultiplier, which occurs during the conversion of the photoelectron. It is measured by the width of the transit time distributions in figure 5.39. For the XP2600 it is dominated by the stochastic emission of secondary photons from the scintillator [91]. For signals with a higher amplitude the time-jitter becomes smaller.

Time slewing Signals of high amplitude have a faster rise-time relative to smaller signals for a fixed discriminator threshold. The response time due to signals of different amplitudes are superimposed in the resulting transit time distribution. This effect can be clearly seen in figure 5.39 (C) and (D). The peaks of the time distributions are shifted to faster transit times for larger amplitudes. This uncertainty can be corrected after calibration if the signal amplitude is measured correlated to the response time. It has to be noted that changes in the high voltage and the small threshold also lead to a significant transit time slewing. E.g. a change of 20% in the low threshold of the DMQT leads to a time slewing of about $1ns$.

A good analytical description of the time distributions is gained, if a Gaussian distribution is convoluted with a decaying Exponential (which is motivated by the scintillator decay). Evaluation of the convolution integral [92] gives

$$S(t) = \frac{\sqrt{\sigma_t}}{\tau} \cdot \exp\left(\frac{\sigma_t^2}{2\tau^2} - \frac{t-t_0}{\tau}\right) \cdot \left(1 + \mathrm{erf}\left(\frac{1}{\sqrt{2}}(\frac{t-t_0}{\sigma_t} - \frac{\sigma_t}{\tau})\right)\right) \quad , \tag{5.81}$$

with the error function

$$\mathrm{erf}(x) = \frac{2}{\sqrt{\pi}} \int_0^x e^{-u^2}\ du \ .$$

The "timing-function" depends on three parameters: t_0, relative transit time; σ_t, the width of the Gaussian and τ, the exponential decay constant. Fits of this function to time distributions are shown in appendix B.2. A parameterization of the parameters allows an analytical description and interpretation of transit time differences, the time jitter and the time slewing. [92]

The analysis of the EOM time properties is done as follows: A fast green LED is attached to the surface of the OM at three different zenith angles[8]. For each LED pulse the pulse energy and response time of the OM are written to disk. The energy distributions are fitted with the "amplitude function" to obtain a calibration of the pulse-width scale (see appendix B.2). The transit time distributions of signals, whose energy falls into a selected energy region, are plotted and fitted with the "timing function". Examples of these fits are shown in appendix B.2. Resulting quantities are plotted versus the number of photoelectrons n_{PE}. The *mean* (figure 5.40 (A)) and *rms* (figure 5.40 (B)) of the distributions are fitted with

$$mean = a_1 + \frac{a_2}{n_{\mathrm{PE}}} \qquad rms = b_1 + \frac{b_2}{n_{\mathrm{PE}}} \ . \tag{5.82}$$

[8]This is done manually and the power to the OM has to be switched off between each change.

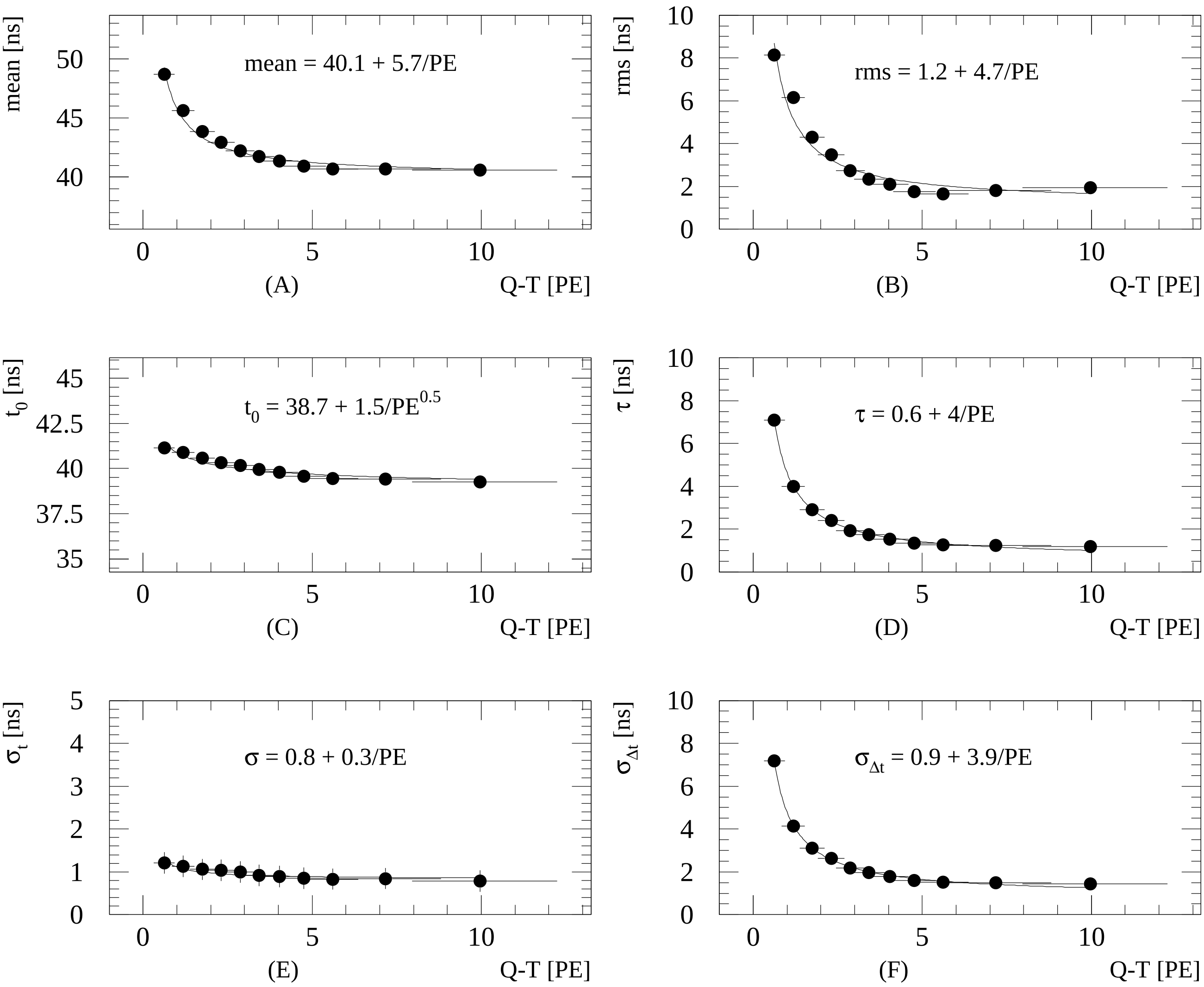

Figure 5.40: Response time characteristics for OM #35. Plotted are the mean (A) and rms (B) of the time distributions, the parameters t_0 (C), τ (D) and σ_t (E) of the fitted "timing function" and the time uncertainty $\sigma_{\Delta t} = \sqrt{\sigma_t^2 + \tau^2}$ (F) versus the pulse energy.

The time uncertainty $\sigma_{\Delta t}$ is calculated from the fit parameters τ and σ via

$$\sigma_{\Delta t} = \sqrt{\sigma^2 + \tau^2} \ . \tag{5.83}$$

These parameters are fitted (figure 5.40 (D),(E) and (F)) also via

$$\tau = d_1 + \frac{d_2}{n_{\mathrm{PE}}} \qquad \sigma = e_2 + \frac{e_2}{n_{\mathrm{PE}}} \qquad \sigma_{\Delta t} = f_1 + \frac{f_2}{n_{\mathrm{PE}}} \ . \tag{5.84}$$

Finally the parameter t_0 is fitted (figure 5.40 (C)) with

$$t_0 = c_1 + \frac{c_2}{\sqrt{n_{\mathrm{PE}}}} \ . \tag{5.85}$$

Results for all EOMs are given in table B.13. It has to be noted that the LED has an intrinsic jitter itself, which is about $2ns$ for 1PE and still $1ns$ for several PE. Therefore the presented results are upper limits on the true time accuracy. The absolute transit times include time offsets of the measurement setup and do not give the intrinsic transit-time of the OM.

OM	mean (45°) [ns]	mean (90°) [ns]	t_0 (45°) [ns]	t_0 (90°) [ns]
11	-1.6	+3.2	-1.6	+0.6
12	-0.2	-2.0	-0.1	-1.9
16	-1.3	-4.3	-1.2	-5.0
19	-1.4	-3.9	-1.6	-4.3
22	-1.9	-0.4	-2.0	-2.0
26	-2.0	-5.1	-2.2	-5.7
33	-3.5	-6.4	-3.5	-6.3
35	+0.3	-2.6	+0.2	-2.7
44	-1.9	-4.6	-1.8	-4.7
53	-3.4	-5.9	-3.4	-6.2
42	–	-0.2	–	-0.3

Table 5.3: EOM geometrical transit time differences for point illumination. The values have been derived via two methods, a) from the differences in the mean of the transit time distributions, b) from the parameter t_0 of the "timing function". The relative time for 0° was set to zero. OM #42 was measured in full illumination with a fast laser.

The geometrical transit time differences are obtained by the comparison of the *mean* measured at different zenith angles. A second characteristic value for the transit time is the parameter $t_0 + \tau$, (τ is the expectation value of the Exponential). In order to avoid time slewing effects, the asymptotic value for an infinite number of PE is taken. Thus

$$\Delta t_{geo}(\vartheta) = a_{1,(\vartheta=0)} - a_{1,(\vartheta)} \qquad \text{or} \qquad \Delta t_{geo}(\vartheta) = c_{1,(\vartheta=0)} - c_{1,(\vartheta)} \; . \tag{5.86}$$

Table 5.3 shows the results for several OMs. The mean transit-time is smaller at large zenith angles with a difference of about $4ns$. Two OMs show strong differences of this behaviour (#11 and #22). These OMs have a low sensitivity at $\vartheta = 90°$ implying that the majority of emitted photoelectrons are emitted from photons hitting the opposite cathode area.

The time jitter Δt_{jit} can be characterised by the *rms* of the distributions or via the parameter $\sigma_{\Delta t} = \sqrt{\tau^2 + \sigma^2}$. The *rms* yields less stable results, due to statistical fluctuations of the distributions, especially for large pulse energies, and due to a long tail in the distributions. As a result of the tail in the transit time distributions, the measured FWHM are significantly smaller (typically $5ns$ for 1PE) than the *rms* values [91]. The results are given in table 5.4.

The time slewing Δt_{slew} is given by the change of the transit time for different energies. Thus one gets

$$\Delta t_{slew}(x_{\mathrm{PE}}) = \frac{a_2}{x_{\mathrm{PE}}} \qquad \text{or} \qquad \Delta t_{slew}(x_{\mathrm{PE}}) = \frac{d_2}{x_{\mathrm{PE}}} + \frac{c_2}{\sqrt{x_{\mathrm{PE}}}} \; . \tag{5.87}$$

Results are shown in table 5.5.

One EOM (#42) was measured in full illumination using a fast laser with pulse width smaller $1ns$ [92]. After the same analysis procedure as above one gets significantly better results for the geometrical transit time differences, which are $< 0.3ns$ between 0° and 90°. The other quantities are comparable to the results obtained in point illumination.

OM	$rms(1\text{PE})$ [ns]	$\sigma_{\Delta t}(1\text{PE})$ [ns]	$\sigma_{\Delta t}(\infty\text{PE})$ [ns]
11	5.7	4.6	0.9
12	6.6	5.4	0.5
16	9.1	10.2	0.4
19	6.8	5.4	0.7
22	6.9	5.9	0.5
26	6.7	5.9	0.6
33	6.9	6.4	0.4
35	6.0	4.9	0.8
44	6.9	4.8	0.8
46	6.7	6.0	0.7
52	8.4	8.3	0.4
53	5.9	5.5	0.3
42	8.0	6.2	0.2

Table 5.4: EOM transit time jitter for point illumination. Printed are the fit results for the rms for 1PE and $\sigma_{\Delta t}$ for 1PE and asymptotically infinity PE. The values for 1PE depend strongly on the calibration of the energy scale which is less accurate for OMs #11 #16 and #52. OM #42 was measured in full illumination with a fast laser.

OM	$mean$			$t_0+\tau$		
	1PE [ns]	2 PE [ns]	5 PE [ns]	1PE [ns]	2 PE [ns]	5 PE [ns]
11	4.8	2.4	1.0	5.2	2.5	1.2
12	6.7	3.4	1.3	6.6	3.5	1.7
16	10.0	5.0	2.0	11.8	6.1	2.7
19	6.3	3.2	1.3	6.9	3.3	1.6
22	7.0	3.5	1.4	7.1	3.7	1.7
26	6.4	3.2	1.3	6.2	3.7	1.7
33	7.5	3.8	1.5	7.8	4.1	1.9
35	6.0	3.0	1.2	6.3	3.2	1.5
44	6.4	3.2	1.3	6.2	3.1	1.5
46	6.4	3.2	1.3	7.4	3.7	1.7
52	8.6	4.3	1.7	9.9	5.1	2.3
53	6.3	3.2	1.3	6.6	3.6	1.7
42	8.1	4.1	1.6	7.3	3.9	1.7

Table 5.5: EOM transit time slewing for point illumination. Printed is Δt_{slew} obtained from changes in the mean and $t_0+\tau$ for 1PE, 2PE and 5PE. The values depend on the calibration of the energy scale which is less accurate for OMs #11 #16 and #52. OM #42 was measured in full illumination with a fast laser.

6 Monte Carlo Simulation

so lass mich dich heissen
wie ich dich liebe:
Siegmund — so nenn' ich dich.

Richard Wagner (1852)

Many programs have been developed for the simulation of deep underwater experiments. They have been designed with respect of a specific experiment and have proven to be very capable performing specific tasks, such as the the optimisation of a detector geometry for the detection of neutrinos [7, 110]. Unlike large accelerator experiments the data stream from underwater experiments is simple and contains essentially only times and amplitudes of hit OMs. The approach of the SiEGMuND [1] program package makes use of this and attempts to provide a high flexibility in combination with standard analysis methods of particle physics. It implements a new philosophy which puts main emphasis on the following aspects.

- A modular structure according to the logical steps of the analysis.
  This provides both a transparency of the analysis and a high variability in the exchange of certain modules for specific steps of the analysis. It is designed independently of the actual experiment. Due to the modular structure it is also possible to include experiment specific tasks on demand.

- A close connection to particle physics.
  It is possible to simulate deep underwater experiments using the concepts developed in large accelerator labs, such as CERN. This enables detailed studies of the detector response considering specific particle reactions using standard event generator programs (like Pythia [159]) and a detector simulation on basis of the GEANT simulation package [153]. GEANT provides a full simulation of the processes responsible for the generation of secondary particles and the stochastic characteristics of energy loss.

- One data stream for all analysis steps.
  The interface between program modules requires a stringent definition. This is supported by a program library *rdmc*[145]. The interface between the modules is independent of the actual data format as long as this format is supported by the library. Different programming languages such as C or Fortran-77 may be mixed.

  The standard data format was chosen to be a line-oriented ASCII format (adapted from an existing DUMAND–format [144]), which provides a highly machine independent data structure. On Unix–platforms this philosophy enables the usage of standard IO–pipes for an elegant processing of data through all analysis steps. An analysis may be done interactively on a command line (or a simple shell script), or via a more sophisticated user interface. It is easily possible to use standard Unix tools within the analysis steps, e.g. "*awk*" for small analysis purposes or the selection of specific events. *gzip* allows automatic (de-)compression in the data stream. Compressed ASCII files require approximately 50% of the disk space used by ordinary binary formats. [160, 146].

6.1 Simulation framework

Figure 6.41 gives an overview on the logical analysis steps during analysis within the SiEGMuND package. The units represent individual programs, which exchange information via data streams. This allows to exchange individual programs or to concatenate several programs sequentially e.g. for the realisation of various trigger and filter conditions. A program library provides standard functions and memory structures for I-O and the processing of these data streams. (see appendix C.4, [145]).

[1] SiEGMuND stands for: **Si**mulation of **E**vents with **G**EANT for **Mu**on and **N**eutrino **D**etectors. It was developed in cooperation with O.Streicher (DESY IfH Zeuthen). [97]

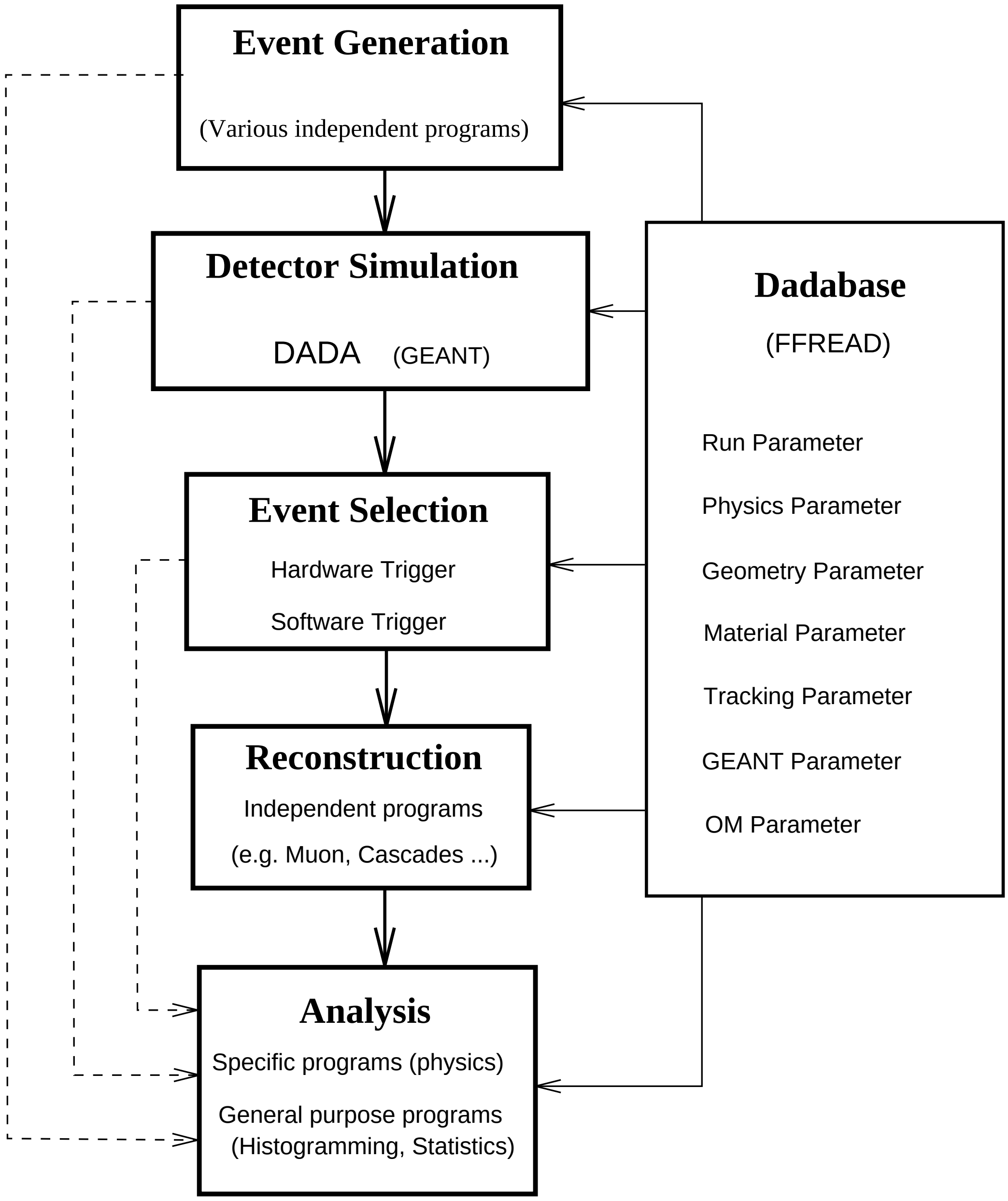

Figure 6.41: SIEGMUND program modules and their relationship

The generation of the initial kinematics and track parameters of particles is independent of the detector simulation itself. Possible event generator programs range from the simulation of muon tracks with a certain direction and kinematics, complex atmospheric shower Monte-Carlo programs, detailed event simulation like charged current neutrino nucleon interactions to the generation of exotic phenomena (e.g.neutrinos from neutralino annihilation). Generators may be custom-written. The portage of a larger event generator program into this framework requires only an implementation of a known data-format. Events are written to disk. E.g. to study effects of different optical sensors the same events may be tracked several times through the detector simulations with each different parameters for the OMs. Appendix C.2 gives more details on the implemented event generators.

A major element of the SiEGMuND concept is the detector simulation program Dada[2] (see section 6.2). Its purpose is the simulation and digitisation of the detector response. It implements a variable geometry and allows to change various physical parameters, which determine the simulation of particles in the detector. The program retrieves its parameters from a database. It is written on basis of the GEANT-package.

During the further processing of events it is necessary to account for detector specific hardware triggers, which affect the experimental selection of events. (e.g. the local coincidence trigger in the BAIKAL experiment). It is also useful to apply filters for the selection of specific events (e.g. events with large OM signals). This is realized by a set of filter programs, which may be concatenated in an arbitrary sequence. It is possible to apply the same filter programs on Monte-Carlo data as well as on experimental data. Thus further analysis is identical for both types of data.

The most important step during analysis is the reconstruction of events. A standard task is the reconstruction of muons tracks and the identification of up-going muons after applying cuts (filters). More details on the analysis utilities are described in appendix C.3.

If program units require information not included in the data stream, they may gather archive data from the database: *Dadabase*. The database was originally designed to provide information for the detector simulation and thus uses the *FFREAD* package, which is also internally used by GEANT. It contains besides GEANT specific parameters various steering information like parameters of detectors (See appendix C.1.1). [152, 153]
The SiEGMuND philosophy is not chained to a certain programming language. The detector simulation and event generators are written in Fortran-77, the analysis tools are written in C.

6.2 The detector response

The Dada program follows the general scheme of GEANT applications [153].

$$\boxed{\text{Initialisation}} \quad \longmapsto \quad \overbrace{\text{Simulation of one event}}^{\text{loop } N \text{ events}} \quad \longmapsto \quad \boxed{\text{Termination}}$$

During the initialisation phase internal data structures are initialised, such as the detector geometry, particles, materials, tracking parameters and cross sections of the different materials. As result the detector is built by geometrical volumes, which may contain different materials and sets of tracking parameters. The program reads necessary information from the external database using the FFREAD package. Several predefined configurations may be selected for detector geometry and tracking accuracy. The program is capable of simulating an almost arbitrary detector configuration. Detailed information on initialisation, termination and limitations are given in appendix C.1.1. [152, 153]
After the initialisation, execution control is handled to GEANT, which is responsible for tracking and the simulation of physical processes. For specific purposes GEANT calls user supplied routines (E.g. for the digitisation of the optical module response) Figure 6.42 shows schematically the execution flow during simulation of one event.
After the initialisation of the kinematics of the event tracking is performed by GEANT. During the tracking secondary interactions are simulated and newly generated particles are stored as new tracks in a stack. GEANT loops over all tracks until all primary and secondaries particles have disappeared[3].
With the beginning of each track, or upon the entry of a new detection volume, the distance to the next interaction point is calculated for all valid physical processes according to all valid physical processes and pseudo processes allowed for the current medium. The later are effects, which influence

[2] Dada =**D**igitisation **A**nd **D**etector **A**nalysis.
[3] E.g. due to decay, disappearance in a reaction,the exit of the simulation volume or the energy has fallen below a tracking threshold.

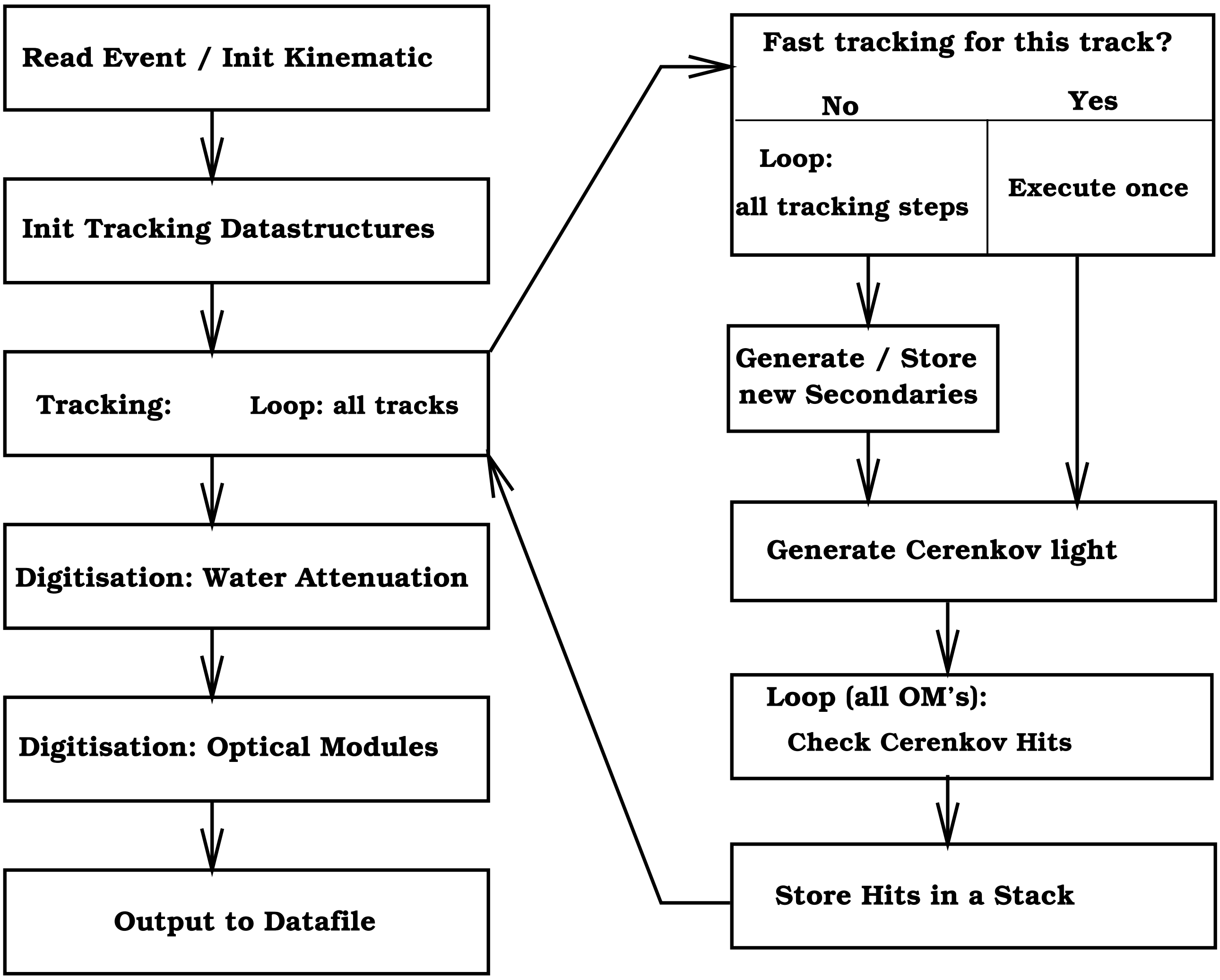

Figure 6.42: Execution flow during the simulation of one event

the tracking apart of the physical mechanisms[4]. This distance is calculated according to the inverse of the cross section for the specific mechanism. The necessary cross section values are calculated and tabulated during initialisation.

For each tracking step the distance to the next interaction point is simulated. The particle is being transported along a straight line, and the final state is generated. If the particle survives the process, the distance to the next interaction point of the current physical process is recalculated and the distances to the other processes are updated. The transportation of the particle from one point to the next is called "tracking step".

DADA makes use of the GEANT environment for all physical processes (including some patches to the original GEANT code), but not for the generation of the Čerenkov light and the digitisation of the detector. At the end of each tracking step a user routine is executed. New secondaries are stored in a GEANT-stack, and the Čerenkov angle is calculated, if the current track fulfills the Čerenkov conditions. The program loops over all optical modules and detects Čerenkov hits[5]. The time of hit,

[4] E.g.the step size due to continuous energy loss or a boundary crossing between two different tracking media.

[5] This is the most CPU time consuming part of the program.

the distance to the OM, the length[6] of the hitting track, the angle between the Čerenkov cone and the PMT axis and a track identification are stored in a stack for later digitisation. (see appendix C.1.3)
Neutrino detectors naturally involve extremely large volumes together with a low tracking threshold down to the Čerenkov thresholds of electrons ($T \approx 250keV$). The above approach leads to a large amount of CPU time for the tracking of one event[7]. One the other hand large statistical samples of events are required, e.g.to check large rejection factors for down-going muons ($\mathcal{O}(10^6)$).
This problem has been solved by the inclusion of additional fast parameterization (e.g.the effective Čerenkov light from showers). These parameterizations are deduced in chapter 7 from full GEANT simulations. If a "fast tracking"-mode is active for the current step, tracking is not performed by GEANT but rather the Čerenkov light is generated directly for the current track including the light from secondary particles.
After all particles have been tracked through the detector, the data in the stack is reduced via a recombination of hits from the same track at about the same time. Then the photon flux hitting each OM (see section 3.4 and appendix A.2) is calculated. The photon flux, the time of hit and a reference to the hitting particle are stored in a new stack; hits occuring at the same time are combined.
The response of the optical modules depends on the type and the characteristics of the individual module. The OMs may be simulated with different accuracy. The digitised time of hits and the amplitudes are stored with the reference to the tracks, which caused the hit. After the digitisation is finished the event is written to a data file. One special mode allows to calculate the number of photons hitting the geometrical OM area instead of the full simulation of the OM response. If the number of photons are written instead of photoelectrons to the datafile a later digitisation with an external program in the data stream (e.g.referring to an OM database) becomes possible.
Figure 6.43 shows the cross sections for μ^-, $e^{\pm}$, γ, and π^+ for fresh water and a set of tracking parameters down to the Čerenkov threshold, as they are calculated by GEANT. The maximum energy of GEANT is limited to $10TeV$. Above this value, cross sections may be tabulated but have to be used with caution. Figure 6.43 shows the extrapolation up to $100TeV$.
The muon interactions are calculated according to [57]. Though bremsstrahlung and nuclear interaction events occur relatively rarely, they involve a large energy transfer (e.g.[72]) and may initiate bright local cascades (see chapter 3.3.1).
During the analysis of muon events in the Fréjus detector a discussion arose about the correctness of the implemented bremsstrahlung cross section ([78]). The cross section used in [57] refers to [75]. The differential cross section $d\sigma/dy$ (y is the fractional energy transfer) is proportional to an atomic and nuclear screening function Φ, which differs between [75] and [79] for atomic numbers $Z > 10$. For fresh water the difference between both formulae is not serious, because most ingredients have atomic numbers $Z < 10$. DADA implements both cross sections but keeps the original GEANT as default. This difference becomes stronger for ocean water.

It is possible to set several options for debugging and physical cuts. An interface to the HIGZ package allows to plot the detector, its components and also to visualise trajectories during tracking time. The graphical output may be written to a graphical meta-file (e.g. postscript). Histograms (e.g. cross sections or statistical output) may be generated and written to an HBOOK data file [155, 154].

6.3 Data analysis

The general philosophy of data analysis within the SiEGMuND environment is to concatenate individual programs in a serial data stream to process or filter out events of interest. This philosophy is

[6] In fact not the length λ but rather the relative length $\mathcal{L}$, as defined in eq.(A.129) is stored.

[7] The realisation of this approach to perform a detailed tracking for large scale neutrino telescopes has only become reasonable due to recently available computing power. The necessary amount of computing time increases strongly with the number of tracks, the number of steps during tracking and the number of optical modules in the detector.

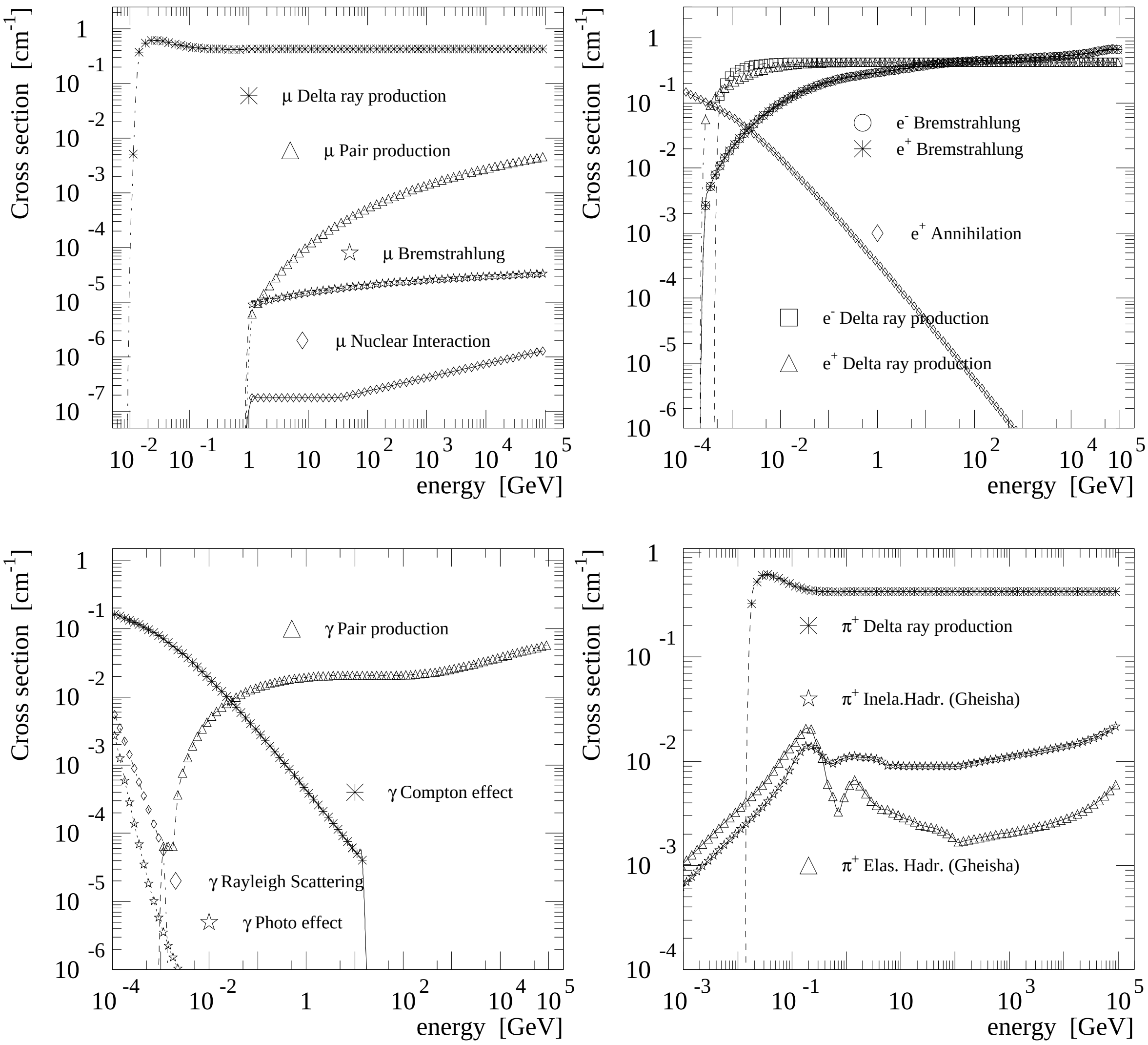

Figure 6.43: GEANT cross sections for "River–water" and standard tracking parameters

strongly supported on Unix-platforms.

`input-file` $\rightarrow$ $\boxed{\texttt{program1 +options}}$ $\rightarrow$ $\boxed{\texttt{program2 +options}}$ $\rightarrow \ldots \rightarrow$ `output-file`

This allows any combination of analysis applications in any order according to a box of bricks yielding a high degree of flexibility and speed in data processing.
The tools include a muon reconstruction program [148], a graphical display program [149], trigger and filter programs [146], and programs to generate histograms and N-tuples for the further processing with PAW [157]. More details on the concepts and programs are given in appendix C.4 and C.3.

6.4 Extension of the simulation

Several extensions of the detector simulation are under consideration.

- Implementation of ice instead of water as a detector material.
- Scattering of Čerenkov light.
- Variable OM positions during tracking, to study effects of water currents in the detector.

- Further extensions to GEANT, e.g tracking routines for slow moving magnetic mono-poles (Rubakov effect), or an extension of the valid energy range.

In addition it is intended to add further program modules

- Development of further event generation programs.
- Further reconstruction programs. E.g. for the reconstruction of point-like light sources.
- A filter based on a neural network to reject down-going muons.
- A detailed simulation program for individual optical modules.
- Implementation of a graphical user interface, e.g. on base of *Khoros* or *Tcl/Tk*.

SiEGMuND was ported to various Unix flavours such as DEC-Ultrix, DEC-OSF1, HP-UX, IRIX, Convex, Linux .... It is desirable to expand this list also to non-Unix systems.

7 Simulation Results

Alea jacta est

This section investigates fundamental characteristics of Čerenkov signals in underwater Čerenkov detectors. As mentioned in section 6.2 the execution of a GEANT based program for these experiments requires a large amount of CPU-time. The parameterizations obtained in section 7.1 and 7.2.1 allow the implementation of a fast simulation mode.

7.1 Čerenkov light from electromagnetic and hadronic cascades

Within the following simulations a parameterization of the total Čerenkov light output and it's angular distribution is calculated for electromagnetic and hadronic cascades. Each simulation has been carried out by positioning an initial particle with the energy E_0 at the coordinates $\vec{r}_0 = (0., 0., 0.)$. The initial momentum points into positive z-direction ($\vec{p}_0 = p_0 \cdot \vec{e}_z$). The resulting cascade is tracked until the energies of all (secondary) particles falls below the Čerenkov threshold. These simulations have been done with various initial particles at different energies:

Electromagnetic cascades: e^-: $1MeV$, $10MeV$, $100MeV$, $1GeV$, $10GeV$, $100GeV$, $1TeV$, $10TeV$. e^+: $100GeV$. γ: $100GeV$. π^0: $100GeV$.

Hadronic cascades: π^+: $10GeV$, $100GeV$, $1TeV$, $10TeV$. p^+: $10GeV$, $100GeV$, $500GeV$, $1TeV$. K^+: $100GeV$.

In order to get rid of statistical fluctuations, the simulation is repeated m–times and averaged.
The angular Čerenkov light distribution is calculated via a transformation method, which transforms the angular distribution of all shower tracks to the resulting Čerenkov distribution. Explicit details are described in appendix A.1. The calculation proceeds via the following steps:

1. A histogram of zenith angles of all charged tracks pieces with energies above the Čerenkov threshold is created and the length of the current step is filled into the histogram versus the zenith angle, defined as

   (7.88) $$\cos\alpha = \frac{\vec{p} \cdot \vec{p}_0}{|\vec{p}| \cdot |\vec{p}_0|} \ .$$

   Thus the histogram contains the distribution $dl/d\alpha$, called the *Angular track-length distribution*

   (7.89) $$\frac{dl}{d\alpha} \equiv \sum_{tracks} \sum_{steps} l_i \cdot \delta(\alpha_i) \ ,$$

   with l_i being the length of the current step and $\delta(\alpha_i)$ a delta function of the current direction angle. This distribution contains the differential distribution of the total amount of Čerenkov radiating track-length versus the zenith angle to the initial direction (see figure7.44(A)).

2. In order to preserve the longitudinal information of the shower, a second histogram is created. It contains the distribution

   (7.90) $$\frac{dl}{dz} = \sum_{tracks} \sum_{steps} \delta(z) \cdot l_i \ ,$$

   with the Dirac delta function $\delta(z)$. This histogram corresponds to the distribution of the total longitudinal Čerenkov radiating track lengths along the shower axis[1]. This distribution is called *Longitudinal track-length distribution* (see figure 7.44(B)).

[1]The maximal step-size during tracking is small compared to the bin width of the target histogram.

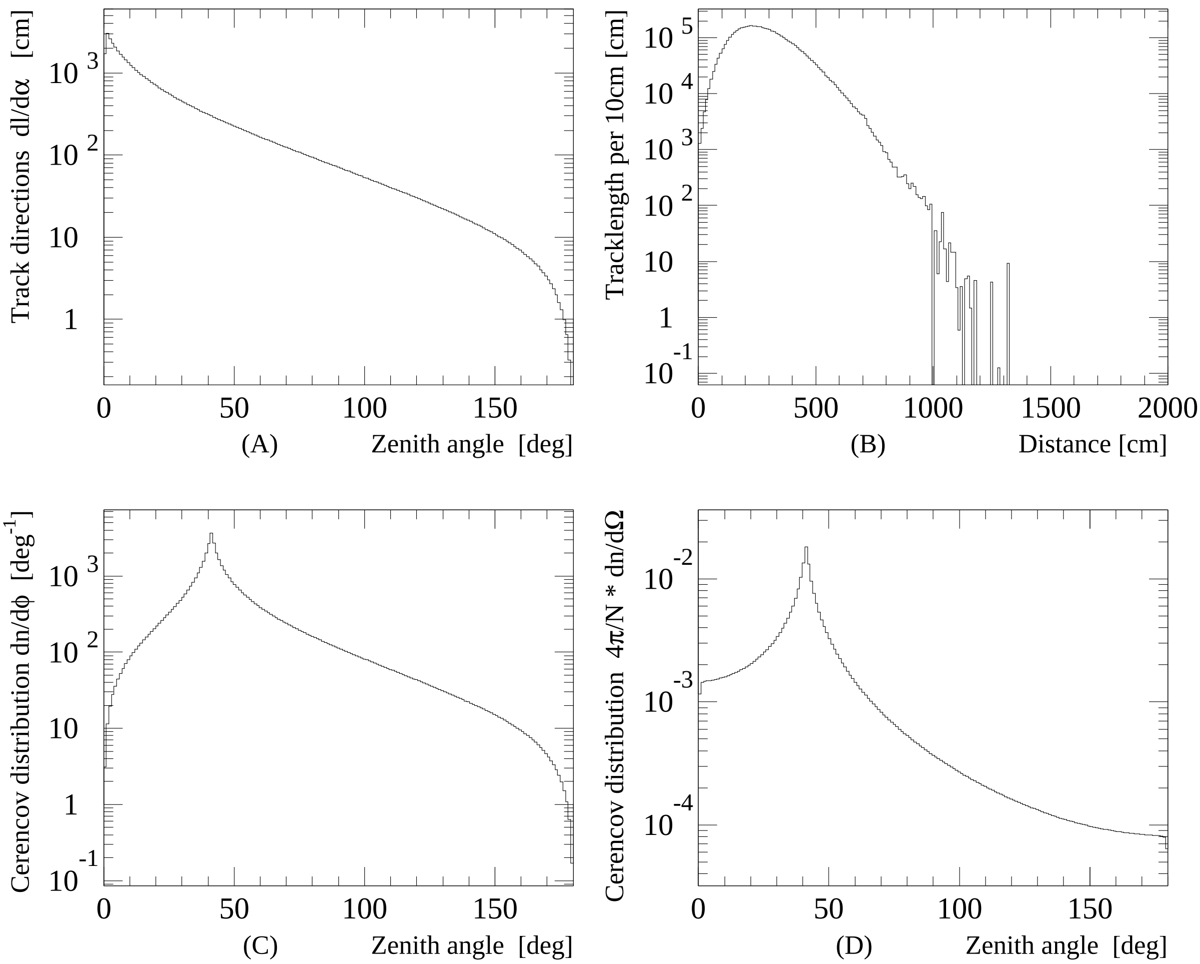

Figure 7.44: Track and Čerenkov distributions for $100 GeV$ electron–cascades.
(A) the absolute angular track-length distribution, (B) the longitudinal track-length distribution, (C) the absolute angular Čerenkov light distribution, (D) the effective angular Čerenkov light distribution (normalised to 1).

3. According to the method described in appendix A.1 the distribution $dl/d\alpha$ is transformed into a distribution $dn/d\varphi$. The distribution $dn/d\varphi$ contains the mean number of photons emitted into the zenithal direction φ. This distribution is called the *Angular Čerenkov light distribution* (see figure 7.44(C)).

4. In order to calculate the photon flux at a given distance and angle, the distribution $dn/d\varphi$ is further transformed (see appendix A.1) into the distribution $dn/d\Omega$ which is the number of photons per unit solid angle, called *Effective Angular Čerenkov light distribution* (see figure 7.44(D)).

Figure 7.44 shows the simulation results for $100 GeV$ electron cascades. The absolute angular track-length distribution is plotted in figure 7.44 (A). The tracks are pointing strongly into forward direction but also tracks with large angles occur. A longitudinal track-length distribution is shown in figure 7.44 (B). The result of the Čerenkov light transformation can be seen in figure 7.44 (C) and (D). The photon distributions are strongly peaked around the Čerenkov angle. Above an energy of $\sim 1 GeV$ these distributions are almost similar for electromagnetic cascades. Below $\sim 1 GeV$ the distributions become broader with decreasing energy until they are almost flat for $\sim 1 MeV$ with no visible Čerenkov peak, shown in figure 7.45.

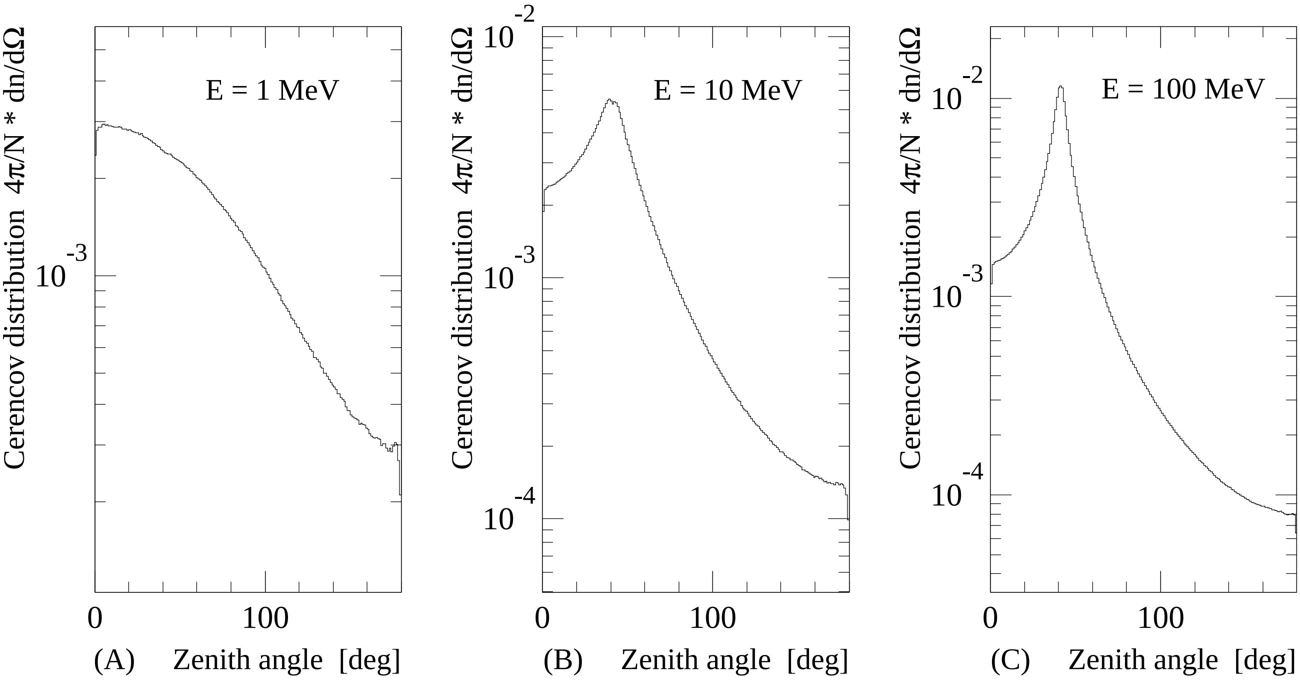

Figure 7.45: Relative effective Čerenkov light distribution for low energy electrons

The following points have to be noted considering limitations and interpretation of the above transformation method.

- The effective angular Čerenkov light distribution gives the angular distribution per unit of the longitudinal evolution of the shower. All tracks are assumed to be on the shower axis. Only in case of a point-like light source the photon flux at a given distance can be explicitly calculated from $dn/d\Omega$. In general $dn/d\Omega$ has to be convoluted with the longitudinal evolution of a shower.

- The calculation assumes a constant Čerenkov angle and a constant Čerenkov photon yield for all particles. This is not the case for low energy particles. The effect of the low energy tail of showers is respected by an empirical formula (eq.7.94) applied to the actual implementation of the parameterizations described below.

Longitudinal distribution

In general the longitudinal energy deposition for electromagnetic cascades can be approximated with a gamma distribution (see section 3.3.2, eq.(3.40)). The longitudinal track-length distribution has been fitted with

$$\frac{dl}{dt} = 10cm \cdot E_0 \cdot m \cdot K \cdot b \cdot \frac{(bt)^{a-1} \exp(-bt)}{\Gamma(a)} , \tag{7.91}$$

with $t = z/L_{rad} = z/35.8cm$ the number of radiation lengths, K a normalisation factor, E_0 the initial energy, a, b the shower parameters and m the number of simulated cascades.

In case of hadronic cascades, an additional process occurs: the decay of mesons into muons. These muons do not further contribute to the evolution of the shower, but may produce long tails in the longitudinal track distribution. Though this process is rare it has to be taken into account for summary distributions of several cascades. This is done in eq.(7.92) with an additional exponential term to

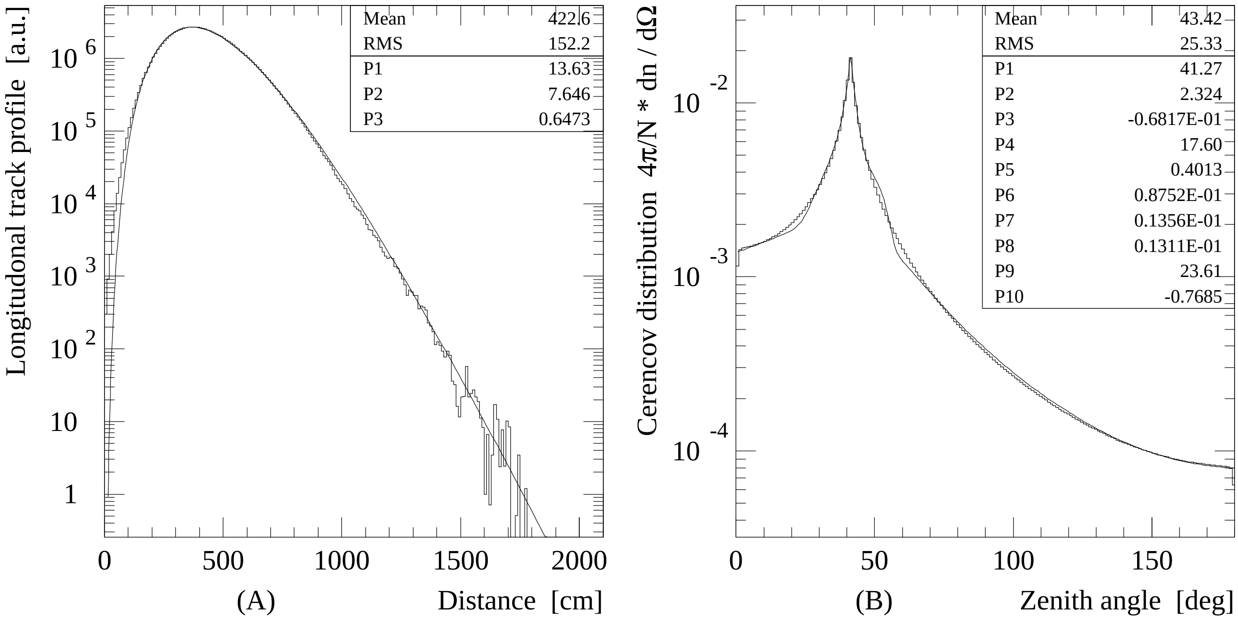

Figure 7.46: Fit to longitudinal track and angular Čerenkov distributions for $10TeV$ electron cascades (A) the longitudinal track-length distribution. The fit parameters P_1, P_2, P_3 correspond to the parameters K, a and b of eq.(7.91). (B) the effective angular track-length distribution normalised to 1. The fit parameters P_1, P_2, P_3, P_4, P_5, P_6, P_7, P_8, P_9, P_{10} correspond to the parameters Θ_c, σ_1, ϵ_1, σ_2, ϵ_2, N_1, N_2, N_3, σ_3, ϵ_3 of eq.(7.93)

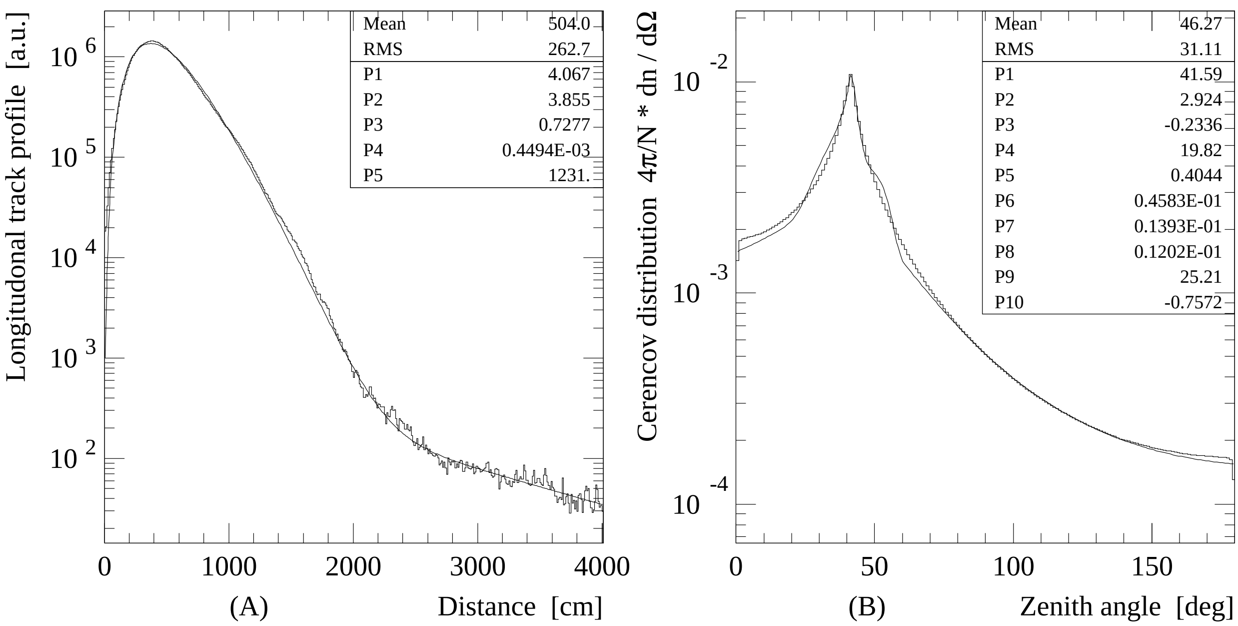

Figure 7.47: Fit to longitudinal track and angular Čerenkov distributions for $1TeV$ pion$^+$ cascades
(A) the longitudinal track-length distribution. The fit parameters P_1, P_2, P_3, P_4, P_5 correspond to the parameters K_1, a, b, k_2 and λ of eq.(7.92).
(B) the effective angular track-length distribution normalised to 1. The fit parameters P_1, P_2, P_3, P_4, P_5, P_6, P_7, P_8, P_9, P_{10} correspond to the parameters Θ_c, σ_1, ϵ_1, σ_2, ϵ_2, N_1, N_2, N_3, σ_3, ϵ_3 of eq.(7.93)

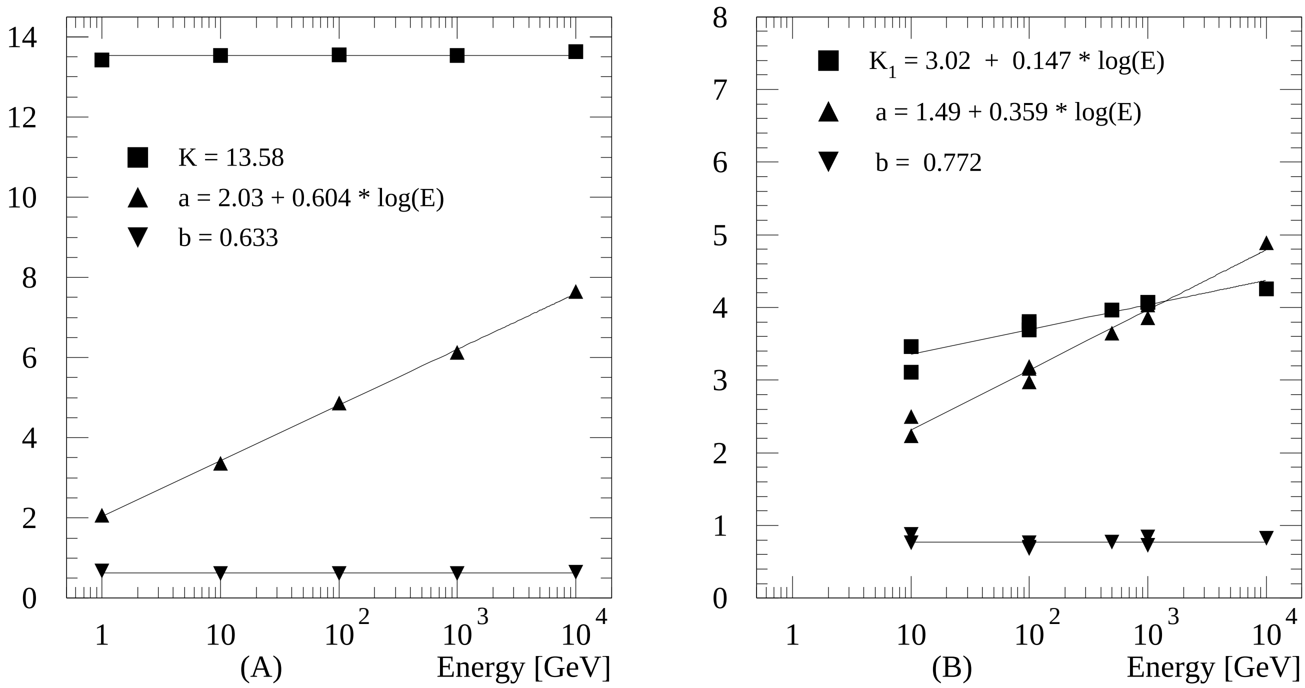

Figure 7.48: Parameters of the longitudinal fit versus energy .
Plotted are the fit parameter K, a and b. (A) shows the fit values for electromagnetic cascades. (B) shows the values for hadronic cascades.

Particle	Energy $[GeV]$	m $[\#events]$	K_1 $[GeV^{-1}]$	a	b	K_2 $[10^{-4}GeV^{-1}]$	λ $[cm]$
e^-	1	300	13.43	2.073	0.6716	—	
e^-	10	200	13.54	3.363	0.6124	—	
e^-	100	100	13.55	4.864	0.6132	—	
e^-	1000	20	13.54	6.131	0.6204	—	
e^-	10000	20	13.63	7.645	0.6472	—	
π^+	10	500	3.105	2.502	0.8795	33.3	1124
π^+	100	200	3.804	2.980	0.6798	4.915	2693
π^+	1000	200	4.067	3.855	0.7277	4.494	1231
π^+	10000	25	4.253	4.893	0.8240	1.534	2114
p^+	10	500	3.463	2.231	0.7623	—	
p^+	100	200	3.695	3.160	0.7655	3.622	2694
p^+	500	100	3.962	3.649	0.7693	0.317	> 4000
p^+	1000	200	4.074	4.032	0.8417	20.56	999
K^+	100	200	3.769	3.188	07013	6.35	2143

Table 7.6: Fit results for longitudinal cascade parameterizations. Input parameters have been $L_{rad} = 35.8cm$ for electromagnetic and $\lambda_I = 95cm$ for hadronic shower.

eq.(7.91).

$$\frac{dl}{dt} = 10cm \cdot E_0 \cdot N \left(K_1 \cdot b \cdot \frac{(bt)^{a-1} \exp(-bt)}{\Gamma(a)} + K_2 \cdot \exp\left(-\frac{z}{\lambda}\right)\right) \quad . \tag{7.92}$$

Table 7.6 gives the fit results for electromagnetic and hadronic cascades. No longitudinal fits have been applied for electrons with energies smaller $1GeV$ and hadrons smaller $10GeV$.

Figure 7.46 (A) shows a typical fit for $10TeV$ electromagnetic showers. The fit parameters (eq.(7.91)) are plotted versus the energy in figure 7.48 (A). The scaling of the constants is fitted with constant or a linear (in $log(E)$) function.
Figure 7.47 (A) shows the fit for $1TeV$ pion cascades. A long tail is visible which is fitted with the exponential term of eq.(7.92). The fit results are tabulated in table 7.6 and plotted versus the energy in figure 7.48 (B). The fluctuations for hadronic cascades are larger than for electromagnetic cascades. Thus the fit results are less stable. The scaling of the parameters is parameterized and shown in figure 7.48 (B).

Particle	Energy $[GeV]$	Events [#]	Θ_c [°]	σ_1 [°]	σ_2 [°]	σ_3 [°]	ϵ_1 $[10^{-3}]$	ϵ_2 $[10^{-3}]$	ϵ_3 $[10^{-3}]$	N_1 $[10^{-3}]$	N_2 $[10^{-3}]$	N_3 $[10^{-3}]$
(e^-)	0.001	$1 \cdot 10^6$	12.29	—	54.0	55.2	—	356	362	0.	8.90	9.25
e^-	0.01	$1 \cdot 10^4$	40.85	19.6	61.5	60.4	−356	268	−265	26.7	4.23	3.85
e^-	0.1	$5 \cdot 10^3$	41.59	4.95	17.4	33.0	−198	399	−789	59.2	12.7	7.34
e^-	1	$1 \cdot 10^3$	41.25	2.34	18.0	23.2	−53	397	−769	85.6	13.5	13.4
e^-	10	$1 \cdot 10^3$	41.27	2.32	17.6	23.6	−67	401	−767	87.7	13.6	13.1
e^-	100	500	41.27	2.34	17.6	23.6	−69	401	−770	87.3	13.6	13.1
e^-	1000	100	41.27	2.32	17.6	23.6	−69	401	−769	87.4	13.6	13.1
e^-	$1 \cdot 10^4$	20	41.27	2.32	17.6	23.6	−68	401	−768	87.5	13.6	13.1
e^+	100	500	41.27	2.32	17.6	23.6	−68	401	−769	87.6	13.6	13.1
γ	100	500	41.27	2.32	17.6	23.6	−69	401	−770	87.4	13.6	13.1
π^0	100	100	41.28	2.33	17.6	23.6	−69	401	−770	87.3	13.6	13.1
(π^+)	10	500	41.17	0.61	25.4	20.9	216	353	−807	48.4	13.2	16.9
π^+	100	200	41.69	2.84	20.4	23.2	−226	425	−798	33.2	14.0	13.9
π^+	1000	20	41.61	2.44	19.1	22.9	−203	423	−789	48.8	14.2	13.5
π^+	$1 \cdot 10^4$	10	41.55	2.49	18.1	22.7	−189	423	−776	53.9	14.6	13.3
(p^+)	10	500	41.06	0.13	46.3	35.2	193	378	−753	100.	8.2	13.1
p^+	100	200	41.90	2.19	22.4	21.8	−239	427	−781	21.6	13.5	15.7
p^+	500	30	41.61	2.67	20.0	23.2	−202	431	−792	40.2	13.8	13.9
p^+	1000	10	41.59	2.54	19.2	22.8	−198	419	−788	45.9	14.3	13.7
K^+	100	200	41.73	2.60	21.8	23.4	−236	424	−779	30.3	13.3	14.3

Table 7.7: Fit results for angular cascade parameterizations . The fits for particles in '()' show bad convergence and thus these results are given only for terms of completeness.

Angular distribution

The angular distribution has been fitted with following function:

$$
\begin{aligned}
(7.93)\qquad \frac{dn}{d\Omega} &= \frac{1}{2\pi} \cdot \left[N_1 \cdot \exp\left(- \left| \frac{\varphi - \Theta_c}{\sigma_1 + \epsilon_1 \cdot (\varphi - \Theta_c)} \right| \right) \right. \\
&\quad + N_2 \cdot \exp\left(- \left| \frac{\varphi - \Theta_c}{\sigma_2 + \epsilon_2 \cdot (\varphi - \Theta_c)} \right|^2 \right) \\
&\quad \left. + N_3 \cdot \exp\left(- \left| \frac{\varphi - \Theta_c}{\sigma_3 + \epsilon_3 \cdot (\varphi - \Theta_c)} \right|^3 \right) \right] .
\end{aligned}
$$

Each Exponential contains a width parameter σ_i and a skew term ϵ_i.
The fit results for both electromagnetic and hadronic cascades are printed in table 7.7. A typical fit is shown in figure 7.46 (B) for $10TeV$ electron cascades. The scaling of the electromagnetic fit parameters versus the energy is plotted in figure 7.49. The Čerenkov angle θ_C fitted as a free parameter is constant

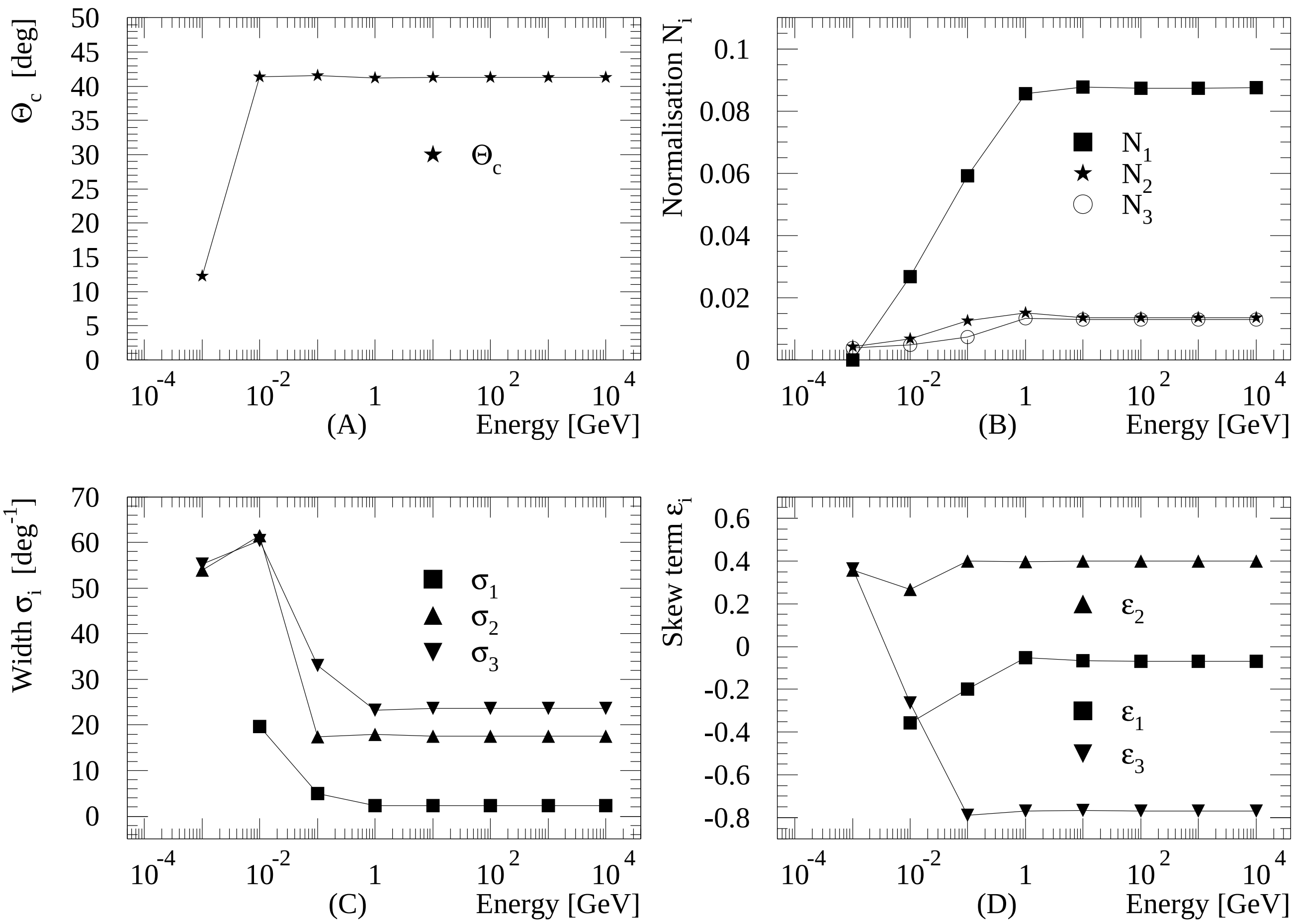

Figure 7.49: Parameters of the angular fit for electrons versus energy (A) shows the fit result for the Čerenkov angle Θ_c. (B) shows the fit result for the normalisation constants N_1, N_2, N_3. (C) shows the fit result for width constants σ_1, σ_2 σ_3. (D) shows the fit result for the skew terms ϵ_1 ,ϵ_2 ,ϵ_3

.

above $\sim 10MeV$. The input value (41.2°) of the simulation is reproduced to better than 0.1° (figure 7.49(A)). The other parameters N_i, σ_i and ϵ_i are constant above $1GeV$ (figure 7.49(B)-(D)).
Analogous a typical angular fit is shown for $10TeV$ pion cascades in figure 7.47(B). The results of the parameterizations are plotted in figure 7.50 versus the energy. The fit results for hadronic cascades are stable except for the increasing normalisation parameter N_1. This corresponds to small changes in the corresponding parameters σ_1 and ϵ_1.

The following strategy is used to yield a good approximation for non point-like showers. If the initial energy E_0 is above $1GeV$, it is divided into n energies. n vertices starting from the original vertex are generated into the momentum direction according[2] to the "Incomplete Gamma function". Thus a large cascade is approximated by n smaller cascades which are assumed to be point-like light sources. As noted above non-relativistic tracks produce less Čerenkov light with a different angular distribution. In order to include this effect the angular distribution $dn/d\Omega$ is corrected with an empirical formula.

$$\frac{dn_{cor}(\phi)}{d\Omega} = \frac{dn(\phi)}{d\Omega} \cdot (a + b \cdot \cos\phi) \quad . \tag{7.94}$$

[2]The cumulative distribution of the Gamma-distribution is given by the the "Incomplete Gamma-function" (eq.A.143).

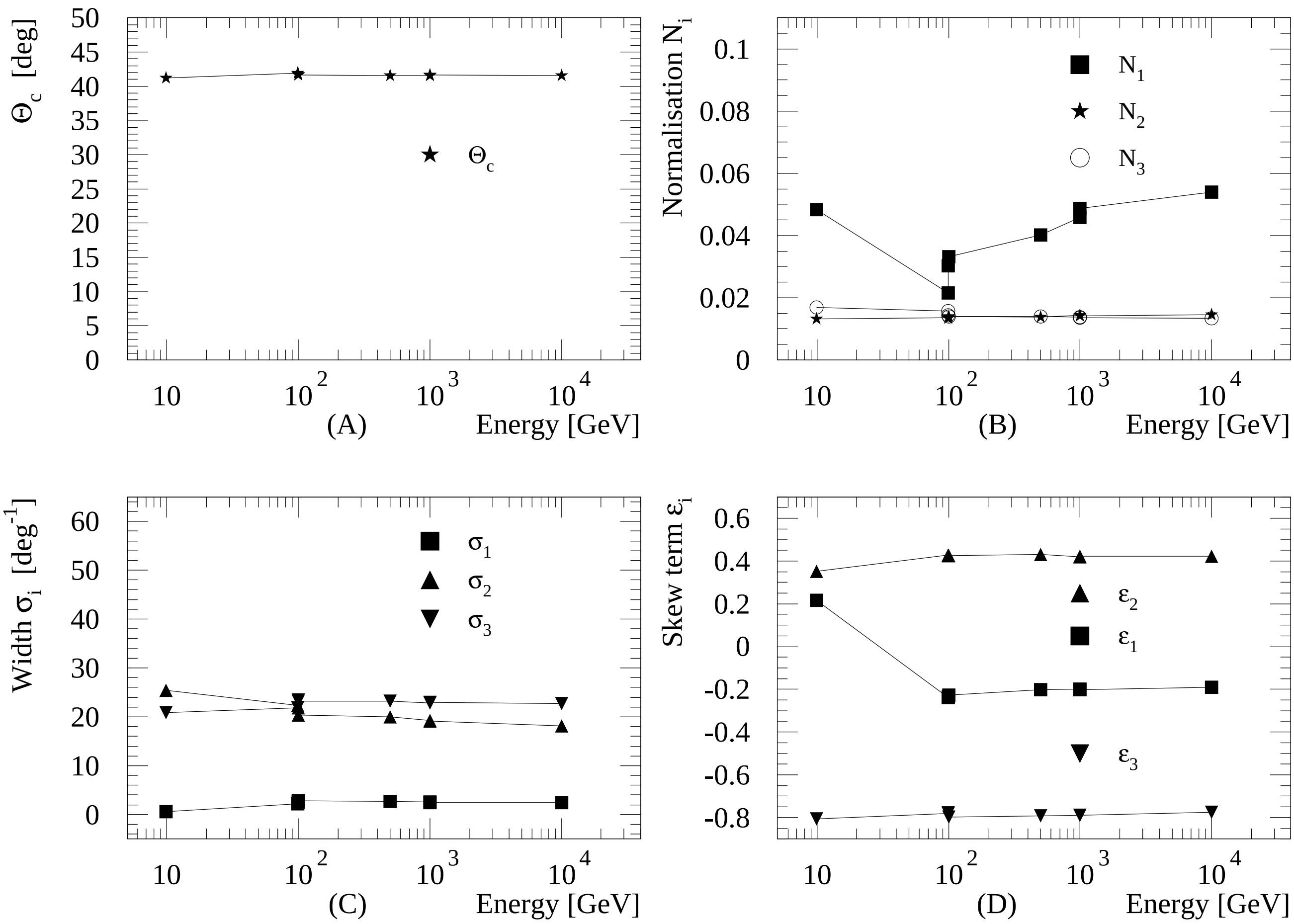

Figure 7.50: Parameters of the angular fit for hadrons versus energy
(A) shows the fit result for the Čerenkov angle Θ_c. (B) shows the fit result for the normalisation constants N_1, N_2, N_3. (C) shows the fit result for width constants σ_1, σ_2 σ_3. (D) shows the fit result for the skew terms ϵ_1 ,ϵ_2 ,ϵ_3

.

This strategy is implemented in DADA for fast simulations. The parameters a and b are obtained by a comparison with simulations including the explicit calculation of the Čerenkov angle and the photon yield. A simulation in the TRIAD gives values $a = 0.730$, $b = 0.266$ for electromagnetic cascades and $a = 0.86$, $b = 0$ for hadronic cascades. An electron initiated cascade with $100GeV$ pointing upwards has been simulated 1000 times in the centre of the TRIAD detector. This simulation has been done with the full GEANT tracking. The same simulation was repeated with the fast simulation once including the longitudinal evolution and a second time assuming a point-like light source. Figure 7.51 (A) shows the mean number of photons hitting each OM. While the longitudinal simulation reproduces the full simulation well, the fast simulation gives only the right order of magnitude. The difference of the arrival times for the full GEANT and the fast simulations is shown in figure 7.51 (B) Arrival times for a point-like simulation (P-G) show large time differences to the full GEANT simulation (up to $20ns$), whereas the longitudinal simulation (L-G) agrees well with the full GEANT simulation. Optical modules at a large distance from the cascade have a low hit probability. Due to only few recorded photons in this simulation they show larger statistical fluctuations.

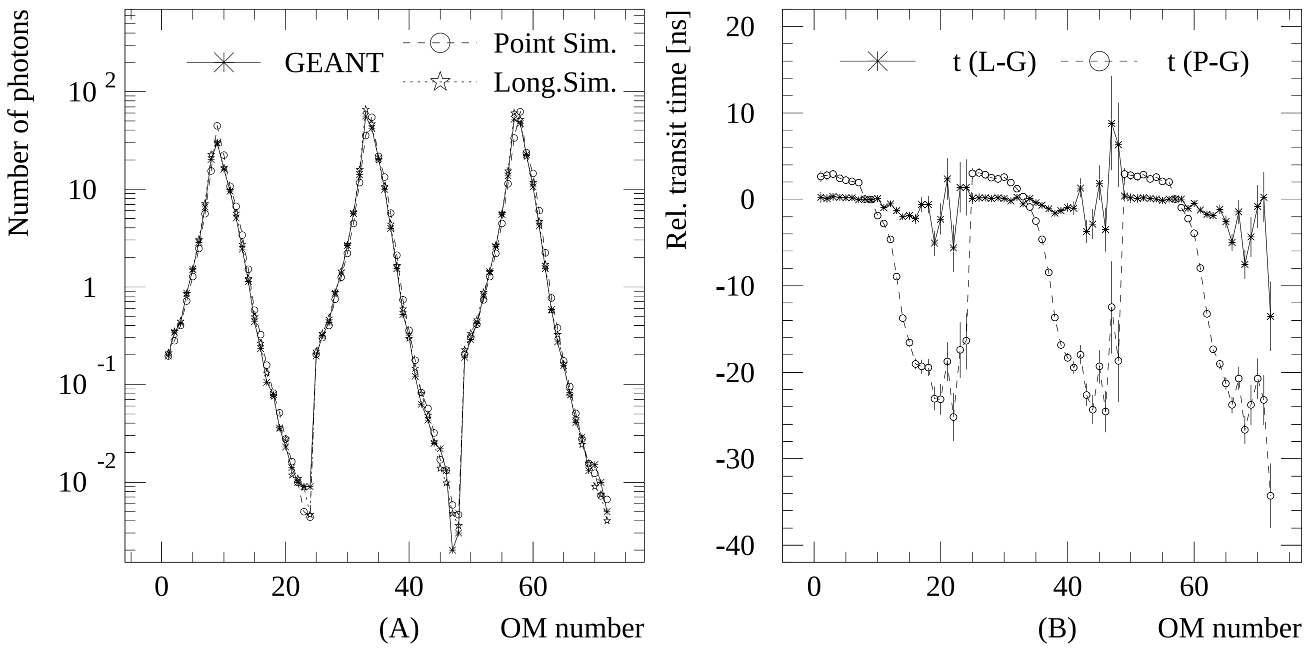

Figure 7.51: Comparison of the full GEANT and fast cascade simulations. Simulated are Čerenkov photons hitting OMs for electron showers ($100 GeV$) in the centre of the TRIAD detector. (A) The mean number of photons hitting each OM. (B) The arrival time of the first photon minus the arrival time of the GEANT simulation. (P-G): Point-like; (L-G): Longitudinal

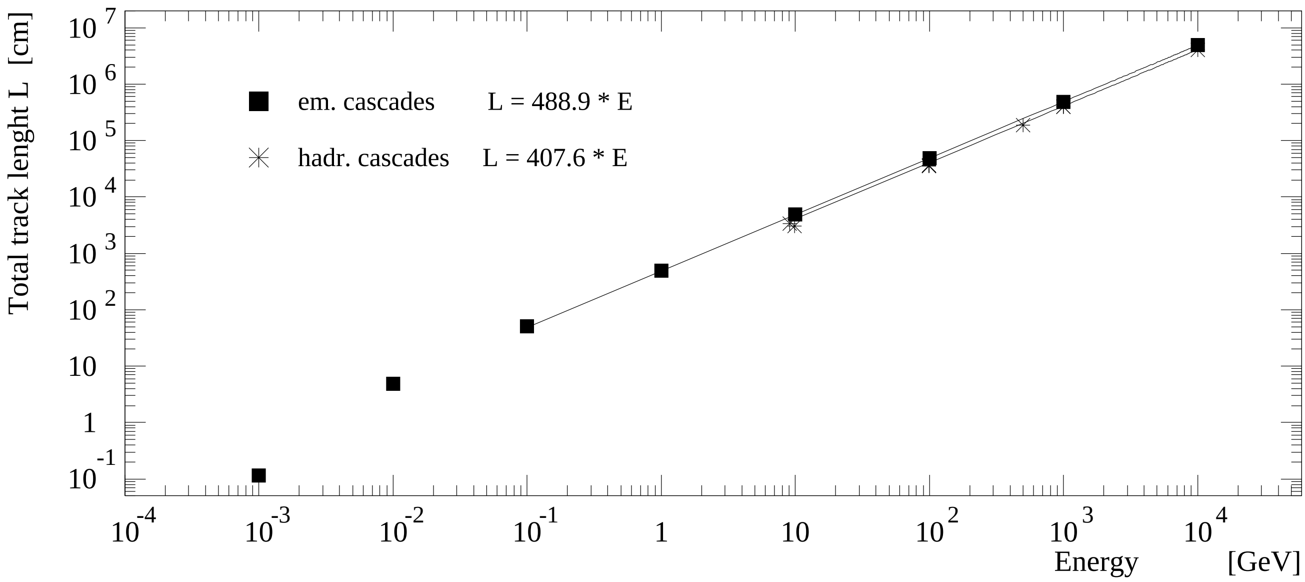

Figure 7.52: Integrated track length for electromagnetic and hadronic cascades

The total integrated track length

$$L = \int_0^{180} d\alpha \, \frac{dl}{d\alpha} = \sum_{tracks} \sum_{steps} l_i \ . \tag{7.95}$$

is proportional to the total amount of emitted Čerenkov photons.

Figure 7.52 shows the total integrated track-length L (see appendix A.1 eq.(7.95)) versus the energy of electromagnetic and hadronic cascades. The track-length depends linearly on the initial energy with

$$L[cm] = E[GeV] \cdot \begin{cases} 488.9 & \text{for e.m. cascades} \\ 407.6 & \text{for hadr. cascades} \end{cases} [cm/GeV]$$

The track-length is roughly proportional to the total amount of generated Čerenkov photons. If one applies the correction eq.(7.94) to the angular distribution of the resulting Čerenkov distribution one gets a correction factor 0.894 for electromagnetic and 0.86 for hadronic cascades for the total photon yield. This corresponds to approximately $0.96 \cdot 10^5$ Čerenkov photons per GeV energy for an electromagnetic cascade and $\sim 0.77 \cdot 10^5$ for hadronic cascades (assuming 220 photons per cm track).

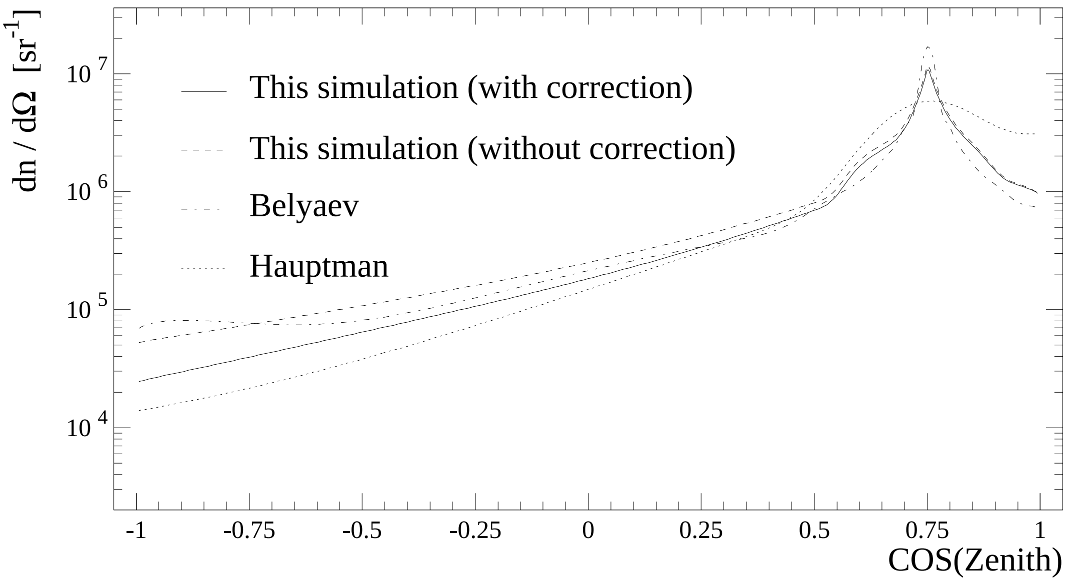

Figure 7.53: Comparison of the effective angular Čerenkov light distribution in point-like approximation with earlier parameterizations by Belyaev and Hauptman. The effective angular Čerenkov light distribution is shown with and without the correction according to eq.(7.94). Shown are the distributions for $100GeV$ electrons assuming an infinite distant observer.

Figure 7.53 shows the parameterization of the effective angular Čerenkov light distribution with and without the correction by eq.(7.94). The results of two previous simulations are plotted in comparison. These parameterizations are implemented in the *phocas*–function [51] which bases on two calculations by Belyaev et.al.[12] and J.Hauptman. The figure shows the effective photon flux per steradian resulting from $100GeV$ electrons. No light attenuation was used and the cascade is assumed as a point-like light source. All distributions differ in their integral by less than 10%. It has to be noted, that the assumption of a point-like light source does not yield a proper description (see figure 7.51). A full longitudinal simulations broadens the sharp Čerenkov peak. Therefore this simulation is not in disagreement to the Hauptman parameterization, which already takes account of the longitudinal distribution.

7.2 Čerenkov light from muons

The primary challenge for a neutrino telescope is to detect muons and reconstruct the direction of the muon track using the arrival time and amplitude of Čerenkov light measured with the OMs. Due to energy loss processes a muon is accompanied by secondary particles, which also produce Čerenkov light (see section3.3.1). Therefore the amplitude and time of the measured Čerenkov signal does not match the expectation for a pure muon track. Processes with large energy transfers (e.g. bremsstrahlung) give rise to bright local cascades. Processes with smaller energy transfer (e.g. δ-ray production) occur more frequently and can be approximated as a quasi continuous process (see also figure 6.43 (A)).

A muon including the low energy quasi-continuous particles will be named "*naked muon*" in the following, in contrast to a *minimal ionising muon*, which represents only a pure muon.

7.2.1 Parametrisation of the effective Čerenkov light from muons

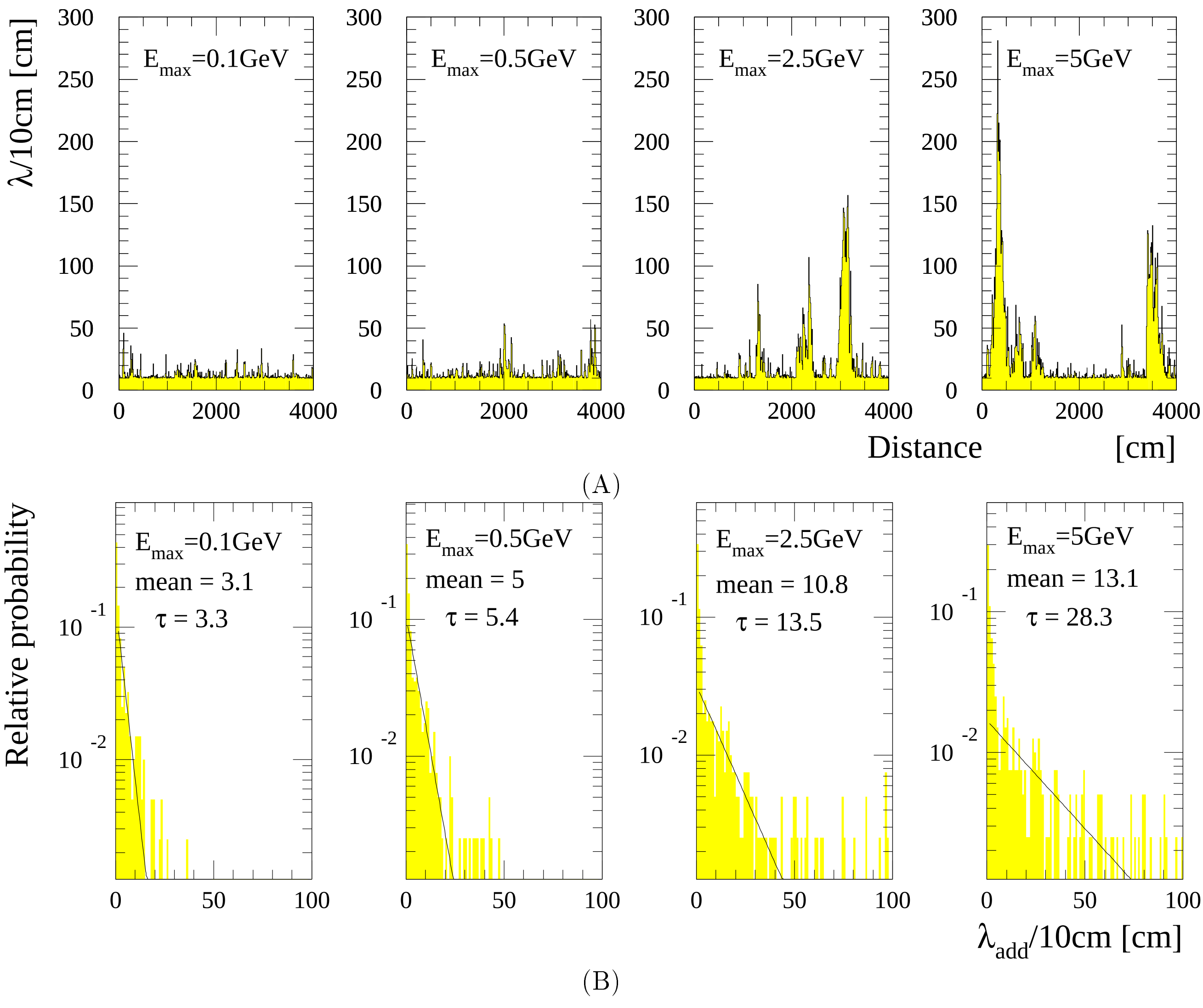

Figure 7.54: Low energy secondary tracks accompanying $5TeV$ muon tracks. (A) the integrated track-length λ per $10cm$ of the covered distance by a muon. Four muon tracks are shown with different upper boundaries on the maximum energy of secondary particles. (B) Shows the frequency distributions of the occurrence of additional track-length λ_{add} per $10cm$ for the same tracks. A decaying Exponential is fitted to the distributions.

In order to investigate the characteristics of the quasi-continuous secondary light production, muons are tracked in a test volume from the position $(0, 0, 0)$ for $40m$ into positive z-direction. The integrated Čerenkov radiating track-length λ including secondaries is summed every $10cm$ along z (in analogy to the longitudinal track-length distribution of a shower eq.(7.90)). Obviously one expects $\lambda_0 = 10cm$ Čerenkov radiating track-length per $10cm$ covered distance for a minimal ionizing muon. Including secondaries one gets

$$\lambda = \lambda_0 + \lambda_{add}\ . \tag{7.96}$$

Figure 7.54 (A) shows a simulation of four $5TeV$ muons. An upper limit E_{max} on the maximum energies of generated secondary tracks is varied. For small E_{max} only small local energy depositions are visible. For values of $E_{max} > 0.5GeV$ larger local fluctuations occur, which cannot be approximated as continuous processes. Figure 7.54 (B) shows the distribution of λ_{add} per $10cm$ muon track. An exponential distribution gives a sufficient description for small values E_{max}.

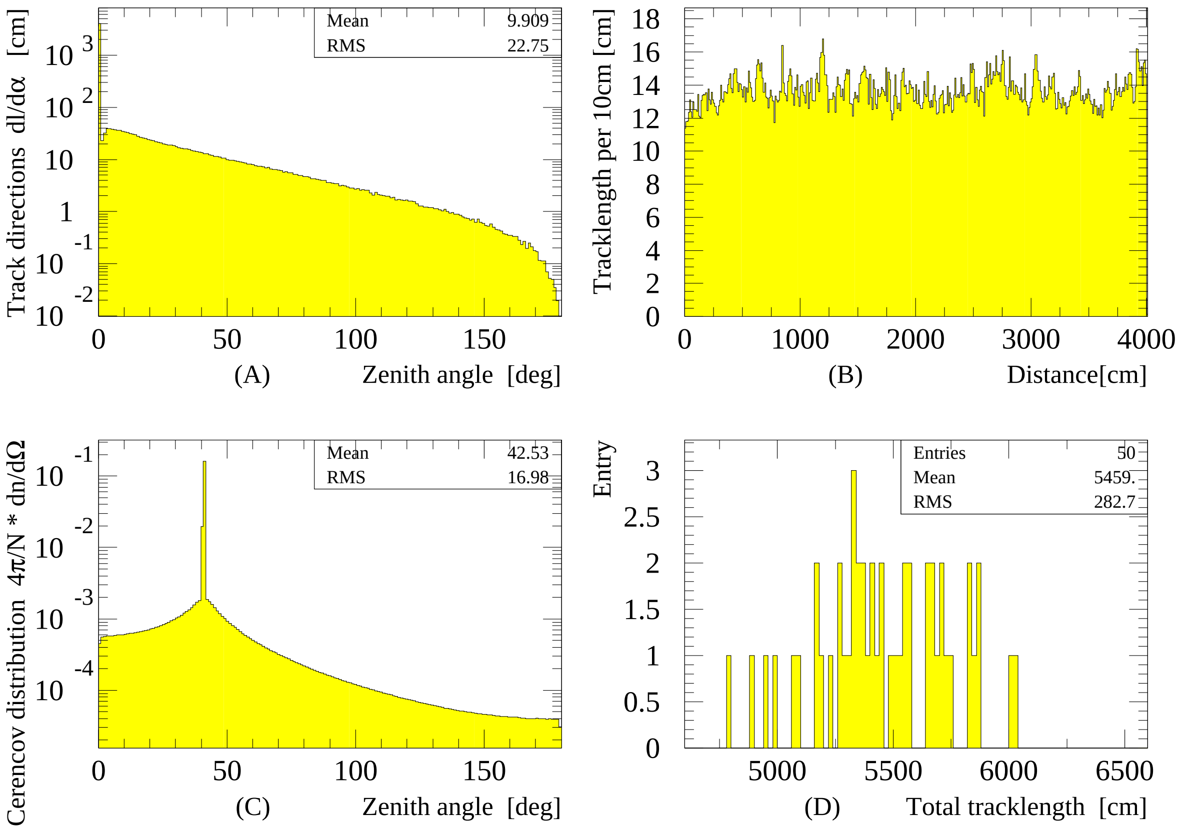

Figure 7.55: Track and Čerenkov distributions for $300GeV$ muons including only low energy quasi continuous secondary tracks ($E_{max} \leq 0.5GeV$) averaged over 50 tracks. (A) Angular track-length distribution. (B) Longitudinal track-length distribution. (C) Effective angular Čerenkov light distribution. (D) Distribution of the total track-length.

A parameterization of the Čerenkov light due to quasi-continuous processes is obtained in close analogy to the simulation of cascades (section 7.1). All 50 muons have been simulated for different energies and averaged. The threshold E_{max} is set to $0.5GeV$ for secondary $e^{\pm}$ and $1GeV$ for secondary γ. Using the angular track-length distribution eq.(7.89) the effective Čerenkov light distribution is calculated (see appendix A.1). Figure 7.55 shows the results for $300GeV$ muons (see also figure 7.44). The effective Čerenkov distribution shows a sharp peak at the Čerenkov angle and a broad distribution of light due to secondary particles. The calculation of the Čerenkov light neglects the smaller Čerenkov light yield and changed angular distribution of non relativistic tracks. A consideration of this would reduce the total amount of light especially into backward direction (analogous to eq.(7.94)).
Figure 7.56 shows a parameterization of λ_{add} versus the energy of the muon. The total track-length λ_{tot} for a muon track λ_0 can be expressed via

$$\lambda_{tot} = \lambda_0 \cdot (1.172 + 0.023 \cdot \log(E_\mu[GeV]))\ . \tag{7.97}$$

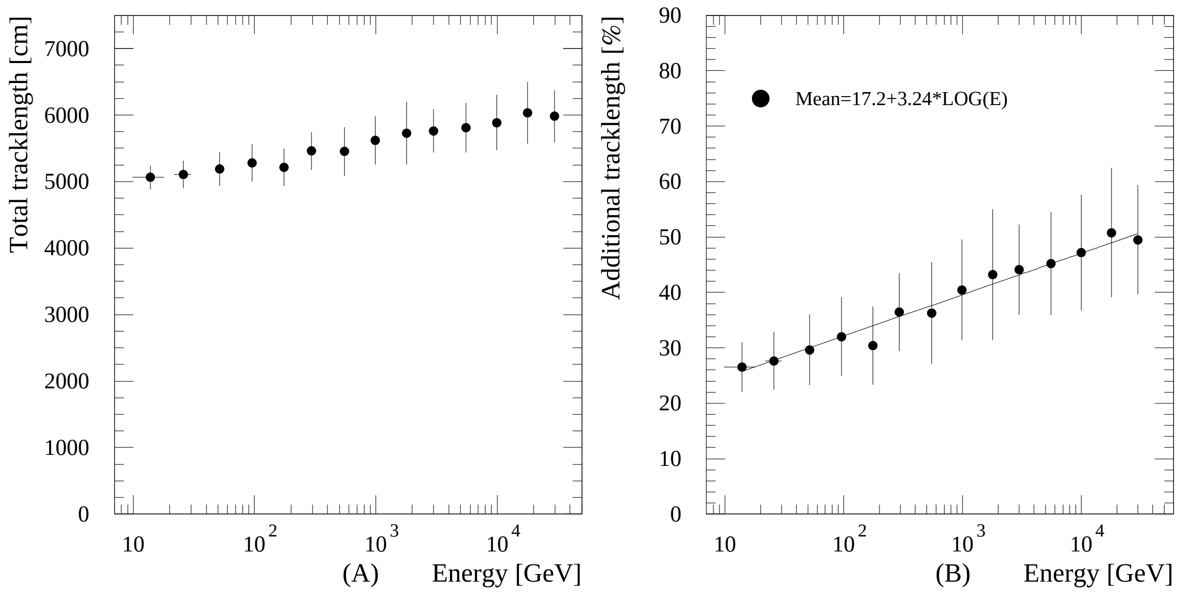

Figure 7.56: Additional track-length due to quasi-continuous secondaries versus the muon energy. (A) the mean total track-length for $40m$ muon tracks. (B) The relative additional track-length.

The above parameterization is implemented in the DADA program. The GEANT tracking parameters are set to $0.5GeV$ for mechanisms generating $e^{\pm}$ and to $1GeV$ for produced γ's. If a mechanism generates a secondary above the tracking thresholds a local cascade is simulated according to the parameterization in section 7.1. The loss of low energy tracks is compensated by adding λ_{add} to each muon track piece λ_0, assuming an Exponential distribution with the decay constant λ_{add} (see figure 7.54 (B)). The angular distribution is neglected[3].

This method, called *Fast GEANT*, yields an enormous increase in the execution speed by typically a factor 1000 and enables a mass production of muon events. Though it neglects small fluctuations of cascades and the stochastic generation of low energy secondaries along a muon track, it keeps the full stochastic tracking with respect to the production of charged high energy secondaries with $E \geq 0.5GeV$.

Figure 7.57 shows a comparison of the fast parameterization with a full GEANT simulation. A specific $1TeV$ muon track is simulated through the centre of the TRIAD detector. The photons, which hit the OMs are simulated instead of the full digitisation of OMs. The same track is repeated and results are averaged. Three different simulations are applied: full Geant, fast Geant and simulation of a minimal ionising muon track.

The mean number of photons hitting each OM (A), and the total number of photons per event (B) matches well between the fast and the full GEANT simulations but disagrees with the simulation of minimal ionising muons. The time residual is defined as difference between the time of hit and the expected time derived from the track kinematics

$$\Delta t \equiv t_{hit} - t_{expected}, \tag{7.98}$$

assuming a pure Čerenkov cone. (C) shows the distribution of the time residuals in all hit OM. Each entry in the distribution is weighted with the number of hit photons. Thus the distribution shows the arrival times of photons. Minimal ionising muons generate a small peak. The simulation of the muon including secondary processes leads to a long tail of photons arriving at later times. The secondary light causes a distortion of the clean Čerenkov signature, which makes a reconstruction of the track

[3]Photons, which are not emitted under the Čerenkov angle, usually arrive later and thus generate only subsequent hits within the dead time of the OM.

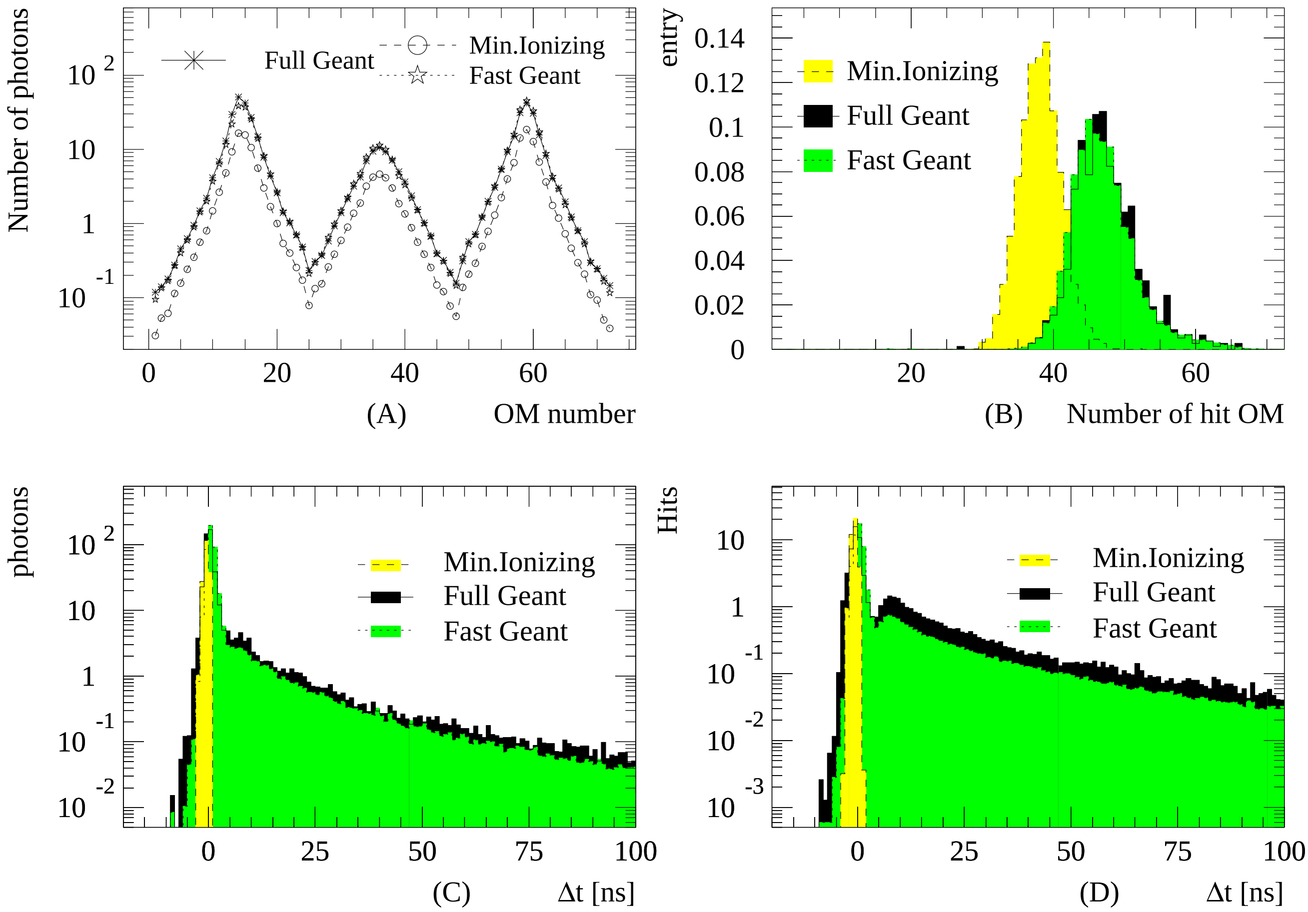

Figure 7.57: Detector response for a repeated Muons track in the TRIAD detector. A $1TeV$ muon track was repeatedly simulated in the TRIAD detector. The figures show comparisons of simulations with full GEANT, fast GEANT and minimal ionising muons. (A) The mean number of photons hitting each OM. (B) Distribution of the total number of hitting photons per event. (C) Distribution of relative arrival time of photons. (D) Distribution of relative arrival time of photon-hits.

less robust. The fast GEANT simulation reproduces well the full GEANT simulation. (D) shows the time residuals for all hits, not weighted with the number of photons. The distributions shows a dip at $\Delta t = +3ns$. This dip occurs due to the internal recombination of hits during tracking. Photons arriving within a time window of about $3ns$ are regarded as equal in time and recombined (see appendix C.1.3). As expected the full simulation generates more hits of smaller light intensity compared to the fast simulation. These hits are related to secondaries of small energies, which produce a subsequent hit to a previous direct muon hit. If one applies the dead time of the OMs to the data, the dip disappears and the distribution agrees well between fast and the full simulation.

7.2.2 Čerenkov light from secondary processes

The characteristics of the individual stochastic energy loss process are investigated by the simulation of muon tracks of fixed energy through the NT-200 detector. The tracks have a fixed energy and are isotropically generated over the lower hemisphere. The same data-set of tracks is simulated with certain physical processes switched on or off for different simulation runs. The geometrical plane for the simulated vertices has a radius of $45m$ which is only slightly larger than the NT-200 detector. The trigger is set to minimum 3 hit strings and 5 hit channels. Multiple hits in one OM are integrated if they occur within the dead-time of $300ns$ and the local coincidence between two OMs is simulated with a time window of $15ns$.

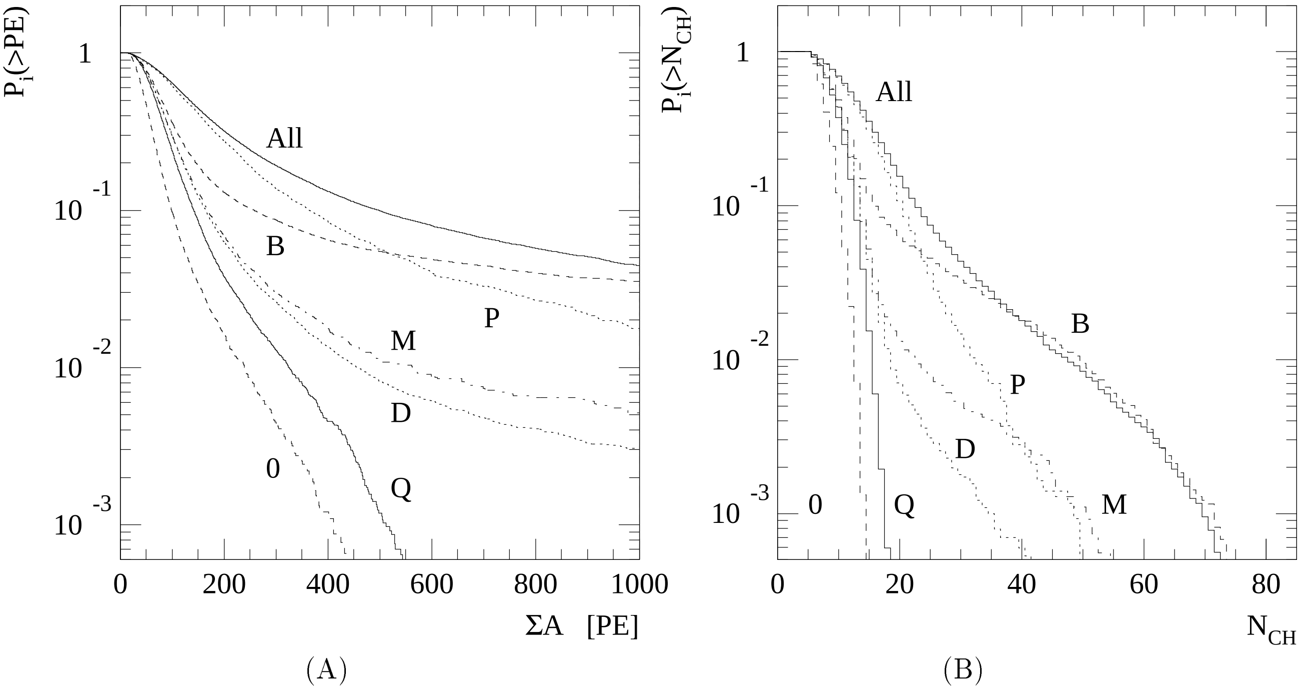

Figure 7.58: Amplitude response of the NT-200 for isotropic $5TeV$ muons. (A) shows the relative number of events $P_i(>\text{PE})$ with the total energy above a threshold. (B) shows the relative number of hit channels $P_i(>N_{CH})$ above a threshold. The different simulations are indicated with: 0 only minimal ionising muons, Q with quasi-continuous energy loss, D delta ray production ($+Q$), M muon nuclear interactions ($+Q$), P pair production ($+Q$), B bremsstrahlung ($+Q$). For "All" all processes have been switched on. Each process except for "0" includes the quasi-continuous secondary light ($+Q$).

Figure 7.58 displays integral distributions of the total number of PE and hit channels N_{CH} for $5TeV$ muons. Shown are the results for different simulations: minimal ionising muons (0), naked muons (Q), full simulation (All), and the individual discrete processes: bremsstrahlung (B), delta-ray production (D), pair production (P) and nuclear interactions (M). All but (0) include also the quasi-continuous light (Q) of a naked muon. The distributions for each process i are normalised to the number of triggered events and thus yield the probability of the occurrence of events with a total amplitude $P_i(>\text{PE})$ above a threshold and a number of hit channels $P_i(>N_{CH})$ above a threshold

$$P_i(>\text{PE}) = \frac{N_{>PE}}{N^i_{trig}} \qquad P_i(>N_{CH}) = \frac{N^i_{>CH}}{N^i_{trig}} \tag{7.99}$$

The trigger efficiencies $\epsilon_i = N^i_{trig}/N_{gen}$ are given in following table.

Process	Full	0	Q	D	M	P	B
ϵ_i [%]	60.5	30.3	40.6	42.8	43.0	58.5	46.0

The total number of 20 hit OM is not exceeded by naked muons while about 25% of the events with the full simulation exceed this value. Events with larger amplitudes are dominated by the pair production process and for the largest amplitudes by bremsstrahlung. The contribution by delta rays is relatively weak, since only delta rays above $0.5GeV$ are considered (see section 7.2.1). Though muon nuclear interactions have only a rare occurrence, their contribution is still visible, especially for large numbers of hit channels.

Figure 7.59 shows how the relative contributions of the different processes summarise up to the total amplitude response. The comparison has to respect the different trigger efficiencies and is calculated

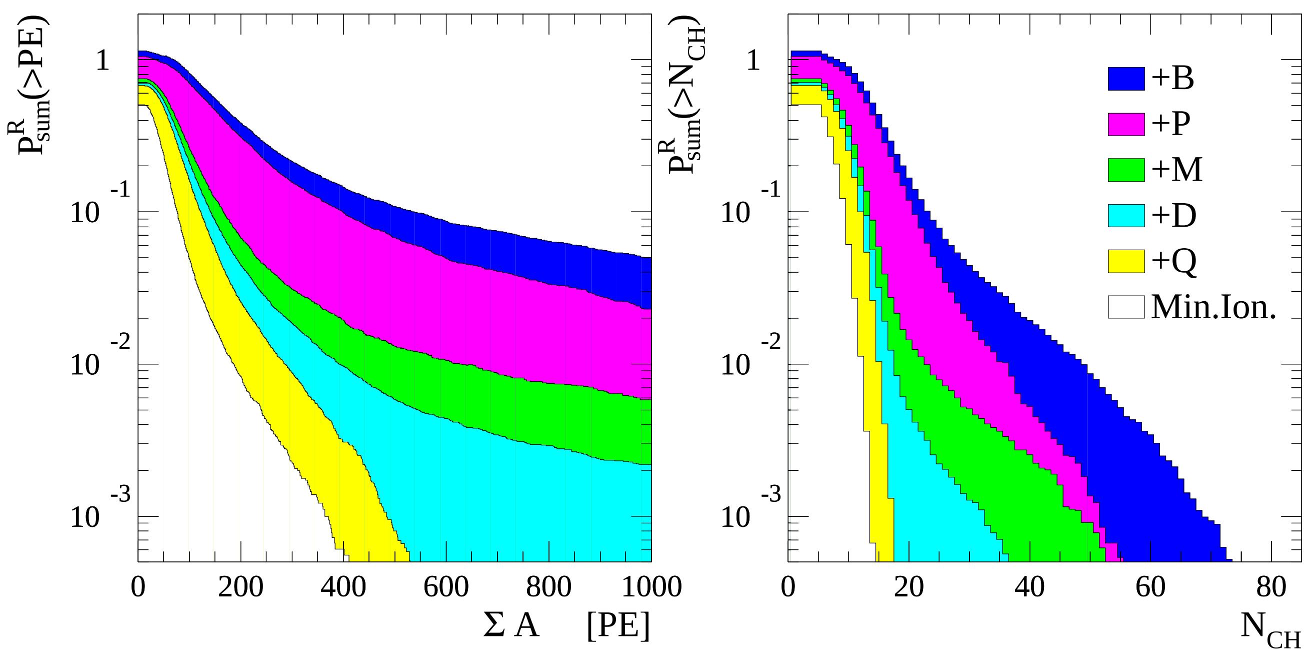

Figure 7.59: Contributions of discrete muon energy loss processes ($E_\mu = 5TeV$) to the amplitude response of the NT-200 detector. Shown is how the processes add up to the total response.

as follows: Each distribution P_i of figure 7.58 is weighted with its relative trigger efficiency $\epsilon_i/\epsilon_{Full}$ compared to the full simulation

$$P_i \rightarrow P_i^R = P_i \cdot \frac{\epsilon_i}{\epsilon_{Full}} \tag{7.100}$$

The distribution for naked muons Q is subtracted from B, P, M, D and the distribution for minimal ionizing muons 0 is subtracted for Q. Finally the contributions of the different simulations are subsequently added to the contribution of minimal ionizing muons in figure 7.59 giving the summed probability of the relative contributions P^R_{sum}. It has to be noted, that this calculation is not exact and yields a slightly larger distribution than for the full simulation. This is explained by the fact that during the simulation of one process with the other processes switched off the total energy loss of the muon itself is smaller. Since the cross sections rise for higher energies the probability of the occurrence of a process is slightly larger if no other processes occur in the same simulation run. The individual simulations may also involve a slightly different event topology which may be differently affected by the trigger condition (3 strings, 5 hit channels).
Not only the amplitude response but also the time response of the detector is differently influenced by secondary processes, as shown in figure 7.60 and 7.61. The majority of hits arriving at later times than expected from the model of a naked muon are strongly dominated by bremsstrahlung events. Pair production events significantly enlarge the hit probability at the expected time. As discussed in more detail in section 7.2.4 late secondary hits are strongly suppressed by the local BAIKAL coincidence condition. Only secondary cascades with large energy transfer, such as bremsstrahlung events, are likely to produce enough light for a coincident hit to trigger both OMs.

Figure 7.62 and 7.63 show the time residuals for muons with the energies $50GeV$, $500GeV$, $5TeV$ and $50TeV$ simulated in the NT-200 detector. Tracks from same data set as in the above simulation have been tracked through the NT-200 detector using only a changed muon energy. The figure shows the time distribution of hits in OMs, which are not weighted with the hit amplitude. The plots are normalised to the total number of events. The figure does not include the relative trigger efficiencies. Figure 7.64 shows the corresponding amplitude distributions. Especially from (C) one concludes that

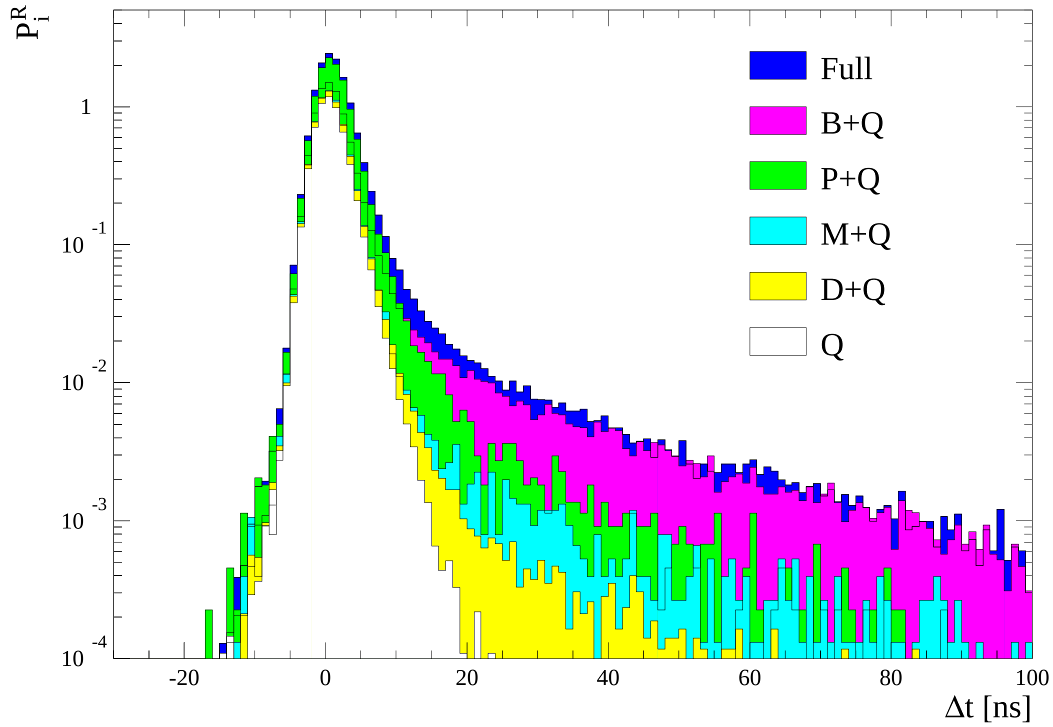

Figure 7.60: Contributions of discrete muon energy loss process to the time residuals eq.(7.98) of hits in the NT-200 detector. The distributions are normalized on the number of triggered events for the full simulation of $5TeV$ muons.

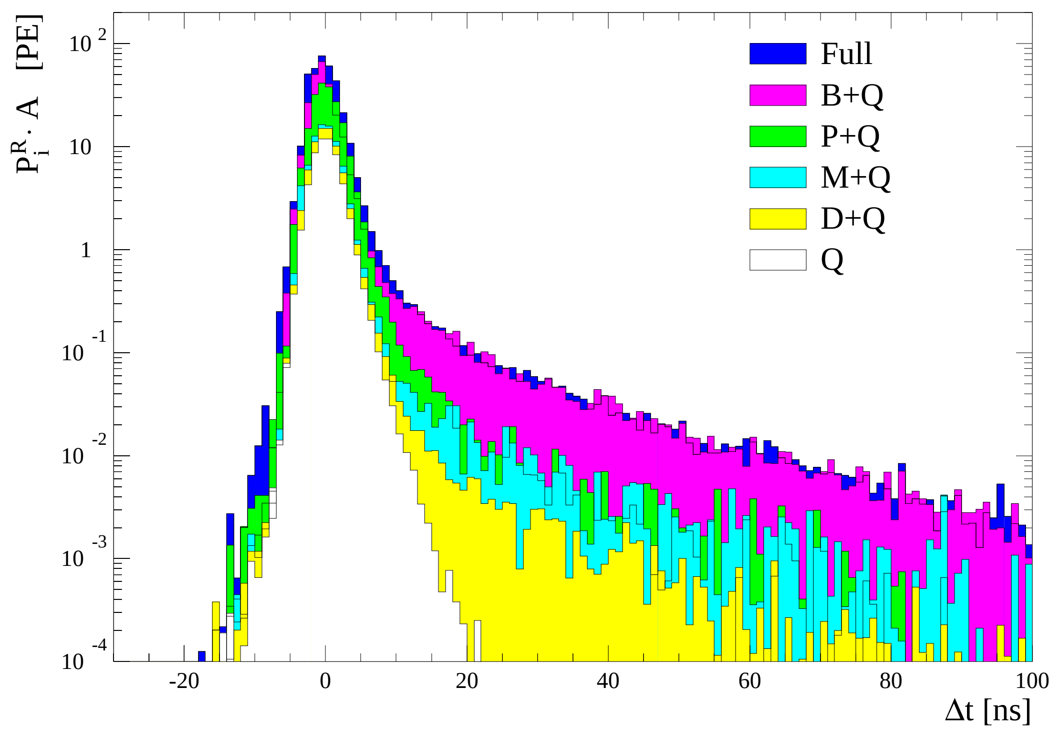

Figure 7.61: Contributions of discrete muon energy loss process to the time residuals (amplitude weighted) of hits in the NT-200 detector.

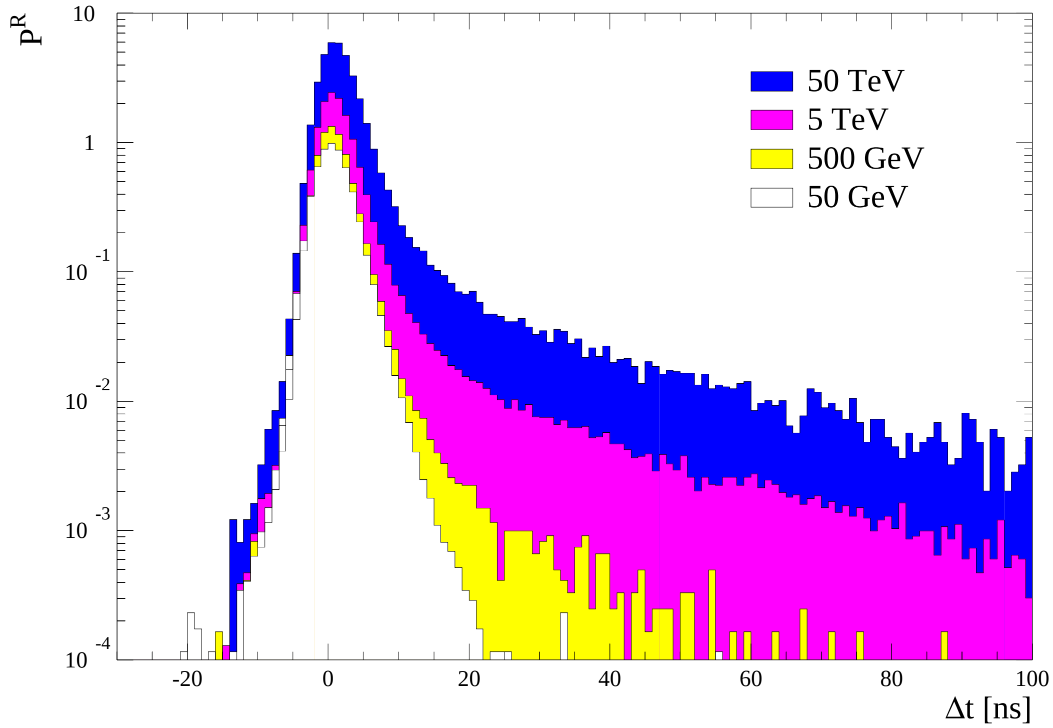

Figure 7.62: Time residuals for muons of different energies in NT-200. Shown are the time residuals of each hit normalised to the trigger efficiency of $5TeV$ muons.

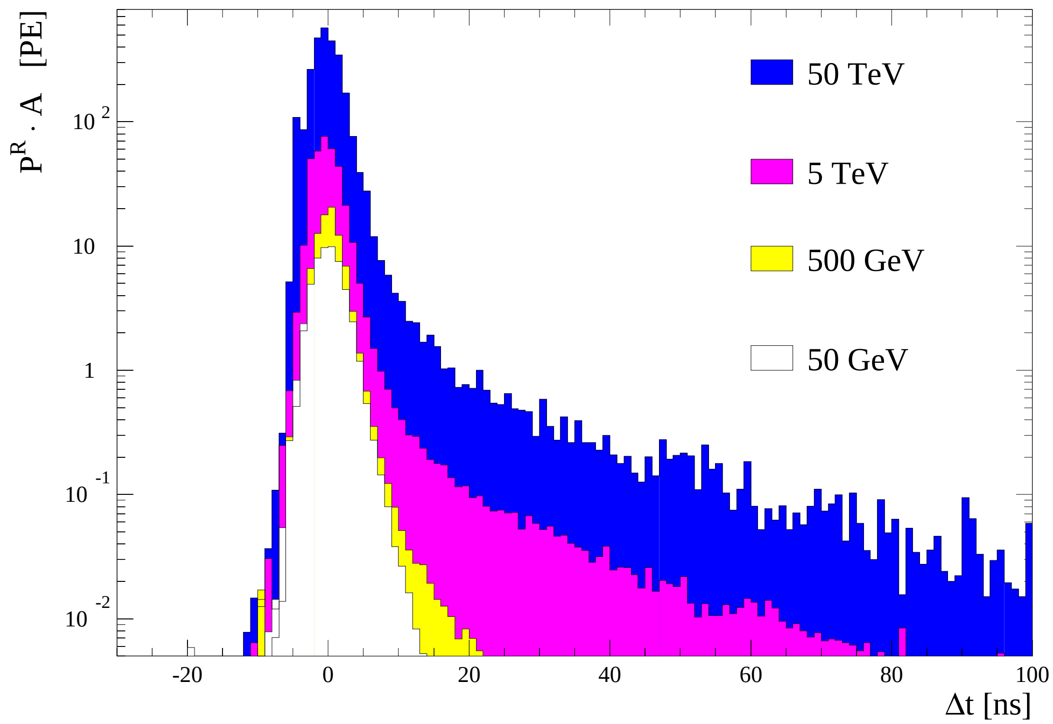

Figure 7.63: Time residuals (amplitude weighted) for muons of different energies in NT-200.

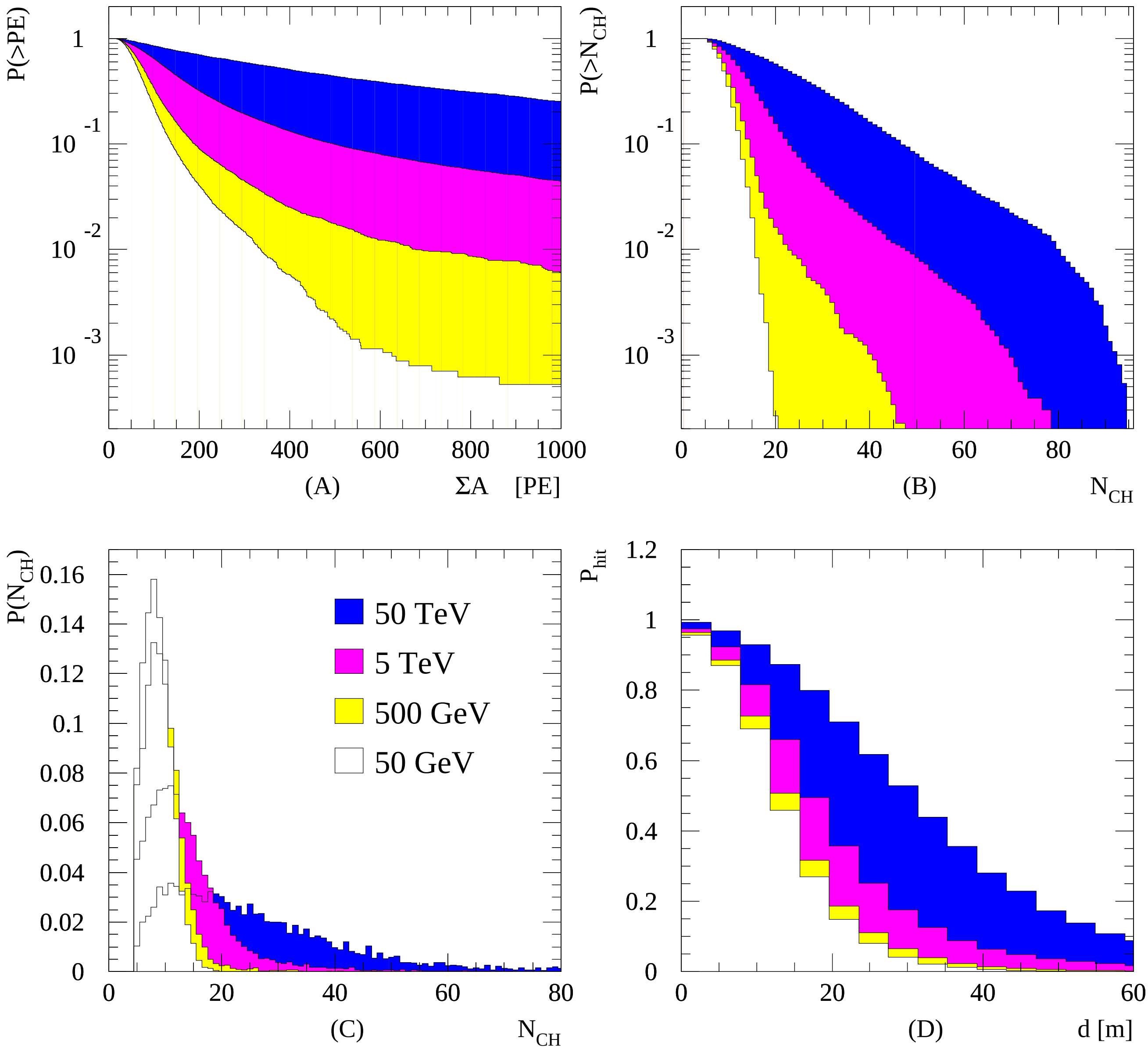

Figure 7.64: Amplitude response of the NT-200 detector for different energies. (A) the integral distribution of the total energy in the detector. (B) the integral distribution of hit channels. (C) the differential distribution of hit channels. (D) the hit probability as a function of the length d of the Čerenkov light path. The distributions in (A), (B) and (C) are normalised to the number triggered events of each energy. The distribution (D) is determined by the individual occurrence of a hit in each OM for all triggered events.

a measurement of the muon energy is difficult, especially for low energies $< 10 TeV$, unless one uses more sophisticated methods as described in e.g. [101].

7.2.3 Pointing accuracy of muons

An interesting aspect for the operation of a neutrino telescope is the pointing accuracy of a detected muon track into the initial neutrino direction. Three effects provide deviations from the initial direction of the neutrino. The dominant deviation is due to the kinematics of the neutrino nucleon interaction with an average scattering angle given in eq.(2.12). A negligible contribution comes from the deflection by the Earth magnetic field. A conservative estimate gives

$$\vartheta_B[rad] \leq \frac{L' \cdot 0.3 \cdot B}{p_\mu} \tag{7.101}$$

with the muon momentum p_μ in units GeV/c. A field value of $35\mu T$ gives $\vartheta_B[rad m^{-1}] \approx 10^{-5}/p_\mu$ per m track length. Typical deviations after a muon traveled its half mean range (see eq.3.36) are of the order of 10^{-3} degrees.
In addition, during propagation through water, the muon is affected by multiple scattering and recoiling effects in secondary processes. This effect is treated in detail in the following.

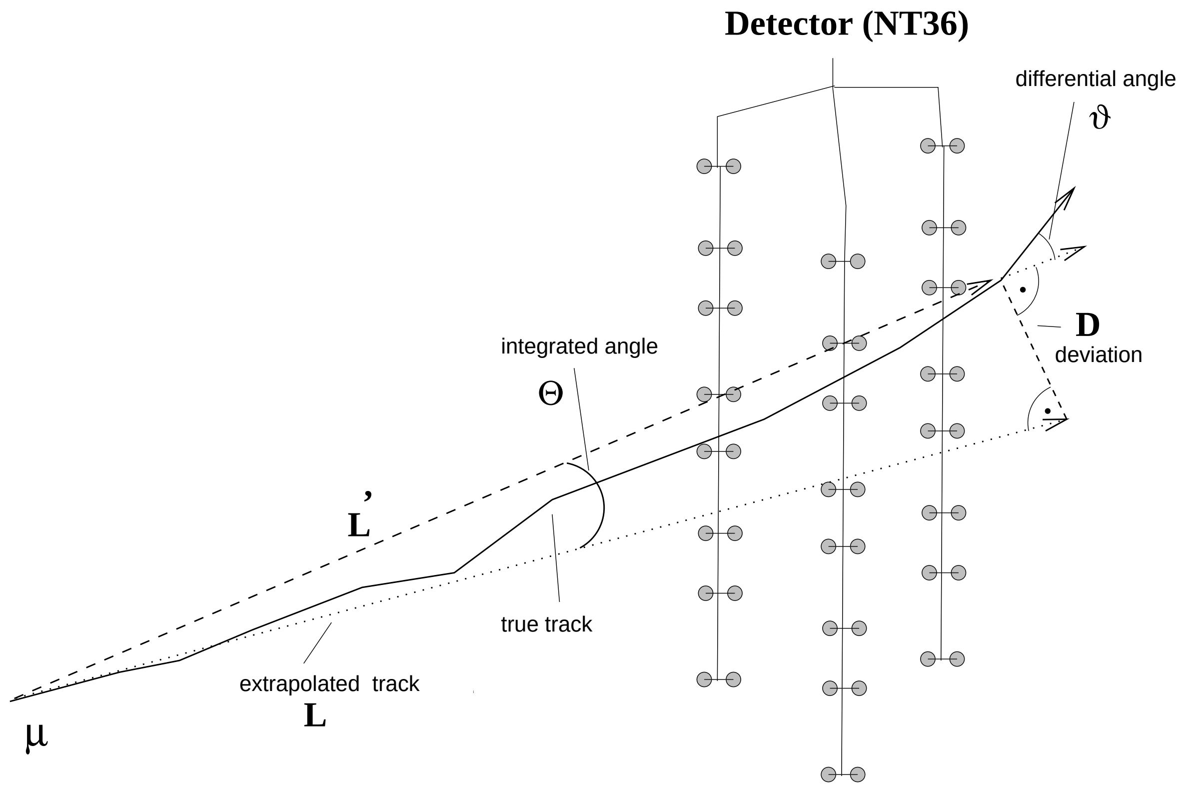

Figure 7.65: Sketch of a muon track traveling through a detector.

The situation is sketched in figure 7.65. A muon wobbles along its initial track and eventually changes its direction. Two characteristic quantities determine the pointing accuracy of a muon. The "differential angle" ϑ gives the angle between the initial direction and the direction of the muon after traveling a certain distance L'. The deviation D gives the distance between the actual position of the particle and the extrapolated initial track. It allows to calculate the "integrated angle" Θ between the initial direction $\vec{L}$ and the averaged direction $\vec{L}'$. The two angles play a complementary role for the evaluation of the pointing accuracy. In case of a high energy muon and a small detector (e.g. NT-36) the muon travels most of the time outside the detector and thus ϑ limits the pointing accuracy. In case of a large detector (e.g. KM^3) and a low muon energy the angle Θ becomes more interesting. In general ϑ has a larger value than Θ.

The pointing accuracy due to recoiling effects and multiple scattering are investigated by the simulation of muons tracks through water. As an example figure 7.66 shows typical distributions of differential angle ϑ_W and the deviation D_W for $50GeV$ muons after traveling $50m$.

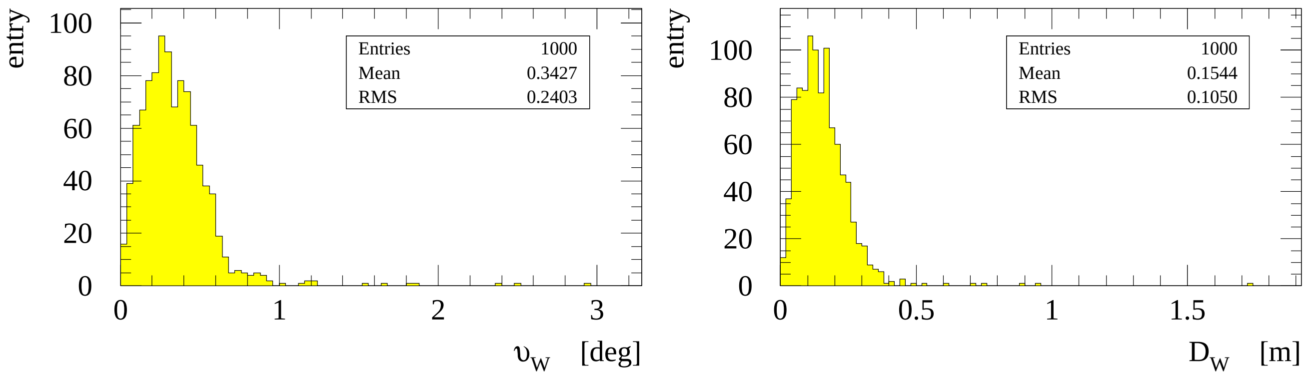

Figure 7.66: Typical distributions of ϑ_W and D_W. Shown is the simulation of muons with $50GeV$ initial energy after track-length of $50m$.

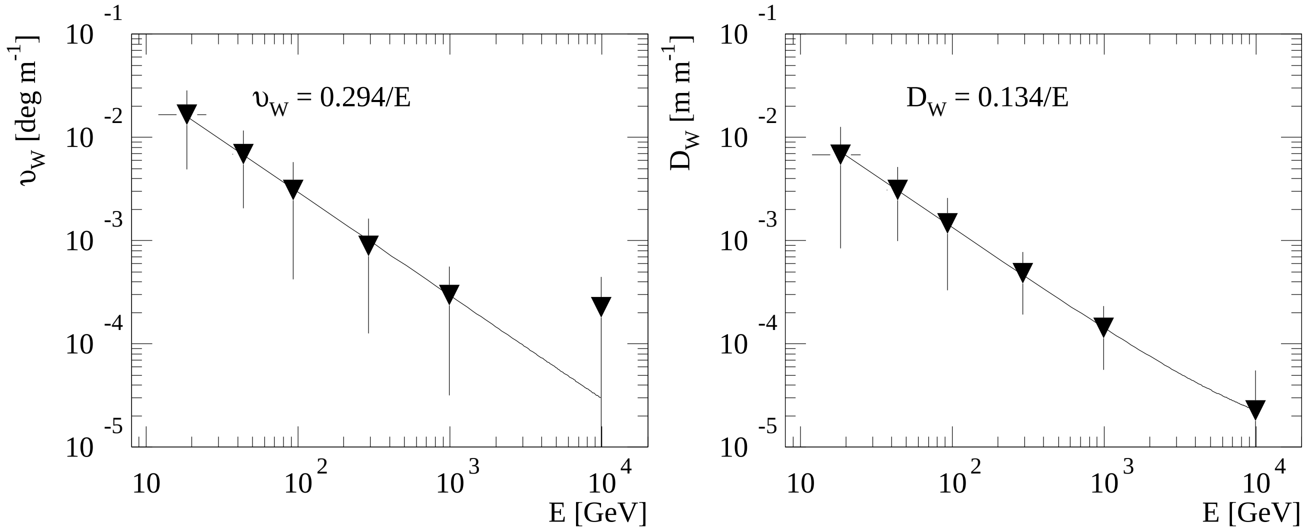

Figure 7.67: Parametrisation of the mean ϑ_W and the mean D_W versus the energy. The error bars indicate the mean deviations of the simulated distributions.

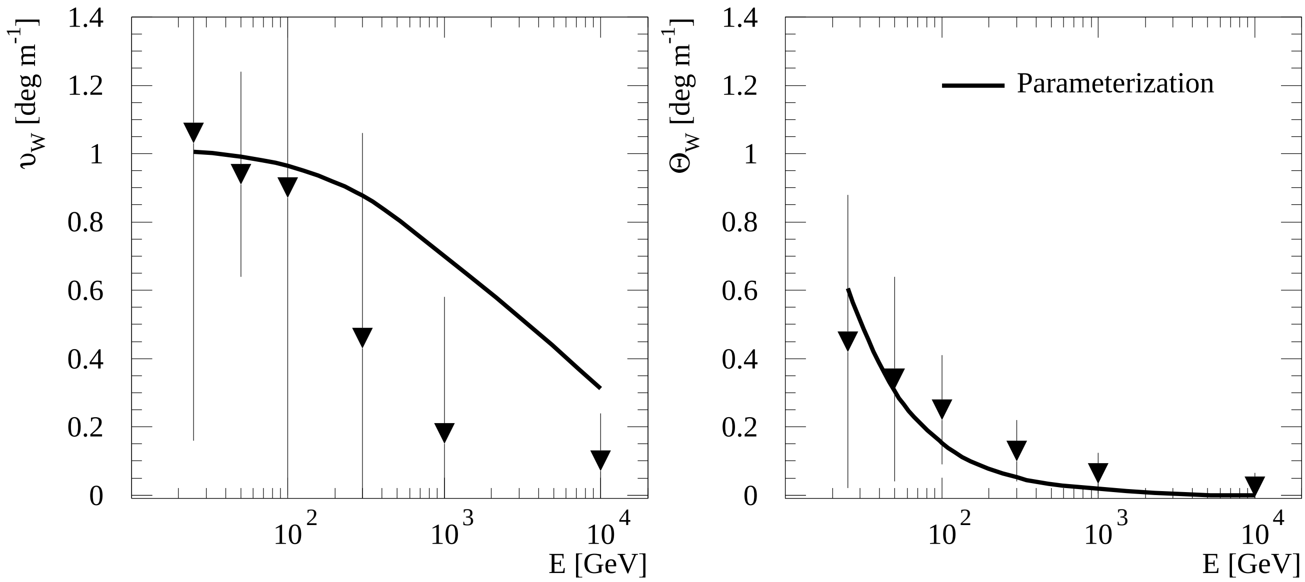

Figure 7.68: ϑ_W and Θ_W after the half mean muon range versus the initial muon energy. Plotted are also data points obtained by direct simulations.

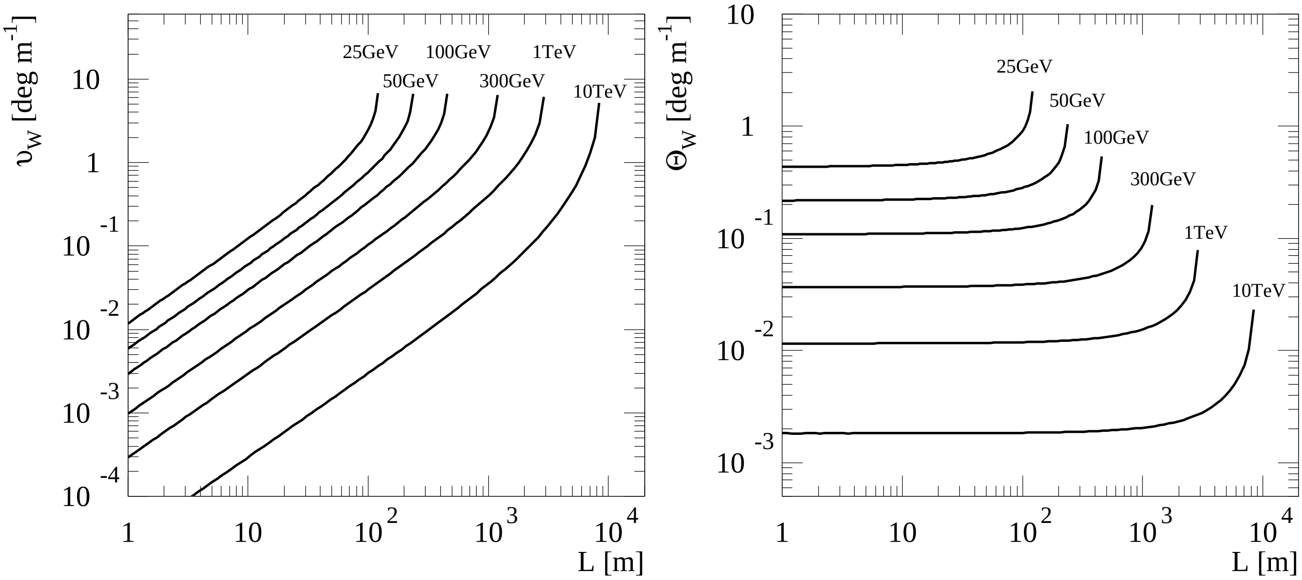

Figure 7.69: ϑ_W and Θ_W versus the muon track-length for different initial energies.

The integrated angle Θ_W is calculated from the track-length L' and the deviation D_W via

$$\cos\Theta_W = \frac{L'^2 + L^2 - d^2}{2LL'} \approx 1 - \frac{d^2}{2L'^2} \ . \tag{7.102}$$

Muons of different initial energies are simulated and tracked via a distance of $50m$. The values ϑ_W and D_W per meter track are calculated and plotted versus the average energy of the muon (the muon looses energy during the $50m$ track). Figure 7.67 shows a parameterization versus the energy using

$$\vartheta_W = \frac{\alpha_{\vartheta_W}}{E} \qquad D_W = \frac{\alpha_{D_W}}{E} \qquad . \tag{7.103}$$

In order to calculate the mean values ϑ_W and D_W for a muon traveling a certain distance one has to take it's energy loss into account. Using eq.(3.35) one gets

$$\begin{aligned} \vartheta_W(r) &= \int_0^r \frac{\alpha_{\vartheta_W}}{E(r)} dr \\ &= \frac{\alpha_{\vartheta_W}}{a} \cdot \left(\ln\left(\frac{a \cdot E_0}{exp(-b \cdot r) \cdot (E_0 + \frac{a}{b}) - \frac{a}{b}}\right) - b \cdot r \right) \end{aligned} \tag{7.104}$$

and similar for W_W. The value Θ_W is calculated via eq.(7.102).

An estimate of the typical pointing accuracy may be achieved using the half mean range $R_{1/2}$ of the muon as calculated via eq.(3.36). Figure 7.68 shows the result of the calculation. By comparison with simulated data one sees that the parameterization yields a good estimate for low energy tracks but overestimates ϑ_W and underestimates Θ_W for large energies. The differences occur due to large stochastic fluctuation especially for long track length and high energies. Also the calculation eq.(7.104) does not take into account a possible scattering of the muon into it's original direction and uses a very simple approximation of the muon energy loss. It has to be noted that muons traveling upward may also travel through rock before reaching the detector giving rise to larger scattering angles. Figure 7.69 shows the results for ϑ_W and Θ_W versus the track-length for muons of different initial energies.

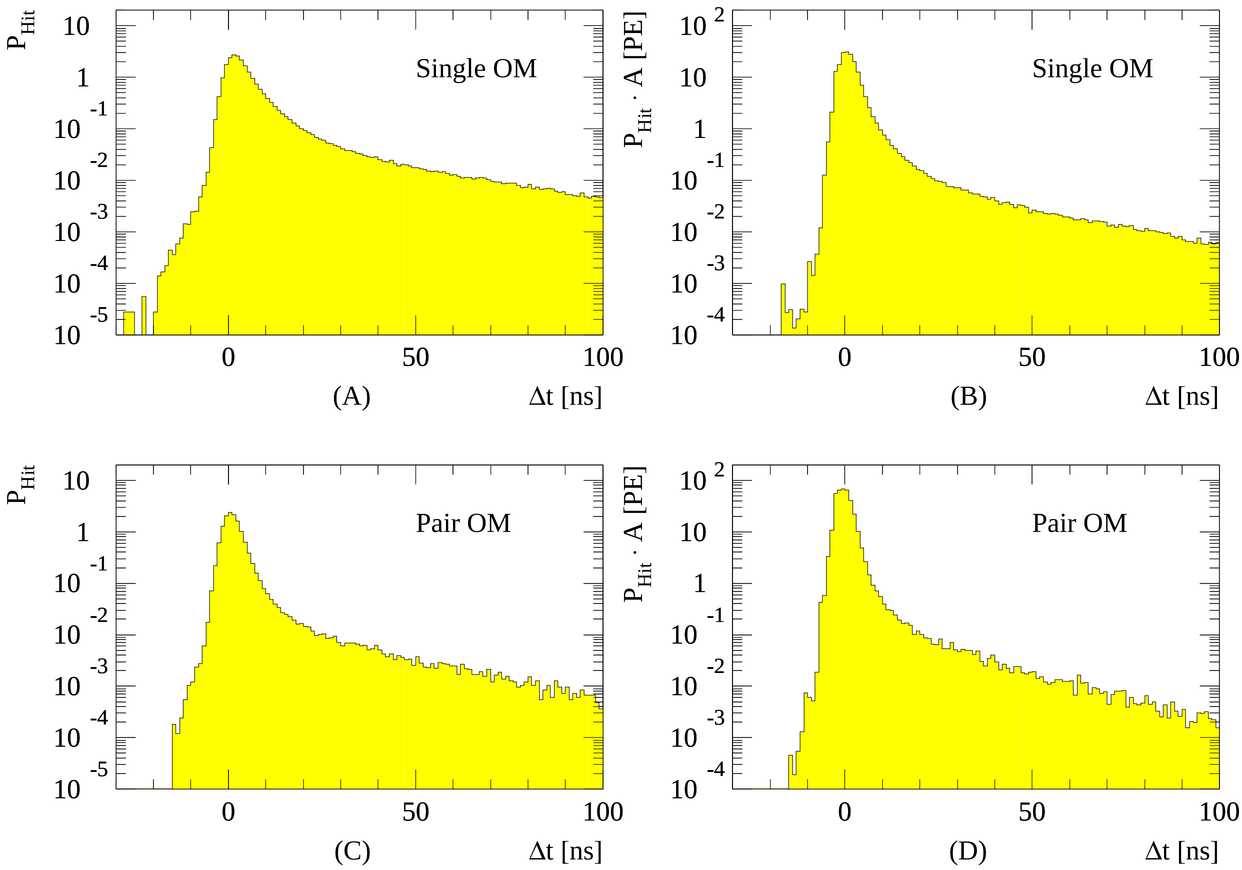

Figure 7.70: Time residuals of hits P_{Hit} and weighted with the hit amplitudes $P_{Hit} \cdot A$ for isotropic $5TeV$ up-going muons for the NT-200 detector with single and pair OMs. The trigger condition is 3 hit strings (3/3). The distributions are normalised on the number of triggered events

7.2.4 Muon detection in BAIKAL

The capability of detecting and reconstructing muon events depends critically on the sensitivity of the detector and the signal topology of the registered events. In the BAIKAL approach both quantities are strongly influenced by the local coincidence condition between two OMs. Figure 7.70 shows time residuals (eq.(7.98) for isotropically simulated up-going $5TeV$ muons in the NT-200 detector. The detector is equipped with either single OMs or pairs of OMs switched in a local coincidence at the space points. The same trigger condition (3 hit strings) is applied to both simulations. The tails in the time residuals are approximately one order of magnitude smaller in case of a local coincidence. The mean amplitude is calculated via

$$\bar{A}(t) = \frac{P_{Hit}(t) \cdot A}{P_{Hit}(t)} \ . \tag{7.105}$$

For single OMs one finds $A(0ns) \approx 11$PE, $A(20ns) \approx 1.5$PE, $A(100ns) \approx 1.2$PE, while for pairs (per OM) $A(0ns) \approx 14$PE, $A(20ns) \approx 3.3$PE, $A(100ns) \approx 2.2$PE.

The additional presence of noise requires much stronger trigger conditions for single OMs but not for pairs[4] Therefore the trigger condition for singles is raised to a typical trigger of the DUMAND experiment, but the trigger for singles remains unchanged. The simulated time residuals for $100kHz$ noise are shown in figure 7.71. The trigger efficiency for the single OM trigger condition is only 57% of the pair condi-

[4]It has to be noted that only noise hits have been simulated into muon events, but no events due to “pure” noise hits have been generated.

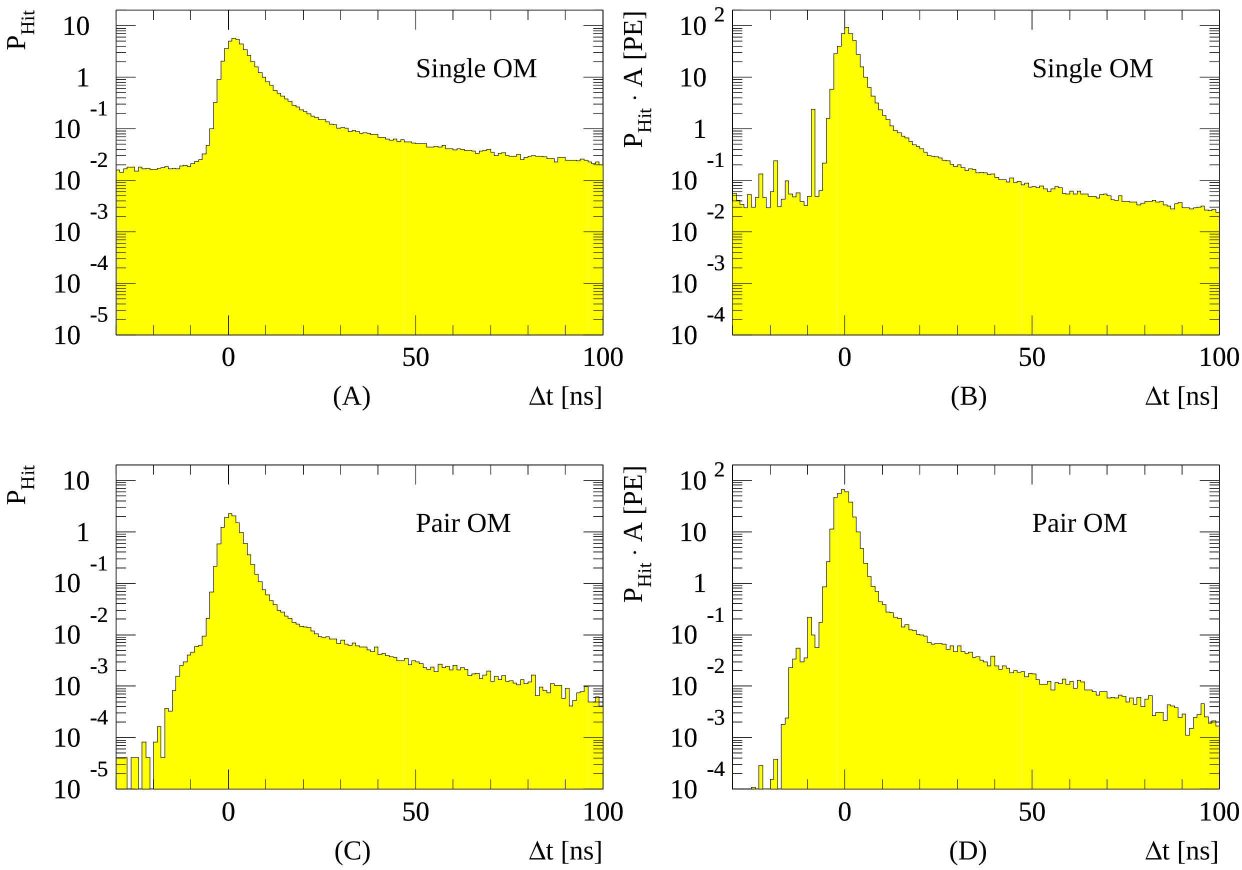

Figure 7.71: Time residuals of hits P_{Hit} and weighted with the hit amplitudes $P_{Hit} \cdot A$ under presence of $100kHz$ noise. The figure shows the same muon events as figure 7.70 but uses the trigger condition 3 hit strings (3/3) for pair OM and 3 hit neighbouring OMs in 3 strings or two times 2 hit neighbouring OMs in 3 strings ($(T-3-1-3) \vee (T-3-2-2)$, eq.(4.60)) for single OMs

tion. Even under the presence of noise the muon events with a local coincidence may be still regarded as almost "noise–free" (see also [94]). Without the coincidence condition sophisticated noise reduction algorithms would be required to enable a good reconstruction.

Figure 7.72 shows the effective area for the NT-36 (1993), NT-36 (1994), NT-72 (1995) and NT-200 detectors[5] Simulated are isotropic up-going muons without noise. Each diagram shows two graphs. The first gives the effective area for all events that passed the condition of minimum 3 hit strings and 6 hit channels. These triggered events are reconstructed with the *recoos* program. Events, which are reconstructed with a pointing-error better than 5° are selected. The second graph shows the effective area for these events. Though NT-36 (1994) has a larger geometrical volume than NT-36 (1993) it has a smaller effective area for small energies. This is due to the fact, that the spacing between channels was enlarged in 1994 to a value optimised for NT-200. The much smaller detector NT-36 does not efficiently trigger muon events of low energies. This effect was already discussed in section 4.4. The effective area for NT-200, especially for high energies, is slightly underestimated, because only muon tracks with a distance to the detector centre smaller than $45m$ have been simulated. Tracks further outside may also contribute to the effective area.
It has to be stressed, that the selection of well reconstructed tracks on basis of the information on the generated track does not represent the experimental situation. Since the original track is unknown in

[5]The detectors NT-36 (1994), NT-72 (1995) are simulated by removing not installed OMs from the events simulated with the NT-200 detector.

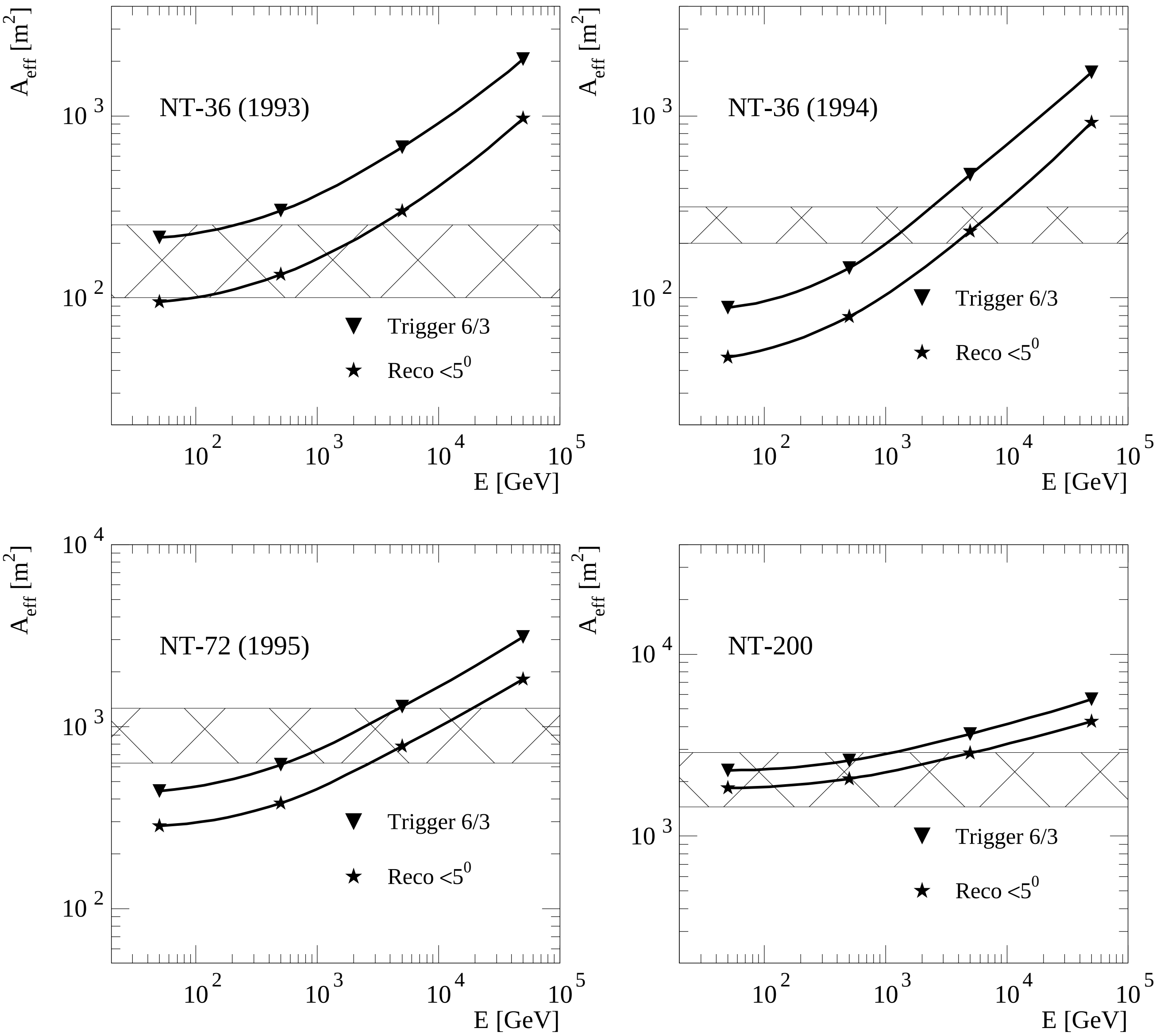

Figure 7.72: Effective area for the NT-36 (1993), NT-36 (1994), NT-72 (1995) and NT-200 detectors versus the energy of isotropic up-going muons. The hatched areas indicate the geometrical area of the detectors.

experimental data, quality cuts on the reconstruction results have to be applied. The evaluation and optimisation of cut criteria depends on the specific detector.[8, 87, 49]

8 Experimental Results

The following sections show initial data from the BAIKAL and the DUMAND II experiments. The discussion concentrates on atmospheric muons in Baikal and background noise due to ^{40}K in the ocean.

8.1 Atmospheric muons in NT-36

The detector NT-36 started operation on April 14th 1993. This section uses the calibrated data taken in the runs *d0145* and *d0196*. The data files correspond to a runtime of about $6h$ with 18 operating channels and $14h$ with 16 operating channels respectively. The detector configuration with 16 operating channels will be named NT-32 in the following. The data-files contain $205 \cdot 10^3$ and $450 \cdot 10^3$ triggered events, which are reduced to 56850 and 106174 events after application of a trigger requiring 3 hit strings and 6 hit channels.

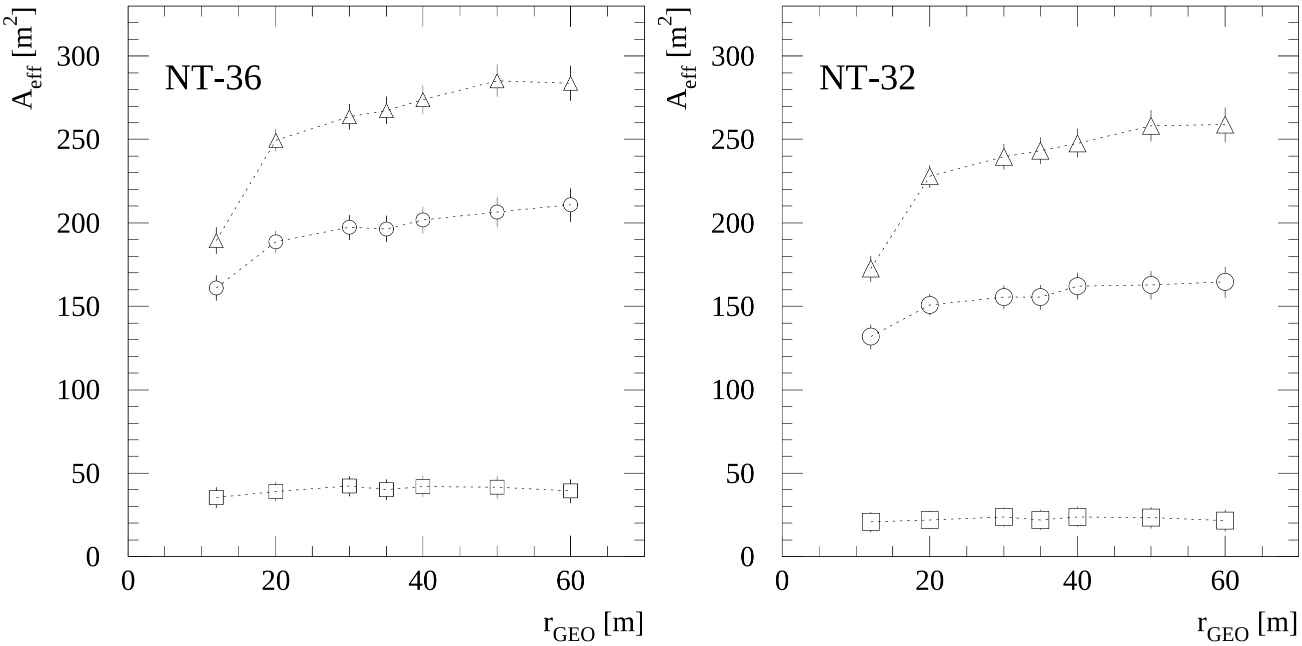

Figure 8.73: Effective area of NT-36 and NT-32 for atmospheric muons versus the radius of the geometrical simulation plane. The trigger is set to 3 hit strings (always) and 3 ($\triangle$), 6 ($\circ$), 10 ($\square$) hit channels. The error bars include an assumed systematic error of $5m^2$ and statistical errors.

In order to compare the experimental data with simulated data, atmospheric muons are generated using the *basiev* event generator program (see appendix C.2). Atmospheric muon events are generated for two depths $1070m$ and $1170m$ with a threshold of $1GeV$ and zenith angles from $0°$ to $85.5°$. The corresponding vertical energy thresholds are set to $345GeV$ and $383GeV$ for muons and to $1.04TeV$ and $1.15TeV$ for the initial proton respectively. The generated muons, which are passed to the DADA detector simulation, are simulated on a plane, whose radius is varied in different simulation runs from $12m$ to $60m$. The plane itself is at a distance of $150m$ to the detector. The radius of the plane on which the initial protons are simulated is typically $80m$ larger. The detector simulation uses spline-functions for the the sensitivity of a typical Baikal OM and standard water properties from the standard Baikal Monte Carlo program (see appendix C.1.3). After the detector simulation events are further processed: Hits with an amplitude smaller than $0.35 \cdot A(1\text{PE})$ are rejected and noise pulses ($\bar{A} = 1\text{PE}$) are simulated

into the data stream with a rate of $50kHz$ per OM. A dead time of $300ns$ is simulated[1] for each OM and the local coincidence is applied with a coincidence window of $15ns$. Events with 3 hit strings and 6 hit OMs are selected. Events for the NT-32 detector are generated by removing hits in the non operating channels 1 and 16 before the application of the above trigger conditions.
Figure 8.73 shows the effective area A_{eff}, calculated via eq.(2.19), of the NT-36 and NT-32 detector for atmospheric muons versus the radius r_{GEO} of the simulation plane for three different triggers. Below $r_{GEO} = 20m$ the effective area is drastically reduced. For a 6/3 trigger and above values of $r_{GEO} \geq 40m$ the effective area is roughly constant with a value of about $200m^2$. Noise pulses, which occur in one OM, may prevent the local coincidence to trigger within the dead-time. For a higher ($100kHz$) or a lower ($0kHz$) simulated noise rate the effective area is changed by about $10m^2$. For a threshold of $0.05 \cdot A(1\text{PE})$ in each OM the effective area rises by about $20m^2$.

A further data set (*nt36gr104*) contains atmospheric muons simulated with the standard Baikal Monte Carlo program. After application of the same trigger conditions (6/3) $1.66 \cdot 10^5$ events remain for NT-36 and $1.34 \cdot 10^5$ for NT-32. The initial muon tracks also were generated with the above *basiev* program. [49, 139]

8.1.1 Hit efficiency and channel multiplicity

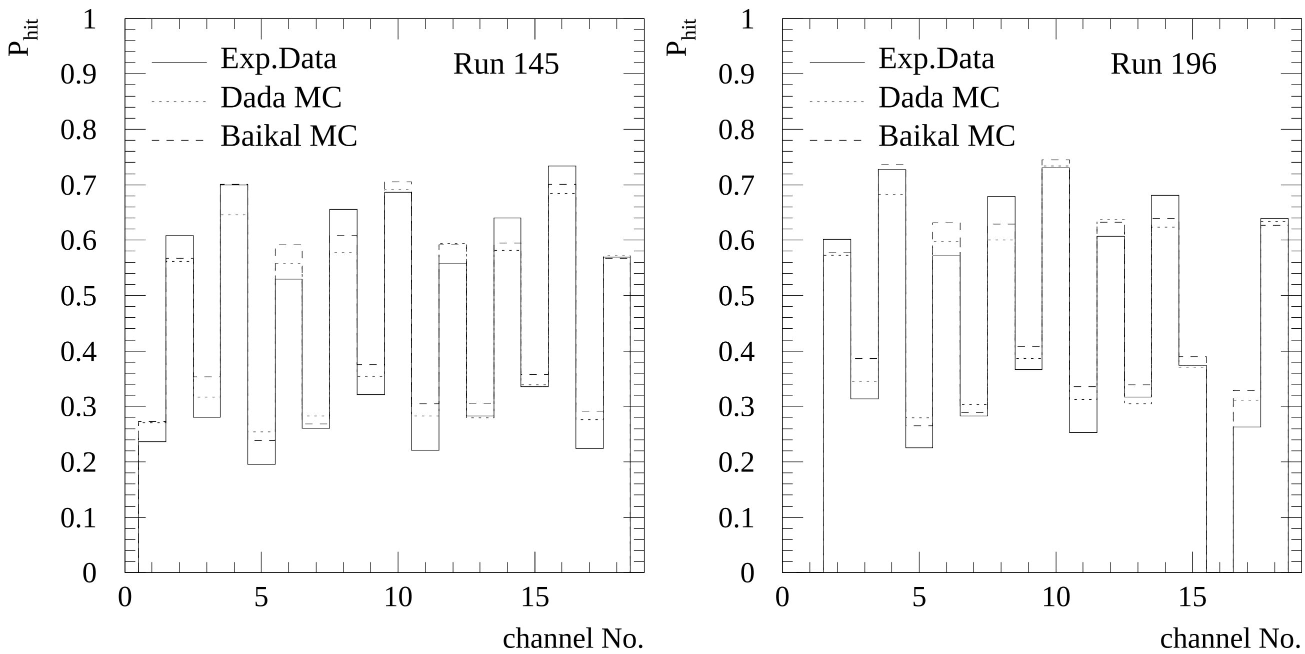

Figure 8.74: Hit probability versus the channel number for a trigger of 6 hit channels and 3 hit strings.

The total number of hits in each channel is normalized to the total number of triggered events gives the hit probability P_{hit} for each channel. Figure 8.74 shows P_{hit} for the experimental data in comparison to the Monte-Carlo result. The alternating orientation of the OMs is clearly visible by a lower hit probability for down-looking OMs. The differences between data and MC are not due to statistical fluctuations. The major contributing error results from the individual quantum efficiencies of the PMTs and the thresholds individually set in each OM during the experiment. The down-looking OMs seem to have a lower relative hit probability. A detailed analysis of the absolute hit probability showed, that the down-looking channels give correct values, but the up-looking channels show an

[1]This time is larger than the nominal value of about $130ns$. On the other hand the simulated noise rate is smaller than the typical rate of $100kHz$. Also no additional dead time for the digitisation process is simulated.

increased hit probability. [73] Comparing NT-36 and NT-32 one observes, that for the applied trigger the topology of the hit probability is only slightly changed with two not operating channels. Though the three strings are arranged in a non-symmetric triangle the Monte Carlo calculations predict almost symmetric relative hit probabilities between the strings. The differences to the experimental data indicate the maximum attainable level of accuracy in describing the data by MC-calculations.

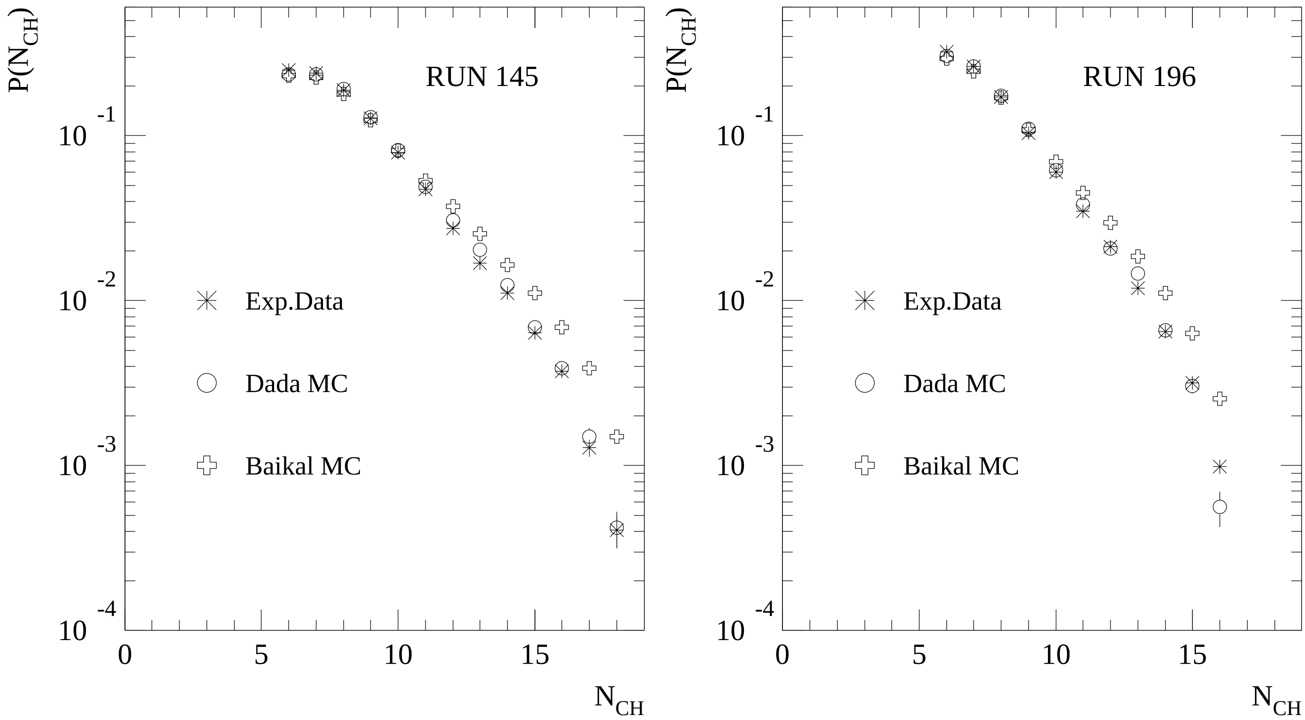

Figure 8.75: Channel multiplici ty for triggered events in NT-36 and NT-32. A general trigger requiring 3 hit strings is set. The distributions are normalised on the total number of triggered events. The data for Baikal Monte Carlo includes a simulation of measured inefficiencies of individual channels [63].

Figure 8.75 shows the distribution of the number of hit channels. The distribution is well described by the DADA program and the Baikal Monte Carlo within the experimental uncertainties due to OM parameters and water attenuation. A different simulated noise rate also changes the shape slightly. Without simulated noise the simulation yields results above the experimental results. For $100kHz$ noise the simulation results are slightly below the experimental data. The Baikal Monte Carlo produces a harder distribution. If this is attributed to incorrectly simulated water properties, a larger light output from physical processes, or more sensitive OMs, one also expects larger signal amplitudes in each channel (see chapter 8.1.2). It has to be noted that a different trigger condition or normalization also yields a good agreement of the Baikal MC with the measured multiplicities [94]. A fit to the distributions with an Exponential gives a decay constant, which agrees better than 10% between both simulations and the experimental data.

8.1.2 Signal amplitudes of individual channels

A comparison of the amplitude distributions in each channel between experimental data and simulation results shows a rough agreement for a part of the channels, e.g. #3 in figure 8.76, but a poor agreement for most channels, e.g. #6 in figure 8.76. The Baikal Monte Carlo generally produces higher signal amplitudes and yields a slightly better agreement for most channels. Several experimental distributions show an obvious shift on the x-axis. For instance the distribution for channel #6 starts approximately at 3PE instead of 1PE. Reasons for this discrepancy may be due to a wrong determined pedestal during

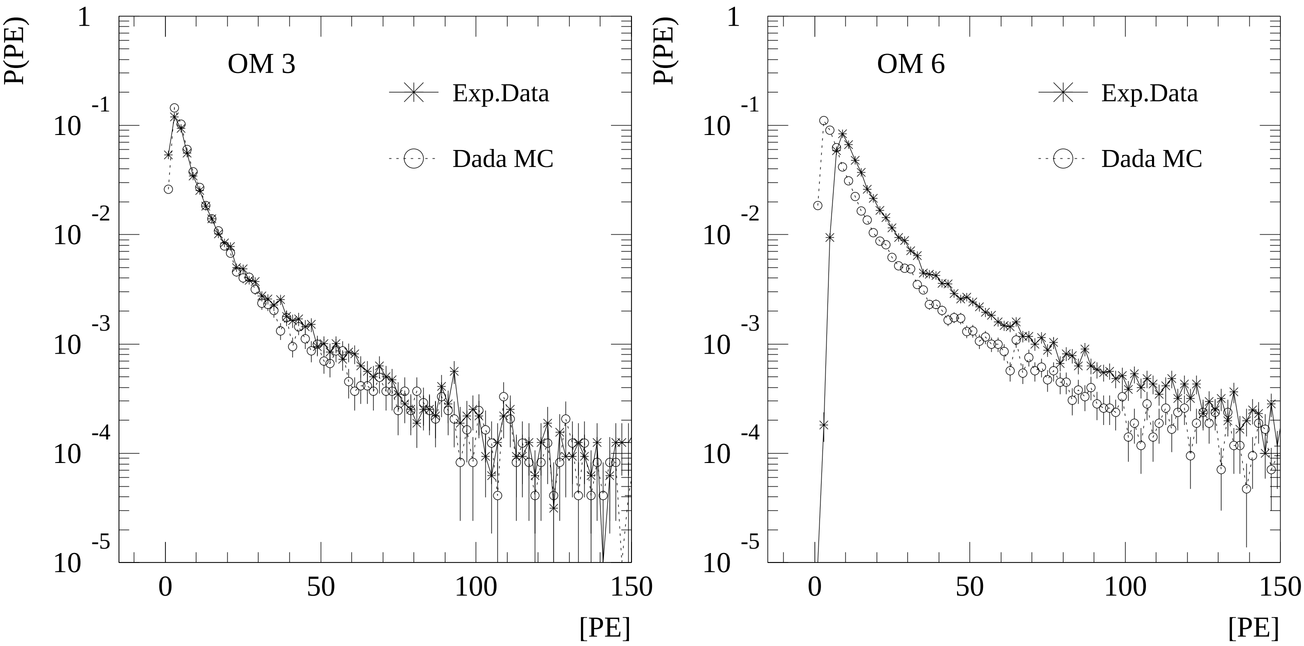

Figure 8.76: Amplitude distributions for channel #3 and #6 of string #1. The distributions are normalised on the number of hits in the OM. Each point represents a bin width of 2PE.

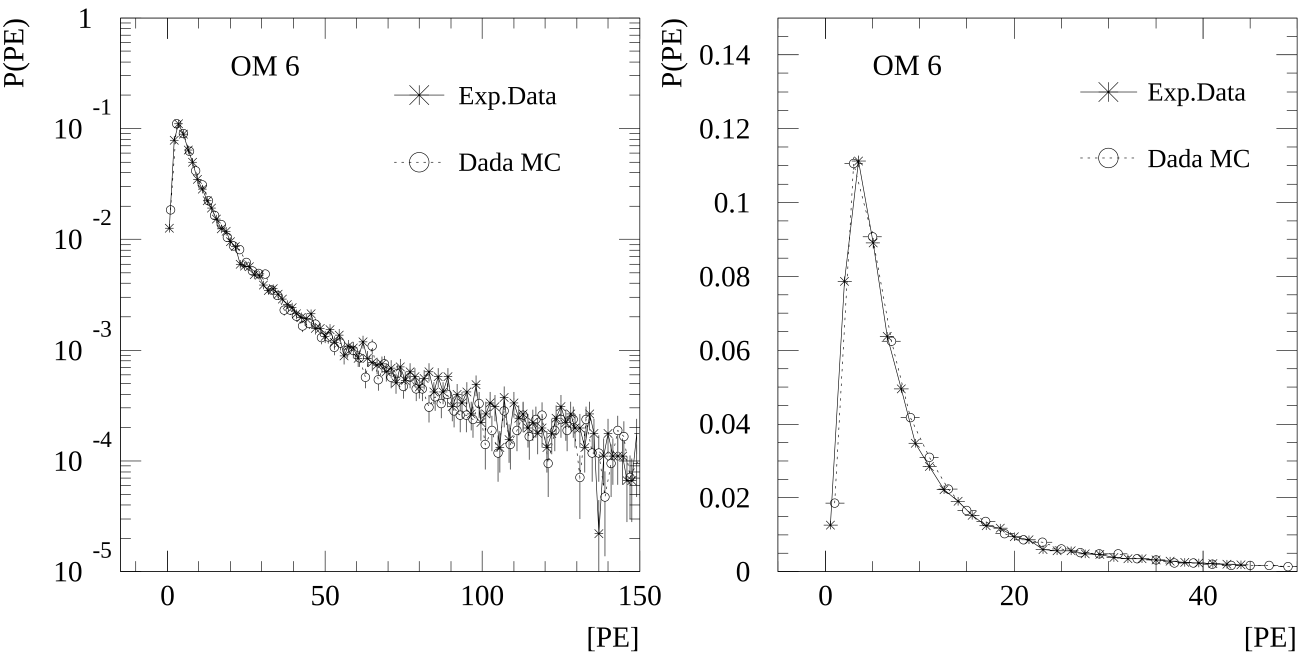

Figure 8.77: Corrected amplitude distribution of channel #6 in comparison to simulated data. The distributions are shown in a logarithmic and a linear plot. Each point represents a bin width of 2PE.

the calibration procedure (see section 4.1.3) and a different sensitivity of a specific OM compared to the simulated standard OM.

A simple correction is applied to the data. The horizontal scale is multiplied with a correction factor λ. The normalisation is changed according to the changed bin-width. The resulting distribution is moved horizontally by the shift ϵ. This achieves a good description of the shape and the pedestal of the distributions for all channels. Though the distributions are independently normalized also the absolute

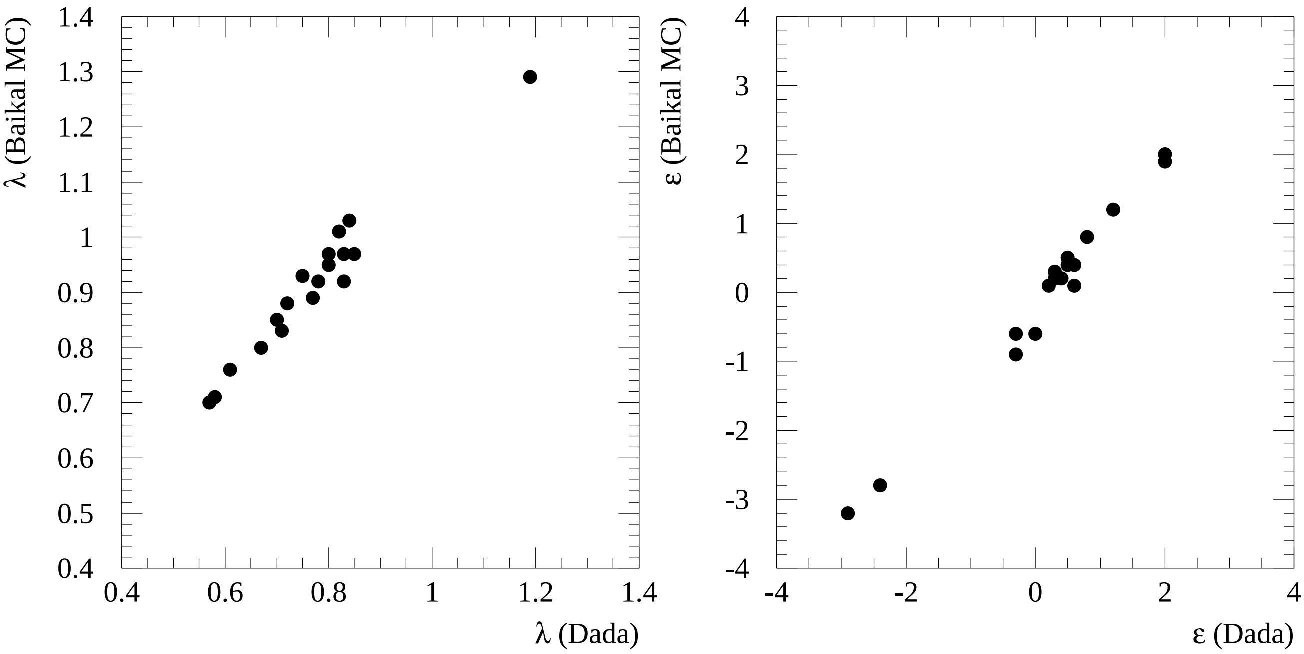

Figure 8.78: Correlation between amplitude corrections between the Baikal and DADA Monte Carlo.

	Run 145 (DADA)		Run 145 (Baikal MC)		Run 196 (DADA)	
OM	λ	ϵ [PE]	λ	ϵ [PE]	λ	ϵ [PE]
1	0.82	2.0	1.01	1.9	—	—
2	0.72	0.3	0.88	0.2	0.73	0.5
3	0.84	0.6	1.03	0.1	0.89	0.7
4	0.80	0.5	0.95	0.4	0.84	0.5
5	0.80	-0.3	0.97	-0.6	0.84	-0.3
6	0.75	-3.2	0.93	-4.4	0.78	-3.3
7	0.61	1.2	0.76	1.2	0.64	1.4
8	0.71	0.3	0.83	0.3	0.74	0.5
9	0.57	0.8	0.70	0.8	0.57	0.9
10	0.83	-2.9	0.92	-3.2	0.85	-3.0
11	0.58	0.4	0.71	0.2	0.59	0.5
12	0.85	-0.3	0.97	-0.9	0.84	-0.3
13	0.83	0.6	0.97	0.4	0.84	0.7
14	0.78	2.0	0.92	2.0	0.83	2.0
15	0.67	0.0	0.80	-0.6	0.69	-0.5
16	1.19	-2.4	1.29	-2.8	—	—
17	0.70	0.5	0.85	0.5	0.70	0.5
18	0.77	0.2	0.89	0.1	0.75	0.5

Table 8.8: Results for the correction of signal amplitudes.

vertical values are in good agreement. The result is shown for OM #6 in figure 8.77. This correction was applied to all channels for run #145 and run #196 in comparison with the DADA results and for run # 145 in comparison with the Baikal Monte Carlo. A good agreement is achieved for each channel and the correction factors are well reproduced between run #145 and #196. They are given in table 8.8.

An important aspect to identify probable errors in the simulation programs is the comparison of

corrections between DADA and the Baikal Monte Carlo. Figure 8.78 shows the correlations between the determined correction values. Both programs yield strongly correlated correction factors. Due to higher signal amplitudes of the Baikal Monte Carlo program the correlation for λ is shifted upwards.
For the interpretation of these results it is important to distinguish between ϵ and λ. Since the pedestal ϵ is barely affected by simulation parameters, it seems to indicate errors during the calibration. The scale parameter λ may be attributed to both: errors in the simulation and in the calibration. This is discussed in the following.
The simulation of physical processes in the two programs is realized in completely independent ways. Other than the DADA program, the Baikal Monte Carlo treats individual sensitivities of the OMs. Despite of this, all channels show approximately the same correlation. Large errors in the determination of the light attenuation may lead to larger or smaller signal amplitudes, but also to different hit multiplicities (figure 8.75), which agree in first for both programs and the experimental data. A comparison of the individual hit probabilities, figure 8.74, shows no correlation to the correction factors λ. This contradiction between the well reproduced hit probabilities and multiplicity compared to the poorly reproduced shapes of the amplitude distributions may indicate that mostly calibration errors are responsible for the λ correction, with an additional contribution due to the individual quantum efficiencies. At least, it is possible to adjust experimental data and Monte-Carlo results on each other.

8.1.3 Time characteristics

The time characteristics of signals from atmospheric muons are shown in figure 8.79. (A) shows the time residuals, eq.(7.98), for all hits calculated from the generated tracks. In case of multiple muons the residual is calculated for the first track in the data file. Opposite to single muons, which produce a sharp peak with a tail due to hits attributed to secondary processes (see figure 7.62), a shoulder of hits earlier than expected occurs. These hits are attributed to multiple muon events. The leading muon in a bundle is defined as the muon, which produces most hits in the detector. Additional muons may hit channels earlier than expected from the leading muon. Both Monte Carlo programs show a good agreement for the central peak and the shoulder at earlier times, but disagree for late hits. A second characteristic quantity is the reduced χ_t^2 function, calculated in eq.(C.150) and shown in (B). The χ_t^2 function calculated for the generated tracks corresponds to the maximum reconstruction accuracy achievable via a pure χ_t^2 minimisation.
In a comparison with experimental data, the true track parameters are not available. Therefore one has to use the track parameters of a reconstructed track. Due to the reconstruction method, which minimises the χ_t^2 function assuming symmetric Gaussian errors (see section C.3), the resulting time residuals become also more Gaussian (figure 8.79 (C)). The reconstructed residuals are in agreement between both Monte Carlos and the experimental data. The DADA residuals are peaked slightly stronger, which may be attributed to the different reconstruction program. For large time differences one observes a larger discrepancy between experimental data and both Monte Carlo calculations. (D) shows the reduced χ_t^2 calculated from the reconstructed tracks.

The time differences measured between two OMs is an additional experimentally accessible quantity. The time differences for selected OMs of string #2 are plotted in figure 8.80 for run #196. The measured distributions are generally met by those simulated, but especially for the first OMs in string #2 and #3 the measured distribution is wider than that simulated. The experimentally observed distributions, though statistically significant, show a shape which is not flat but shows a distinct structure. This suggests a systematic time uncertainty, which occurs during signal processing. As shown in figure8.79, the reconstruction is not strongly affected by this discrepancy.
For the interpretation of the discrepancies between the simulation and experimental data one has to consider additional effects such as scattering of light in the water, calibration errors and the time jitter

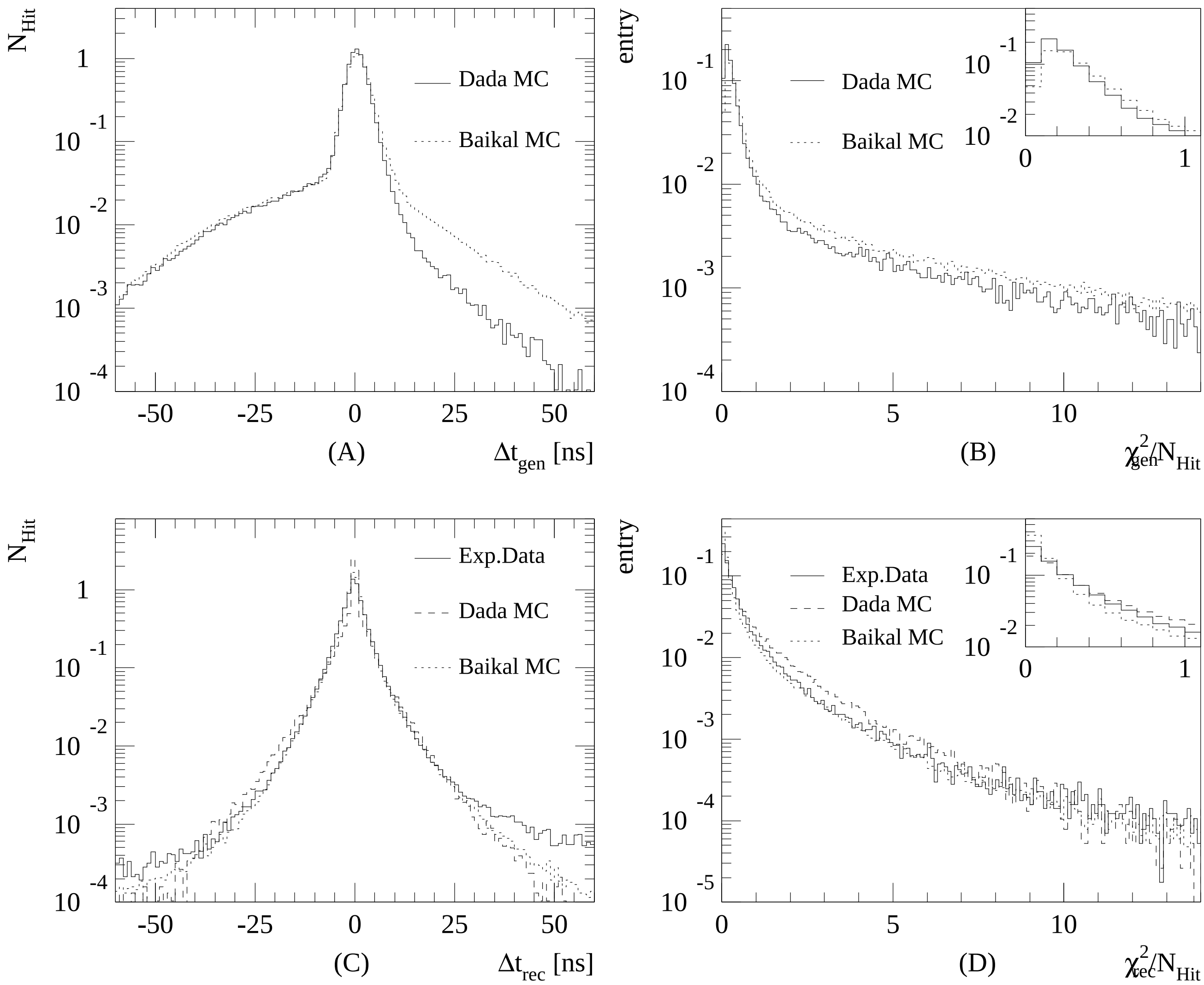

Figure 8.79: Time residuals and time-χ^2 for atmospheric muons. (A) shows the time residuals for the generated muons. (B) shows the reduced time χ^2-values for the generated muons. (C) shows the time residuals for the reconstructed tracks. (D) shows the reduced time χ^2-values for the reconstructed tracks. The distributions are normalized on the number of triggered events (6/3). The experimental data and the Baikal MC data are reconstructed with the the standard Baikal reconstruction [49]; the DADA MC data is reconstructed with the *recoos* program (see appendix C.3) No quality cuts are applied to the data and the fit results.

of the OMs.

8.1.4 Vertical muon intensity

The vertical muon intensity I_v (eq.(3.30)) can be measured using the experimental counting rates R_{Trig}, given by

$$R_{Trig} = \frac{J_2}{A_{eff,Trig}} \; , \tag{8.106}$$

The total flux J_2 is defined in eq.(3.30) and the effective area $A_{eff,Trig}$ is calculated for the angular and energy distribution of atmospheric muons with the same trigger level as the experimental data.

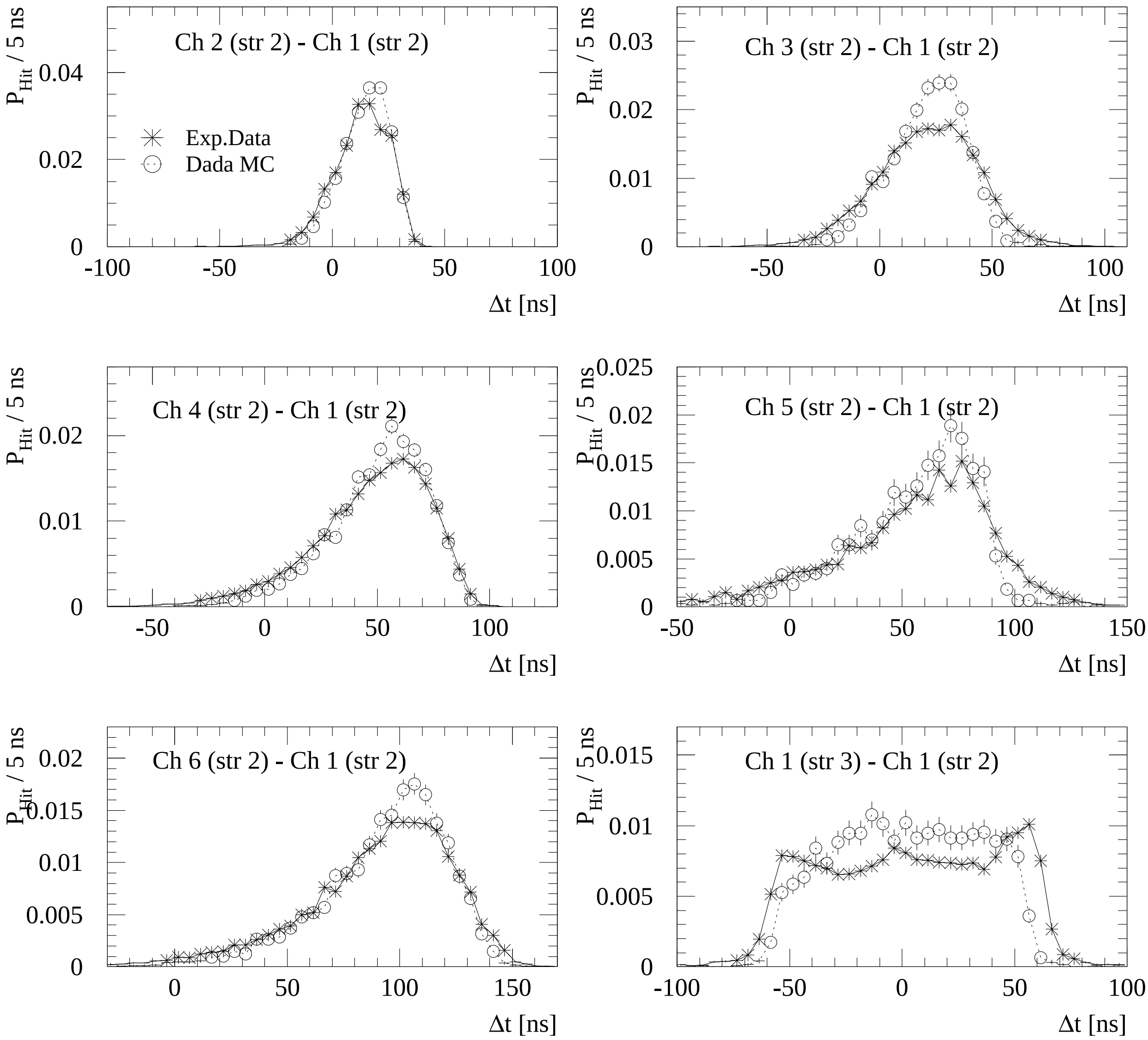

Figure 8.80: Time differences between channels along string #2 and between the first channels in string #2 and #3.

Evaluation gives

$$I_v = \frac{R_{Trig}}{2\pi A_{eff,Trig} \underbrace{\int f(\theta) \sin\theta d\theta}_{:=K_\theta}} . \tag{8.107}$$

The integral K_θ is calculated from the angular distribution of generated tracks. It's averaged value 0.304 does not change significantly for the two simulated depths $1070m$ and 1170.
The value for I_v is calculated for both detector configurations NT-36 (run 145), NT-32 (run 196) and the simulation for both depths. Figure 8.81 shows the results for different trigger levels. The results are stable and give an averaged value $I_v = 6.75 \cdot 10^{-7} cm^{-2} s^{-1} sr^{-1}$ with an estimated error of 8%, due to fluctuations in figure 8.81, systematic errors in the angular and energy distribution of atmospheric muons and the determination of A_{eff}.
Figure 8.82 shows the results in comparison with other experiments and an independent analysis of the BAIKAL experiment [9].

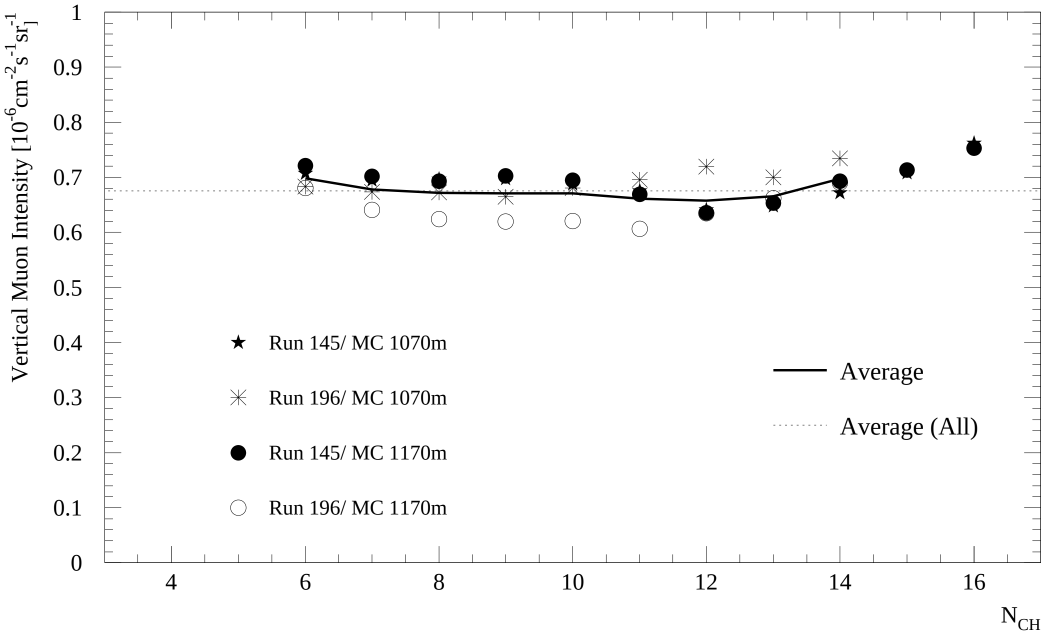

Figure 8.81: Calculation of vertical muon intensity. The calculated values are plotted for different runs and simulated depths versus the minimum required hit channels. A general trigger of 3 hit strings is set. The results are averaged.

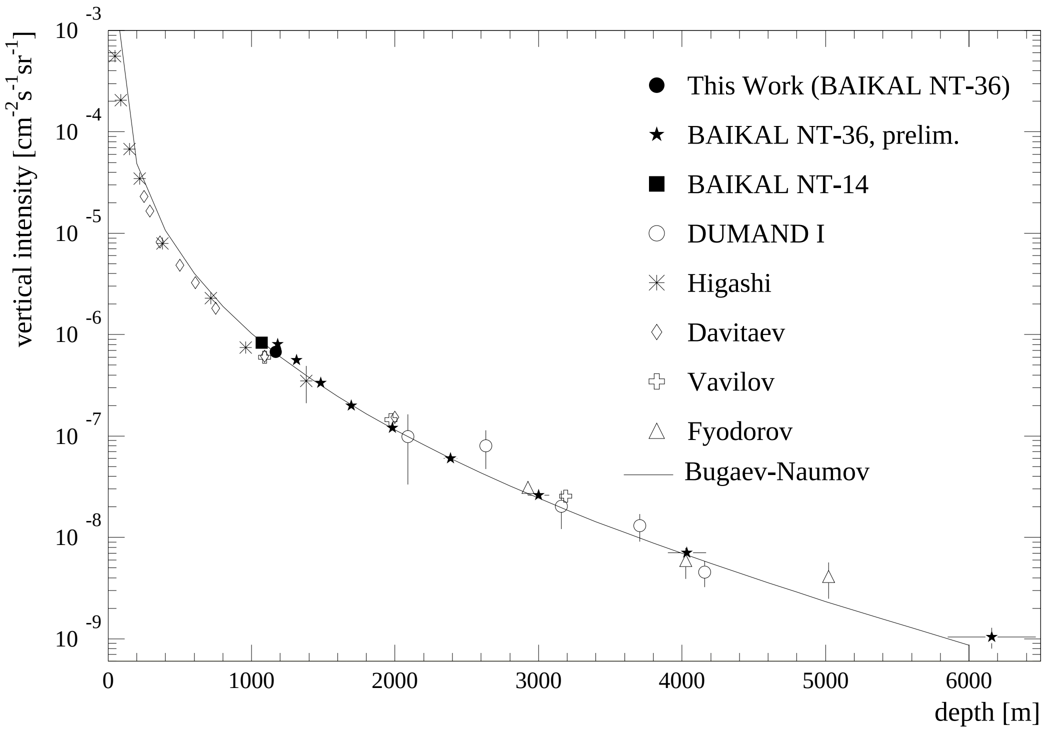

Figure 8.82: Vertical muon intensity as measured by the NT-36 experiment in comparison with other underwater experiments [5, 9, 45] (adapted from [9]). The solid line corresponds to the parameterization by Bugaev et.al.[27]

8.2 Ocean background

After the installation of the first string of DUMAND II in December 1993 the counting rate of 13 operating OMs, 12 JOM and one EOM have been measured until the string controller failed due to a water leak. The sampled counting rates approximately cover a real time of 2.7 hours (see figure 3.18). The measured counting rates are shown and their characteristics are analysed in [84]. The EOM shows a high but decreasing counting rate due to the previous exposure to intense sun-light and the recent switch on of the power-supply. Therefore it will not be regarded in the following discussions.

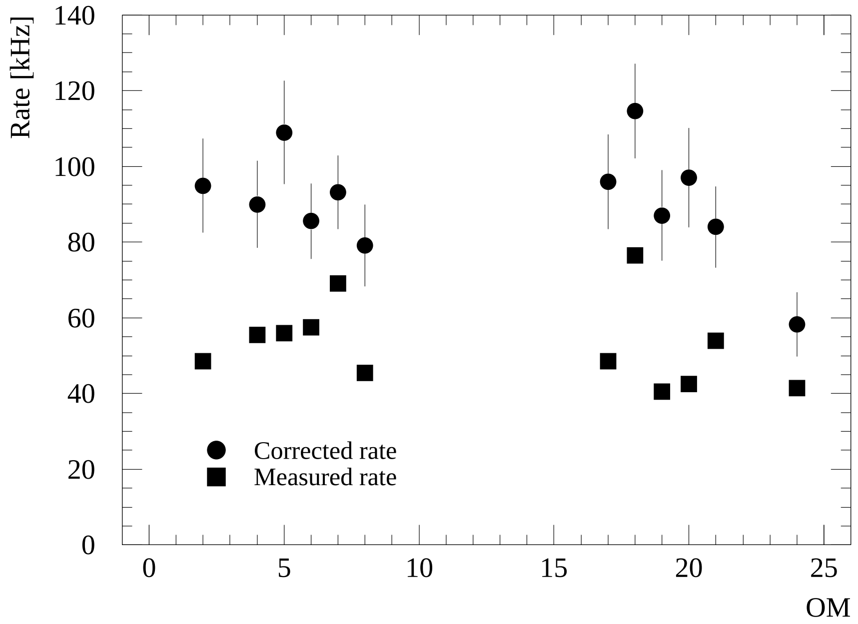

Figure 8.83: Measured and corrected count rates during the December 93 DUMAND II deployment.

The JOMs were operated with high voltage approximately $180V$ below the nominal value. Because of the smaller gain and thus reduced detection efficiency for 1PE signals, the measured ^{40}K counting rate is reduced. In order to obtain the true rate of ^{40}K signals a correction has to be applied to the measured counting rates. The following approach involves large uncertainties, and results have to be regarded with caution!

No laboratory measurements of the dark noise rate of the OMs and its 1PE detection efficiency are available for the lowered HV. The noise rate N_0 is only known for the nominal high voltage. The reduction of the detection efficiency η_{-50} was measured for a $50V$ reduced HV. The detection efficiency at the nominal operating voltage ϵ is typically 90%. The measured values for η_{-50} are between 5% and 12%. The detection efficiency is expected to decrease more strongly for a further lowered HV and is thus assumed to $\eta_{-180} \approx 4 \cdot \eta_{-50}$. The dark noise rate is expected to decrease even more and is thus assumed $\eta^{noise}_{-180} \approx 6 \cdot \eta_{-50}$. [62]

The first step is to subtract the dark noise rate of each PMT from the measured rate R_0 in the ocean. The rate $\tilde{R}$, corrected for the dark noise, is assumed

$$\tilde{R}_i \approx R_{0,i} - N_{0,i} \cdot (1 - 6 \cdot \eta_{-50,i}) \ .$$

In the next step the rates $\tilde{R}_i$ have to be corrected for the reduced detection efficiencies and the the detection efficiency at the nominal operational voltage. The true rate of ^{40}K signals R_{cor} is approximated by

$$R_{cor,i} = \frac{\tilde{R}_i}{\epsilon \cdot (1 - 4 \cdot \eta_{-50,i})} \ .$$

Figure 8.83 shows the results of the correction. Typical ^{40}K rates are of the order of $90kHz$. The errors-bars depend mainly on the systematic errors of the above assumptions. It has to be noted, that no dead time correction is applied.

Theoretical expectations are calculated according to the method described in section 3.5 and appendix C.5, using the wavelength dependent parameterization eq.(3.49) by J.Learned for the calculation of the light attenuation. ^{40}K decays in a spherical shell with the radius r around an OM contribute to the total counting rate I_{tot} with the rate $R(r)dr$. The total rate is given by $I_{tot} = I(\infty)$ with the integral count rate $I(d)$ defined as

$$I(d) = \int_0^d R(r)dr \ . \tag{8.108}$$

The simulation results for $I(d)$ are shown in figure 8.84 for different attenuation lengths and the product of the collection efficiency and peak quantum efficiency $\kappa = 0.15$.

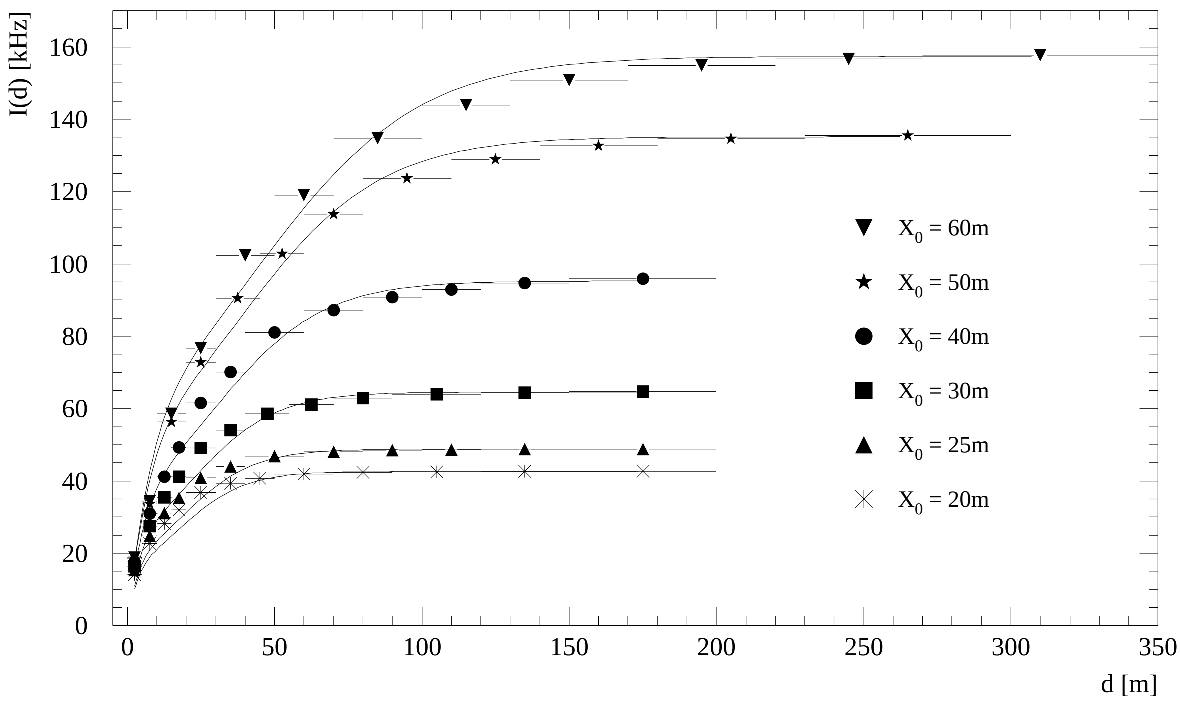

Figure 8.84: Integrated ^{40}K count-rate $I(d)$ for different attenuation lengths X_0. Simulated is a JOM using a peak quantum efficiency times collection efficiency $\kappa = 0.15$.

X_0 [m]	20.	25.	30.	40.	50.	60.
$\alpha[kHz]$	3.48	3.15	2.63	1.70	1.10	0.83
β	2.54	2.94	3.02	3.06	2.95	3.06
$I_{tot,1\mathrm{PE}}[kHz]$	40.6	48.7	64.5	95.3	135.1	157.4
$I_{tot,2\mathrm{PE}}[kHz]$	1.04	1.11	1.17	1.22	1.27	1.29
$I_{tot,3\mathrm{PE}}[kHz]$	0.36	0.38	0.39	0.40	0.41	0.41
$I_{tot,4\mathrm{PE}}[kHz]$	0.19	0.20	0.21	0.21	0.21	0.21

Table 8.9: Fit results for $I(d)$ and simulated total ^{40}K rates ($\kappa = 0.15$).

A simple function

$$R(r) = 4\pi \cdot r^2 \cdot \alpha \cdot \exp\left(-\beta \frac{r}{X_0}\right) \ , \tag{8.109}$$

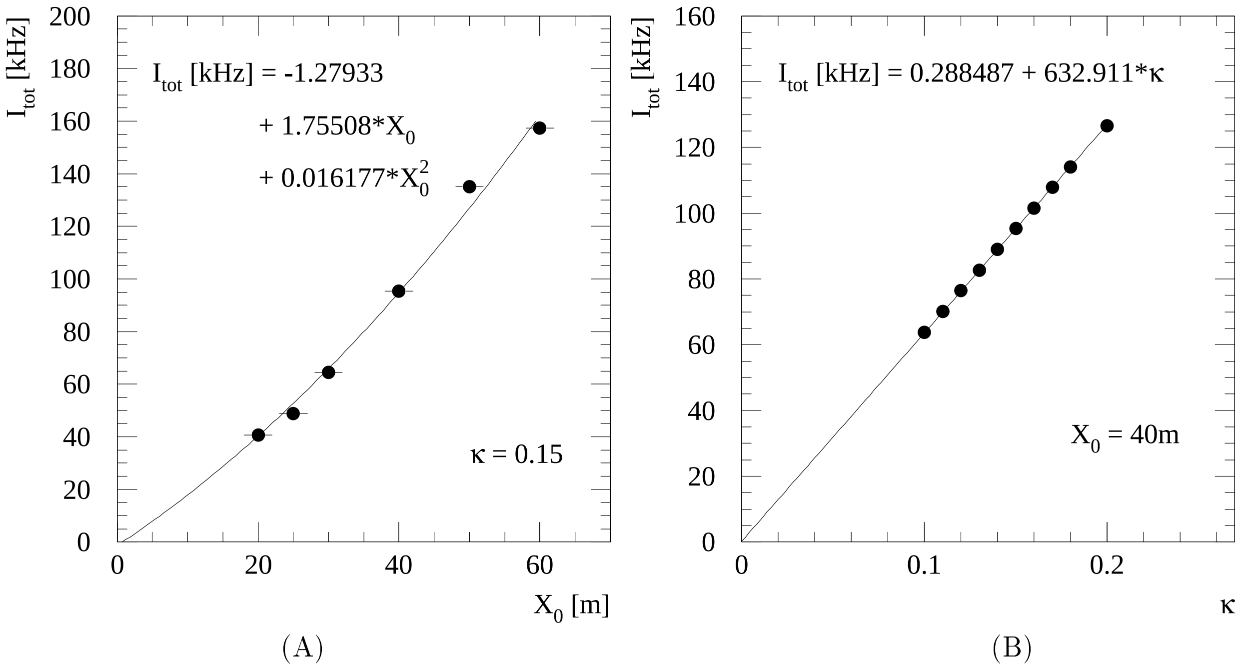

Figure 8.85: Total ^{40}K signal rate as a function of the attenuation length X_0 (A) and as a function of the quantum times collection efficiency of the photo-cathode κ (B). The values are fitted with Polynomials of 1st and 2nd order.

with the two parameters α, β and the attenuation length X_0 is assumed for a parameterization. Evaluation of eq.(8.108) yields

$$I(d) = \frac{4\pi \cdot \alpha \cdot X_0}{\beta^3} \cdot \left(2X_0^2 - (\beta^2 \cdot d^2 + 2X_0^2 + 2X_0 \cdot \beta \cdot d) \cdot \exp(-\beta \frac{d}{X_0}) \right) \ . \tag{8.110}$$

The total rate is given by

$$I_{tot} = 8\pi \cdot \alpha \cdot \left(\frac{X_0}{\beta} \right)^3 \ . \tag{8.111}$$

The function $I(d)$ is fitted to the simulated rates in figure 8.84. Table 8.9 gives the results for the fit parameters as well as the calculated total signal rate I_{tot} above $1 \dots 4$PE. The parameterization does not give an accurate description of the shape but yields good values for I_{tot}. The attenuation length strongly affects the total counting rate. It is important to note, that especially for large attenuation lengths the dominant contribution to the signal rate is due to decays far from the OM. For $X_0 = 40m$ the region $200m$ from the OM still contributes more than $1kHz$ to the total rate. This is different for larger signals. About 98.5% of signals larger 2PE originate from a distance closer than $5m$ to the OM. Figure 8.85 shows the dependence of the total ^{40}K signal rate from the sensitivity of the cathode (B) and the attenuation length (A). The dependence on the attenuation is fitted with a second order Polynomial. The dependence on κ is linear.

A comparison with the experimental rates of typically $90kHz$ gives a typical value of $\kappa = 0.14$ for $X_0 = 40m$ and $\kappa = 0.17$ for $X_0 = 30m$. Hamamatsu published a value for the peak quantum efficiency of 21% [112]. This corresponds to a collection efficiency of 67% and 80.1% averaged over the cathode area.

The ^{40}K counting rate is measured with high accuracy in a neutrino telescope under permanent operation. The attenuation length can be well measured for a known cathode sensitivity. However for an OM with good energy resolution, capable of discriminating 1PE and more PE, it is possible to estimate both: the attenuation and the cathode sensitivity. As mentioned above, the counting rate

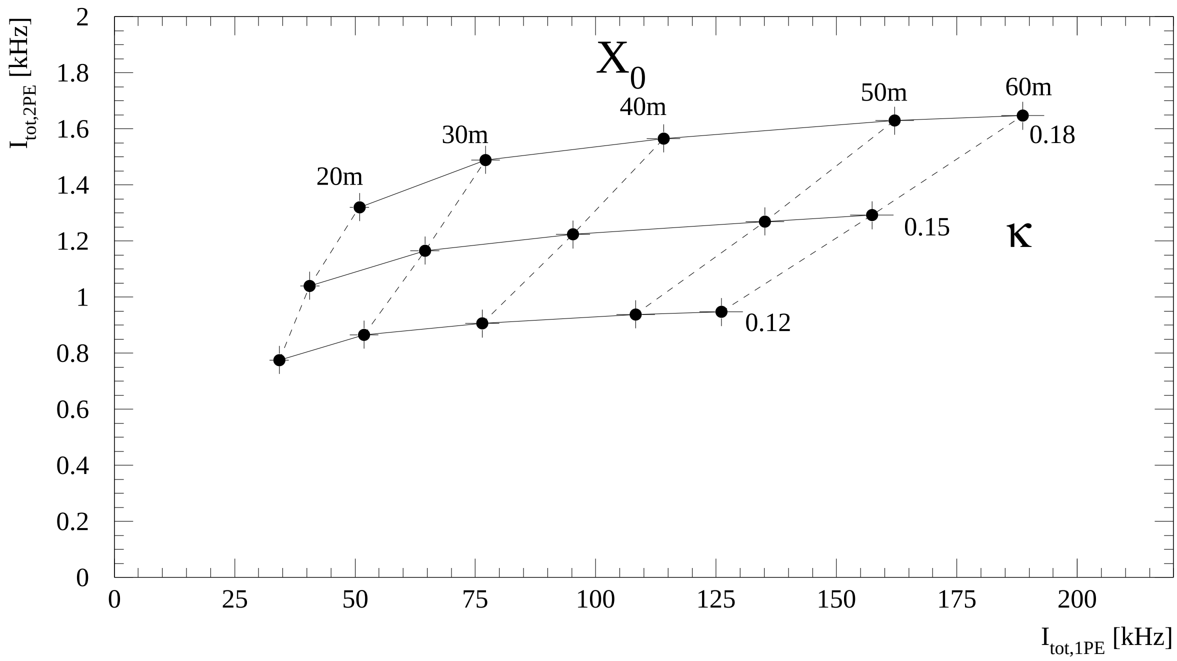

Figure 8.86: Counting rate for ^{40}K signals above a threshold of 2PE ($I_{tot,2\mathrm{PE}}$) and above 1PE ($I_{tot,1\mathrm{PE}}$) for different values the attenuation length X_0 and collection times quantum efficiency κ. Points of constant κ are connected with solid lines, points of constant X_0 with dashed lines.

above 2PE originates mainly from distances $< 5m$ and is only marginally affected by the attenuation (see table 8.9). The two measured values of ($I_{tot,1\mathrm{PE}}$) and ($I_{tot,2\mathrm{PE}}$) define a point in a two dimensional space[2], which corresponds to certain values of the attenuation length X_0 and cathode sensitivity κ. This is shown in figure 8.86.

Background to this measurement comes from the dark noise of the OM and random coincident signals of two independent ^{40}K decays. The second can be calculated from the dead-time of the OM and the absolute 1PE counting rate. In case of the dark noise the situation is more complicated and requires a good calibration of the single and multi-PE dark noise rate of the OM. The thermal emission of photoelectrons from the cathode contributes only to the 1PE rate and depends only on the temperature. Effects, such as decays of ^{40}K in the glass of the pressure housing and the PMT, provide a constant rate of additional dark noise pulses, which have often multi-PE amplitudes. A third contribution of pulses with 1PE and multi-PE energies is connected to the ionization of residual gas in the PMT by photoelectrons (after-pulses). This rate depends on the rate of all other signals.

This measurement may yield an accuracy of the order of $5m$ for the absolute value of the attenuation length X_0. For a telescope under permanent operation this method is extremely sensitive for small relative changes of the water transparency. This can be thus monitored online with high accuracy. Using additional information, e.g. from Laser calibrations, improves the accuracy of the absolute measurement.

As an application for ocean and environmental science a system consisting out of a single OM can be designed to operate remotely and to measure continuously changes of the water transparency. The EOM is capable of separating 1PE, 2PE and higher PE signals (see figures B.92,B.95). Unfortunately due to the previous exposure to sun light, the operating EOM of December 1993 still showed too high count rates during the short time of detector operation.

[2]The ^{40}K rates ($\kappa = 0.15$) are still of the order of $400Hz$ above 3PE and $200Hz$ above 4PE. These rates can be used independently or alternatively to check the results.

9 Summary and Conclusions

> Damit ist dann die Brücke vom Mikrokosmos zum Makrokosmos geschlagen. Angesichts ihrer gewaltigen Spannweite und angesichts der Winzigkeit unserer menschlichen Maßstäbe im Vergleich dazu empfindet man einen Anflug von Unwirklichkeit.
>
> *Ch.Spiering in* [133]

This work investigates fundamental aspects for the design and operation of deep underwater water Čerenkov detectors, which aim at the detection of muons induced by cosmic neutrinos. It thus covers methodical, hardware and software issues. Focus is put on the BAIKAL and the DUMAND experiments, but results may be applied to similar experiments like AMANDA , NESTOR or next generation detectors.

Two main technical developments have been achieved during this work:
First is the design, construction and calibration of an optical sensor, the "European Optical Module" (EOM), for the DUMAND II experiment.
Secondly a new detector simulation program, DADA , based on the GEANT detector simulation library was written. This program is embedded in a general modular frame for the analysis of neutrino telescope data, the SIEGMUND software.

Following items are discussed.

- A review of the production mechanisms of high energy cosmic neutrinos and a discussion of candidate objects for possible neutrino sources is given. A methodical discussion of the detection methods shows, that next generation experiments may detect a large variety of sources and thus open a new observational window to the universe. The prototype experiments currently under construction will improve upper limits on neutrino fluxes by two orders of magnitude. The experimental detection of a few neutrino sources and the measurement of diffuse extra-galactic neutrinos from the cores of active galaxies is already possible at this stage. Additional aspects such as the search for atmospheric neutrino oscillations or the annihilation of super-symmetric dark matter particles in the sun may lead to results significant to elementary particle physics and cosmology.

- Current stage experiments, especially BAIKAL and DUMAND II , are discussed with emphasis put on the general design, calibration and signal processing. It is found, that the optical properties of deep water, especially light attenuation, strongly determine the mean visual range of optical sensors and thus the detection capability and design of neutrino telescopes.

- The "European Optical Module" (EOM) is designed as a self-contained optical sensor for faint light embedded in a glass pressure housing. It is equipped with the large area photomultiplier Philips XP-2600, a fast read-out for the charge integration of photomultiplier signals and a remote computer system for the survey of the module parameters and communication to an external host. The photomultiplier is constructed according to a new technology and provides advanced characteristics for the time and energy resolution.

  The EOM was designed during this work and 12 modules have been produced. The integration of the new type photomultiplier required measurements of characteristic parameters and the development of a special charge integrating circuit "DMQT". Measurements and simulations show, that a linear "charge to time" conversion sliding over to a logarithmic dependency yields the best performance for the EOM. The properties of the produced EOMs are investigated and calibrated, covering mainly sensitivity and characteristics of the time and amplitude response. It is found, that the calibration of time and amplitude characteristics is mostly described by two analytical functions, which are fitted to the data from test measurements.

- Secondary particles from neutrino interactions, mainly muons, electrons and hadrons, lead to the emission of Čerenkov light, which is measured by optical sensors. The propagation of these particles involves several different physical energy loss mechanisms and leads to the production of further secondary particles along a muon-track, an electro-magnetic or a hadronic cascade. These secondary processes are simulated with the GEANT library and visualised. The characteristics of Čerenkov light from muons and cascades are analysed and parameterized. A transformation method, which allows the calculation of the angular distribution of the Čerenkov light from cascades from the angular distribution of tracks in the cascade, is developed. The simulation of cascades shows, that the approximation of a point-like source of light gives only a rough description of the arrival times of photons at the optical sensors in a detector.

- The application of the GEANT library to a deep underwater Čerenkov detector involves a large amount of required CPU time due to low tracking thresholds $\approx 200keV$ and an extremely large detector volume. Parameterizations for the Čerenkov light from muons and cascades are implemented in the DADA program. This drastically improves the execution speed and enables a mass production of muon events.

- Simulations of muons in the BAIKAL NT-200 detector are presented. Secondary processes occuring during muon propagation affect the amplitude and arrival time of registered Čerenkov signals as well the number of hit optical sensors. The results of the simulations show, that the dominant process producing larger signal amplitudes and hit multiplicities is connected to pair production and bremsstrahlung. These two processes also dominate the differences of the arrival time distributions of detected light signals in comparison to distributions expected from minimal ionising muons. Light due to pair-production mainly increases the signal amplitudes at the mean expected arrival time. A tail of signals arriving at later times than expected is almost entirely connected to bremsstrahlung events. The simulations with muons of different energies indicate that a separation of muons with energies above typically $1TeV$ is possible via an analysis of the hit multiplicities. An improved topological analysis of the track kinematics, signal amplitudes and hit multiplicities should give better results. The effective area for several stages of the BAIKAL experiment is calculated versus the energy of single isotropic muons.

- The maximum achievable angular resolution of a neutrino telescope is not only limited by the reconstruction accuracy but also by the pointing–accuracy of the neutrino induced muon. This accuracy is mostly limited by the deviation of the muon direction from the initial neutrino direction due to the interaction. Additional recoiling effects due to secondary processes affect the muon direction. The recoiling effects are found to produce scattering angles in the order of 0.1° to 1°, depending on the muon energy and the covered distance of the muon.

- Though the usage of two optical sensors in a local time coincidence reduces the effective detector area for triggered muon events, a less stringent detector trigger condition may be used, which again enlarges the effective area. The simulations show, that the time signature of registered Čerenkov signals is strongly improved for a local coincidence, especially under the presence of a high noise rate. This allows the usage of a more simple and less robust reconstruction method.

- A comparison of simulated atmospheric muons to experimental data from the BAIKAL NT-36 detector shows an overall good agreement. Discrepancies for the hit efficiencies, individual signal amplitudes and response times may be accounted to the neglection of individual optical sensor properties in the simulation and calibration errors of the data. The application of a plausible correction to the amplitudes in the experimental data or simulated data gives an excellent agreement.

- The BAIKAL NT-36 detector (1993) achieves an effective area for atmospheric muons of approximately $200m^2$ for 18 and $150m^2$ for 16 operating channels. The vertical muon intensity at a depth of $1100m$ is measured to $(6.75 \pm 0.54) \cdot 10^{-7} cm^{-2}\ s^{-1}\ sr^{-1}$.

- Apart of Čerenkov light from cosmic rays also ambient sources of light like bioluminescence and natural radioactivity are detected in deep underwater Čerenkov detectors. Monitoring and analysis of these light signals may provides important information on these processes such as studies on the populations of light emitting species and the long-term variations of these sources.

  A general method to calculate signal rates for uniformly distributed faint sources of light is derived. It is used for the calculation of expected signal rates due decays of ^{40}K, the dominant radioactive isotope in the ocean, as a function of the light attenuation and the sensitivity of the optical sensor.

  A comparison of experimentally measured counting rates in DUMAND is presented and gives an indirect measurement of the sensitivity of the involved optical sensors. Using an optical sensor with a good amplitude resolution allows to measure both the optical attenuation length and the sensitivity of the optical sensor by the comparison of signal counting rates of certain amplitudes. This method is extremely sensitive to changes of the attenuation and the sensitivity. It provides thus an in-situ method for on-line monitoring. Already a single optical sensor provides a self-contained detector, which may be autonomously installed at remote underwater locations to measure variations of the water transparency.

A Additional calculations

A.1 Transformation from a track to a Čerenkov light distribution

The purpose of the following calculation is the transformation from a given *angular track-length distribution* $dl/d\alpha$ into the resulting angular Čerenkov light distribution $dn/d\varphi$. The angular track length distribution is calculated during the tracking of an initial particle and its secondaries. $dl/d\alpha$ is defined as the distribution of the length of track pieces l_i with a directional angle α to the direction of the initial particle (defined as (z)-axis) (see eq.(7.89)). The idea is to summarize all fractions of Čerenkov cones, which contribute to a photon flux into the direction φ over all angles α. The geometry is sketched in figure A.87. For each direction α of a track in a shower, the Čerenkov cone is divided in fractions ds, which point into different directions φ. The angular distribution of Čerenkov photons emitted into direction φ is

$$\frac{dn}{d\varphi} = \int_0^\pi d\alpha \cdot n_\gamma \cdot \frac{dl}{d\alpha} \int_{\phi_{min}(\alpha)}^{\phi_{max}(\alpha)} d\varphi \cdot \frac{2}{S} \cdot \frac{ds(\varphi,\alpha)}{d\varphi} \ . \tag{A.112}$$

n_γ is the number of Čerenkov photons per unit track-length. S is the total length of the rim and $ds/d\vartheta$ is the fraction of the rim of the Čerenkov cone, which points into the zenithal direction φ. It is proportional to the number of photons emitted into this direction. The integration boundaries ϕ_{max} and ϕ_{min} depend on the possible directions of the Čerenkov light in respect of α.
Figure A.87 shows the geometry used to calculate $ds(\vartheta,\alpha)$ for two angles α. The length of the outer neck F is normalised to $F \equiv 1$. Thus one finds

$$S = 2 \cdot \pi \cdot \cos\Theta_c \qquad \text{with } \Theta_c : \text{Čerenkov angle} \tag{A.113}$$

and

$$\frac{2}{S} \cdot \frac{ds(\varphi,\alpha)}{d\varphi} = \frac{1}{\pi} \cdot \frac{d\Psi}{d\varphi} \ . \tag{A.114}$$

In order to calculate $\Psi(\varphi,\alpha)$ a triangle is drawn into figure A.87. The cosine–law gives

$$\cos\Psi = \frac{b^2 + c^2 - a^2}{2bc} \ . \tag{A.115}$$

From the figure one obtains

$$c = \cos\Theta_c \cdot \tan\alpha \quad , \quad b = \sin\Theta_c \quad , \quad a = \sqrt{d^2 + v^2} \ ,$$

and

$$d = \sin\varphi \quad , \quad v = |u - w| \quad , \quad u = \cos\varphi \quad , \quad w = \frac{\cos\Theta_c}{\cos\alpha} \ .$$

Evaluating the above gives

$$\cos\Psi = \frac{\cot\Theta_c}{\sin\alpha} \cdot \left(\frac{\cos\varphi}{\cos\Theta_c} - \cos\alpha\right) \ . \tag{A.116}$$

Tracks with $\alpha = 0$ emit Čerenkov light only into the direction $\vartheta = \Theta_c$. For this case eq.(A.116) diverges except for $\vartheta = \Theta_c$. If the Čerenkov cone does not hit the (z)-axis ($\alpha > \Theta_c, \alpha < \pi - \Theta_c$), the angles ϕ_{min}, ϕ_{max} are given by

$$\begin{aligned} \phi_{min} &= |\alpha - \Theta_c| \ , \\ \phi_{max} &= \alpha + \Theta_c \ . \end{aligned} \tag{A.117}$$

Except for $\alpha > (\pi - \Theta_c)$:

$$\phi_{max} = 2\pi - \alpha - \Theta_c \ .$$

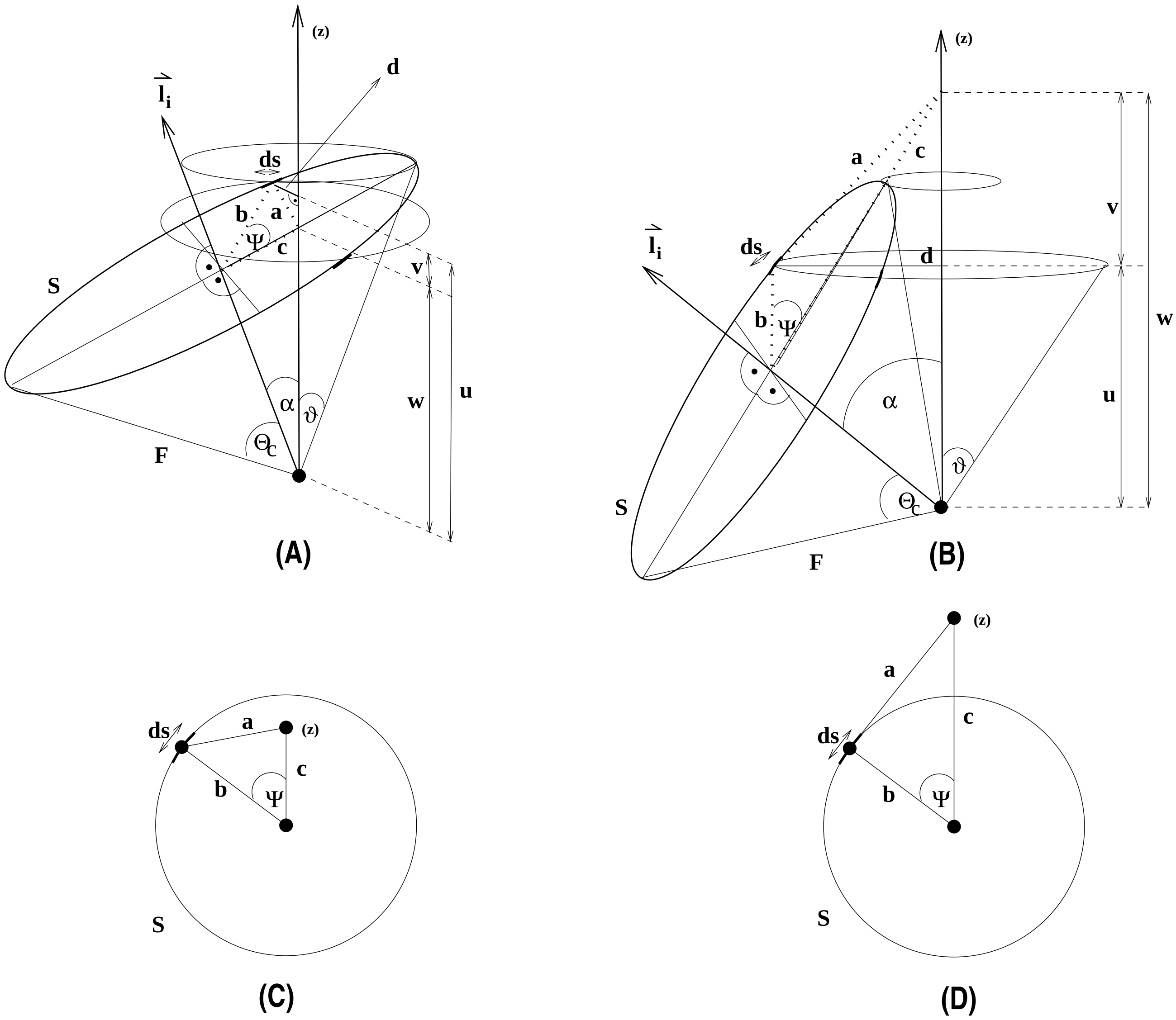

Figure A.87: Geometry used for the calculation of the effective Čerenkov light distribution (A): Geometry for a Čerenkov cone in forward direction. (B): Geometry for a Čerenkov cone distinct from the (z) axis. (C) and (D): The triangle used in the calculation projected onto the plane of the Čerenkov cone (Directions as in (A) and (B))

For a calculation with discrete values n_i one has to replace

$$\frac{dn}{d\varphi} \rightarrow \frac{n_i}{\Delta\varphi_i} = \frac{n_i \cdot K}{\pi}$$

with the total number of bins K. The calculation may be sketched as follows: The initial distribution forms a histogram with discrete values l_i, α_i. For each value i, α_i the angles ϕ_{min}, ϕ_{max} are calculated. Derived from the binning of the target histogram $dn_i/d\varphi_i$ the angles Ψ_l and Ψ_k are calculated from the upper and lower borders of each histogram bin φ_i within ϕ_{min}, ϕ_{max}. The integrand from eq.(A.112) is given by

$$\frac{2}{S}\left(\frac{\Delta s(\vartheta,\alpha)}{\Delta\vartheta}\right)_i = \frac{\Psi_l - \Psi_k}{\pi} \cdot l_i \ .$$

For a point like light source the photon flux per unit area on a sphere $dn/d\Omega$ is given by

$$\frac{dn}{d\Omega} = \frac{1}{r^2} \cdot \frac{dn}{d\phi \; d(\cos\varphi)} \;, \tag{A.118}$$

with the radius r and the azimuthal angle ϕ. Due to azimuthal symmetry one gets

$$\frac{dn}{d\Omega} = \frac{1}{2\pi r^2 \cdot \sin\varphi} \cdot \frac{dn}{d\varphi} \tag{A.119}$$

A.2 Timing and amplitude for minimal ionizing tracks

For a given locatation of an optical sensor $\overrightarrow{OM}$ and the track parameters (the vertex $\vec{V}$ (this can be any point on the trajetory) and the momentum vector $\vec{p}$) it is possible to calculate the time of a hit and the amplitude of the Čerenkov signal. The geometry is sketched in figure A.88.

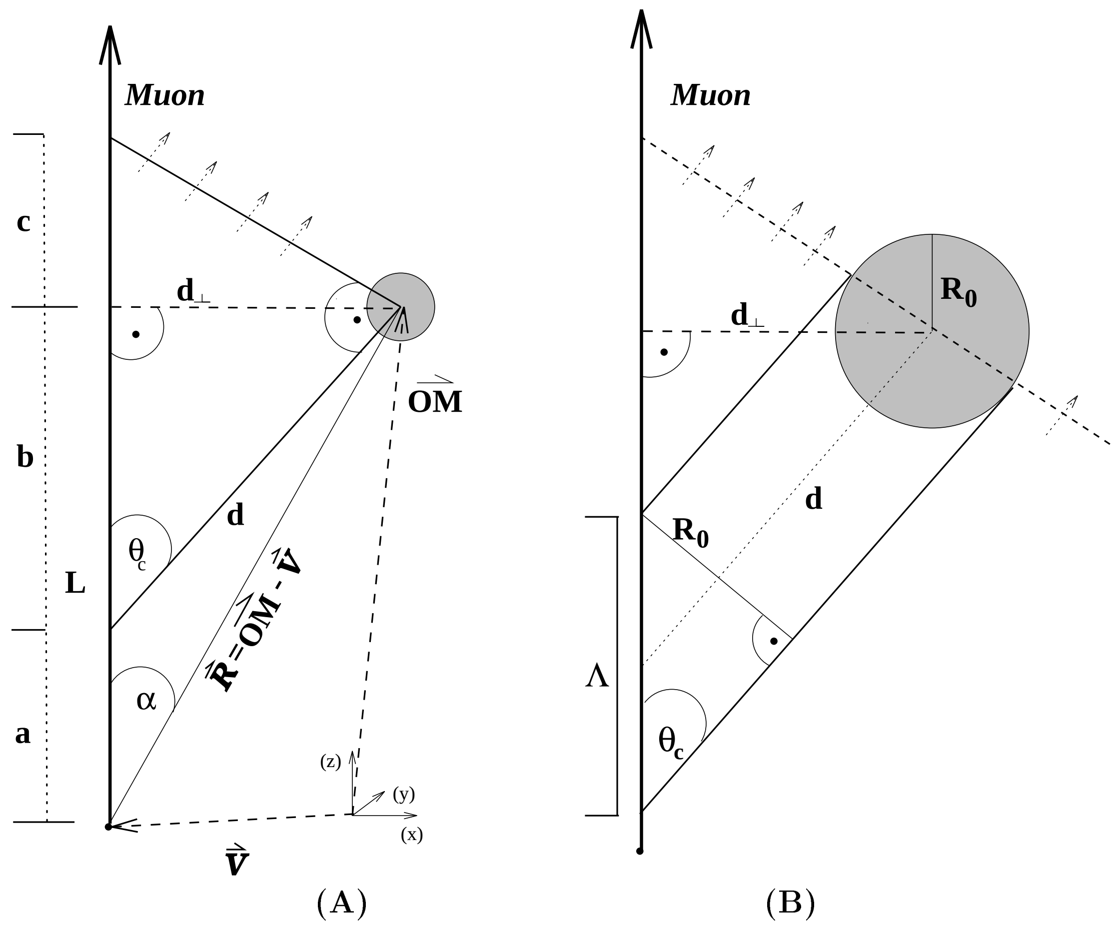

Figure A.88: Geometry for a minimal ionizing track. (A) Expected time, (B) Photon flux calculation.

Time of Hit
Using the distance $\vec{R} \equiv \overrightarrow{OM} - \vec{V}$ between the vertex $\vec{V}$ and the OM one gets the angle α

$$\cos\alpha = \frac{\vec{p}\cdot\vec{R}}{|\vec{p}|\cdot|\vec{R}|} \;. \tag{A.120}$$

The perpendicular distance of closest aproach $d_\perp$ is given by

$$d_\perp = R \cdot \sin\alpha = d \cdot \sin\Theta_c \ . \tag{A.121}$$

The time of hit, relative to the time t_0 (at the vertex) is given by

$$t - t_0 = \frac{1}{c_{vac}} \cdot (a + d \cdot n) = \frac{1}{c_{vac}} \cdot (L + c) = \frac{1}{c_{vac}} \cdot (a + b + c) \ , \tag{A.122}$$

with the index of refraction n and the speed of light c_{vac}. One finds the identities

$$a + b = L \ , \quad c = \frac{d}{\cos\Theta_c} - b \ , \quad b = d \cdot \cos\Theta_c \ , \quad d = \frac{R \cdot \sin\alpha}{\sin\Theta_c} \ , \quad L = R \cdot \cos\alpha \ .$$

Photon flux
The resulting photon density ρ_γ hitting the OM is

$$\rho_\gamma = \frac{\epsilon(d) \cdot N_\gamma}{A_{tot}} \ . \tag{A.123}$$

$\epsilon(d)$ represents the photon attenuation (see section 3.4). N_γ is the number of photons emitted from the part of track, which hits the OM. A_{tot} is the area which is populated by these photons (see also figure 3.11(B)). Therfore

$$N_\gamma = \Lambda \cdot n_\gamma \tag{A.124}$$

with n_γ the number of photons generated per unit tracklength ($n_\gamma \approx 2.2 \cdot 10^4 m^{-1}$) and

$$\Lambda = \frac{2 \cdot R_0}{\sin\Theta_c} \tag{A.125}$$

with R_0 the area of the OM. The area A_{tot} is given by

$$A_{tot} = 2\pi \cdot d \sin\Theta_c \cdot 2R_0 \ . \tag{A.126}$$

Evaluation of eq.(A.123) gives

$$\rho_\gamma(d) = \frac{\epsilon(d) \cdot n_\gamma}{2\pi \cdot d \cdot \sin^2\Theta_c} \ . \tag{A.127}$$

If the length λ of a Čerenkov radiating track is shorter than Λ the photon flux eq.(A.127) has to be multiplied with a relative tracklength $\mathcal{L}$ given by

$$\mathcal{L} = \frac{\lambda}{\Lambda} = \frac{\lambda \cdot \sin\Theta_c}{2 \cdot R_0} \ . \tag{A.128}$$

For non relativistic ($\beta < 1$) the Čerenkov photon yield becomes smaller (eq.(3.27))

$$\mathcal{L} = \frac{\lambda \cdot \sin\Theta_c}{2 \cdot R_0} \cdot \left(\frac{\sin\Theta_c}{\sin\Theta_c^0}\right)^2 \ , \tag{A.129}$$

with Θ_c^0 the Čerenkov angle for $\beta = 1$ and Θ_c calculated from eq.(3.28).

Amplitude
The mean amplitude $\bar{m}$ of an optical module is calculated from the photon flux and with projected sensor area $A_{OM}(\theta)$ and its sensitivity η

$$\bar{m}(d) = \rho_\gamma(d) \cdot A_{OM}(\theta) \cdot \eta \ . \tag{A.130}$$

In case of a photocathode the amplitude is measured in units PE; η becomes the quantum efficiency times the collection efficiency κ. The projected area of the OM is

(A.131) $$A_{OM} \equiv \pi \cdot R_0^2 \cdot \zeta(\theta) \ .$$

$\zeta(\theta)$ is the relative angular efficiency of the OM, depending on the angle θ between the incident light and the orientation of the OM. The angle θ is given by

(A.132) $$\cos\theta = -\xi \cdot \frac{\vec{d} \cdot \vec{e}_z}{d} = \begin{cases} -d_z/d & \text{for up-looking OM} \\ +d_z/d & \text{for down-looking OM} \end{cases} \ .$$

$\xi \equiv \vec{R}_0 \cdot \vec{e}_z$ defines the orientation of the OM in detector coordinates, +1 for up-looking and −1 for down-looking OM.

If the length λ of the Čerenkov radiating track is shorter than Λ the amplitude depends on the position of the photons hitting onto the surface of the sensor. The average amplitude may be approximated by (see eq.(A.129))

(A.133) $$\bar{m} \approx \rho_\gamma \cdot A_{OM} \cdot \eta \cdot \mathcal{L} \ .$$

A.3 Time and amplitude for spherical and plane waves

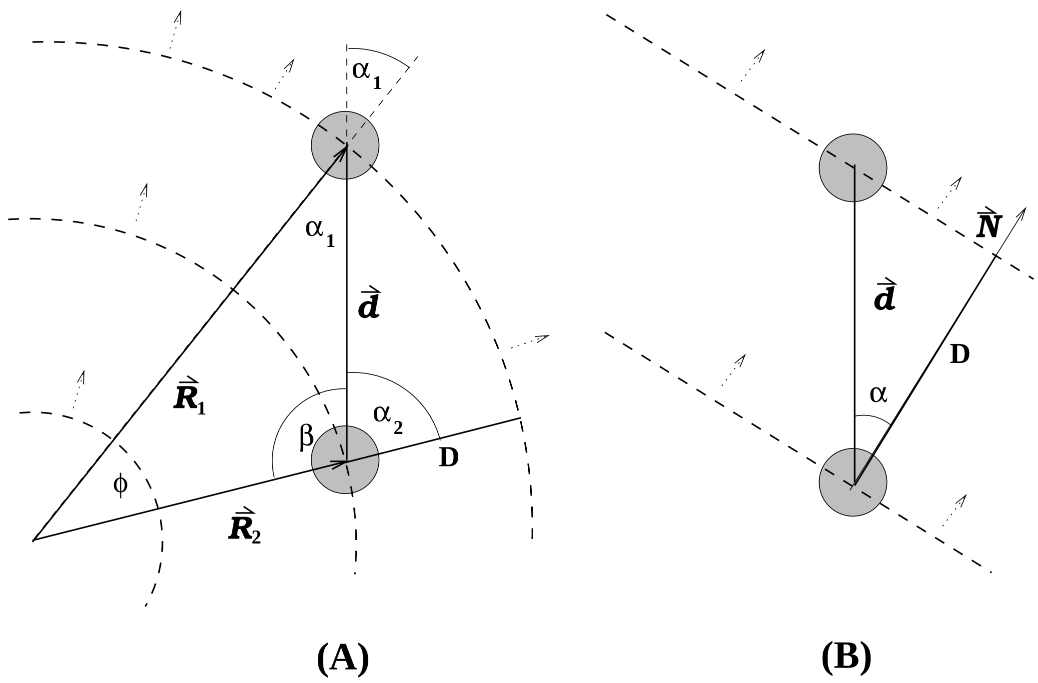

Figure A.89: Geometry for a spherical (A) and a plane wave (B).

The spherical geometry is an important case for point-like sources of light (see figure A.89 (A)).
The time of arrival at each optical module OM_i is given by

(A.134) $$t_i = \frac{|\vec{R}_i| \cdot n}{c_{vac}}$$

relative to the initial time at the vertex. The time difference between two OMs is given by

(A.135) $$\Delta t = \frac{D \cdot n}{c_{vac}} \ ,$$

with

$$D = |\vec{R}_1| - |\vec{R}_2| \ . \tag{A.136}$$

To express the distance D via the two polar angles α_1, α_2 one may use the sine-law

$$R_1 = d \cdot \frac{\sin\beta}{\sin\phi} \qquad R_2 = d \cdot \frac{\sin\alpha_2}{\sin\phi} \tag{A.137}$$

Evaluating the angles β, ϕ in α_1 and α_2 gives

$$D = d \cdot \frac{\sin\alpha_1 - \sin\alpha_2}{\sin(\alpha_1-\alpha_2)} = d \cdot 2 \cdot \cos\frac{\alpha_1+\alpha_2}{2} \cdot \frac{\sin\frac{\alpha_1-\alpha_2}{2}}{\sin(\alpha_1-\alpha_2)} \ . \tag{A.138}$$

The plane wave (figure A.89 (B)) is the special case of a spherical wave, when the light source is located at infinite distance or $\alpha_1 = \alpha_2 = \alpha$. Using the normal vector $\vec{N}$ of the plane one gets

$$\Delta t = \frac{\vec{N} \cdot \vec{d}}{d} \cdot \frac{n}{c_{vac}} = \cos\alpha \cdot \frac{n}{d \cdot c_{vac}} \ . \tag{A.139}$$

The photon flux ρ_γ for a point-source at the distance r and the angle ϕ is given by

$$\rho_\gamma(r,\phi) = \frac{4\pi}{r^2} \cdot \epsilon(r) \cdot I(\phi) \ . \tag{A.140}$$

$\epsilon(r)$ is the attenuation and $I(\phi)$ the relative angular intensity of the light emission. $\int_{-1}^{+1} I(\phi) \sin\phi \ d\phi$ is normalised to 2. One may define the relative track-length $\mathcal{L}$ representing the relative number of minimal ionising tracks producing the same amount of light at the distance r (see appendix A.2)

$$\mathcal{L} = \frac{2 \cdot \pi \cdot \sin^2\Theta_c}{n_\gamma \cdot r} \cdot \frac{\rho_\gamma(1,\phi)}{\epsilon(1)} \ . \tag{A.141}$$

A.4 The cumulative Poisson probability

Several calculations require the space integration of a function P, which gives the probability to produce a signal above an amplitude A. Assuming a Poisson-like probability for a signal with a mean amplitude $\bar{m}$ the cumulative Poisson probability to produce a signal above the amplitude A is

$$P_{\bar{m}}(>A) = \sum_{i=A}^{\infty} \frac{\bar{m}^i \cdot e^{-\bar{m}}}{i} = \mathcal{G}(\bar{m}, A) \ , \tag{A.142}$$

with the *Incomplete Gamma-function* $\mathcal{G}$. The Incomplete Gamma-function is defined by

$$\mathcal{G}(\bar{m}, A) \equiv \frac{1}{\Gamma(A)} \int_0^{\bar{m}} e^{-t} \cdot t^{A-1} \cdot dt \quad (A > 0) \ , \tag{A.143}$$

with the gamma function

$$\Gamma(A) = \int_0^\infty t^{A-1} \cdot e^{-t} \cdot dt$$

[158].

B EOM test and calibration measurements

During the construction phase of the EOMs a larger sample[1] of Philips XP2600 PMTs have been tested. Table B.10 gives a summary of the measured PMTs. Serial numbers below 26 have been produced in Eindhoven (Netherlands), the rest in Brive (France).

Number	Remarks
# 11	EOM delivered 1993.
# 12	EOM delivered 1993.
# 16	EOM delivered 1993. JULIA OM.
# 26	EOM delivered 1993, lost Dec.1993. (JULIA OM)
# 27	PMT accidently damaged during assembly. (JULIA OM)
# 33	EOM delivered 1993, (EOM prototype Jan.1992).
# 35	EOM delivered 1993, lost Aug.1993.
# 42	EOM delivered 1994 (1 year operation in Lake Baikal, 1992).
# 44	EOM delivered 1993.
# 46	EOM delivered 1993.
# 52	EOM delivered 1993, lost Sep.1993.
# 53	EOM delivered 1993.

Table B.10: List of measured photomultipliers XP2600

B.1 Point sensitivity

The relative sensitivity of 12 photomultipliers has been measured with a blue LED directly attached to the surface. The measurement was done for 49 measurement points, spread in a grid, approximately 22.5° distant from each other. Each measurement point represents the same cathode area. In order to achieve this, two zenith angles θ_x, θ_y, which represent a Cartesian grid on the spherical PMT surface, were defined. Each point was measured twice with opposite directions in respect to the magnetic field. Both measurements are combined by calculation of the average and difference values. No measurements were done with zenith angles larger than 90°. The LED was adjusted to a high intensity $\approx$ 10PE, for which the PMT still works linearly. Energy distributions have been measured with a charge sensitive ADC (LeCroy 2249A). The mean of the energy distribution minus the pedestal of the ADC is proportional to the sensitivity. The sensitivity of the central point ($\theta_x = \theta_y = 0°$) was normalised to 1.0. Several control measurements of the ADC pedestal and the sensitivity of the central reference point are done in order to check the stability of the measurement.

Figures B.90 and B.91 show the result of the measurements, plotted as contour levels of the relative sensitivity. Different shades correspond to a change of 20%. The exact location of each measure point is indicated by a (•). Since no measurement has been done for a zenith angle larger than 90° the corresponding sensitivity is set to to 0.0. Earlier measurements showed that the sensitive area extends to more than 120°. [23]

Except for PMT # 11 all photomultipliers show a high sensitivity up to $\theta_{x,y} = 90°$, which is usually uniform. Good are #19, #33 and # 52. Two photomultiplier (# 35, # 53) show a 20% decreased sensitivity on one side. These PMTs also show a weak dependency on the earth magnetic field in the order of $\approx$ 10% visible by the difference of the two measurements at each point.

[1] Three additional testet PMTs are not considered in this discussion, #17 did not fit into the glass housing, #20 showed a too high noise rate and a ghost peak at high PE energies, #38 had larger insensitive cathode areas.

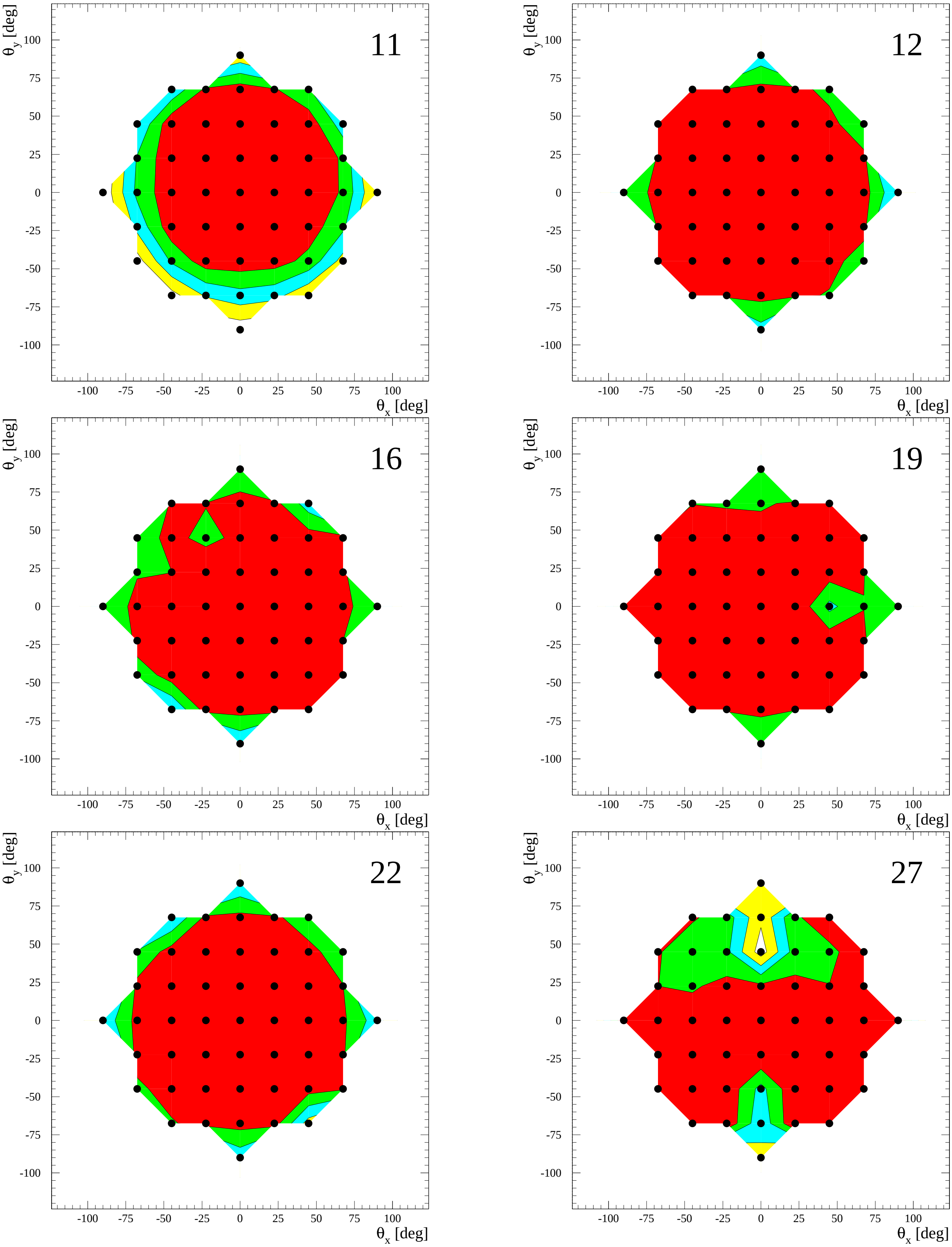

Figure B.90: Relative sensitivity for point illumination.

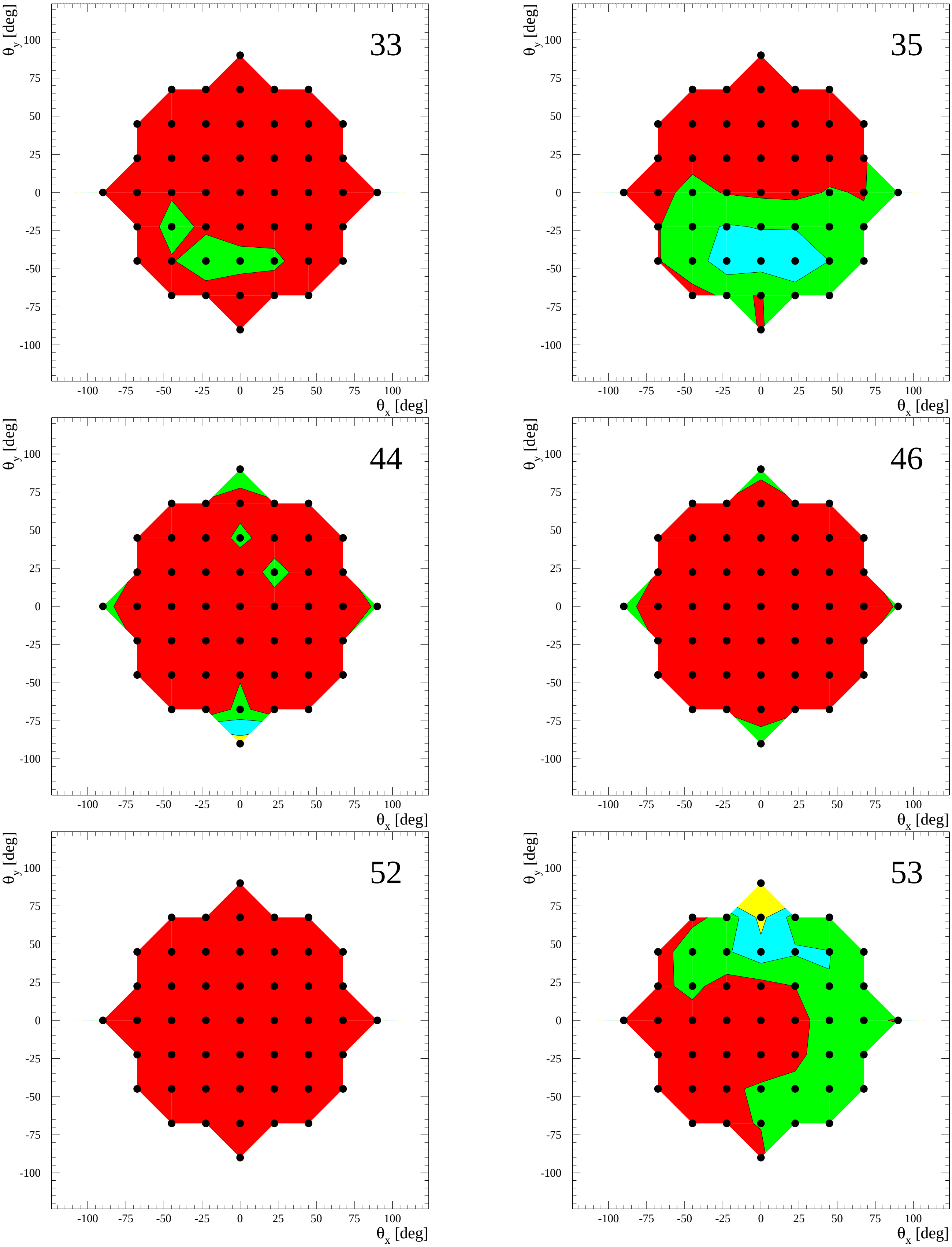

Figure B.91: Relative sensitivity for point illumination.

Some PMTs show a dip at certain points (e.g. #19, #27, #44 and #53). It was discovered after the measurement, that these points agree with the small contact stripes, which supply the cathode with the high voltage.
If one summarises the relative sensitivities over all points

$$\bar{S} = \frac{\sum_{i=1}^{49} S_i}{49} , \tag{B.144}$$

one gets a characteristic quantity for the effective sensitive cathode area relative to the absolute sensitivity of the centre point. The results are summarised in the table B.11.

#	11	12	16	19	22	27	33	35	44	46	52	53
$\bar{S}$[%]	72.3	87.1	84.3	100.6	83.4	88.9	104.0	95.7	99.0	92.4	91.1	78.5

Table B.11: Effective sensitive cathode area, relative to the absolute sensitivity of the cathode centre.

In a separate measurement the LED was switched to a low intensity and distributions of the integrated charge have been measured for different zenith angles. Examination of the position of the 1PE peak yields an estimation of the stability of the gain for different zenith angles. The position of this peak was found to be constant except for PMT #35 and #53, which show a shift of about 10% for certain zenith angles.

B.2 Amplitude and time response

Figure B.92 shows energy distributions of EOM #19 for different light intensities. The relative height of the contributions from different photoelectrons changes according to a Poisson distribution. The "amplitude function", eq.(5.76), is fitted to the distributions. It shows a good description of the linear, but gives only a rough estimate of the logarithmic region of the read-out. The fit parameter n_{log} is not constant for very high intensities.

EOM No: #	x_1 [ns]	σ_1 [ns]	c_1 [ns]	c_0 [ns]	n_{log} [PE]	x_{log} [ns]	$\Delta E/E$ (FWHM) [%]
11	189	26	86	103	2	276	70
12	203	38	160	43	4.7	795	56
16	170	49	98	72	5.2	582	72
19	220	49	190	30	3.0	600	60
22	217	54	195	22	2.8	566	65
26	223	50	181	42	2.6	512	65
33	219	44	184	35	4.5	863	56
42	235	34	200	59	3.3	692	70
44	168	31	122	46	4.8	627	59
46	222	41	170	52	8	1412	57
52	220	60	210	10	6	1270	67
53	250	49	205	45	2.9	640	56

Table B.12: Results of the EOM energy calibration with the "amplitude function.

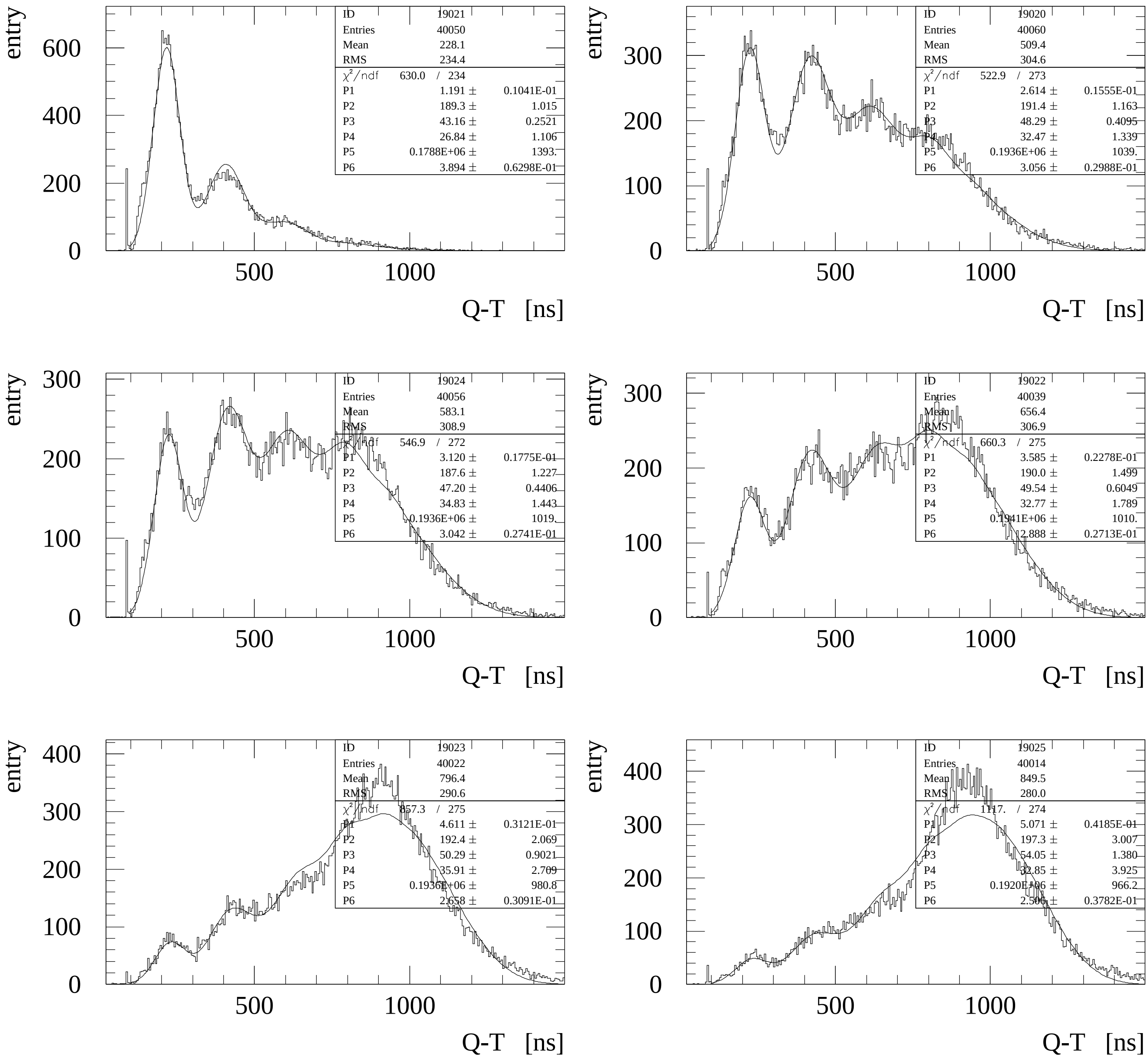

Figure B.92: Amplitude response of OM #19 for increasing light intensities. The "amplitude-function" eq.(5.76) is fitted to the data. The fit parameters $P1$, $P2$, $P3$, $P4$, $P5$, $P6$ correspond to $\bar{m}$, c_1, σ_1, c_0, a normalisation and n_{log}.

In order to achieve a calibration of the energy scale, this procedure has been performed for each OM. Table B.12 shows the results of this calibration. Previously reported results in [56], table 1, require a correction factor 1.25 for all constants except for n_{log}. In addition some fit results have been improved. The fits to OMs #11, #16 and #52 show only a poor convergence[2] Therefore the results for these OMs have to be applied with care. Due to a weakness of the produced circuit boards the energy resolution is less good than for the naked PMT.

Figure B.93 shows time distributions for pulses of a certain energy. These distributions are fitted with the "timing function", eq.(5.81), yielding characteristic time constants. Fit results for all EOMs are given in table B.13.

[2]These OMs show a much better fit if one introduces the additional constant $c_2 \approx 0.6$ of eq.(5.77)

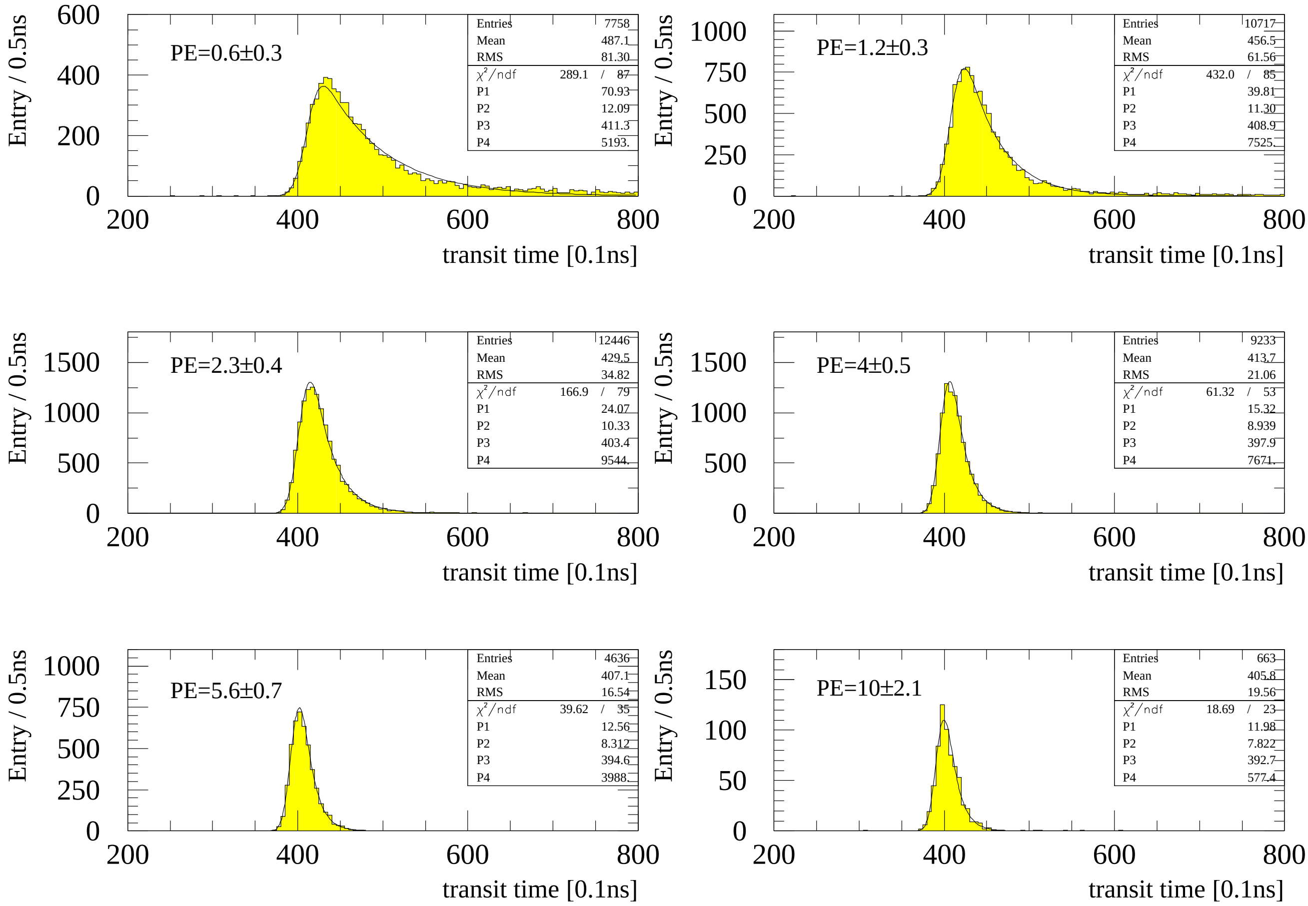

Figure B.93: Transit time distributions for OM #35. The "timing-function" eq.(5.81) is fitted to the data. The fit parameters $P1$, $P2$, $P3$, $P4$ correspond to τ, σ, t_0 and a normalisation.

OM	$a_{1,(\vartheta=0°)}$ [ns]	a_2 [ns]	b_1 [ns]	b_2 [ns]	$c_{1,(\vartheta=0°)}$ [ns]	c_2 [ns]	d_1 [ns]	d_2 [ns]	e_1 [ns]	e_2 [ns]	f_1 [ns]	f_2 [ns]
11	33.2	4.8	1.2	4.5	32.0	1.3	0.7	3.2	0.6	0.6	0.9	3.7
12	38.7	6.7	0.9	5.7	37.6	1.5	0.2	4.9	0.5	0.8	0.5	4.9
16	38.1	10.0	1.3	7.8	37.0	1.3	0.1	10.4	0.8	0.6	0.4	9.8
19	37.8	6.3	1.5	5.3	36.7	1.4	0.8	4.7	0.7	0.6	0.7	4.7
22	38.7	7.0	1.4	5.5	37.7	1.3	0.2	5.6	0.6	0.7	0.5	5.4
26	40.6	6.4	1.7	5.0	39.6	1.3	0.4	5.5	0.6	0.8	0.6	5.3
33	39.8	7.5	1.6	5.3	38.6	1.4	0.1	6.3	0.7	0.7	0.4	6.0
35	39.8	6.0	1.1	4.9	38.6	1.5	0.5	4.3	0.6	0.7	0.8	4.1
44	37.0	6.4	0.8	6.1	35.8	1.4	0.6	4.2	0.6	0.7	0.8	4.0
46	39.8	6.4	2.0	4.7	38.5	1.3	0.6	5.5	0.7	0.6	0.7	5.3
52	38.5	8.6	2.6	5.8	37.0	1.3	0.1	8.5	0.8	0.5	0.4	7.9
53	42.5	6.3	1.3	4.6	41.4	1.4	0.1	5.2	0.6	0.8	0.3	5.2
42	39.4	8.1	0.6	6.4	39.3	1.1	0.0	6.2	0.7	0.2	0.2	6.0

Table B.13: Fitted parameters of the time response measurements. The values are averaged over the measured zenith angles. OM #42 was measured in full illumination with a fast laser.

B.3 Dark noise measurements

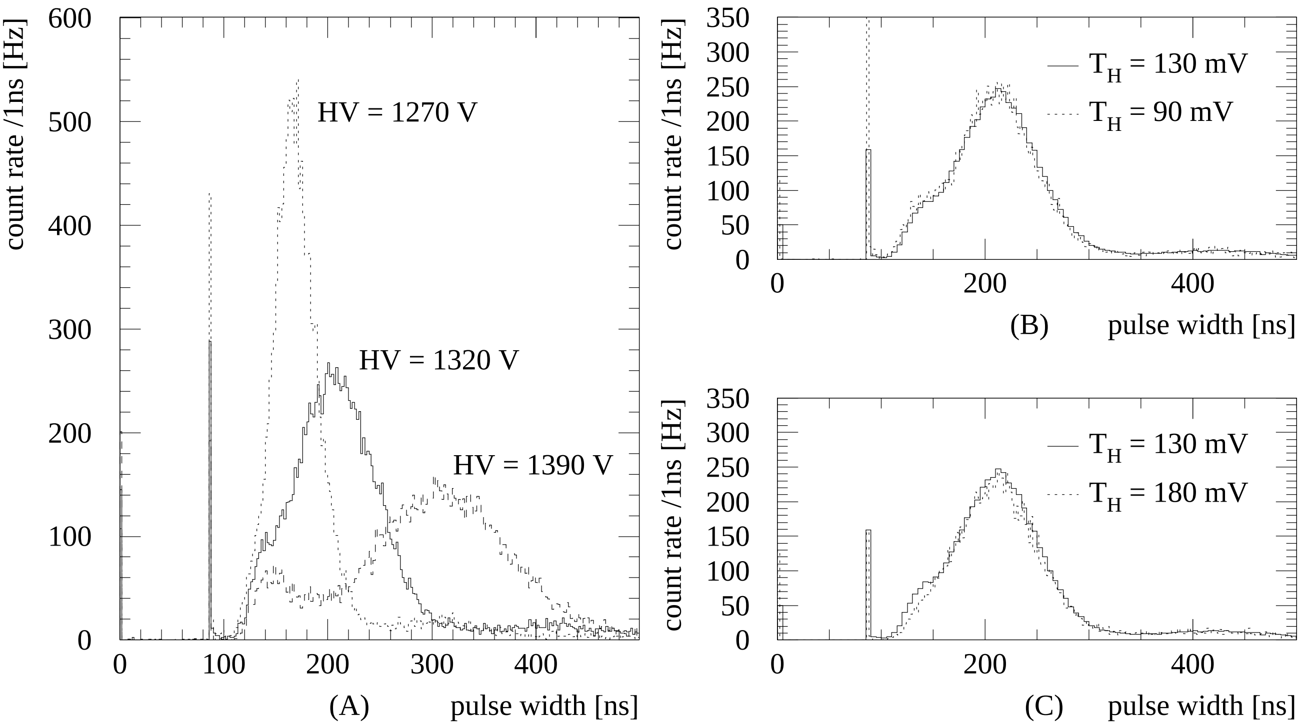

Figure B.94: Dark noise for different high voltage and thresholds measured with OM # 19. (A) shows the energy distribution for three different high voltages. (B) and (C) show the influences of a small and a large value of the high threshold in comparison with a moderate choice.

A major demand of the calibration procedure is the adjustment of the internal operational parameters, namely the high voltage of the small PMT and the two thresholds of the fast circuit. This can be excellently performed using the energy distributions and counting rates of dark noise pulses. This is demonstrated in figure B.94. The figures show the energy distributions of dark noise pulses, which are mostly 1PE signals due to thermionic emission at the photocathode. The sharp peak at $90ns$ is an artefact of the read-out and corresponds to the minimal conversion time, due to small signals ($\ll$ 1PE), e.g. noise of the small PMT.
(A) shows the energy distribution for three different high voltages. The thresholds have been adjusted in such a way, that the total counting rate stays constant. For a large high voltage ($1390V$) the 1PE peak becomes visible at large conversion times ($\approx 320ns$), showing a shoulder on the left edge ($\approx 140ns$). For a small high voltage ($1270V$), the peak ($\approx 160ns$) becomes non-Gaussian and the energy resolution decreases due to non-linearities of the fast circuit and too short integration times. A good choice combining a small conversion time together with a good energy resolution is seen for the HV $1320V$; the shoulder at the left edge of the 1PE peak is still visible.
The high threshold has to be adjusted in such a way, that noise smaller 1PE is efficiently discriminated but signals of 1PE, which have a small pulse-amplitude (in mV) are not rejected. (B) shows a moderate choice of $130mV$ and a smaller value $90mV$. The smaller threshold gives no improved efficiency for 1PE signals but significantly rises the counting rate of small pulses. (C) shows that an enlargement of the threshold to $180mV$ does not yield a better rejection of small pulses but leads to a loss of 1PE pulses. The low threshold is generally set to a small value, typically $30mV$ to $50mV$.
Each OM has to be adjusted individually (see [140]). As an example figure B.95 shows the energy distribution of dark noise pulses in a linear and a double logarithmic plot after this adjustment. A peak for 1PE and 2PE signals is clearly visible. The rate of dark noise pulses extends to high pulse-

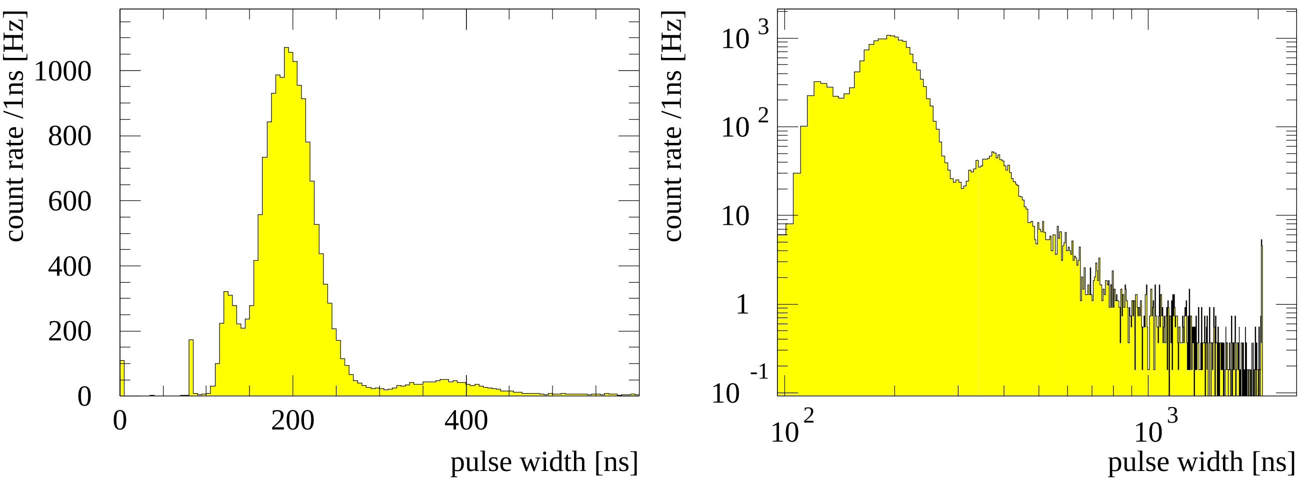

Figure B.95: Dark noise distribution of OM#12 in a linear and double logarithmic plot.

energies. Several mechanisms can be identified, which are responsible for these large signals. The most dominant are due to Čerenkov light produced by ^{40}K decays in the glass of the PMT, after-pulses due to ionisation of residual gas in the PMT and cosmic rays, which hit the PMT during the calibration measurement. [137]

The integral counting rates have been measured with their energy distribution for the individual PMTs and the OMs. During the final test of the EOMs, the temperature has been too high to apply useful numbers for deep ocean temperatures. The counting rates range between $5kHz$ to $30kHz$ for room temperature and decrease down to few kHz for $0°C$. For higher temperatures $> 30°C$ the rates strongly increases up to $30kHz$ – $80kHz$.

C Software details

C.1 The DADA program

C.1.1 Geometry definition, data structures and initialisation

The initialisation phase follows the general structure of GEANT. [153].

- Initialisation of ZEBRA, GEANT, HBOOK and HIGZ via standard calls.
- Initialisation and parsing of the database: GEANT, uses the FFREAD package to read necessary information from a format-free database. Archive data required by the DADA program are stored in the same file, called *Dadabase* .[152]
- Definition of the particle data structures: These are standard particles of GEANT with the extension of τ's, charmed mesons and the $Z^0W^{\pm}$ bosons.[153]
- Definition of materials according to their chemical composition. Materials included in the *Dadabase* are ocean–water, fresh–water, basalt for the ocean ground and some additional materials (glass, air and vacuum). [131]
- Definition of tracking media: A tracking medium is a material with kinetic energy cuts and a list of allowed GEANT-mechanisms. [153]
- Definition of the detector geometry: This is a complex hierarchic data structure, which is described below.
- Definition and initialisation of: histograms, the random generator, data streams ... [150]
- Calculation of cross section and energy loss tables. This is done by GEANT, using the previously defined data structures. [153]

Several sets of standard configurations for known detector geometries and tracking parameters are defined in the *Dadabase*. They may be independently selected. Implemented detector geometries cover various configurations of DUMAND and BAIKAL as well as other geometries. Most important sets of tracking parameters are “TEXA” and ”TFAS”, which implement the full tracking down to the Čerenkov threshold and the “fast–tracking”. [150]

Following data streams are (optionally) opened:

- The output file for event output.
- A file for the input of the initial kinematics of events.
- A Dadabase file, e.g. *dada.steer*
- A HBOOK-file for histograms, which are filled during tracking, *dada.rz.*
- A postscript file for graphical output, *dada.ps.*
- An additional file for the output of special data (requires re-compilation).

The definition of a detector geometry is done according to a fixed hierarchy of embedded detector volumes. Each detection volumes is encapsulated by a volume of higher hierarchy and surrounds volumes of lower hierarchic order. Each volume is filled with a tracking medium.

Up to 200 strings may be defined. Each string represents a cylindrical volume and a certain configuration of optical modules. The configuration of OMs is defined by the data structure *string-type*, which is assigned to each string. A *string-type* defines orientation, positions in the string and types of OMs. Up to 10 different string–types with each up to 50 OMs may be defined. The typical radius of a string volume is $10m$. Each OM represents a spherical OM-volume of lower hierarchy with a typical radius of $5m$. The OMs are not necessarily positioned in the centre of the OM-spheres because of a non uniform cathode sensitivity.
The string volumes are positioned into a larger cylindrical volume which is of the order of two times the light-attenuation length larger than the detector itself. This volume is designed to define the effective sensitive detector volume. The absolute positions of OMs are mirrored into a separate data structure (independent of the GEANT geometries). This structure is used for the detection of Čerenkov hits and may be changed during tracking. The detector volume is again enclosed by a larger cylinder which is typically 10 attenuation lengths larger. This cylinder is located in the centre of a large box with typically $2km$ long sides, which defines the total simulation space and encloses all other volumes. If the outer volumes overlap with the ocean/lake bottom, they are divided into two volumes of different materials (e.g.rock and water).
The tracking parameters for each volume may be individually adjusted, which allows to select an accurate tracking close to OMs and a tracking with higher thresholds further outside. Each volume may be declared passive to increase the speed of the tracking procedure. In passive volumes secondary particles are stored only in a temporary GEANT stack and tracking is abandoned for particles, that do not point into the detector.
Six different optical modules may be used and simulated with different levels of accuracy. The BOM, EOM and JOM may be simulated with detailed routines, a standard $8''$–PMT, $16''$–PMT and the AMANDA OM are only rudimentarily implemented.

C.1.2 Fast tracking

The fast tracking mode allows to bypass the standard GEANT tracking and to calculate the resulting Čerenkov light according to a parameterization. During initialisation a "fast-tracking type" is assigned to each GEANT particle. Default is the full tracking with GEANT for all particles. Within certain energy ranges particles may be declared to be treated as a muon, electro-magnetic cascade or a hadronic cascade. For each of these three types several parameterizations are implemented. Each secondary particle, e.g. a bremsstrahlung photon, is tested if a fast tracking type is assigned to this particle and if its energy falls into the corresponding range. In this case the further tracking is not passed to GEANT, but done via the fast tracking mode and the Čerenkov light is simulated according to the selected parameterization. Parameterizations[1] are deduced in section 7.1 for cascades and in 7.2 for muons. Cascades are simulated including their longitudinal evolution. The implementation of "fast" muons is done as follows. Energy losses smaller $0.5GeV$ are assumed to occur continuously along the muon trajectory and the amount of Čerenkov light from the muon is enlarged (see section 7.2.1). The muon is tracked by GEANT with tracking thresholds enlarged to $0.5GeV$.

C.1.3 Signal generation

Generation and attenuation of Čerenkovlight. During the execution of a tracking step the simulation loops[2] over all OMs and checks for Čerenkov hits.

[1]Other implemented parameterizations cover the treatment of muons as a minimal ionising tracks and the point-like simulation of cascades for parameterizations of Belyaev and Hauptman.[51]

[2]This loop is only executed, if the energy is above the Čerenkov threshold; if the particle has left the active detector volume the direction has to point into the detector and if the current track length is above a minimal cut (e.g.$> 1mm$).

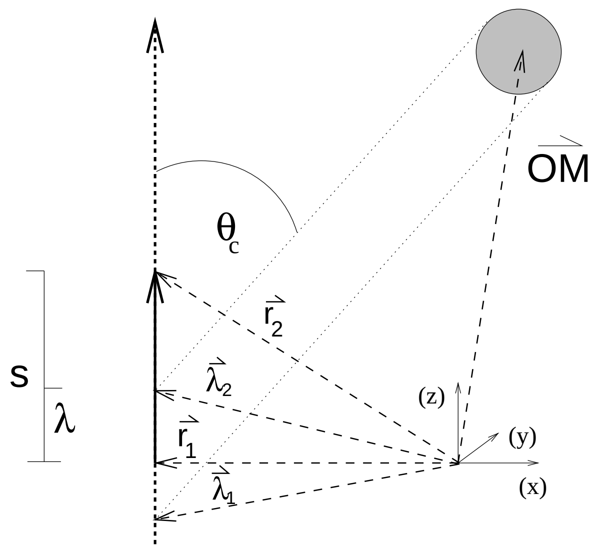

Figure C.96: Geometry for the evaluation of a Čerenkov hit.

The geometry is shown in figure C.96. The current track piece is defined by the length s, the start point $\vec{r}_1$, the end point $\vec{r}_2$ and its direction $\hat{p} = \vec{p}/p$. In order to minimise the computing time during the evaluation of a possible Čerenkov hit and the length of the hitting track λ several tests are performed in sequential order. If one check fails the generation of Čerenkov light is abandoned

1. Is the angle between $\hat{p}$ and $O\vec{M} - \vec{r}_1$ smaller 90°?
2. Is the point $\vec{r}_1$ before $\vec{\lambda}_2$?
3. Is the point $\vec{r}_2$ behind $\vec{\lambda}_1$?

If these conditions are fulfilled a hit has happened and the length λ is interpolated. The relative length $\mathcal{L}$ is calculated via eq.(A.129) (for fast cascades via eq.(A.141)) and the angle between the Čerenkov wave-front and the OM-axis θ_H (eq.(A.132) are calculated and stored together with a reference to the hitting track in a stack. The time of the hit t_H is calculated from the centre of the hitting track piece λ via eq.(A.122). A value proportional to the time spread Δ_H is assumed using

$$\Delta_H = 0.5 \cdot \lambda / c_{vac} \; . \tag{C.145}$$

If two hits in one OM originate from the same track and occur within the time window t_w (typically $2ns$), the values for the length are added $\mathcal{L} = \mathcal{L}_1 + \mathcal{L}_2$, the angles θ_H, the distance d, and the times t_H are averaged, weighted with $\mathcal{L}$, e.g.

$$\theta_H = \frac{\theta_{H1} \cdot \mathcal{L}_1 + \theta_{H2} \cdot \mathcal{L}_2}{\mathcal{L}_1 + \mathcal{L}_2} \tag{C.146}$$

The new time spread Δ_H is calculated via

$$\Delta_H = \min\left(t_w \; , \; \frac{\Delta_{H1} \cdot \mathcal{L}_1 + \Delta_{H2} \cdot \mathcal{L}_2}{\mathcal{L}_1 + \mathcal{L}_2} + \min(|t_H - t_{H1}| \; , \; |t_H - t_{H1}|) \right) \; . \tag{C.147}$$

After the tracking is finished, the photon flux ρ_γ is calculated for each hit with eq.(A.127). Hits occuring in one OM at the same time are recombined analogous to the above method eq.(C.146),(C.147), except that values are weighted with ρ_γ instead of $\mathcal{L}$. The attenuation is calculated according to the Learned parametrisations eq.(3.49). except for Baikal water. The attenuation here is calculated according to a spline parametrisation, which was extracted from the standard BAIKAL Monte Carlo [139].

All tracks are numerated in a straight order $(1, 2, 3 \ldots)$. Hits from secondary tracks, which are only stored temporarily in a GEANT stack, receive the negative number of the initial track. During recombination of the reference to the hitting track emphasis is put on the track with the lowest positive number. Only if both combined tracks have a negative number the least negative value is kept. After this procedure the stack contains no hits occuring at the same time at the same OM.

Simulation of Optical Modules. The simulation of OMs generates the amplitude in units of PE eq.(A.133) and the response time. The simulation of the response time t involves time deviations due to the initial spread of the arrival time of photons Δ_H and due to the time accuracy of the OM Δ_{OM}. The response time is calculated without the fixed transit-time of an OM. The time deviation due to Δ_H is simulated according to an Exponential distribution ϱ_E

(C.148) $$t = t_H + \frac{\Delta_H}{n_{pe}} \cdot (\varrho_E - 1) + \Delta_{OM} \ ,$$

with n_{pe} the number of photoelectrons.

The simulation of OMs may be done with 4 levels[3] of accuracy:

1. No PMT but only the number of photons hitting the OM is simulated.
2. The number of photoelectrons are simulated according to Poisson distribution. No time and amplitude response is simulated for the PMT ($\Delta_{OM} = 0$).
3. In addition to 2 time-deviations and the amplitude-response are simulated according to Gaussian distributions.
4. Detailed simulation for BOM, EOM and JOM according to standard parameterisations.

The parameters necessary for 1 to 3 are taken from the Dadabase, the simulation level 4 is implemented via special routines regarding details of the OMs. The routine for the JOM was kindly provided by A.Okada [71] and contains only minor modifications. The angular sensitivity is simulated via $S = 0.52 + 0.48 \cos\theta_H$ with an absolute peak quantum efficiency times collection efficiency $\kappa = 0.17$ and a geometrical area of $0.114m^2$. The sensitivity of the EOM is simulated according to eq.(5.69) assuming $\kappa = 0.2$ and the area $0.1m^2$. The amplitudes are simulated according to the "amplitude-function" eq.(5.76) with an energy resolution of 60%. The calculation of the time deviations uses the "timing-function" eq.(5.81) with the parameters derived in [92]. The routines to simulate the sensitivity and the amplitude of the BOM were taken from the Baikal Monte Carlo program [139]. The program uses a spline parametrisation for the angular sensitivity. The absolute quantum efficiency is already included in in the parametrisation of the light attenuation of Baikal-water. The time jitter for the BOM may be simulated according to 4 functional dependencies using the Exponential distribution

[3] A 5th level, which respects the properties of individual OMs, is under consideration.

ϱ_E and the Gaussian distribution ϱ_G

$$
\begin{aligned}
&(1)\quad \Delta_{OM} &=& \quad \varrho_E \cdot \frac{4.0}{\sqrt{n_{pe}}} + \varrho_G \cdot 1.6 && [139]\ , \\
&(2)\quad \Delta_{OM} &=& \quad \varrho_E \cdot \frac{5.0}{n_{pe}} && [49]\ , \\
&(3)\quad \Delta_{OM} &=& \quad \varrho_E \cdot \frac{1.8}{n_{pe}} + \varrho_G \cdot \left(0.8 + \frac{3.9}{\sqrt{n_{pe}}}\right) && [87]\ , \\
&(4)\quad \Delta_{OM} &=& \quad \varrho_E \cdot \max\left(0.9\ ,\ \frac{4.8}{n_{pe}}\right) + \varrho_G \cdot 0.7 && [92]\ .
\end{aligned}
\tag{C.149}
$$

All units are ns. The second simulation requires an additional Gaussian jitter of $1ns$ after the local coincidence of two OMs in Baikal is calculated.

The final amplitudes and times are written to the data file. No local coincidence is performed within the DADA program, but may be applied later using the *deff* utility (appendix C.3).

Noise generation. It is possible to simulate noise or to sample additional noise hits into an event either within the DADA program or during later data processing using the *deff* program (appendix C.3). Signals are simulated uniformly distributed in the time window τ of the event (typically $\pm 1\mu s$). The probability P of a hit is $P = \tau \cdot R$, with the total noise rate R. Two different choices for the amplitudes of these signals are possible. The first generates 1PE signals, second choice allows to generate the amplitudes according to a potential law.

C.1.4 Internal event generation

Besides the possibility to read the initial event kinematics from a data file, three alternate methods are included in DADA .

1. Initial kinematics, vertex and particle type may be interactively provided. The same track may be simulated several times.
2. An internal generator *muoi* allows to generate isotropic muons. The functionality is a subset of the *muo0* generator (see appendix C.2).
3. Simulation without initial kinematics in order to simulate only noise events.

C.2 Event generation

The event generator program *basiev* simulates atmospheric muons. The program code was developed for the Baksan experiment at the INR Moscow by Boziev et.al. [25]. The program generates proton induced hadronic cascades in the top of the atmosphere and simulates resulting muons at sea level. The muons are transported to the depth of an underwater experiment using the mean energy loss. It was extracted from the standard Baikal Monte Carlo as a stand-alone program. Several parameters can be adjusted, such as the minimum muon energy at the detector site, or the distance of muons to the detector (from where tracking is taken over by DADA). The program yields good results compared to experimental data and other air shower programs. [49]

The general purpose generator *muo0* generates single particle trajectories. The particle may be any GEANT-particle, whose energy is simulated either according to a logarithmic, potential or constant energy distribution within a certain energy range. The vertex is simulated either on a plane at a certain distance from the detector or within a surrounding volume. The second is useful for the generation of showers inside the detector, the first for the generation of muon tracks passing through the detector. Directions may be simulated isotropically or within certain ranges (e.g. simulation of muons from the lower hemisphere).

A third event generator program *nue0* is under development. Its purpose is to simulate charged current and neutral current neutrino (ν_e, ν_μ and ν_τ) interactions with nucleons or electrons close to the detector, using the PYTHIA program. Particle tracks can be also generated with the built in generators of the DADA program (appendix C.1.4).

C.3 Triggering, event selection and reconstruction

During the first step of data analysis it may be desirable to apply triggers or to reconfigure the data. The following discussion uses the term "channel" instead of OM. This expresses that filter conditions are equivalent for individual OMs and several OMs forming a local coincidence. The term "OM" is only used if explicitly required. In case of the BAIKAL experiment a pair of OMs forms a channel, in case of DUMAND II one OM is equivalent to one channel.
The *deff* program intends to implement hardware-specific features as well as a possible reconfiguration of the data.[146] Most important items are:

- Implementation of a local coincidence condition between OMs (e.g. OM-pairs in BAIKAL). Coincident hits are detected and non coincidence hits are deleted.
- Implementation of the dead time of channels. If multiple hits in one channel are detected to occur within a specified time-window (dead-time), the second hit is deleted and the amplitude added to the first.
- Simulation of noise hits into the data stream.
- Simulation of an additional time-jitter, e.g. to handle time uncertainties due to digitisation.
- Simulation of the efficiency of channels. Hits may be removed from the data stream according to a random number.
- Hits in certain channels may be deleted. This allows to apply MC-data, simulated for a full detector, to experimental data with certain modules switched off during a specific run period.
- Removal of hits with amplitudes smaller than a certain threshold.
- Removal of detector elements (strings and channels) from the data stream. Smaller detectors are often a subset of a larger detector (E.g. NT-36, 1994, is a subset of NT-72, 1995). This allows to simulate data for a larger detector. Data subsets may be extracted and applied to smaller detectors.

The second program, *soff*, provides trigger conditions, which may be applied to the data-stream and combined in `AND` or `OR` conditions. Possible triggers are:

- A minimum number of total hits, a minimum number of hit channels or a minimum number of PE in the event.
- Implementation of the T-trigger eq.(4.60), which allows to require a minimum number of neighbouring hit channels in several strings.

- Several special trigger conditions such as: minimum number of hits in a certain string, minimum number of PE in a certain channel ....

The trigger logic, to select all events which fulfill a trigger condition, may be inverted, to select those events, which do not pass.

The reconstruction of events is the most important step during data analysis. The reconstruction usually involves the minimisation of a χ^2 function or uses a more sophisticated likelihood method. The χ^2 function for the muon track reconstruction may be written as sum of three contributions corresponding to the response times χ_t^2 and amplitudes χ_a^2 and the probability of non hit channels χ_p^2

$$\begin{aligned} \chi^2 &= \chi_t^2 + W_a \cdot \chi_a^2 + W_p \cdot \chi_p^2 \\ &= \sum_{i=1}^{N_h} \frac{(t_{theo,i} - t_i)^2}{\sigma_{t,i}^2} + W_a \cdot \sum_{i=1}^{N_h} \frac{(a_{theo,i} - a_i)^2}{\sigma_{a,i}^2} + W_p \cdot \sum_{i=N_h+1}^{N} P_h(i)^2 \,. \end{aligned} \tag{C.150}$$

t_i, a_i are the response times and amplitudes of the hit channels $(1, 2, \ldots, N_h)$, $\sigma_{t,i}$ and $\sigma_{t,i}$ are the corresponding deviations. $t_{theo}(i)$ and $a_{theo}(i)$ are the expected response times and amplitudes e.g. for a reconstructed muon track. $P_h(i)$ is the probability of the occurrence of a hit in the not hit channel i. The contribution χ_t^2 has the largest significance determining the track reconstruction. The amplitude accuracy is strongly limited due to additional light from secondary cascades. Therefore the contributions χ_a^2 are χ_p^2 are weighted with factors W_a and W_p or completely neglected ($W_p = W_p = 0$). The fit of a muon track involves 5 free parameters, 4 for the geometrical track parameters and one for the time. It thus requires at least 5 hit channels. [87, 101, 69]

The presence of noise significantly complicates the fitting procedure and requires sophisticated noise reduction methods, e.g. causality criteria, during the fitting procedure, in order exclude suspected noise hits from the calculation of the χ^2. [107, 108]

After the calibration of BAIKAL events, they are fitted with a standard BAIKAL reconstruction program assuming a single muon track. For each fit result several quality criteria, such as an investigation of the covariance matrix, are applied and a quality value is assigned to the result. [8, 11, 49]
The *recoos* program, by O.Streicher, provides a fast fit program for the reconstructions of single muons. Together with the filter program *muff* a large variety of quality criteria may be applied to a data stream to identify mis-reconstructed tracks and especially reject down-going (fake) muons. [87, 148]

C.4 Data processing

Usually the user has to deal with various different, mostly incompatible, data formats. The data-format used for the SiEGMuND software is based on a line-oriented ASCII–format introduced for the DUMAND II experiment in [144]. A second format is a binary format used at Zeuthen for the BAIKAL experiment [143]. Within the development of the *rdmc–library* [145] the initial ASCII–format was extended considering following requirements.

- Full downward compatibility with the DUMAND ASCII-format and logical compatibility with the BAIKAL binary format.
- One general format for all analysis steps. Possible pipelining of data streams on UNIX platforms.
- Possible user specific extensions, especially for data analysis purposes.
- Independence on the specific detector.

The *rdmc* library provides format independent I/O routines and memory data-structures. A user application program written on basis of *rdmc* may access any data-format known to *rdmc* via format independent calls. The library provides automatic decompression of "gzip'ed" data-files. Changes in formats require no change of the application program. The program *cpfeil* converts data files between different formats and provides further data manipulation options. [145]

Name	Description	Reference
rdmc	I/O library and memory data structures for data files	[145, 146]
cpfeil	File handling and format conversion program	[145]
dada	Detector response Monte Carlo (GEANT) program	6.2,C.1,[150]
deff	Hardware simulation and data-manipulation program	C.3,[146]
soff	Trigger and event selection program	C.3,[146]
geff	Filter program for generator specific information	[146]
recoos	Fast muon reconstruction program	[148, 87]
muff	Reconstruction filters	[148, 87]
rtt	Display program (X11/Postscript)	[149]
basiev	Generator for atmospheric muons (bundles)	[25, 139, 49, 151]
muo0	Generator for generic tracks	C.2, [151]
nue0	Generator for neutrino nucleon/electron interactions (PYTHIA)	[151]
fint	MC/data histograming program	[146]
calib	Baikal specific calibration of raw data	[147]
danton	Data histograming program	[147]

Table C.14: Summary of SIEGMUND programs. [97]

Table C.14 shows an overview on the most important SIEGMUND programs. The programs for triggering, data filtering and reconstruction, *soff*, *deff*, *muff* and *recoos* are described in appendix C.3. The event generator programs are described in appendix C.2.
The *rtt* program implements a small 3-dimensional event display. It shows the detector, hits and if available the reconstructed and generated tracks. It is possible to rotate and to zoom the picture as well as to print verbose information on the event. [149]
Two programs *fint* and *danton* generate "HBOOK"-files with "standard" histograms and "n-tuples" for further analysis with PAW.[146, 147, 157]
The *calib* program reads raw data-files from BAIKAL and performs a calibration according to a small database. It writes calibrated events to a file, readable by *rdmc*. [147]

C.5 Calculation of ^{40}K rates

The expected counting rate of signals due to decays of ^{40}K are calculated via a Monte Carlo integration of eq.(3.51). Besides the three spatial coordinates, which are simulated spherically within an inner and an outer radius, the type of decay and its energy is randomised (see section 3.5).
If a resulting electron is above the Čerenkov threshold the number of Čerenkov photons n_γ is simulated with a constant distribution between 0 and 120 photons for Compton electrons and via the (not normalised) probability function

$$\varrho(n_\gamma) = \begin{cases} 1816 - 247 \cdot \ln(n_\gamma) & \text{for} \quad n_\gamma < 68.45 \\ 6029.4 - 1244 \cdot \ln(n_\gamma) & \text{for} \quad 68.45 \leq n_\gamma < 127.33. \end{cases} \tag{C.151}$$

for β-electrons. These assumptions are supported by detailed simulations of the ^{40}K decay and the resulting Čerenkov photons [90]. After the simulation of the decay, the mean number of photo-electrons

$\bar{m}$ for a PMT, which is hit by the non isotropic Čerenkov cone in the distance d, is calculated via

$$\bar{m}(d) = \frac{\epsilon(d) \cdot F_{OM,eff} \cdot \kappa \cdot n_\gamma}{4\pi \cdot \Omega (d - 0.5 \cdot R_{OM})^2}, \tag{C.152}$$

with the attenuation $\epsilon(d)$ (eq.3.49), the radius of the OM R_{OM}, the collection times the quantum efficiency of the photo-cathode κ and the solid angle $\Omega = \pi sr$ for the emission of the photons. The effective area $F_{OM,eff}$ of the OM is simulated according to the geometrical cathode area and the angular sensitivity parameterized for the JOM, EOM, BOM and the AMANDA OM. to a specific OM type. Finally the hit probability is calculated via eq.(3.52). A volume integration and multiplication with the decay rate yields the noise rate.

D The BAIKAL and the DUMAND collaboration

The Baikal *Collaboration :*

I.A. Belolaptikov[7], L.B. Bezrukov[1], B.A. Borisovets[1], N.M. Budnev[2], A.G. Chensky[2], I.A. Danilchenko[1], Zh.-A.M. Djilkibaev[1], V.I. Dobrynin[2], G.V. Domogatsky[1], L.A. Donskykh[1], A.A. Doroshenko[1], S.V. Fialkovsky[4], A. Gaponenko[2], A.A. Garus[1], O.A. Gress[2], T.A. Gress[2], H. Heukenkamp[8*], A. Karle[8], A.M. Klabukov[1], A.I. Klimov[6], S.I. Klimushin[1], A.P. Koshechkin[2], J. Krabi[8], V.F. Kulepov[4], L.A. Kuzmichov[3], B.K. Lubsandorzhiev[1], M.B. Milenin[4], T. Mikolajski[8], R.R. Mirgazov[2], N.I. Moseiko[3], S.A. Nikiforov[2], E.A. Osipova[3], A.I. Panfilov[1], Yu.V. Parfenov[2], A.A. Pavlov[2], D.P. Petukhov[1], K.A. Pocheikin[2], P.G. Pokhil[1], P.A. Pokolev[2], M.I. Rosanov[5], V.Yu. Rubzov[2], S.I. Sinegovsky[2], I.A. Sokalski[1], Ch. Spiering[8], O. Streicher[8], B.A. Tarashansky[2], T. Thon[8], I.I. Trofimenko[1], Ch. Wiebusch[8], R. Wischnewski[8]

[1]*Institute for Nuclear Research, Russian Acad. of Science, Moscow, Russia*
[2]*Irkutsk State University, Irkutsk, Russia*
[3]*Moscow State University, Moscow, Russia*
[4]*Nizhni Novgorod State Technical University, Nizhni Novgorod, Russia*
[5]*St. Petersburg State Marine Technical University, St.Petersburg, Russia*
[6]*Kurchatov Institute, Moscow, Russia*
[7]*Joint Institute for Nuclear Research, Dubna, Russia*
[8]*DESY - Institute for High Energy Physics, Zeuthen, Germany*
[*] *now at University of Wisconsin*

The DUMAND *Collaboration :*

W. Anderson[7], T. Aoki[14], H.G. Berns[16], J. Bolesta[5], P.C. Bosetti[15], H. Bradner[12], U. Camerini[17], V. Chaloupka[16], R.J. Clark[11], H.J. Crawford[4], S.T. Dye[3], I. Flores[4], M. Fukawa[8], J. George[16], P.W. Gorham[5], P.K.F. Grieder[2], W. Grogan[17], H. Hanada[13], J.M. Hauptman[7], T. Hayashino[13], E. Hazen[3], M. Jaworski[17], A. Kibayashi[5], T. Kitamura[10], S. Kondo[5], P. Koske[9], C. Kuo[4], J.G. Learned[5], J.J. Lord[16], R. March[17], T. Matsumoto[13], S. Matsuno[5], K. Mauritz[7], M. Mignard[5], P. Minkowski[2], R. Mitiguy[5], K. Mitsui[14], T. Narita[17], D. Nicklaus[17], D.J. O'Connor[5], Y. Ohashi[14], A. Okada[14], S. Olsen[5], V.Z. Peterson[5], A. Roberts[5], M.D. Rosen[5], G. Shapiro[4], V.J. Stenger[5], A. Suzuki[13], R.C.Svoboda[11], T. Takayama[13], D. Takemori[5], S. Tanaka[6], E. Torrente[2], S. Uehara[8], C.H. Wiebusch[1], R.J. Wilkes[16], G. Wilkins[5], A. Yamaguchi[13], K.K. Young[16].

1) RWTH-Aachen University of Technology, Germany;
2) University of Bern, Switzerland;
3) Boston University, Massachusetts, USA;
4) University of California, Berkley, USA;
5) University of Hawaii, Manoa, USA;
6) Hirosaki U., Japan;
7) Iowa State University, Ames, USA;
8) KEK (National High Energy Physics Lab.), Japan;
9) University of Kiel, Germany;
10) Kinki University, Japan;
11) Louisiana State University, Baton Rouge, USA;
12) Scripps Institution of Oceanography, USA;
13) Tohoku University, Sendai, Japan;
14) Institute of Cosmic Ray Research, University of Tokyo, Japan;
15) Vijlen Institute for Physics, Vijlen, Netherlands;
16) University of Washington, Seattle, USA;
17) University of Wisconsin, Madison, USA.

References

[1] Alexander et.al. Contributions to [116] by the DUMAND II Collaboration
Update on the status of DUMAND .
Optical Module for DUMAND II — Japanese Version.
An Optical Sensor for DUMAND II — European Version.
Trigger strategies an processing for DUMAND .
On the Detection of UHE Cascade Showers with DUMAND II .
The DUMAND II Digitiser.
Acoustical Detection of Cascades in DUMAND .
Estimate of Downgoing Atmospheric Muon Background Events in DUMAND II .
Capabilities of the DUMAND II Phase I 3-string Array.
Acoustical Locating System for DUMAND II .
Atmospheric Neutrino Oscillations with DUMAND .

[2] van Aller et.al. A "smart" 35cm Diameter Photomultiplier. *Helvetia Physica Acta*, 59:1119 ff., 1986.

[3] Contributions to [120] by the AMANDA Collaboration
Status and Capabilities of AMANDA 94.
Measurements of the Absorption Length of the Ice at the South Pole in the Wavelength Interval 410nm to 610nm.
Indirect Evidence for Long Absorption Lengths in Antarctic Ice.
The Design of a Neutrino Telescope Using Natural Deep Ice as a Particle Detector.
A system to Search for Supernova Bursts with the AMANDA Detector.

[4] Atsuno et.al. Single photon light detector for deep ocean applications. *NIM*, A276:359–366, Sep, 1988.

[5] Babson et.al. Cosmic–ray muons in deep ocean. *Phys.Rev.D*, 42:3613–3620, Dec, 1990.

[6] S.Barwick Transparency of Antarctic Ice: First Results (in [134]).
F.Halzen AMANDA: Antarctic Muon And Neutrino Detector Array (in [114]).

[7] I.Belolaptikov and Ch.Spiering Optimisation of NT-72 with respect to Neutrino Detection. Baikal-Note 95-01.

[8] Belolaptikov et.al. Track Reconstruction and Background Rejection for the Baikal Neutrino Telescope. (in [118])

[9] Belolaptikov et.al.
Results from the Baikal Underwater Telescope 3rd Conf.on *Trends in Astroparticle Physics*. Stockholm, September 1994. Nucl.Phys.B (Proc.Suppl.) **43** (1995) 241-244
Status of the Lake Baikal Neutrino Detector. Proceedings of the 26th Int.Conference on High Energy Physics, Dallas, August 1992.

[10] Belolaptikov et.al. The BAIKAL Underwater Telescope — Status and Results. Proc. of the Int.Conf.on High Energy Cosmic Rays, RIKEN, Tokyo, 1994.

[11] Belolaptikov et.al. Contributions to [120] by the BAIKAL Collaboration.
The Lake BAIKAL Neutrino Project: Status Report.
Analysis of Muon Events Recorded with the NT-36 Detector in Lake Baikal.
Search for Magnetic Monopoles with the Baikal Neutrino Telescope.
Separation of Upward going Muons with the Baikal Underwater Telescope.
Response of the NT-36 to a Distant Point-Like Light Source.
Variations of Water Parameters at the Site of the Baikal Experiment and their Effect on Detector Performance.
A Sonar Triangulation System for Position Monitoring of the Baikal Underwater Array.

[12] A.A.Belyaev, I.P.Ivanenko and V.V.Markov
Čerenkov Radiation from showers developing in saline water, (in [102]).
Čerenkov Radiation from electron-photon showers developing in water, (in[103]).

[13] V.S.Beresinsky High Energy Cosmic Neutrinos of Acceleration and Non–Acceleration Origin. INFN, Gran Sasso, INR, Moscow. January 1992 *LNGS - 92/21*.

[14] V.S.Beresinsky Dark Matter and High Energy Neutrinos. (in [114])

[15] V.S.Bersinsky On astrophysical Solution to the Solar Neutrino Problem. Preprint *LNGS-94/101*, June 1994.

Gallex–Collaboration. Implications of the Gallex determination of the solar neutrino flux *Phys.Lett.B* 285 (1992) 390-397.

N.Hata Solar Neutrinos: Hint for Neutrino Mass. Preprint University Pennsylvania *UPR-0612T*.

D.R.O.Morrisson Brief review of theory and experiments on the Solar Neutrino Problem. Preprint *CERN–PPE/93-196*, Nov.1993.

A.Y.Smirnov The Solar neutrino Problem: Neither Astrophysics nor Oscillations? International Workshop on: "Solar neutrino problem: Astrophysics or Oscillations" Gran Sasso, Feb.1994.

[16] U.Berson Entwicklung und Test eines optischen Moduls zum Nachweis schwacher Lichtquellen in Wasser-Čerenkov-Detektoren. Diploma thesis, RWTH Aachen, Feb. 1993.

[17] Berson et.al. Messungen zu den optischen Eigenschaften des Gels. Julia internal report, Juli 1991.

[18] Bezrukov et.al. Search for superheavy magnetic monopoles in deep–underwater experiments at Lake Baikal Yad.Fiz.**52**, 86-95. July 1990.

[19] Bezrukov et.al. The Optical Module of the Baikal Neutrino Telescope NT-200. (in [116])

[20] Bezrukov et.al. The Electronic system of the BAIKAL Neutrino telescope NT-200. Izvest.Acad.Nauk, Fiz.58 (1994), No.9 150. (in Russ.)

[21] Bionta et.al. Observation of a Neutrino Burst in Coinidence with Supernova 1987a in the Large Magelanic Cloud. *Phys.Rev.Lett.*, 58:1494–1496, April 1987.

Hirata et.al. Observation of a Neutrino Burst from the Supernova SN1987A. *Phys.Rev.Lett.*, 58:1490–1493, April 1987.

Alexeyev et.al. Detection of the Neutrino signal from SN1987A in the LMC using the Baksan Underground Scintillation Telescope. *Phys.Lett.B 205,209*, April 1988.

[22] Bird et.al. Evidence for Correlated Changes in the Spectrum and Composition of Cosmic Rays at Extremely High Energies Phys Rev.Lett.71, 3401, 1993.

Sigl et.al. On the Origin of Highest Energy Cosmic Rays. Preprint 1994, Subm. to Astr.Part.Phys.

B.A.Khrenov Spectrum and composition of high energy cosmic rays. (in [115])

[23] T.Bolln Untersuchungen an neuartigen, hochempfindlichen großflächigen Photomultipliern für den Einsatz in der Tiefsee. Diploma thesis, University Kiel, Juli 1993.

[24] P.C.Bosetti JULIA (in [114])

C.H.Wiebusch Signal Processing with JULIA (in [114])

[25] Boziev et.al. INR-Preprint P-0630 (1989).

[26] Bradner et.al. Bioluminescence profile in the deep Pacific Ocean. *Deep-Sea Research*, **34** 11,1831–1840. 1987.

Webster et.al. Mechanical stimulation of bioluminescence in the deep Pacific Ocean. *Deep-Sea Research*, **38** 2, 201–217. 1991.

[27] Bugaev et.al. Muon Depth-Intensity Relation and Data of Underground and Underwater Experiments. (in [117])

[28] Burrows et.al. The future of supernova neutrino detection. *Phys.Rev.D* 45 3361-3385, May 1992.

Y.Suzuki Kamikande Results on Solar Neutrinos and a Supernova Search. Preprint *ICRR-Report*-294-93-6, May 1993.

[29] D.J.O'Connor Cosmic–ray muons in the deep ocean. Dissertation, University Hawaii, UH-511-706-90, Aug, 1990.

[30] H.J.Crawford Mapping the Earth's Interior with astrophysical Neutrinos. (in [120])

[31] Davis et.al. Search for Neutrinos from the Sun. *Phys.Rev.Lett.*, 20:1205ff, 1968.

Hirata et.al. Real-time, directional measurement of ^8B solar neutrinos in the Kamiokande II detector. *Phys.Rev.D 44,2241* October 1991.

Abasov et.al. *Phys.Rev.Lett. 67,3332* 1992

Gallex–Collaboration. Solar Neutrinos observed by Gallex at Gran Sasso. *Phys.Lett.B* 285 (1992) 367-389.

[32] J.Edsjö Neutrino–induced muon fluxes from Neutralino annihilations in the Sun and in the Earth. ISSN 02484-2769. Diploma thesis, Uppsala University, Dec 1993.

[33] D.Eichler SS433: A possible Neutrino Source? (in [106])

[34] H.Falcke What is SGR A? Preprint, (IAU Symp.169). MPIfR Bonn, 1994.

[35] S.O.Flyckt The Philips "Smart" 15 inch PMT. (in [112])

[36] J.A.Frieman The Standard Cosmology. Preprint *Fermilab-Conf-94/090-A*, (Lectures at TASI'93). NASA/Fermilab Astrophysiscs Center, April 1994.

[37] T.K.Gaisser, F.Halzen, and T.Stanev Particle Astrophysics with High Energy Neutrinos Phys.Rep.258 (1995) 173–236.

[38] T.K.Gaisser and A.F.Grillo Energy spectra of neutrino–induced upward muons in underground experiments. *Phys.Rev.D* **36**, 2752, Nov 1987

[39] B.D.Geelhood Impact of ^{40}K on DUMAND — Unwanted Light in the Ocean (in [107])

D.E.Alburger Beta-ray spectrum of ^{40}K. Physical Review, **75**, 1442–1443. 1949.

[40] P.K.F.Grieder The Bern Penetrator. (in [112])

[41] K.Griest The Particle and Astrophysics of Dark Matter. Plenary talk Snowmass 94, Snowmass, Colorado, 1994.

[42] F.Halzen and J.G.Learned. High energy Neutrino Astronomy: Toward a $1km^3$ Detector.

J.G.Learned and A.Roberts. Toward a $1km^3$ Neutrino Telescope. (in [116])

Bezrukov et.al. Possibilities of Construction and Deployment of Big Underwater Neutrino Telescope on the Lake Baikal. (in [120])

[43] T.Hayashino A Monte Carlo Simulation of muon bundles in the Frèjus detector and DUMAND. (in [112])

[44] E.P.J.van den Heuvel and J.van Paradijs Röntgen–Doppelsterne. Spek.d.Wiss., Jan., 1994

P.K.MacKeown and T.Weekes. Kosmische Strahlen von Cygnus X3. Spek.d.Wiss., Jan.1986

[45] Higashi et.al.Nuovo Cimento 43A (1966) 334.
Davitaev et.al.,Acta Phys.Hung.29,supp 4 (1969) 53.
Vavilow et.al,Bull.Acad.Sci.USSR 34 (1970), 1759.
Fedorov et.al.,Proc.19th ICRC (1985) 8, 39.

[46] P.A.Johnson Contribution to the local cosmic ray flux from the Geminga supernova. Preprint Astro-PH-9404004, 1994.

[47] Punch et al. Detection of TeV photons from the active galaxy Markarian 421. Nature, 358,477 (1992).
Quinn et.al. "TeV gamma-rays from Markarian 501". Int.Astron.Union Astronomical Telegram No.6178, June 1995.

[48] Krabi, et.al. Sensitivity of the Baikal Neutrino Telescope NT–200 to Point Sources of Very High Energy Neutrinos. Preprint *DESY PHE 91-013*, Dec.1991.

[49] J.Krabi Suche nach hochenergetischen Neutrinos kosmischen Ursprungs mit dem Baikal-Neutrinoteleskop. Dissertation, DESY-IfH Zeuthen, March 1995.

[50] J.G.Learned Attenuation of Čerenkov photons in the ocean. *HDC Memo 81-10*, Hawaii Dumand Center. April 1981

[51] J.G.Learned Attenuation functions:*phomiz, phocas.* Private communication 1993.

[52] J.G.Learned Physics Goals and Triggering DUMAND II (in [111])

[53] J.G.Learned
DUMAND II System Description, DIR-13-91, May 1991
DUMAND II Specifications, DIR-14-91, May 1991

[54] C.Ley Berechnungen über den Nachweis hochenergetischer Neutrinos mit dem DUMAND Detektor. Diploma thesis, RWTH Aachen, May 1990.

[55] C.Ley Untersuchungen zur Rekonstruktion des radiativen D^{*0}-Zerfalls im H1-Experiment. *PITHA 94/55.* Phd thesis, RWTH Aachen Nov 1994.

[56] C.Ley and C.H.Wiebusch. The shape of EOM pulse-height distributions. Dumand Internal Report, 4-94, Jan. 1994.

[57] Lohmann et.al. Energy loss of muons in the energy range 1–10 000 GeV. *CERN 85-03.*

[58] E.Lorenz High energy gamma astronomy above $200 GeV$ (in [115]).

[59] Lubsandorzhiev et.al.
The optical sensor for the lake Baikal project (in [114]).
QUASAR-370 — The optical sensor of the Lake Baikal Neutrino Telescope (in [117]).

[60] K.Mannheim High energy neutrinos from extragalactic jets. Ast.Part.Phys, in press, 1995.

[61] M.A.Markov On high energy neutrino physics. Proc.Int.Conf.on High Energy Physics. Rochester, 1960.

[62] T.Matsumoto and S.Matsuno, private communication, 1995.

[63] T.Mikolajski Methodische Untersuchungen und Entwicklung eines Kalibrationssystems für das Neutrinoteleskop NT-200 im Baikalsee. Dissertation,DESY-IfH Zeuthen, December 1994.

[64] K.Mitsui Muon energy–loss distributions and its application to muon energy determination. *Phys.Rev.D* 45-9.3051–3059.May 1992.

[65] S.Miyake Emperical Formula for Range Spectrum of Cosmic Ray μ Mesons at Sea Level. J.Phys.Soc Japan **18** (1963) 1093.

[66] P.Mohrmann Untersuchung von Wechselwirkungen mit hoher Energiedeposition in einem Unterwasser–Neutrino–Teleskop. Diploma thesis, DESY IfH–Zeuthen, Okt.1994.

[67] M.Mori Upward going muons in Kamiokande. (in [134])

[68] D.J.Nicklaus Three String DUMAND Triggers University of Wisconsin, August 1993.

[69] A.Okada A Monte Carlo Study of the DUMAND II Array. ICRR-Report-209-90-2, March 1990.

[70] A.Okada Sensitivity of DUMAND II to AGN Neutrinos (in [134]) and ICRR-Report-269-92-7, June 1992.

[71] A.Okada Simulation of JOM Signal Generation and Muon Reconstruction . Dumand Internal Report, *DIR-3-93*, August 1993.
Private comunication, 1994.

[72] A.Okada On the Atmospheric Muon Energy Spectrum in the Deep Ocean and its Parametrisation. ICRR-Report-319-94-14, ISSN 1340-3745, June 1994.

[73] E.Osipova, private communication.

[74] R.D.Peccei The Physics of Neutrinos. Preprint *DESY 89-043*, April 1989.

[75] A.A.Petrukhin and V.V.Shestakov The influence of nuclear and atomic form factors on the muon bremsstrahlung cross section. Can.J.Phys.**46** (1968) 377.

[76] F.A.Raupach Point–Like Sources of High Energy Cosmic Rays Inaugural dissertation, RWTH Aachen, 1989.

Berger et.al. A search for high energy neutrinos from SN 1987A, the Crab, Hercules X-1 and Cygnus X-3 with the Frèjus detector. Z.Phys.C, 48, 221-226, 1990.

[77] L.K.Resvanis NESTOR: A Neutrino Particle Astrophysics Underwater Laboratory for the Mediteranian. (in [118])

L.K.Resvanis NESTOR: A neutrino particle astrophysics underwater laboratory for the Mediteranean. (in [134])

[78] W.Rhode Untersuchungen der Energiespektren hochenergetischer Muonen im Fréjusdetektor. Dissertation, WUB-DIS 93-11, Wuppertal Oktober 1993.

[79] I.L.Rozental Interaction of Cosmic Muons of High Energy Sov.Phys.Usp. 11 (1968) 49.

[80] R.C.Smith and K.Baker Optical properties of clearest natural waters ($200 - 800\ nm$). Appl.Opt.**20**No.2, Jan 1981.

[81] P.Sommers Neutrino fluxes from Compact Sources in the Galaxy (in [134])

[82] Ch.Spiering and P.Mohrmann Dependence of the muon visual range in water on the attenuation length and the PMT diameter. Baikal-Note 94-03.

[83] V.J.Stenger Optimizing Deep Underwater Neutrino Detectors. Proc.of 2nd NESTOR Int. Workshop, Pylos,Greece, Oct.1992.

[84] R.Svoboda Characteristics of the December 1993 Monster Buffer Data. DUMAND Internal Report 5-94, 1994.

[85] T.Stanev Astrophysical Sources of High Energy Neutrinos. Nucl.Phys.B (Poc.Suppl.) 14A 17-29, North Holland 1990.

[86] Stecker et al. High–Energy Neutrinos from Active Galactic Nuclei *Phys.Rev.Lett.* **66**, 2697–2700, May 1991. **Erratum** 69, 2738–1992.

[87] O.Streicher Nachweis von Myonen aus Wechselwirkungen atmosphärischer Neutrinos in Unterwasser–Neutrino–Teleskopen. Diploma thesis, DESY IfH–Zeuthen, Okt.1994.

[88] A.P.Szabo and R.J.Protheroe Implications of particle acceleration in active galactic nuclei for cosmic rays and high energy neutrino astronomy. Preprint ADT-AT-94-4, acc.f.pub. in *Ast.Part.Phys* University Adelaide, 1994.

[89] K.O.Thielheim Fundamental processes relevant for cosmic particle dynamics in compact objects – pulsars as cosmic accelerators. (in [115])

J.E.Gunn and J.P.Ostriker Acceleration of High–Energy Cosmic Rays by Pulsars. Phys.Rev.Lett.22,728-773, 1969.

[90] R.Tomski Über Messungen schwacher Lichtquellen in der Tiefsee Diploma thesis, RWTH Aachen, Feb.1992.

[91] C.H.Wiebusch Zum Nachweis schwacher Lichtquellen im Ozean mit Hilfe eines neuartigen großflächigen Photomultipliers. Diploma thesis, *PITHA 91/20*, RWTH Aachen, Dec.1991.

[92] Wiebusch et.al. Plane-wave Measurements with an EOM Dumand Internal Report, 6-94, June 1994.

[93] C.H.Wiebusch and G.Wurm Report to the DUMAND meeting, Hawaii, July 1993.

[94] R.Wischnewski The Lake Baikal Telescope NT-36 — A first Deep Underwater Multistring Array. Preprint *DESY 94-049, ISSN 0418-9833*, March 1994. (also in [117])

[95] R.Wischnewski Private communication.

[96] J.R.V.Zaneveld Optical Properties of the Keahole–DUMAND – Site. (in [106])

H.Bradner and G.Blackminton Measurements of uncolliminated Light transmission Distance (in [106])

Proposals, proceedings and text books

[97] BAIKAL WWW-server *http://www.ifh.de/baikal/baikalhome.html.*

[98] DUMAND WWW-server
http://www.phys.hawaii.edu/dmnd/dumand.html.
http://web.phys.washington.edu/local_web/dumand/aaa_dumand_home.html.

[99] AMANDA WWW-server *http://dilbert.lbl.gov/www/amanda.html.*

[100] KM-3 WWW-server
http://dilbert.lbl.gov/.
http://web.phys.washington.edu/local_web/km3/aaa_readme.html.

[101] The Baikal Collaboration. The Baikal Neutrino Telescope NT–200. Project Description *BAIKAL-92-03*, Nov., 1992.

[102] A.Roberts, editor. DUMAND Proceedings of the 1976 DUMAND Summer Workshops at Honolulu, Fermilab, 1976.

[103] A.Roberts and G.Wilkins editors. DUMAND Proceedings of the 1978 DUMAND Summer Workshops at Honolulu, Scipps Institute of Oceanography San Diego, 1978.

[104] J.G.Learned, editor. DUMAND 1979 Summer Workshops at Khabarovsk and Lake Baikal. August 22–31, 1979. University Hawaii.

[105] A.Roberts, editor. DUMAND Signal processing Workshop, University of Hawaii, February 1980.

[106] V.J.Stenger, editor. DUMAND –80. Proceedings of the 1980 International DUMAND Symposium Vol.1 & 2. July 24 – Aug.2, 1980. University Hawaii.

[107] A.Roberts, editor. DUMAND Signal processing Workshop. University of Hawaii, Feb.1982.

[108] DUMAND Collaboration. DUMAND, Proposal to Construct a Deep–Ocean Laboratory for the Study of High–Energy Neutrino Astrophysics, Cosmic Rays and Neutrino Interactions. The International DUMAND Collaboration, Okt.1982.

[109] A.Roberts, editor. Proceedings of the 1988 DUMAND Workshops on 1.Ocean Engineering and Deployment 2.Signal Processing. University of Hawaii, Jan.,Mar.1988.

[110] DUMAND Collaboration. DUMAND II — Proposal to Construct a Deep–Ocean Laboratory for the study of High–Energy Neutrino Astrophysics and Particle Physics. *HDC-2-88*, DUMAND Collaboration, University Hawaii, Aug,1988.

[111] K.K.Young and R.J.Wilkes, editors. Proceedings of the DUMAND 1990 Trigger Workshop University of Washington Seattle, July 1990.

[112] S.Tanaka and A.Yamaguchi, editors. Proceedings of the DUMAND 1990 Optical Module Workshop. Tohoku University Sendai Japan, Oktober 1990.

[113] DUMAND Collaboration. DUMAND II — Supplementary Proposal to Complete Construction of a Deep–Ocean Laboratory for the study of High–Energy Neutrino Astrophysics and Particle Physics. University Hawaii, Aug.1994.

[114] P.C.Bosetti, editor. Proceedings for the second conference on *Trends in Astroparticle–Physics*. ISBN 3-8154-3017-8. Teubner, 1994.

[115] P.K.F.Grieder, editor. Cosmic Rays 92 — Proceedings of the 13th European Cosmic Ray Symposium. Nucl.Phys.B (Proc.Suppl.) 33A,B, May 1993.

[116] Proceedings of the 23rd International Cosmic Ray Conference. Calgary, July 1993.

[117] L.K.Resvanis, editor Proceedings of the 3rd NESTOR Int. Workshop. Pylos, Greece, Oct. 1993.

[118] TAUP 93 Nucl.Phys.B (Proc.Suppl.) 35, May 1994.

[119] Neutrino Astrophysics Technology Workshop, JPL, Pasadena USA, March 1994.

KM^3 meeting , Saclay France, June 1994

Astroparticle-Physics in the next millenium, Snowmass USA, August 1994.

High Energy Neutrino Astrophysics, Irkutsk Russia, October 1994.

[120] Proceedings of the 24th International Cosmic Ray Conference. Rome, 1995.

[121] J.N.Bahcall Neutrino Astrophysics. Cambridge University Press, 1990.

[122] M.Fukugita and A.Suzuki, editors. Physics and Astrophysics of Neutrinos. Springer, ISBN 4-431-70136-2, Tokyo, 1994.

[123] T.K.Gaisser Cosmic Rays and Particle Physics. Cambridge University Press, 1990.

[124] F.Halzen and Alan D.Martin. Quarks and Leptons. Wiley & Sons, 1984.

[125] S.Hayakawa Cosmic Ray Physics. *Wiley* 1969.

[126] N.G.Jerlov Marine Optics ISBN 0-444-41490-8. Elsevier, 1976.
N.G.Jerlov and E.S.Nielsen, editors. Optical Aspects of Oceanography ISBN 0-12-3849050-0. Academic Press, 1976.

[127] W.J.Kaufman III. Universe. 3rd.ed. ISBN 0-7167-2094-9, 1991.

[128] W.R.Leo Techniques for Nuclear and Particle Physics Experiments. *Springer*, 1987.

[129] M.S.Longair High energy astrophysics. *Cambridge University Press*, 1981.

[130] D.H.Perkins Introduction to High Energy Physics. Addison–Wesley, 1987.

[131] E.Seibold and W.H.Berger. The Sea Floor – An Introduction to Marine Geology. Springer.

H.J.Rösler and H.Lange. Geochemische Tabellen. Ferdinand Enke Verlag Stuttgart.

James Kennett Marine Geology.

[132] S.L.Shapiro and S.L.Teukolsky Black Holes, White Dwarfs and Neutron Stars Wiley, ISBN 0-471-87316-0, 1983.

[133] Ch.Spiering Auf der Suche nach der Urkraft. ISBN 3-322-00315-9, Leipzig 1989.

[134] V.J.Stenger, J.G.Learned, S.Pakvasa, X.Tata, Editors. Workshop on High Energy Neutrino Astrophysics Proceedings, ISBN 981-02-1039-6, World Scientific 1992.

[135] C.Sutton. Spaceship Neutrino. Cambridge University Press, 1992.

Technical Books, Tables and Manuals

[136] Particle Data Group. Review of Particle Properties – August 1994. Phys.Rev.D 50,3, ISSN 0556-2821.

Particle Data Group. Particle Physics Booklet – July 1994. from Phys.Rev.D 50,1173.

[137] Photomultiplier handbooks:

Photomultiplier tubes — principles & applications. Philips photonics, 1994.
Data Handbook Photomultipliers Philips Components, 1991
Photomultiplier Handbook — Theory, Design Application RCA.

[138] Several manuals and data sheets
Vitrovex — Glass Instrument Housings for Deep ocean use. & Private comunication. Nautilus Marine service GmbH, Germany.
Glass Flotation spheres. Benthos, Inc, USA. Semicosil 912, SilGel 604. Wacker-Chemie GmbH, Germany.

[139] I.Belolaptikov and E.Osipova Baikal Monte Carlo. Program description. In preparation.

[140] U.Berson and C.H.Wiebusch The European Optical Module for DUMAND II — A technical description. Dumand Internal Report, 5-93, September 1993.

[141] F.Beißel und V.Commichau. A fast Charge to Time Converter V04. Internal Report HD04 IIIB, III.Phys.Inst.RWTH Aachen, Feb.1991.

[142] V.Commichau. FADC unit Version V02B. Internal report III.Phys.Inst.RWTH Aachen, Feb.1984. H.K.Trieu. Entwicklung eines 8 Bit Transientenrecorders (FADC) mit 200 MHz Abtastrate zur Untersuchung von Driftkammersignalen. Diploma thesis, *PITHA 93/05*, RWTH-Aachen, March 1993

[143] J.Krabi and R.Wischnewski. Short description of MC- and Data-Formats used for Reconstruction and Higher level analysis software. Internal note, Zeuthen, Okt.1993.

[144] D.J.Nicklaus DUMAND Archived Data Format Description. Dumand Internal Report, *DIR-10-92*. University of Wisconsin, Aug., 1992.

Private comunication.

[145] O.Streicher and C.H.Wiebusch RDMC 1.08 Installation and user's guide. DESY IfH Zeuthen, Mai 1995.

[146] O.Streicher and C.H.Wiebusch merz 1.1.0 Installation and user's guide. DESY IfH Zeuthen, June 1995.

[147] O.Streicher and C.H.Wiebusch calib 1.00 Installation and user's guide. DESY IfH Zeuthen, March 1995.

[148] O.Streicher recoos Installation and user's guide. DESY IfH Zeuthen, in preparation.

[149] O.Streicher rtt Installation and user's guide. DESY IfH Zeuthen, in preparation.

[150] C.H.Wiebusch Dada Installation and user's guide. DESY IfH Zeuthen, in preparation.

[151] Wiebusch et.al. gen - event generators for neutrino telescopes. Installation and user's guide. DESY IfH Zeuthen, in preparation.

[152] FFREAD, Format Free Input Processing. CERN Program library Q123.

[153] GEANT, Detector Description and Simulation Tool. CERN Program library, W 5013 Version 3.16, 1993.

[154] HBOOK, Statistical Analysis and Histogramming. CERN Program library Y250.

[155] HIGZ, High Level Interface to Graphics and Zebra. CERN Program library Q120.

[156] P.Horowitz and W.Hill. The Art of Electronics. Cambridge University Press, 1989.

[157] PAW, Physics Analysis Workstation. CERN Program library Q121, Oct.1993.

[158] W.H.Press, B.P.Flannery, S.A.Teukolsky, W.T.Vetterling. Numerical Recipes — The art of scientific computing *Cambridge University Press*, 1986

[159] T.Sjöstrand Pythia 5.6 and Jetset 7.3 Physics and Manual. Theory division, CERN, May 1992.

[160] M.G.Sobel A practical guide to the Unix system. 3rd ed., ISBN 0-8053-7565-1. 1995.

[161] Helmut Kopka. LaTeX— Eine Einführung. *Addison-Wesley*, 1988.

Helmut Kopka. LaTeX— Erweiterungsmöglichkeiten. *Addison-Wesley*, 1990.

List of Figures

List of Tables

Glossary

ADC	**A**nalog **D**igital **C**onverter
AGN	**A**ctive **G**alactic **N**uclei
AMANDA	**A**ntarctic **M**uon **and** **N**eutrino **D**etector **A**rray
BAND	BAIKAL AMANDA NESTOR DUMAND
BOM	**B**aikal **O**ptical **M**odule **A**nd **N**eutrino **D**etector **A**rray
CAMAC	**C**amps **A**ttacks **M**an **A**t **C**omputer
CM	**C**alibration **M**odule for DUMAND
CEM	**C**entral **E**lectronic **M**odule for BAIKAL
DAC	**D**igital **A**nalog **C**onverter
Dada	**D**igitisation **A**nd **D**etector **A**nalysis — detector simulation program (GEANT)
DMQT	**D**u**M**and **Q**–**T** — fast circuit of the EOM
DUMAND	**D**eep **U**nderwater **M**uon **A**nd **N**eutrino **D**etection
EOM	**E**uropean **O**ptical **M**odule
FWHM	**F**ull **W**idth **H**alf **M**aximum
GEANT	Detector description and simulation package from CERN
HEPTAGON	Epoxiframe (7 arms) for the BAIKAL detector
JB	**J**unction **B**ox for DUMAND
JBEM	**J**unction **B**ox **E**nvironmental **M**odule for DUMAND
JOM	**J**apanese **O**ptical **M**odule
JULIA	**J**oint **U**nderwater **L**aboratory and **I**nstitute for **A**stro–Particle–Physics
MDF	**M**inimum **D**etectable **F**lux
OCTAGON	DUMAND II , full detector
OM	**O**ptical **M**odule
QT	Charge (**Q**) to **T**ime conversion
PE	**P**hoto**e**lectron
PMT	**P**hoto**m**ultiplier **T**ube
RCU	**R**emote **C**ontrol **U**nit
RDMC	**R**ea**D** **M**onte **C**arlo Data — SiEGMuND I/O library
SC	**S**tring **C**ontroller for DUMAND
SM	**S**ystem **M**odule for BAIKAL
SEM	**S**tring **E**lectronic **M**odule for BAIKAL
SiEGMuND	**Si**mulation of **E**vents with **G**EANT for **Mu**on and **N**eutrino **D**etectors.
SVJASKA	Hierarchical unit of the BAIKAL detector
TOT	**T**ime **O**ver **T**hreshold
TRIAD	DUMAND II , stage 1 (3 strings)
UHE	**U**ltra **H**igh **E**nergy
VHE	**V**ery **H**igh **E**nergy

Index

Acknowledgement

This work would not have been realized without the help and support of various people and institutions. I thank Prof.Dr.G.Flügge and Prof.Dr.Ch.Berger for taking over the responsibility for this thesis and for giving me the chance to continue this exciting branch of physics at Aachen.
I am indebted to Dr.Christian Spiering, who not only supervised this work, but also spent large efforts getting me through all difficulties and has last but not least been an excellent teacher and friend.
Also thank you, my inofficial co-advisor and friend Dr.Christoph Ley, for quite a lot!
The electronic team around Dr.V.Commichau, especially C.Camps, has continuously supported me. Their help went far beyond the scope of electronics. I thank also all other members of the III. Physikalische Institut, RWTH Aachen.
Special thanks goes to to Olè Streicher for his smart ideas during our SiEGMuND project and to my companion during the EOM development Ulrich Berson.
Спасибо to the whole BAIKAL collaboration, namely Igor Belolaptikov, Alexander A.Doroshenko, Dr.Bayarto K.Lubsandorzhiev, Dr.Elonora Ossipova and Dr.Igor Sokalski. Prof.Dr.G.V.Domogatzky made it possible for me to join this excellent team of physicists. Special thanks also to the great Zeuthen team: Stephan Hundertmark, Dr.Albrecht Karle, Dr.Jaanus Krabi, Dr.Thomas Mikolajski, Dirk Pandel, Olè Streicher, Dr.Thorsten Thon, Dr.Ralf Wischnewski.
Prof.Peter C.Bosetti introduced me to this field of physics. He is responsible for the initial idea of this thesis and strongly enriched it at various stages. His group, the Aachen DUMAND – gang was a vital platform.
A big mahalo goes to the DUMAND – collaboration, especially to Prof.Dr.P.K.F.Grieder, Prof.Dr.John G.Learned, Prof.P.Minkowsky and Dr.A.Okada.
I thank all contributors to the EOM-project. I personally thank Prof.P.Koske for his engagement in this project and his support for my work at Kiel and Hawaii. The people involved in this project are listed in details in [140]. Especially I want to mention F.Beißel, Eduard Hermens, Dr.Michael Rietz, Gerhard Wurm from RWTH Aachen, Thomas Bolln, Dr.Urban Keussen, Dr.Jürgen Rathlev from University Kiel, Dr.Lars Thollander from University Stockholm, S.O.Flyckt from Philips Photonics Brive, Dr.Shigenobu Matsuno and Marc Mignard from University Hawaii. I thank also my house-mate Volker Pichinot for his friendship and patience during the long time at Kiel.
I thank all proof-readers, especially Dr.Christoph Ley, Dr.Christian Spiering, Dr.Reiner Schulte, Dr.Ralf Wischnewski.
I wish to thank all my friends and my family especially Jutta, Stephanie and my parents.
This work was supported by the *Claussen Stiftung im Stifterverband für die Deutsche Wissenschaft* (Projekt-Nr.:TS 082/48/92).

I dedicate this work to the memory of my dear friend Dr.Andreas Kaser, who died due to a sudden leukemia on 3 April 1995. He was strongly involved in the evaluation of eq.(5.76) and eq.(A.116) and accompanied me during the time of scientific education with help and good fellowship.

Lebenslauf

Persönliche Daten

Name	Wiebusch
Vornamen	Christopher, Henrik, Viktor
Geboren	10. Juni 1966 in Bonn

Ausbildungsweg

1972 - 1976	St.Andreas Grundschule in Bonn-Bad Godesberg
1976 - 1985	Besuch des Pädagogiums Godesberg, Abitur
Okt. 1985	Beginn des Studiums der Physik an der RWTH Aachen
April 1988	Diplom Vorprüfung in Physik
März 1992	Abschlußdes Diploms in Physik
März 1992	Beginn der Promotionsarbeit Förderung durch ein Stipendium der "'Claussen Stiftung"' im Stifterverband für die Deutsche Wissenschaft
Dez.1995	Promotionsprüfung in Physik